GEOPHYSICAL SIGNATURES OF HYDROTHERMAL ALTERATION FOR VOLCANO MONITORING

Shreya Jagdish Kanakiya

A thesis submitted in fulfillment of the requirements for the degree of Doctor of Philosophy in Geology, the University of Auckland, 2022.

Abstract

Hydrothermal alteration changes the petrophysical properties of stratovolcanoes worldwide. But, how these changes affect volcano dynamics and manifest themselves in geophysical data used to monitor and study the internal structure of volcanoes is not as simple as suggested by prior investigations. This thesis aims to address this challenge by systematically measuring, in the laboratory, the petrophysical and geophysical (elastic and magnetic) properties of variably altered volcanic rocks, from Whakaari and Mt. Taranaki, New Zealand. This thesis adds three new ideas to the current understanding of acid-sulfate hydrothermal alteration in volcanoes.

First, in volcanic conduits, acid-sulfate alteration affects the fluid pathways and elastic properties of lavas, tuffs, and breccias differently. In lavas, alteration creates fluid pathways and decreases rock stiffness by net dissolution. In contrast, in the inherently porous and permeable tuffs, alteration reduces fluid pathways and increases rock stiffness by net precipitation of secondary minerals. Compaction of tuffs under subsurface pressures and alteration-related sealing can form low porosity and low permeability zones within the conduit. Such zones could promote fluid-pressure build-up and predispose the volcano to explosive eruptions.

Second, altered lavas can have higher remanent magnetization (NRM) than fresh lavas. For most rocks from Whakaari and Mt. Taranaki, NRM dominates induced magnetization (susceptibility), highlighting the importance of measuring both induced and remanent magnetization of samples used to constrain field-scale data. These findings urge caution in assuming that altered regions in volcanic environments would only manifest as areas of reduced magnetization in field magnetic surveys. Altered regions posing a potential edifice collapse hazard could be associated with high magnetization resulting from high NRM.

Third, the role of hydrothermal alteration in weakening volcanic rocks is not merely dependent on the degree of alteration but also on the type of alteration. Altered rocks with precipitation of strong secondary minerals and without extensive dissolution, are unlikely to have been substantially weakened to cause slope instabilities. The implications

of the thesis results are discussed in the context of analyzing and interpreting ground deformation and magnetic survey data for volcano monitoring. Furthermore, the elastic and magnetic properties data presented in this thesis provides needed constraints for geophysical inversions of acid-sulfate altered volcanic regions.

Acknowledgements

This research is made possible with the support of many colleagues, family, and friends. Firstly, a big thank you to my supervisors, Ludmila Adam, Michael C Rowe, and Jan M Lindsay, for their help and guidance on research and immense support and encouragement. My deepest gratitude to family and friends who have been a part of the journey. Especially my parents, Jagdish and Varsha Kanakiya, and partner Arnold Fernandes for always believing in me. Thanks also to my siblings, their partners, my parents-in-law, and cousins for their love and support. My journey would have been challenging without the unwavering encouragement from all these people, especially during setbacks. Special mention to my nieces and nephew for always keeping my curiosity alive with their questions.

Thanks to Kasper van Wijk for reviewing my Ph.D. proposal and helping in the PORO lab when needed. I'd also like to thank my Ph.D. proposal committee and thesis examination committee for their time and valuable feedback. Thank you to Ben Kennedy and Geoff Lerner for help with sample collection, Joel Sarout for insights into designing the multi-stage porosity experiment, Geoff Kilgour and Shane Cronin for valuable discussions regarding Whakaari, Gillian Turner for her help and guidance with magnetic properties measurements and interpretation, Lionel Esteban for helping with porosity and permeability measurements, and Andres Arcila-Rivera for help with thin section preparation and technical support.

Thanks to the New Zealand eScience Infrastructure for providing high-performance computing infrastructure to analyze the XRD data. Thanks to David Wackrow and Neville Hudson for their technical support and readiness to help. Thank you also to Simrin Ahmed, Anna-Marie Simcock, Kamalini Gnaniah, and Samantha Huang for making administrative work relatively less tedious during my time at the University of Auckland with their willingness to help.

I'd also like to acknowledge the funding organizations that supported this research through scholarships and research grants: Earthquake Commission (Doctoral scholarship - University of Auckland-Earthquake Commission Capability Building Fund), University

of Auckland (R N Brothers Memorial Scholarship, Faculty Research Development Fund), Royal Society of New Zealand (Hutton Fund), and Geoscience Society of New Zealand (Jim Ansell Geophysics Scholarship). I'd also like to thank the Geoscience Society of New Zealand and the American Geophysical Union for their travel grants (Young Researcher Travel Grant and Fall Meeting General Student Travel Grant, respectively) which allowed me to present my research findings at the annual meeting of the American Geophysical Union.

Thank you to fellow students: Stephanie, Pablo, Jonathan, Evert, Steve, and James for always being ready to help when needed. Thanks to my office mates and other colleagues I have crossed paths with during my time at the University of Auckland, who made it a wonderful experience.

Contents

List of Figures

List of Tables

Statement of Contribution

School of Graduate Studies
AskAuckland Central
Alfred Nathan House
The University of Auckland
Tel: +64 9 373 7599 ext 81321
Email: postgradinfo@auckland.ac.nz

Co-Authorship Form

This form is to accompany the submission of any PhD that contains published or unpublished co-authored work. **Please include one copy of this form for each co-authored work**. Completed forms should be included in all copies of your thesis submitted for examination and library deposit (including digital deposit), following your thesis Acknowledgements. Co-authored works may be included in a thesis if the candidate has written all or the majority of the text and had their contribution confirmed by all co-authors as not less than 65%.

Please indicate the chapter/section/pages of this thesis that are extracted from a co-authored work and give the title and publication details or details of submission of the co-authored work. Chapter 2: The role of tuffs in sealing volcanic conduits. Manuscript under review at Geophysical Research Letters.	
Nature of contribution by PhD candidate	Sample collection; conception and design of the study; acquisition and analysis of XRD, thin section, BSE-EDS, porosity, and stiffness data; data interpretation; and writing the manuscript.
Extent of contribution by PhD candidate (%)	90

CO-AUTHORS

Name	Nature of Contribution
Ludmila Adam	Sample collection, conception and design of the study, data interpretation, revision of the manuscript draft.
Michael C Rowe	Sample collection, conception and design of the study, data interpretation, revision of the manuscript draft.
Jan M Lindsay	Data interpretation, revision of the manuscript draft.
Lionel Esteban	Acquisition of permeability data, data interpretation, revision of the manuscript draft.

Certification by Co-Authors

The undersigned hereby certify that:

- the above statement correctly reflects the nature and extent of the PhD candidate's contribution to this work, and the nature of the contribution of each of the co-authors; and
- that the candidate wrote all or the majority of the text.

Name	Signature	Date
Ludmila Adam		6-15-21
Jan M Lindsay		29 June 2021

Michael C Rowe	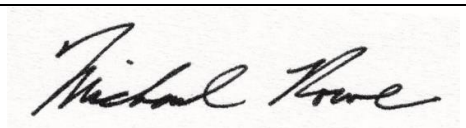	22-07-2021
Lionel Esteban		16 June 2021

School of Graduate Studies
AskAuckland Central
Alfred Nathan House
The University of Auckland
Tel: +64 9 373 7599 ext 81321
Email: postgradinfo@auckland.ac.nz

Co-Authorship Form

This form is to accompany the submission of any PhD that contains published or unpublished co-authored work. **Please include one copy of this form for each co-authored work**. Completed forms should be included in all copies of your thesis submitted for examination and library deposit (including digital deposit), following your thesis Acknowledgements. Co-authored works may be included in a thesis if the candidate has written all or the majority of the text and had their contribution confirmed by all co-authors as not less than 65%.

Please indicate the chapter/section/pages of this thesis that are extracted from a co-authored work and give the title and publication details or details of submission of the co-authored work. Chapter 3: High remanent magnetization measured in hydrothermally altered lavas. Manuscript under review at Geophysical Research Letters.	
Nature of contribution by PhD candidate	Conception and design of the study; acquisition and analysis of magnetic susceptibility, NRM, X-ray map, BSE-EDS, and AFD data; data interpretation; and writing the manuscript.
Extent of contribution by PhD candidate (%)	90

CO-AUTHORS

Name	Nature of Contribution
Gillian M Turner	Design of study, acquisition of magnetic susceptibility with temperature data, data interpretation, revision of the manuscript draft.
Michael C Rowe	Conception and design of the study, data interpretation, revision of the manuscript draft.
Ludmila Adam	Conception and design of the study, data interpretation,revision of the manuscript draft.
Jan M Lindsay	Data interpretation, revision of the manuscript draft.

Certification by Co-Authors

The undersigned hereby certify that:

- the above statement correctly reflects the nature and extent of the PhD candidate's contribution to this work, and the nature of the contribution of each of the co-authors; and
- that the candidate wrote all or the majority of the text.

Name	Signature	Date
Gillian M Turner		14 July 2021
Michael C Rowe	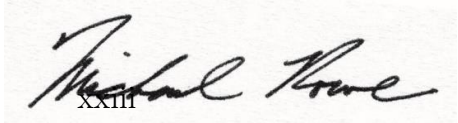	22-07-21

Ludmila Adam		6-15-21
Jan M Lindsay		29 June 2021

School of Graduate Studies
AskAuckland Central
Alfred Nathan House
The University of Auckland
Tel: +64 9 373 7599 ext 81321
Email: postgradinfo@auckland.ac.nz

Co-Authorship Form

This form is to accompany the submission of any PhD that contains published or unpublished co-authored work. **Please include one copy of this form for each co-authored work**. Completed forms should be included in all copies of your thesis submitted for examination and library deposit (including digital deposit), following your thesis Acknowledgements. Co-authored works may be included in a thesis if the candidate has written all or the majority of the text and had their contribution confirmed by all co-authors as not less than 65%.

Please indicate the chapter/section/pages of this thesis that are extracted from a co-authored work and give the title and publication details or details of submission of the co-authored work. Chapter 4: Petrophysical and corresponding geophysical properties of variably altered lavas from Mt. Taranaki. Manuscript in preparation for submission to the Journal of Volcanology and Geothermal Research.	
Nature of contribution by PhD candidate	Sample collection; conception and design of the study; acquisition and analysis of XRD, thin section, ambient porosity, magnetic susceptibility, NRM, and stiffness data; data interpretation; and writing the manuscript.
Extent of contribution by PhD candidate (%)	80

CO-AUTHORS

Name	Nature of Contribution
Ludmila Adam	Sample collection, conception and design of the study, data interpretation, revision of the manuscript draft.
Michael C Rowe	Sample collection, conception and design of the study, data interpretation, acquisition of BSE-EDS data, revision of the manuscript draft.
Lionel Esteban	Acquisition of porosity and permeability data under pressure, revision of the manuscript draft.
Jan M. Lindsay	Data interpretation, revision of the manuscript draft.

Certification by Co-Authors

The undersigned hereby certify that:

- the above statement correctly reflects the nature and extent of the PhD candidate's contribution to this work, and the nature of the contribution of each of the co-authors; and
- that the candidate wrote all or the majority of the text.

Name	Signature	Date
Ludmila Adam		6-15-21

Michael C Rowe	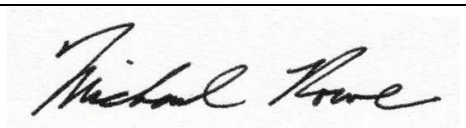	22-07-2021
Lionel Esteban		16 June 2021
Jan M Lindsay		29 June 2021

Chapter 1

Introduction

Hydrothermal alteration changes the physical and chemical properties of volcanoes worldwide (Mayer et al., 2016; Zimbelman et al., 2005). These changes can play a role in predisposing volcanoes to phreatic and phreatomagmatic eruptions or slope failures. For example, hydrothermal alteration is thought to have destabilized lava domes and edifices of several volcanoes such as Merapi (Indonesia) (M. J. Heap et al., 2019), Mt. Rainier (USA) (Reid et al., 2001), Nevado del Ruiz volcano (Colombia) (López & Williams, 1993), and La Soufrière de Guadeloupe (M. J. Heap et al., 2021a). A pressurized hydrothermal seal and volatile accumulation are thought to have triggered the 2017 phreatomagmatic eruption of Poás volcano (Costa Rica) (de Moor et al., 2019). Similar alteration-related sealing processes are also considered to be driving eruptions at other volcanoes like Soufrière Hills (Montserrat) (Edmonds et al., 2003), Ontake (Japan) (Stix & de Moor, 2018), and Whakaari (New Zealand) (Burton et al., 2021; Christenson et al., 2017). But little experimental evidence exists on how such a seal develops in conduit-filling rocks.

Given the potential hazards posed by hydrothermal alteration, it is vital to identify and monitor altered regions within volcanic edifices. But how these altered regions manifest in geophysical data used to monitor volcanoes is not well understood. Field geophysical surveys need petrophysical data from controlled laboratory experiments to make accurate interpretations of subsurface processes. There is, however, a paucity of laboratory-based constraints that encompass both the petrophysical and corresponding geophysical properties of representative samples. This thesis aims to address this with an overarching goal of establishing links between hydrothermal alteration-related petrophysical changes in volcanoes and their geophysical properties to inform volcano monitoring. This goal is achieved by systematically measuring the petrophysical and geophysical properties of volcanic rocks with different degrees of alteration from Whakaari and Mt.

Taranaki at a laboratory scale.

The petrophysical characterization includes determining the rocks' mineralogy and performing geochemical and microstructural analysis. It further involves measuring the porosity and permeability of the rocks at atmospheric and subsurface pressure conditions representative of the volcanic systems. These analyses provide a quantitative measure of the type and intensity of alteration and information on its processes. Furthermore, they inform how alteration-related changes and subsurface pressures would affect fluid flow within the volcano. To relate the petrophysical changes in rocks due to hydrothermal alteration to their geophysical signatures, experimental data on magnetic susceptibility and natural remnant magnetization, as well as compressional and shear wave velocities at in-situ volcano pressure conditions is acquired. Together, these data help us derive links between hydrothermal alteration-related petrophysical changes and their corresponding geophysical signatures to inform volcano monitoring.

1.1 Background

1.1.1 Hydrothermal systems and alteration processes

A hydrothermal system is defined as a region in which hot fluids circulate in the Earth's subsurface at elevated temperatures (50^oC to $>500^oC$) and pressures (Pirajno, 2009). The essential components of a hydrothermal system include a heat source to provide the energy for circulation, a fluid phase such as magmatic fluids, seawater, or meteoric water, and permeable pathways in the host rock through which the fluids can move (Pirajno, 2009; D. White, 1974). In active volcanoes, such a system develops when heat is transferred from a deep magmatic source to the surface resulting in the circulation of hot ground-water and magmatic fluids through the host rock (Hedenquist & Lowenstern, 1994) (Figure 1.1). As these host rocks interact with the circulating fluids, there is a physicochemical disequilibrium between the two (Pirajno, 2009). This sets off fluid-rock reactions that tend to work towards re-equilibration of the system by altering the physical, chemical, and mineralogical properties of the host rock (Mayer et al., 2016; Pola et al., 2012; Navelot et al., 2018). This process is known as hydrothermal alteration.

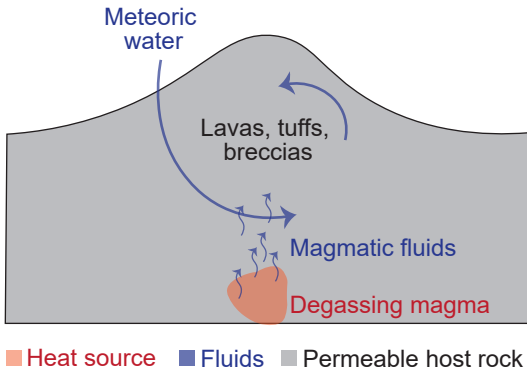

Figure 1.1: Schematic showing the essential components of a volcanic hydrothermal system. The heat from degassing magma drives the circulation of magmatic fluids and meteoric water through fluid pathways in lavas, tuffs, and breccias.

Hydrothermal alteration processes include hydrogen ion metasomatism, base cation exchange, dissolution, secondary mineral precipitation, and replacement (Berger, 1998; Robb, 2013). Hydrogen ion metasomatism involves the decomposition of water into H^+ and OH^-, which are selectively consumed during the reactions with silicate minerals (Hemley & Jones, 1964). Base cation exchange in a mineral involves the replacement of a cation by another (e.g., Na^+ replaces K^+ in microcline and converts it to albite; K^+ is then released into the fluid) (Pirajno, 2009). Dissolution is the leaching of primary volcanic glass and minerals (e.g., plagioclase, muscovite, pyroxene) from the host rock (Hedenquist & Lowenstern, 1994). Secondary mineral precipitation is the formation of new minerals that are stable at the specific alteration conditions (pressure, temperature, pH), in the pores and fractures of the host rock (Ghorbani et al., 2018; Pirajno, 2009; Robb, 2013). Replacement is an alteration process where unstable primary minerals and volcanic glass are replaced by new minerals that are stable at the conditions of alteration (Ghorbani et al., 2018; Shanks, 2012).

Which of the above alteration processes dominate depends on the evolving physicochemical conditions during the fluid-rock reactions. The main factors controlling these physicochemical conditions are (a) temperature, (b) pressure, (c) nature of the fluid (i.e., pH; concentration, activity and chemical potential of the fluid components like H^+, K^+, O_2, CO_2, SO_2, and H_2S) (e) water/rock ratio (f) chemical and physical nature of the host rocks (g) permeability and (h) duration of fluid-rock reactions (Berger, 1998; Hemley & Jones, 1964; Robb, 2013). Figure 1.2 shows how temperature and pH of the fluid control which secondary minerals precipitate and are stable in hydrothermal systems. Depending on the alteration processes at play, the petrophysical and geophysical properties of the host rock can be affected.

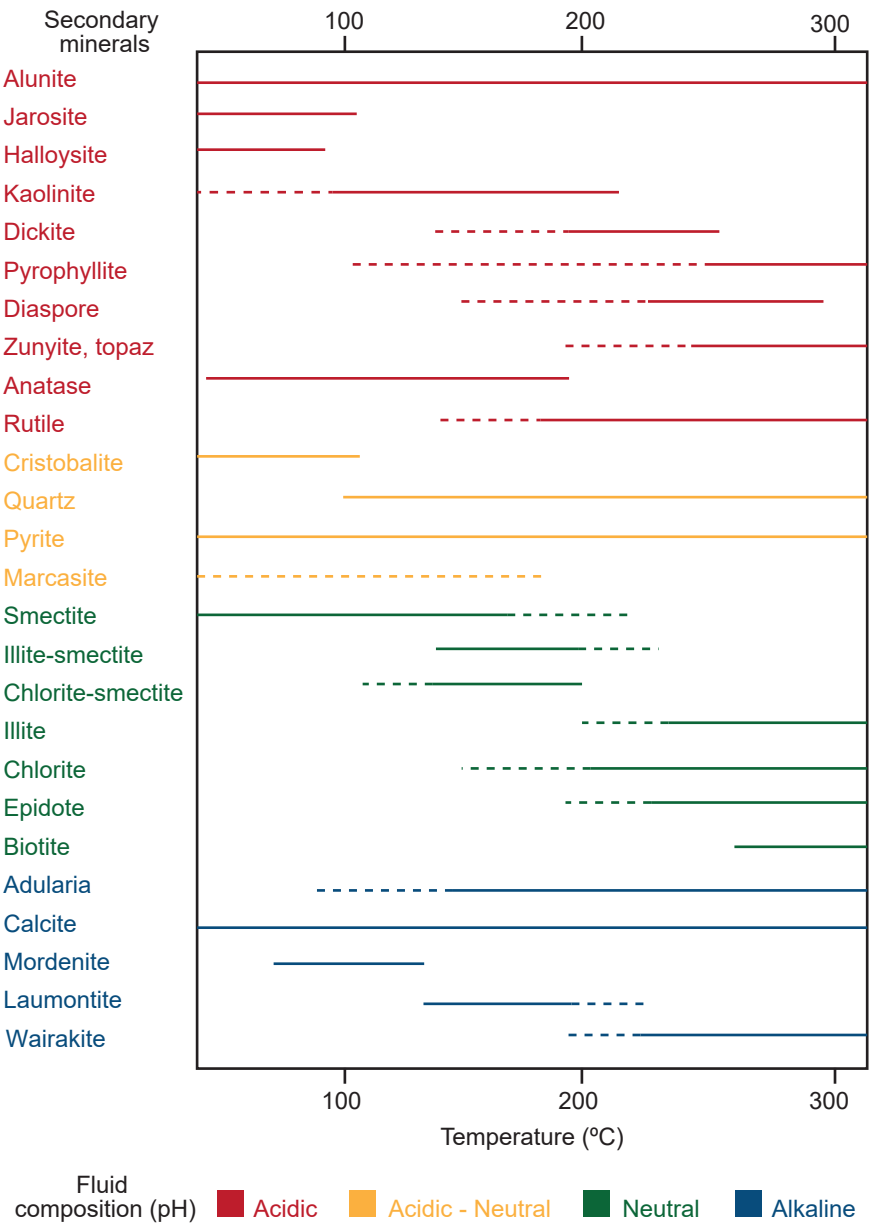

Figure 1.2: Fluid environment (pH) and temperature range at which secondary minerals commonly found in hydrothermal systems precipitate. Modified from Pirajno (2009).

1.1.2 Petrophysical and geophysical properties affected by hydrothermal alteration

Alteration processes such as base cation exchange, hydrogen ion metasomatism, secondary mineral precipitation, and replacement associated with fluid-rock reactions can change the elemental composition and mineralogy of the host rocks (Large et al., 2001). In volcanic environments, some common secondary minerals that precipitate in the pores

and fractures of the host rock include alunite, kaolinite, illite, smectite, and amorphous silica (Mas et al., 2006; Zimbelman et al., 2005). Hydrothermal alteration processes can also increase or decrease the porosity and permeability of the host rocks. If dissolution processes dominate, then leaching of the host rock can lead to the creation of pore spaces or fractures, thereby increasing the porosity of the host rocks (Kanakiya et al., 2017; Sruoga et al., 2004). If these new pore spaces and fractures interconnect with the pre-existing pore network, the permeability of the host rocks will also increase. On the other hand, if the dominating alteration process is secondary mineral precipitation, then the minerals filling the interconnecting pore spaces and fractures of the host rocks reduce porosity and permeability (Dobson et al., 2003; Sruoga et al., 2004).

Changes in mineralogy and porosity of the host rocks due to hydrothermal alteration can, in turn, alter their elastic properties (Durán et al., 2019a) that are of interest to geophysical surveys. If dissolution processes dominate, the rocks' elastic moduli (stiffness) will decrease, whereas if secondary mineral precipitation dominates, their elastic moduli increase. Characterizing alteration-related changes in elastic moduli is critical to wave propagation because when a seismic waveform propagates through the subsurface, the medium is temporarily deformed (strained). This deformation is dependent on the rock elastic properties, which are characterized in terms of the Young's, bulk, and shear moduli, and Poisson's ratio. Overall, rock stiffness controls wave velocities which are used to image and monitor volcanoes. Understanding the effects of rock alteration on elastic moduli is also essential for the interpretation of ground deformation data (Bazargan & Gudmundsson, 2019; M. J. Heap et al., 2020a) and informing volcanic slope stability assessments (Voight & Elsworth, 1997; Voight, 2000).

Hydrothermal alteration also changes the magnetic properties of rocks that are of interest to geophysical surveys. Unlike elastic properties, which represent the bulk rock, magnetic properties of rocks depend on a few Fe-bearing minerals that generally comprise a small volume of the rock's bulk mineralogy (Dentith & Mudge, 2014). The total magnetization of a rock is dependent on a combination of ferrimagnetic, antiferromagnetic, paramagnetic, and diamagnetic minerals. Minerals of particular importance are ferrimagnetic Fe-Ti oxides such as magnetite, maghemite, titanomagnetite, and Fe-sulfides such as pyrrhotite or greigite, which are capable of giving rise to a magnetic field in the absence of an applied field (Dearing, 1994; Tauxe, 2010). This magnetization is called remanent magnetization which is generally acquired by the rock at the time of formation as the rock cools to a temperature below the Curie temperature or Néel temperature of its magnetic minerals (L. Brown & McEnroe, 2011). Other paramagnetic and diamagnetic rock-forming minerals, such as feldspars, pyroxenes, amphiboles, ilmenite, pyrite,

clays can be weakly magnetic only in the presence of an externally applied magnetic field (Dearing, 1994). This magnetization is called induced magnetization. The total magnetization of a rock is a vector sum of its inherent remanent magnetization and induced magnetization (Dentith & Mudge, 2014). The stability of magnetic minerals is sensitive to the physicochemical conditions during hydrothermal alteration, which can either create or destroy the magnetic minerals in volcanic rocks (Riveros et al., 2014). Such changes in the magnetic mineralogy of the rocks directly influence the magnetization signals recorded in geophysical surveys (Airo, 2002).

Given the complexity with which hydrothermal alteration affects the petrophysical and geophysical properties of host rocks, our knowledge on this subject and how alteration plays a role in sealing volcanic conduits or slope failures is still limited as discussed in detail in Section 1.3. This thesis advances our understanding of this topic by using samples from two representative stratovolcanoes - Whakaari (White Island) and Mt. Taranaki.

1.2 Study areas - Whakaari and Mt. Taranaki

1.2.1 Geologic setting, structure, and hydrothermal system

Whakaari and Mt. Taranaki are active stratovolcanoes in New Zealand. Whakaari is New Zealand's most active volcano, located about 50 km east of the North Island (Figure 1.3). It is a part of the Taupō Volcanic Zone which has three segments. The northern and southern parts of the zone are composed primarily of andesitic stratovolcanoes (Whakaari, Mt.Tongariro, Mt. Ngāuruhoe, and Mt. Ruapehu) and no calderas (Leonard et al., 2021; Wilson et al., 1995). Its central 125 km region is dominated by rhyolitic calderas (Wilson et al., 1995). The Taupō Volcanic Zone is a rifted arc resulting from the subduction of the Pacific Plate beneath the Australian Plate (Cole & Lewis, 1981; Stern et al., 2006; Stern & Benson, 2011). The oblique subduction of the Pacific plate begins at the Hikurangi trench (Wallace et al., 2004). This subduction causes the central North Island to rotate clockwise, thereby developing an extensional regime which is accommodated by normal faulting predominantly in the Taupō Fault Belt (Kilgour et al., 2021). Mt. Taranaki is also located on the North Island (Figure 1.3), about 150 km west of the Taupō Volcanic Zone and about 400 km west of the active Hikurangi trench. It is part of the Taranaki Volcanic Lineament, which is a chain of andesitic volcanoes (Cronin et al., 2021). This chain includes three relict volcanoes-Paritutu including the Sugar Loaf Islands, Kaitake, Pouakai, and the currently active and youngest Mt. Taranaki (Locke et al., 1994; Price

et al., 1999). Despite the subduction type signatures in the compositions of erupted material at Mt. Taranaki (Price et al., 1999), its unusual location has been challenging to explain with respect to the current subduction setting of New Zealand (Cronin et al., 2021).

Whakaari and Mt. Taranaki are different in terms of their structure and hydrothermal activity as well. Whakaari is partially submerged, rising 321 m above sea level with a subaerial extent of about 2.5 km $\times$ 2 km (Black, 1970). It has a large submarine extent (Cole et al., 2000) most recently estimated to be approximately 5-6 km in diameter with a base extending to about 200 m below sea level (Kilgour et al., 2021). Whakaari's structure consists of two overlapping cones, the older Ngatoro cone, and the currently active Central cone (Cole et al., 2000). The main crater consists of three (western, central, and eastern) coalescing sub-craters, of which the western sub-crater has been the focus of activity for most eruptions (Kilgour et al., 2021). The crater walls form a horseshoe-shaped amphitheater, the inner walls of which are composed of coherent, interbedded units of lavas, breccias, and tuffs (M. J. Heap et al., 2015, 2017a). Whakaari hosts a dynamic hydrothermal system expressed on the surface in the form of intense fumarolic activity, hot acid springs, steaming ground areas, and a crater lake (Giggenbach et al., 2003; Hedenquist et al., 1993). A magma source 0.8-1 km deep (Jolly et al., 2018) drives the circulation of hot magmatic fluids and meteoric water through the subsurface rocks (Miller et al., 2020; Christenson et al., 2017).

Mt. Taranaki, on the other hand, sits on land rising 2518 m high. Its upper modern edifice is mainly composed of andesitic lavas and pyroclastic flow units (Zernack et al., 2009). A ring-plain of older volcaniclastic deposits, about 15 times larger in volume, surround the modern edifice (Zernack et al., 2011). Mt. Taranaki has four flank lava domes, including the summit dome (Cronin et al., 2021; Zorn et al., 2018). The present-day summit crater has been the main eruptive vent from approximately 14 ka (Torres-Orozco et al., 2017). Unlike Whakaari, however, Mt. Taranaki does not have a surface expression of a dynamically active hydrothermal system with active fumaroles or a history of passive degassing. Only a few warm and cold springs with travertine deposits occur on its ring-plain (Allis et al., 1995; Werner et al., 2020).

A prehistoric sector collapse at Whakaari is thought to have extensively changed the hydrothermal fluid flow by removing low permeability cone lavas, allowing high meteoric water and lateral seawater infiltration (Letham-Brake, 2013). This could be the reason for the relatively dynamic hydrothermal system at Whakaari compared to Mt. Taranaki.

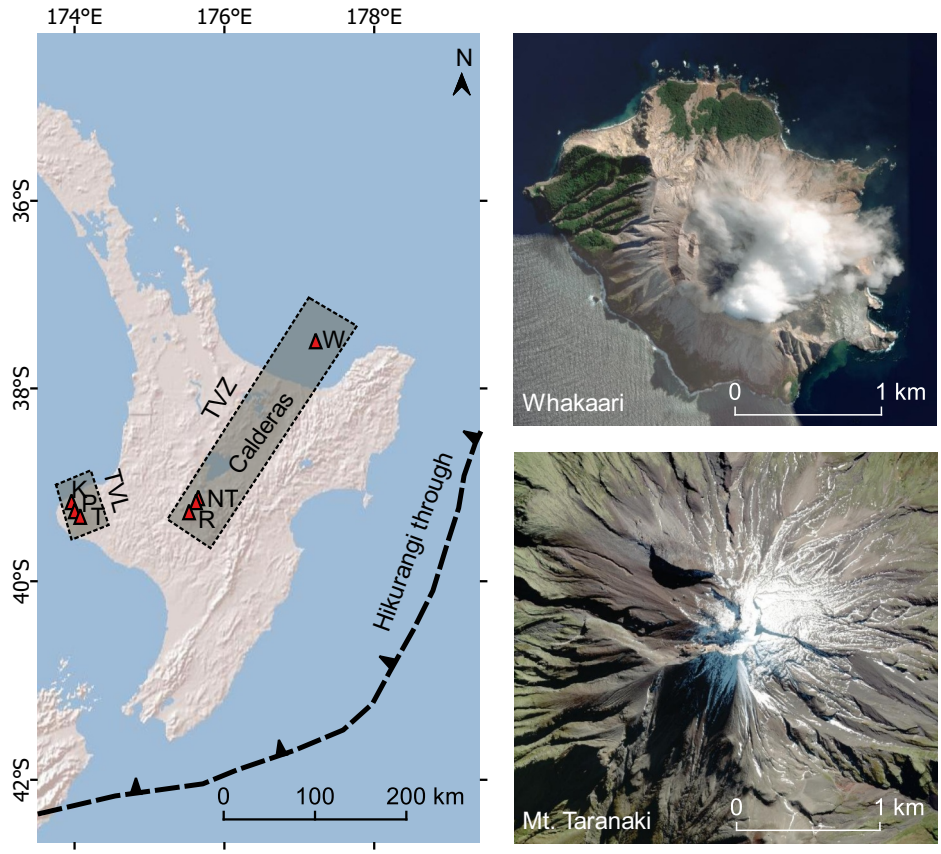

Figure 1.3: (Left) Map of New Zealand's North Island showing the locations of volcanoes and their tectonic setting. Grey shaded regions show the approximate boundary of the Taupō Volcanic Zone (TVZ) and Taranaki Volcanic Lineament (TVL). Red triangles show the locations of volcanoes: Whakaari (W), Mt.Tongariro, and Mt. Ngāuruhoe (NT), Mt. Ruapehu (R), Mt. Taranaki (T), Kaitake (K), and Pouakai (P). (Right) Zoomed images of Whakaari and Mt. Taranaki. Map source: ESRI basemap (2021a) and ESRI basemap (2021b).

1.2.2 Past eruptions and slope failures

Whakaari is New Zealand's most active volcano with a history of passive degassing (Burton et al., 2021). The eruptions at Whakaari have been mainly phreatic and phreatomagmatic in nature, with some strombolian and dome-forming eruptions (Kilgour et al., 2019; Mayer et al., 2015). Its most recent eruption was in 2019, which resulted in the loss of 22 lives and 25 severely injured people (Dempsey et al., 2020). Whakaari also had at least two-sector collapses that generated debris avalanches (Moon et al., 2009). One is a prehistoric failure, and the other occurred in 1914 from the collapse of the southwestern crater wall leading to fatalities and extensive damage to the sulfur factory (Kilgour et al., 2021; Moon et al., 2005, 2009). Hydrothermal alteration is considered to play an important role in driving both the eruptions (Burton et al., 2021; Christenson et al., 2017) and slope failures (Moon et al., 2009) at Whakaari.

Mt. Taranaki has a history of effusive and explosive eruptions (Damaschke et al., 2018; Torres-Orozco et al., 2017) interspersed with cyclic destruction and regrowth of the edifice (Zernack et al., 2012). Its most recent eruption was in AD 1790 $\pm$ 10 years (Cronin et al., 2021; Lerner et al., 2019a). Almost all eruptive periods at Mt. Taranaki, have involved pyroclastic density currents, mostly related to dome emplacement on the summit crater and their collapse generating block and ash flows. These block and ash flows went up to 5 km to more than 13 km from the source. The dome collapses have ranged from those of a syn-eruptive nature involving the collapse of growing hot domes to those of a post-eruptive nature involving the collapse of the cooling dome (Platz et al., 2012; Lerner et al., 2019b, 2019a). Oversteepening, emplacement on a steep slope of unconsolidated material, heavy rain, fracturing, and a hydrothermally altered core are considered to be factors contributing to the destabilization of the dome (Platz et al., 2012). Mt. Taranaki also has a history of more deep-seated edifice collapses that have generated debris-avalanche deposits. Around 16 major edifice collapses have occurred in its more than 130 k.y. history generating debris-avalanche deposits of approximately 1 to 7.5 km^3 in volume (Cronin et al., 2021; Zernack et al., 2012). These avalanches have a run-out distance of at least 25-45 km onshore and a further 6-8 km offshore (Alloway et al., 2005; Zernack et al., 2011).

The history of slope failures and eruptions at both Whakaari and Mt. Taranaki, combined with the dynamic and widespread hydrothermal alteration at Whakaari compared to localized alteration at Mt. Taranaki, makes this study relevant to understand the role hydrothermal alteration plays in volcano dynamics and how it can be monitored with geophysical methods.

1.3 Current knowledge on hydrothermal alteration-related changes in petrophysical and geophysical properties of volcanic rocks

Understanding how hydrothermal alteration affects the petrophysical properties such as mineralogy and fluid pathways of volcanic rocks is vital in determining their effect on the overall volcano dynamics. At Solfatara (Campi Flegrei), hydrothermal alteration of surficial rocks to alunite and amorphous silica increased porosity and permeability, reducing their elasticity and strength, resulting in high fragmentation and ejection speeds (Mayer et al., 2016). Pola et al. (2012) studied the petrophysical properties of surficial rocks with a similar secondary mineral assemblage of mainly alunite and amorphous silica from the Solfatara crater, Ischia Island, and Bolsena volcanic zone. They also observed increased porosity with alteration in surficial lavas, tuffs, pyroclastics, and ignimbrite series, with some exceptions in the lavas and ignimbrites due to secondary mineral precipitation. Navelot et al. (2018) studied the petrophysical and magnetic properties of surficial volcanic rocks from Guadeloupe Archipelago (West Indies) that were altered with a secondary mineral assemblage of illite, chlorite, smectite, gypsum, pyrite, quartz, micas, and calcite.

At Mt. Taranaki, no study has thus far investigated the effect of hydrothermal alteration on petrophysical or geophysical properties of rocks. Several studies have examined one or more of the petrophysical, magnetic, and mechanical strength properties but only for fresh rocks (Higgins, 1996; Lerner et al., 2019a; G. Turner et al., 2018; Zorn et al., 2018). Although rare, reddish-orange clasts observed in some block and ash flow-like deposits are thought to be hydrothermally altered (Lerner et al., 2019b). An 80-m wide hydrothermally altered zone is also observed in the central part of the exposed summit dome (Platz et al., 2012).

At Whakaari, current knowledge on how hydrothermal alteration affects the petrophysical and geophysical properties of lavas, tuffs, and breccias is limited and mainly based on surficial samples. M. J. Heap et al. (2015) studied lava and tuffs collected from the foot of the eastern wall of the volcanic amphitheater near Shark Bay, and M. J. Heap et al. (2017a) studied a lava breccia from the collapse debris of the north-eastern wall of the volcanic amphitheater. They observe that hydrothermal alteration results in a secondary mineral assemblage of mainly cristobalite in the lava, amorphous phases (assumed to be Opal-A) and alunite in tuffs, and amorphous phases (assumed to be Opal-A) and kaolinite in the lava breccia. Other secondary minerals like jarosite, gypsum, anhy-

drite, cristobalite, quartz, where present, occur in minor proportions (<5%). How these changes in mineralogy due to alteration affect fluid pathways are only implied or broadly discussed, mainly in terms of pore-and crack-filling alteration reducing the permeability. Moreover, the samples in M. J. Heap et al. (2015) and M. J. Heap et al. (2017a) do not have the range of alteration required to systematically assess the effects of alteration on each of the lithologies. These samples have, however, been used to develop constraints on phreatic eruption processes like fragmentation and ejection velocities, particle size and shape (Mayer et al., 2015) and to develop an index based on porosity and cation exchange capacity for mapping hydrothermal alteration, permeability, and mechanical properties (Revil et al., 2020).

Rocks ejected as ballistics from Whakaari that represent its conduit environment have been previously studied but not as extensively (Hedenquist et al., 1993; Kennedy et al., 2020). These studies observe precipitation of secondary alunite, cristobalite, opal, tridymite, anhydrite, pyrite, zaherite, and some clays. Christenson et al. (2017) through modeling suggest that sulfur precipitation in the vent can control the permeability of the conduit. Kennedy et al. (2020) on the other hand, propose that fluid advection from the conduit to the surface is facilitated by pressure-controlled mechanisms, mainly by the opening and closure of cracks associated with altered rocks due to variable pore and confining pressures in the subsurface. However, neither of these studies on ballistics provide quantitative data on the mineralogy or microimaging evidence needed to define the degree of alteration or assess the relative effects of complimentary alteration processes like dissolution and secondary mineral precipitation. To determine how hydrothermal alteration affects the petrophysical properties of host rocks at Whakaari and the overall volcano dynamics requires a quantitative study of both the mineralogy and fluid pathways in samples displaying a range of alteration degrees. Furthermore, these samples need to represent the different lithologies in the volcano, and the petrophysical properties need to be measured at pressure conditions representative of the subsurface.

Determining the corresponding effect of alteration-related petrophysical changes on geophysical properties is vital to constrain field-scale geophysical inversions. For example, inversions of ground deformation data rely on the assumptions of the elastic properties of rocks in the subsurface (M. J. Heap et al., 2020a). Inversions of ground deformation data at Whakaari have the underlying assumption that the deforming medium is elastic, homogenous, and isotropic with Young's modulus of either 30 GPa (Fournier & Chardot, 2012; Peltier et al., 2009) or 2.5 GPa (Fournier & Chardot, 2012). But there is a paucity of lab-based constraints on the effect of hydrothermal alteration on such properties (M. J. Heap et al., 2020a). At Whakaari, the only known elasticity data are

of surficial andesitic lavas and tuffs from M. J. Heap et al. (2015) whose Young's moduli range from 21.3-38.2 GPa and 0.7-8.7 GPa, respectively (M. J. Heap et al., 2015). Petrophysical and elastic properties of altered rocks have been studied at other volcanoes and geothermal regions in the Taupō volcanic zone.

Mordensky et al. (2018) observe an advanced argillic alteration-related decrease in Young's moduli of andesites whereas an increase in the modulus of breccias from Pinnacle Ridge on Mt. Ruapehu. Durán et al. (2019a) also observe an increase in elastic moduli of tuffs from the Ngatamariki Geothermal Reservoir due to phyllic-propylitic alteration. M. J. Heap et al. (2020b) observed that silicification increased Young's modulus of the Ohakuri ignimbrite, but alteration to clay minerals did not have a significant influence on its Young's modulus. In rocks from the Ngatamariki, Rotokawa, and Kawerau geothermal fields, Wyering et al. (2014) observed an increase in compressional wave velocities of rocks with chloritic alteration compared to smectite alteration at atmospheric conditions. They observe that Young's modulus of these rocks follows the expected trend with porosity and conclude that hydrothermal alteration does not significantly alter the expected relationships between physical and mechanical or elastic properties. These studies, however, focus on alteration to smectite or kaolinite clays (M. J. Heap et al., 2020b; Mordensky et al., 2018, 2019; Wyering et al., 2014), calcite, muscovite, epidote, pyrite, illite, chlorite, adularia, quartz, zeolites (Durán et al., 2019a; M. J. Heap et al., 2020b; Wyering et al., 2014). Such secondary mineral assemblage is representative of alteration in a neutral-alkaline environment (Figure 1.2).

At Whakaari, the highly acidic fluids in the subsurface environment inhibit the formation of such secondary mineral assemblage and instead favor the precipitation of secondary alunite and cristobalite. Clays occur in low proportion at Whakaari as indicated by the low conductivity (generally $<30 \times 10^{-4}$ Sm^{-1}) (Ghorbani et al., 2018; Revil et al., 2020) and less than 10% kaolinite observed (M. J. Heap et al., 2017a) in Whakaari rocks. Revil et al. (2020) developed an index to map hydrothermal alteration using porosity and cation exchange capacity of soft volcanic rocks, linking it to rock permeability and strength. The cation exchange capacity is, however, predominantly dependent on clay content (Revil et al., 2017). Given the lack of accompanying mineralogical data in Revil et al. (2020) and the generally low proportion of clay minerals observed at Whakaari (Miller et al., 2020), the rock cation exchange capacity and matrix conductivity may not serve as accurate indicators of hydrothermal alteration at Whakaari.

Another geophysical technique widely used to monitor volcanoes and identify hydrothermally altered regions is magnetic surveying (Finn et al., 2001; Kereszturi et al., 2020). Current knowledge on how alteration affects magnetic properties of vol-

canic rocks comes from mid-ocean ridge basalts (Xu et al., 1997; Wang et al., 2020), seafloor hydrothermal systems (Fujii et al., 2015, 2018), geothermal fields (Pandarinath et al., 2019), and mineralized porphyry systems (Byrne et al., 2019). These studies, in general, associate hydrothermal alteration with reduced magnetization. Almost all alteration types, except potassic, which involves magnetite creation, are commonly associated with reduced magnetization (Clark, 2014; Riveros et al., 2014; Tapia et al., 2016). At Whakaari, Hurst and Christoffel (1973) measured the magnetization and magnetic susceptibility of four samples to be in the range of 3.7 to 10.1 A/m and 6.5 $\times$ 10^{-3} to 1.3 $\times$ 10^{-2} (SI), respectively. Woodward and Mumme (1993) measured a further 26 surficial samples from Troup Head, Pinnacle Head, Crater Bay, North Head, Crater floor, and the northern and southern crater wall of Whakaari. They observed that fresh andesitic lavas have high magnetization (up to 20 A/m) while altered andesites and phreatomagmatic deposits have low magnetization (<1 A/m). These data have led to the high magnetization observed in the crater floor during the aeromagnetic survey being interpreted as fresh andesitic flows and sills (Woodward & Mumme, 1993). These studies (Hurst & Christoffel, 1973; Woodward & Mumme, 1993), however, do not have accompanying data on the degree of alteration of the rocks studied and do not include all the lithologies (tuffs, breccias, lavas) that occur in Whakaari. At Mt. Ruapehu, Kereszturi et al. (2020) observed reduced magnetic susceptibility in hydrothermally altered rocks compared to fresh rocks and used this relation to interpret field-scale aeromagnetic data. But how natural remanent magnetization, another vital component of magnetization, is affected by the alteration remains unknown. To help accurately interpret field-scale results, there is a need to systematically evaluate how hydrothermal alteration progressively affects the magnetic properties, both induced and remanent magnetization, of all the lithologies at a laboratory scale.

1.4 Sampling of variably altered volcanic rocks

To advance the current knowledge on the topic, this thesis studies the petrophysical and geophysical properties of variably altered volcanic rocks from Whakaari and Mt. Taranaki. The samples studied were collected from Whakaari's crater floor, Mt. Taranaki's summit dome area, block and ash flow deposits, and debris avalanche deposits over three field-works. These field works were performed targeting potentially altered samples that could be collected safely. The sample locations are shown in Figure 1.4.

From Whakaari, eighteen large blocks were collected comprising lavas, tuffs, and

breccias ejected as ballistics from the conduit during the 2016 eruption and vesicular lava and sulfur flow from the surface outcrops. Overall, these samples are representative of the surface and subsurface lithologies of the conduit. Between 1-5 cylindrical cores (2.54 cm diameter and 2.2 cm length) drilled from each block summing to 45 samples are studied in this thesis (Figure 1.5).

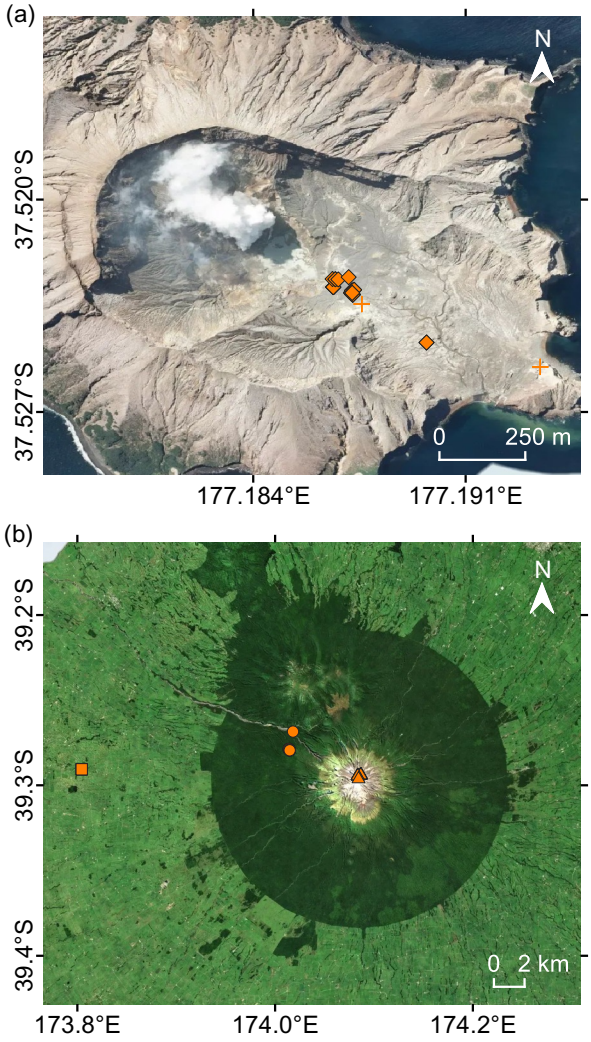

Figure 1.4: Sampling locations of variably altered volcanic rocks from (a) Whakaari and (b) Mt. Taranaki. From Whakaari, the samples include ballistic lavas, tuffs and breccias (diamonds), surficial vesicular lavas, and sulfur flows (crosses). From Mt. Taranaki, the samples include lavas from the summit dome area (triangles), lava clasts from block and ash flow deposits (circles), and lava clasts from debris-avalanche deposits (squares). Map source: (LINZ, 2021)

From Mt. Taranaki, twenty-four large sample blocks of lavas were collected from outcrops near the summit dome, clasts from block and ash flow deposits in Maero stream,

and clasts from roadside debris-avalanche deposits on the western side of Mt. Taranaki. For comparison, ten fresh lavas collected by Zorn et al. (2018) from the summit dome and clasts from block and ash flow deposits in Maero stream and Pyramid Stream are also used. A cylindrical core (2.54 cm diameter and 2.2 cm length) drilled from each sample block summing to 34 samples are studied in this thesis (Figure 1.6). The precise length of the samples, 2.2 cm, was chosen based on requirements for magnetic measurements.

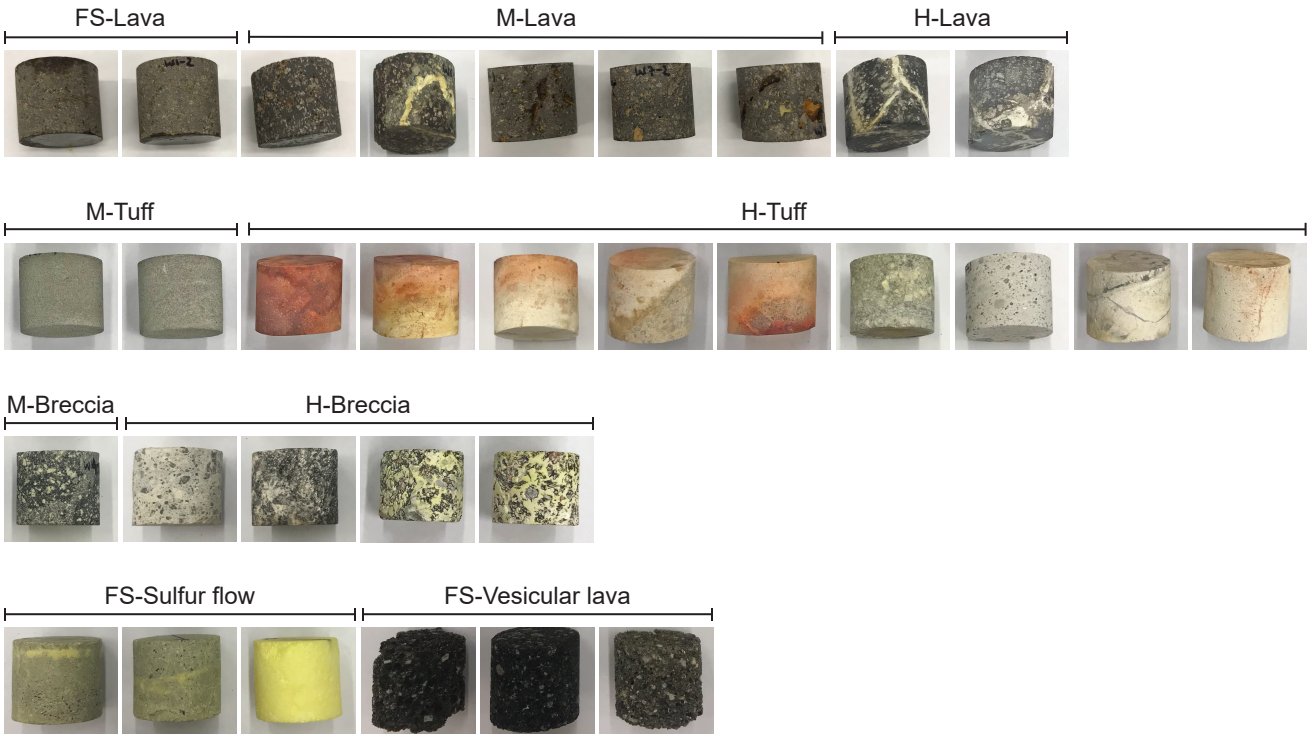

Figure 1.5: Photos of select samples from Whakaari showing the various conduit-filling (lavas, tuffs, breccias) and surficial (sulfur flows and vesicular lavas) lithologies investigated in this thesis. The suffixes indicate fresh to slightly altered (FS), moderately altered (M), and highly altered (H). All cylindrical cores are on average 2.54 cm in diameter and 2.2 cm in length.

Figure 1.6: Photos of lavas from Mt. Taranaki investigated in this thesis. These include lavas from the summit dome area and lava clasts from the block and ash flow and debris avalanche deposits. The suffixes indicate fresh to slightly altered (FS), moderately altered (M), and highly altered (H). All cylindrical cores are on average 2.54 cm in diameter and 2.2 cm in length.

1.5 Aims and objectives

The overarching goal of this thesis is to establish links between acid-sulfate hydrothermal alteration-related petrophysical changes in volcanoes and their geophysical properties to inform volcano imaging and monitoring. To achieve this goal, the petrophysical and geophysical properties of variably altered volcanic rocks from Whakaari and Mt. Taranaki are studied in this thesis. The specific aims of this thesis are listed below and summarized

in Figure 1.7.

1. **To determine how hydrothermal alteration changes the petrophysical properties of volcanic rocks, by**

   (a) Determining their mineralogy and quantifying their hydrothermal alteration intensity.

   (b) Measuring their porosity and permeability at atmospheric conditions and, in select cases, under pressures representative of subsurface conditions.

   (c) Examining how hydrothermal alteration changes the fluid pathways through the rocks.

2. **To understand how these petrophysical changes can affect volcanic dynamics, by**

   (a) Determining the overall influence of alteration-related petrophysical changes and subsurface pressures on fluid pathways.

   (b) Theorizing how such changes might influence predisposition to eruptions in a broader context.

   (c) Theorizing whether these changes would influence volcano stability.

3. **To determine the corresponding geophysical signatures of variably altered volcanic rocks and inform volcano monitoring, by**

   (a) Developing a dataset of corresponding elastic and magnetic properties of the variably altered volcanic rocks.

   (b) Identifying underlying petrophysical properties that influence these geophysical signatures.

   (c) Using key observations of the relationship between petrophysical and geophysical properties to inform geophysical data interpretation at active volcanoes.

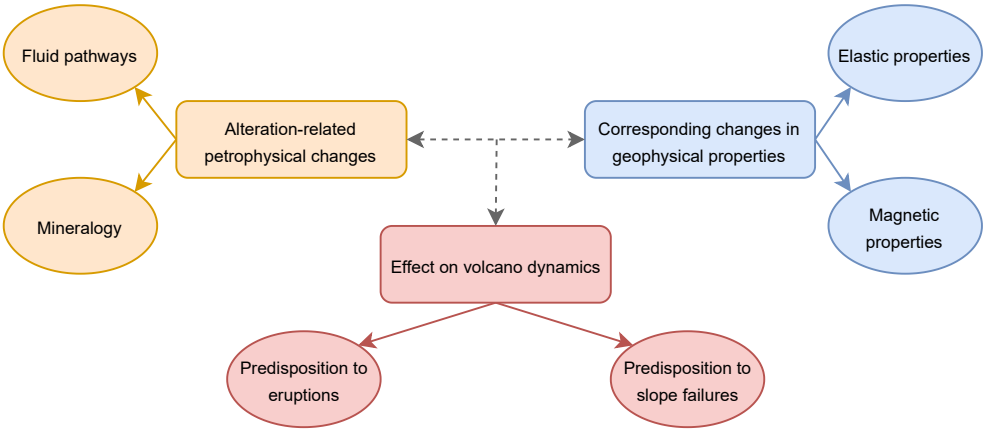

Figure 1.7: Overview of the aims of this thesis.

1.6 Thesis overview

This thesis consists of six chapters, including this Introduction. These chapters together address the aims of this thesis (Section 1.5) to advance the topic of geophysical signatures of hydrothermal alteration for volcano monitoring. Chapter 2 describes the petrophysical and elastic properties of variably altered samples from Whakaari and how they affect volcano dynamics. Chapter 3 describes the magnetic properties of these samples and discusses plausible underlying causes for the observed magnetization. Chapter 4 describes the petrophysical, elastic, and magnetic properties of samples from Mt. Taranaki and discusses the implications for volcano slope stability. Chapter 5 draws key findings from the previous three chapters and discusses them in a broader context on how hydrothermal alteration changes the petrophysical properties of volcanic rocks, the corresponding effect on volcano dynamics, and implications for geophysical monitoring. Lastly, Chapter 6 provides final remarks on the contribution of this thesis and avenues for future research. Below I provide a glimpse of the contributions of this thesis.

Scientific Contributions

- **Key findings from Chapter 2**
  - In volcanic conduits, lavas undergo net dissolution and tuffs net secondary mineral precipitation.
  - The stiffness of conduit-filling lavas decreases and tuffs increases due to alteration.

  - Inherently porous and permeable tuffs, when compacted and highly altered, can form seals within volcanic conduits.

- **Key findings from Chapter 3**
  - Natural remanent magnetization dominates induced magnetization in volcanic rocks from Whakaari.
  - Hydrothermally altered lavas can carry higher remanent magnetization than fresh lavas.
  - Both induced and remanent magnetizations should be used to constrain field-scale data.

- **Key findings from Chapter 4**
  - Hydrothermal alteration changes the crystallinity and mineralogy of lavas and fluid pathways through them.
  - Natural remanent magnetization generally dominates induced magnetization at Mt. Taranaki. Sometimes, however, natural remanent magnetization is similar or lower than induced magnetization.
  - Rock stiffness and thus strength do not always decrease with increasing degree of alteration; the type of secondary mineral assemblage can also be an important controlling factor.

Data and Methods

A dataset of petrophysical and corresponding elastic and magnetic properties of 79 variably altered volcanic rocks is developed in this thesis. These include data on rare samples from Whakaari's conduit ejected as ballistics and, to our knowledge, the first set of measurements on altered rocks from Mt. Taranaki. These data are available on the open-access platform figshare for future use (see Data Availability for details). The methodological contributions of this thesis include a workflow (Appendix B) to characterize the mineralogy and amorphous content of rocks systematically using X-ray diffraction (XRD) analysis and AMORPH (M. Rowe & Brewer, 2018) and determine the hydrothermal alteration intensity of the samples. Following this workflow will help maintain consistency and reproducibility while analyzing XRD data, which is otherwise highly prone to user-related inconsistencies.

Publications

The research conducted in this thesis have been published as two peer-reviewed journal articles in Geophysical Research letters (Kanakiya et al., 2021a, 2021b). The full citations for two articles consisting results of Chapter 2 and Chapter 3 of this thesis are provided below.

- **Chapter 2**: Kanakiya, S., Adam, L., Rowe, M. C., Lindsay, J. M., and Esteban, L. (2021). The role of tuffs in sealing volcanic conduits. *Geophysical Research Letters, 48*, e2021GL095175. `https://doi.org/10.1029/2021GL095175`
- **Chapter 3**: Kanakiya, S., Turner, G. M., Rowe, M. C., Adam, L., and Lindsay, J. M. (2021). High remanent magnetization measured in hydrothermally altered lavas. *Geophysical Research Letters, 48*, e2021GL095732. `https://doi.org/10.1029/2021GL095732`

Results of Chapter 4 are in preparation for submission to a peer-reviewed journal.

Chapter 2

The role of tuffs in sealing volcanic conduits

2.1 Introduction

Hydrothermal alteration by SO_2-rich fluids governs the physicochemical properties of stratovolcanoes worldwide (Mayer et al., 2016; Zimbelman et al., 2005). As these fluids alter the conduit rocks, inevitable changes in rock porosity and permeability can limit outgassing and promote explosive volcanic behavior. This was observed at Poás volcano (Costa Rica), where the formation of a pressurized hydrothermal seal by secondary mineral precipitation and volatile accumulation limited SO_2-emissions for two years and triggered the 2017 phreatomagmatic eruption (de Moor et al., 2019). Similar hydrothermal sealing driven by acid-sulfate alteration also played a role in triggering phreatic and phreatomagmatic eruptions at Soufrière Hills (Montserrat) (Edmonds et al., 2003) and Ontake (Japan) (Stix & de Moor, 2018). At Whakaari-White Island volcano (New Zealand), a partially sealed hydrothermal system is implied to have played a role in the recent 2019 and past eruptions (Burton et al., 2021; Christenson et al., 2017). However, mineralogical and microimaging evidence of such sealing and its evolution for different lithologies within the conduit is lacking. Moreover, the effect of such hydrothermal processes on the fluid flow and elastic properties of conduit-filling rocks remains unconstrained, despite being of paramount importance for accurately inverting geophysical data to understand volcano pressurization.

The development of an effective seal requires conduit rocks with low porosity and low permeability that limit outgassing and favor fluid accumulation and pressure build-up (Stix & de Moor, 2018). So far, experimental studies on the effects of alteration on

porosity and permeability of volcanic rocks have been mainly based on surface-collected rocks and show conflicting observations. For example, pore and fracture filling secondary minerals in lavas (M. J. Heap et al., 2017a, 2019) and tuffs (M. J. Heap et al., 2017a) can help develop a seal. However, the higher porosity observed in altered andesitic lava (Farquharson et al., 2019; M. J. Heap et al., 2019; Mordensky et al., 2018), and pyroclasts (Mayer et al., 2016; Pola et al., 2012) show that alteration can also promote dissolution and hinder the formation of a seal. Studies on samples from the volcanic conduit are rare. Hedenquist et al. (1993) and Kennedy et al. (2020) studied a set of fresh and altered ballistics from Whakaari. However, these studies lack insights into the quantitative mineralogy and microimaging of the ballistics to clearly define the degree of rock alteration and estimate the relative effects of dissolution and secondary mineral precipitation on the different conduit-filling lithologies. Furthermore, Kennedy et al. (2020) suggest that pressure-controlled mechanisms, via the opening and closing of fractures, drive fluid-advection through the conduit. But how macropores in the conduit-filling lithologies are affected by alteration and subsurface pressures and their role in controlling fluid flow still remains to be studied.

We investigate the effect of hydrothermal alteration on fluid pathways and stiffness of variably altered lava, tuff, and breccia from Whakaari volcano's conduit at realistic subsurface pressures. We perform a unique and thorough mineralogical and microimaging analysis of these samples to define their type and degree of hydrothermal alteration. By studying variable lithologies and alteration degrees, we propose a conceptual model on how a seal is built or destroyed in a hydrothermally active volcanic conduit. Whakaari is New Zealand's most active volcano. Its dynamically active hydrothermal system (Giggenbach et al., 2003) results in a modern history dominated by phreatic and phreatomagmatic eruptions (Dempsey et al., 2020; Kilgour et al., 2019, 2021; Mayer et al., 2015), with its most recent eruption in 2019 resulting in tragic loss of life (Dempsey et al., 2020). A magma source 0.8-1 km deep (Jolly et al., 2018) drives Whakaari's hydrothermal system by circulating hot magmatic fluids (Miller et al., 2020; Christenson et al., 2017) and meteoric water through the subsurface rocks. We systematically investigate 45 samples with varying intensity of acid-sulfate alteration that include lava, tuff, and breccia ejected as ballistics from the conduit during the 2016 eruption and vesicular lava and sulfur flow from surface outcrops. Our results show that inherently porous and permeable tuffs, when highly altered, can form low porosity, low permeability zones in the conduit. The high pore-filling alteration in tuffs and compaction under subsurface pressures could reduce the conduit's overall permeability and aid in pressurizing the conduit. Our study provides constraints for ground deformation and seismicity interpretations of

acid-sulfate altered volcanic conduits.

2.2 Materials and Methods

2.2.1 Sampling

Eighteen large blocks of variably altered volcanic rocks were collected from the crater floor of Whakaari. These blocks include lava, tuff, and breccia ejected as ballistics from the conduit during the 2016 eruption and vesicular lava and sulfur flow from surface outcrops. Overall, these samples are representative of the surface and subsurface lithologies of the conduit. Between 1-5 cores were drilled from each block to capture the heterogeneity of alteration, summing to 45 samples (2.54 cm diameter and 2.2 cm length). Representative adjacent sections of these cores were powdered for X-ray diffraction (XRD) analysis and thin sectioning to determine their hydrothermal alteration intensity and mineralogy. A summary of reference ID of samples (Table A.1) and the sampling locations (Table E.1) are provided in the Appendices.

2.2.2 Quantification of hydrothermal alteration intensity

Hydrothermal alteration intensity of the samples was thoroughly determined by XRD and cross-verified independently with backscattered-electron imaging (BSE) and energy disperse spectroscopy (EDS). XRD data were acquired on powdered samples using PANalytical Empyrean X-ray Diffractometer (CuKα, 40 mA, 45 kV, 0.5^o fixed divergence slit, step-scan from 5^o to 70^o 2θ at 0.013^o 2θ increments, 97.92s per step). The raw XRD patterns were analyzed using HighScore Plus software (Panalytical, 2012) in conjunction with thin section analysis. Crystalline mineral phases were identified by comparing raw XRD patterns to reference patterns from the Crystallography Open Database (COD) (Gražulis et al., 2020) and quantified using Rietveld refinement. This method minimizes the difference between the observed XRD pattern and that calculated from the crystal models of individual phases using a nonlinear least-square fit. A fit was considered good when the model explained all major peaks with a goodness of fit statistic less than 4. In some samples with more phases, a goodness of fit less than 7 was also considered acceptable. Relative amorphous phase contents were quantified using the AMORPH program (M. Rowe & Brewer, 2018) and calibrated with known volcanic glass calibration standards (Figure B.1). Amorphous phases were classified as primary, secondary, or a mixture of both, based on the skewness results from AMORPH. Samples with a gaussian curve

were classified to have primary volcanic glass. Samples with curves skewed at 22^o 2θ with skewness above 0.2 were considered to have secondary amorphous silica/aluminosilicates (Figure B.2). Phases identified from XRD analysis were independently verified by performing BSE-EDS analysis on the thin sections. Based on the amount of secondary phases, the samples were categorized as fresh to slightly altered (0-5%), moderately altered (5-40%), and highly altered (>40%). A step-by-step workflow of the methodology followed is provided in appendices (Figure B.3) to allow reproducibility. The raw XRD patterns are available in the data repository (see Data Availability). Data from phase quantification for all samples and BSE images are available in the appendices, Table E.5 and Section E.5, respectively.

2.2.3 Fluid pathways

Fluid pathways through the (dry) samples were quantified by measuring their connected porosity using a nitrogen gas porosimeter from Vinci Technologies (Poroperm) at atmospheric pressure. This instrument measures the porosity by isothermal nitrogen expansion and applying Boyle's law and Charles' law (Technologies, 2022). In addition, nitrogen gas connected porosity of 12 dry samples was measured under effective pressure from 3 to 55 MPa using a multi-stage approach. This range of pressure illustrates the evolution of fluid pathways with subsurface depths of up to 3-4 km, and the measurements were performed at effective hydrostatic pressures: 3 MPa, 7 MPa, 14 MPa, 21 MPa, 28 MPa, 34 MPa, 41 MPa, 48 MPa, and 55 MPa (Figure C.1). Vesicular lava samples were weak and were thus measured only up to 41 MPa. The multi-stage approach used involved raising the confining pressure acting on the sample and then unloading to the previous effective pressure and then to a reference pressure (3 MPa) where the change in porosities is monitored to identify the onset of inelastic compaction (Figure C.1). An effective pressure was considered to have exceeded the elastic limit of the sample if, upon unloading to 3 MPa, a $> 2\%$ porosity difference was observed compared to the initial porosity measurement at 3 MPa. Nitrogen gas connected porosity and permeability of an additional five dry lava and tuff samples were measured under pressure. These measurements were performed using a porosimeter and permeameter AP608 from CoreTest by pycnometer method for porosity and pulse-decay method for permeability with a constant pore pressure at 1.7 MPa while increasing the overburden pressure from 5 to 57 MPa. Data from porosity and permeability measurements of these samples and associated standard deviations are available in the Appendices (Table E.7).

2.2.4 Elasticity (Stiffness)

The rock's elastic properties were computed in terms of dynamic Young's moduli (stiffness). P- and S-wave data for all dry samples were acquired at atmospheric pressure using ultrasonic transducers (0.5 - 1 MHz). The wave speeds were computed by dividing the length of the sample by the P- and S-wave arrival times. In addition, P-and S-wave data of 5 samples were obtained under effective hydrostatic pressure to illustrate the evolution of stiffness with depth. These measurements were made up to 7 MPa under dry conditions and up to 52 MPa effective pressure under water-saturated conditions at a constant pore fluid pressure of 3.4 MPa. To represent realistic volcano conditions, one highly altered tuff sample was also measured at varying pore fluid pressures (1.7 to 20.7 MPa) and effective pressures up to 53 MPa. Care was taken to account for hysteresis before each measurement. Arrival times of P-and S-wave data under pressure were picked using the poropyck program (Durán et al., 2019b). The dynamic Young's moduli (E) was computed from P-(V_p), and S-wave (V_s) speeds and dry bulk density (ρ) using equation 2.1.

$$E = \frac{\rho {V_s}^2 (3{V_p}^2 - 4{V_s}^2)}{({V_p}^2 - {V_s}^2)} \tag{2.1}$$

Dynamic young's moduli are computed only until effective pressures at which the onset of inelasticity occurs, that is, as low as 14 MPa in tuffs and 28 MPa in lavas. The data of P-wave velocity, S-wave velocity, dynamic Young's moduli, and the associated standard deviations of each sample are available in the appendices (Table E.14).

2.3 Results and Discussion

2.3.1 Acid-sulfate alteration in the conduit

The conduits of stratovolcanoes with a history of phreatic and phreatomagmatic eruptions, including Whakaari, are likely to have a complex breccia-filled structure (Kennedy et al., 2020), similar to diatremes (Valentine & White, 2012; J. White & McClintock, 2001; J. White & Ross, 2011) (Figure 2.1a). The upper conduit is composed of bedded tuff with some tuff breccia underlain by relatively massive tuff breccia (Valentine & White, 2012; J. White & McClintock, 2001; J. White & Ross, 2011). The tuff breccia consists of lava and breccia clasts from reworked pyroclasts hosted in a tuff matrix. Our mineralogical analysis shows that in Whakaari's conduit, rock-fluid reactions increasingly replace or dissolve the primary minerals of lava, tuff, and breccia to form secondary

minerals (Figure 2.1b).

The secondary mineral assemblage of alunite ± silica ± anhydrite ± clays ± pyrite ± amorphous phases (silica/aluminosilicates) is indicative of acid-sulfate alteration by hot ($<400^oC$) SO_2-rich fluids (Hedenquist et al., 1993; Zimbelman et al., 2005). The SO_2-rich fluid environment in Whakaari's conduit is also evident from the formation of sulfur flow sublimates near fumaroles that are primarily composed of native sulfur with some detrital silica grains entrapped (Figure 2.1b). These fluids first form secondary cristobalite and tridymite in a highly acidic environment (pH<2) (Stoffregen, 1987). Upon relative neutralization (2<pH<6), they further replace or dissolve primary phases to form secondary alunite, anhydrite, pyrite, and clays (Zimbelman et al., 2005) as observed in our highly altered lava, tuff, and breccia samples (Figure 2.1b). These highly altered samples, especially tuffs, are diverse in composition compared to previous observations of acid-sulfate altered surface outcrops (M. J. Heap et al., 2015, 2017a) and ballistics (Hedenquist et al., 1993; Kennedy et al., 2020) at Whakaari.

The secondary mineralogy observed here is in contrast to the mineralogy of chlorite, epidote, and smectite observed in the geothermal reservoirs of Taupo Volcanic Zone (Durán et al., 2019a; Wyering et al., 2014). This is likely due to the acidic nature of fluids at Whakaari compared to near-neutral thermal waters observed in other long-lived geothermal systems (Giggenbach et al., 2003). Secondary minerals similar to Whakaari have also been observed in phreatic/phreatomagmatic ejecta of other volcanoes that have undergone acid-sulfate alteration (Ikehata & Maruoka, 2016; Del Moro et al., 2011; Boudon et al., 1998). From a mineralogical perspective alone, acid-sulfate alteration forms similar secondary minerals in the conduit irrespective of the rock type (Figure 2.1b). However, based on where these secondary minerals form (pores, fractures, or replacing primary minerals), the fluid pathways through these rock types and rock stiffness can differ drastically.

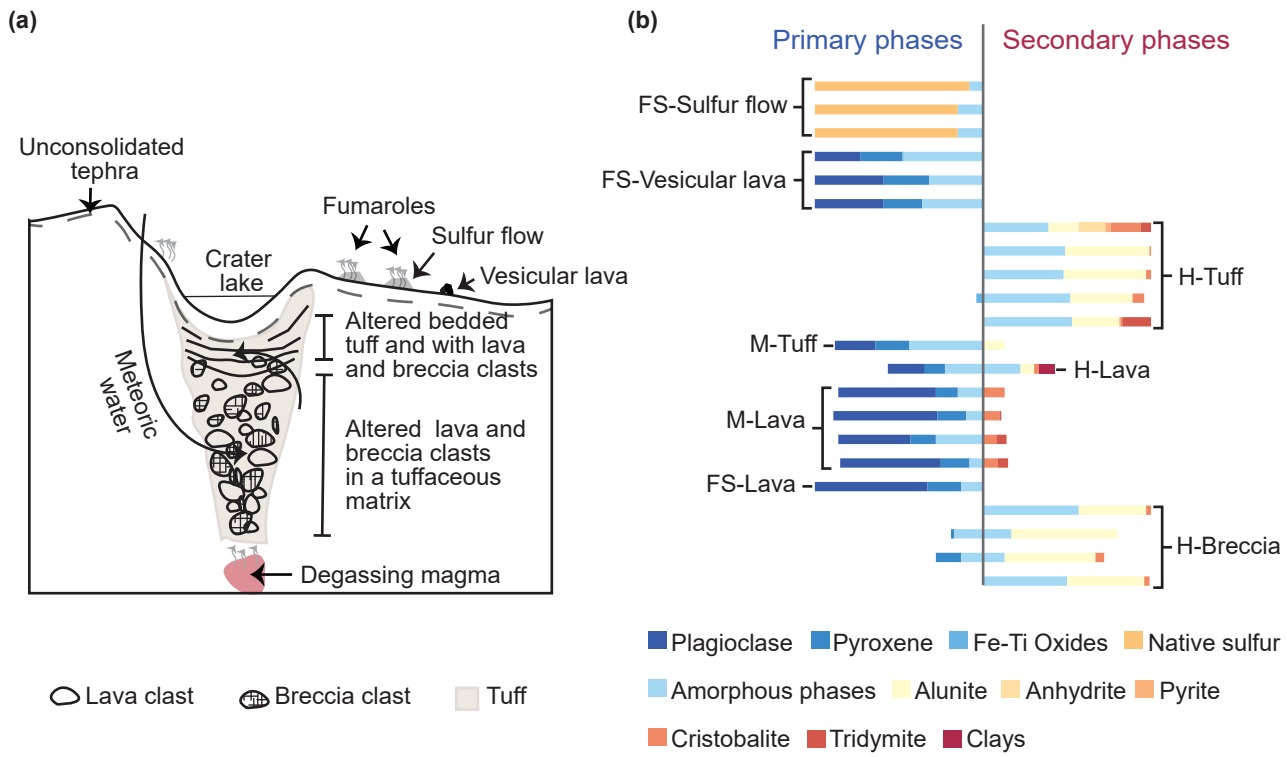

Figure 2.1: (a) Schematic of Whakaari's hydrothermal system. Fluids from degassing magma (0.8-1 km deep (Jolly et al., 2018)) mix with meteoric water and alter lavas, tuffs, and breccias in the conduit. (b) The phase composition of representative samples with variable alteration as determined by X-ray diffraction analysis. Bars represent major volumetric phase compositions, adding to 100%. (FS) Fresh to slightly altered samples are mainly composed of primary phases. Secondary phases increasingly replace primary phases in moderately (M) and highly (H) altered samples. Underlying data for all samples are provided in a tabular form in the appendices (Table E.5).

2.3.2 Evolution of fluid-pathways and stiffness in conduit rocks

From connected porosity data (Figure 2.2a) and backscattered-electron (BSE) images (Figure 2.3), we observe contrasting changes in fluid pathways through lava and tuff with increasing alteration. Fresh to slightly altered lavas have low porosity from fractures (ϕ=2%), and secondary minerals are limited (<3-5%) to those partially filling these fractures. Secondary minerals are widespread (11%-43%), replacing primary minerals (e.g., plagioclase, pyroxene) and partially filling pores and fractures in moderately and highly altered lavas. Despite these pore and fracture-filling secondary minerals, the moderately and highly altered lavas have higher porosity (ϕ=7%-16%) from a combination of primary and secondary (dissolution) pores and fractures. We thus infer that with increasing acid-sulfate alteration in the conduit, fluid-pathways are created in lava blocks by net

dissolution. As lavas inherently have low porosity and permeability, SO_2-rich fluids primarily alter them by developing pathways to flow through. Net dissolution of lava with increasing acid-sulfate alteration is also supported by observations of higher porosity and lower density of altered andesitic lavas from Whakaari (Kennedy et al., 2020; Hedenquist et al., 1993), Kuril-Kamchatka island (Julia et al., 2014), Campi Flegrei (Italy) (Pola et al., 2012), and Mt. Ruapehu (New Zealand) (Farquharson et al., 2019).

In contrast to lavas, we observe an opposite trend in the inherently porous and permeable tuffs through which fluids can readily flow. Moderately altered tuffs have high porosity (ϕ=39%-41%), with secondary minerals ($\approx$13%) filling pores and fractures and partially replacing some primary minerals (e.g., replacement by silica). However, in highly altered tuffs, secondary minerals (96%-100%) replace most of the primary minerals and infill pores and fractures (Figure 2.2 and 2.3), reducing porosity to approximately 20%. Moreover, we observe that the complete replacement of primary minerals and high infilling of pores and fractures changes the tuff's texture from consolidated grains to a coherent lava-like mass with micropores (Figure 2.3). Measurements on select samples show that the permeability of highly altered tuff is two orders of magnitude lower than moderately altered tuff (Figure 2.2b) and equal to moderately altered lavas. We thus infer that fluid pathways reduce with increasing acid-sulfate alteration in conduit tuffs. Previous studies on tuffs (M. J. Heap et al., 2017a; Kennedy et al., 2020; Revil et al., 2020) hint towards pore-filling secondary minerals reducing their porosity and permeability but provide little mineralogical and microstructural evidence for how this might vary with progressively increasing acid-sulfate alteration. Our results show that in terms of fluid pathways alone, highly altered tuffs can form coherent, low porosity, and low permeability zones within the conduit.

In breccias, alteration-related porosity changes are between that of lava and tuff due to their inherent heterogeneity. With increasing alteration, fluid-pathways could be created or destroyed by competing dissolution and precipitation processes, respectively. The high amount of secondary mineral precipitation observed in the breccias can limit the fluid pathways (Figure 2.1b). However, given their fractured structure, breccias are likely to contribute to fluid pathways in the conduit, which ultimately outgas at surface fumaroles. Our findings of a higher amount of secondary mineral precipitation in tuffs and breccias are consistent with observations from the drill cores of the Newberry Volcano, where Bargar and Keith (1999) find pervasive secondary mineral precipitation in interflow breccias and volcaniclastic layers where initial permeability was highest. Over time, tephra from new eruptions will bury surface lithologies, such as the low-porosity (ϕ=7%-10%) sulfur-flow sublimates, locally reducing pathways for fluids to outgas. High

porosity vesicular lava (ϕ=54% to 76%), once buried, would be crushed and become zones of unconsolidated grains that will likely assist fluid flow (Figure 2.2).

Porosities discussed above are at surface conditions. With increasing lithological pressure (depth), porosities decrease due to elastic and inelastic compaction by pore collapse (Figure 2.2). Overall, depth-dependent reductions in fluid-pathways are higher in high-porosity rocks, predominantly affecting tuffs via inelastic compaction beginning as low as 14 MPa (< 1 km). Such inelastic compaction is also observed in tuffs from Campi Flegrei (M. J. Heap et al., 2014), surficial tuffs from Whakaari (M. J. Heap et al., 2015) and the Alban Hills tuffs (Zhu et al., 2011) where pore collapse is the inferred mechanism (Wong & Baud, 2012).

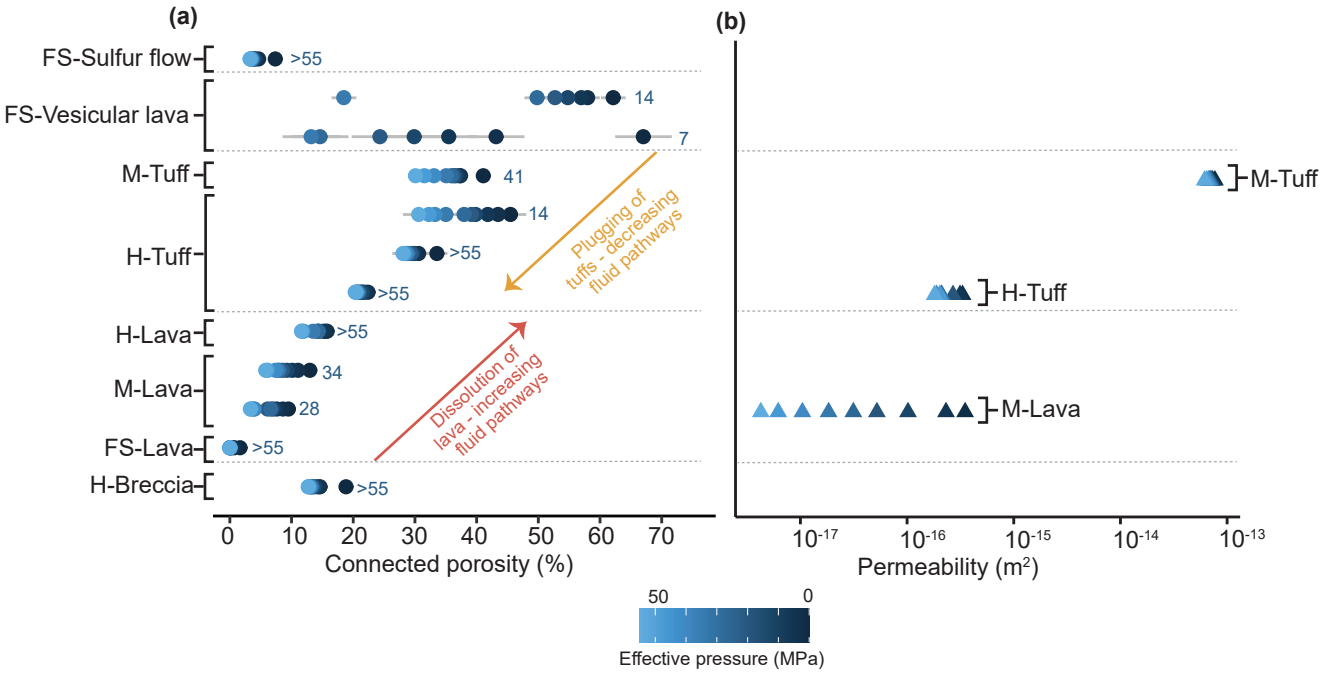

Figure 2.2: (a) Connected porosity of selected samples with pressure conditions showing the dissolution of lavas and sealing of tuffs by secondary minerals. Solid grey lines represent one standard deviation error bar. Values in blue are the effective pressure (MPa) at which the rock's porosity begins to reduce inelastically by inferred cataclastic pore collapse. (b) Permeability of select samples with pressure showing that highly altered tuffs and moderately altered lavas can have similar permeabilities. Permeability error is smaller than the symbols. The prefixes denote the alteration intensity of the samples as in Figure 2.1. Underlying data for all samples are provided in a tabular form in the appendices (Table E.7).

Porosity is the first-order control on elasticity (stiffness) of rocks (Winkler & Murphy, 1995). Thus, the evolution of fluid pathways by acid-sulfate alteration and pore compaction influences the conduit's stiffness. With increasing alteration, the dynamic

young's moduli (E) decreases from 62 GPa in fresh to slightly altered lavas to 24 GPa in highly altered lavas due to primary and secondary porosity created by the dissolution of primary minerals (Figure 2.4). This observation stands for both dry and water-saturated lavas. In contrast, the stiffness of tuffs increases with alteration (Figure 2.4). Highly altered tuffs have E similar to that of highly altered lavas (22 GPa) due to the sealing of pores by secondary minerals. These E are much higher than surface-collected tuffs from Whakaari and Campi Flegrei, which average at 1.8 GPa (M. J. Heap et al., 2020a).

Although dynamic E are higher than static experiments (Adelinet et al., 2010; Blake et al., 2019), the trend of weakening of lava and stiffening of tuffs with alteration is likely to remain. Alteration-related stiffness changes in breccia are hard to discern due to their heterogeneous nature, but overall their stiffness is low to moderate due to fractures. Since Whakaari's conduit is unlikely to have fresh rocks and is primarily composed of moderately to highly altered lava, tuff, and breccia, we estimate its stiffness to be low to moderate, with an average E of 21 GPa. As sulfur-flow sublimates get buried over time, they will also form low stiffness zones locally due to the low elasticity of native sulfur (Figure 2.4).

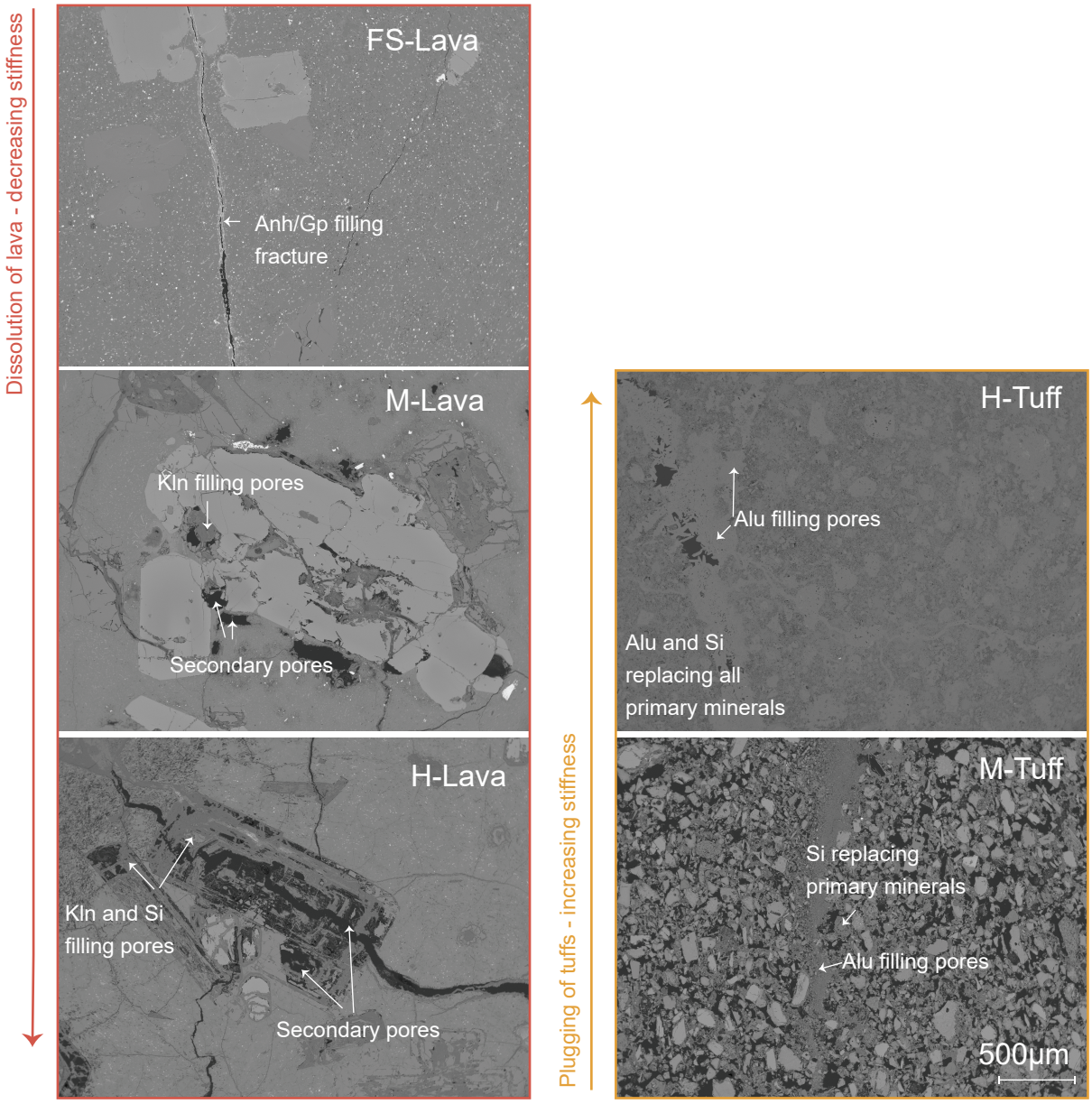

Figure 2.3: Backscattered-electron images showing the development of secondary pores via mineral dissolution in lavas, and in contrast, sealing of pores by secondary minerals in tuffs. All images have the same scale. The prefixes denote the alteration intensity of the samples as in Figure 2.1.

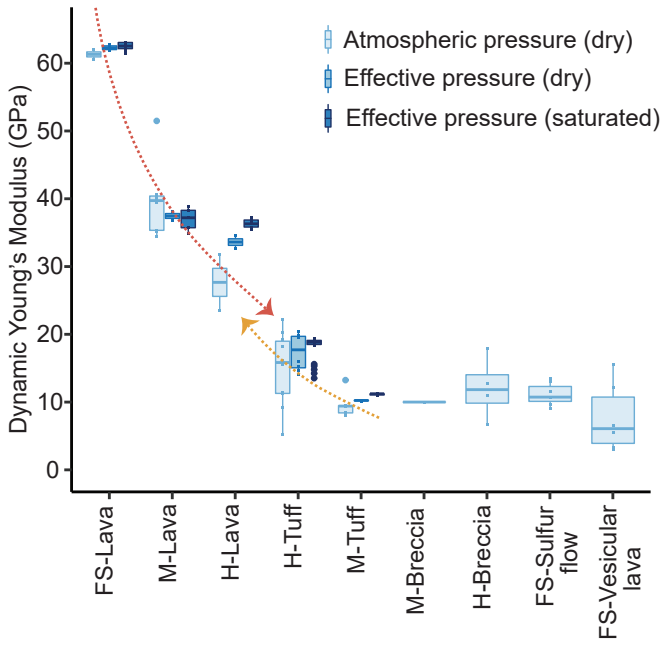

Figure 2.4: Distribution of stiffness (Dynamic young's moduli) of representative samples showing that acid-sulfate alteration reduces the stiffness of lavas (red dotted line) and increases the stiffness of tuffs (yellow dotted line). The box and whisker plot elements represent median (centerline), upper and lower quartiles (box limits), 1.5x interquartile range (whiskers), outliers (filled large circles), and individual data points (small dots). Moduli data under effective pressure are up to maximum effective pressure before the onset of inelasticity occurs, that is, 14 MPa for tuffs and 28 MPa for lavas. The prefixes denote the alteration intensity of the samples as in Figure 2.1.

2.3.3 Sealing of the volcanic conduit

We propose a conceptual model for stratovolcanoes (Figure 2.5), where acid sulfate alteration and compaction of tuffs create partial seals within the volcanic conduit that can aid pressurization. Over months to years, as hydrothermal fluids navigate the conduit, they progressively alter the conduit rocks while degassing at the surface. In the lower conduit (Figure 2.5a), composed of lava and breccia within a tuff matrix, the fluids create secondary pathways in the lava by net dissolution and fill the pores in the tuffaceous matrix by net precipitation of secondary minerals (Figure 2.5b). They also partially fill the macro fractures with secondary minerals. Once the fluids reach the shallow porous tuff layers in the upper conduit (Jolly et al., 2012), they begin to seal them as well. This reduces the overall fluid pathways between the conduit rocks and the surface (Figure 2.5b).

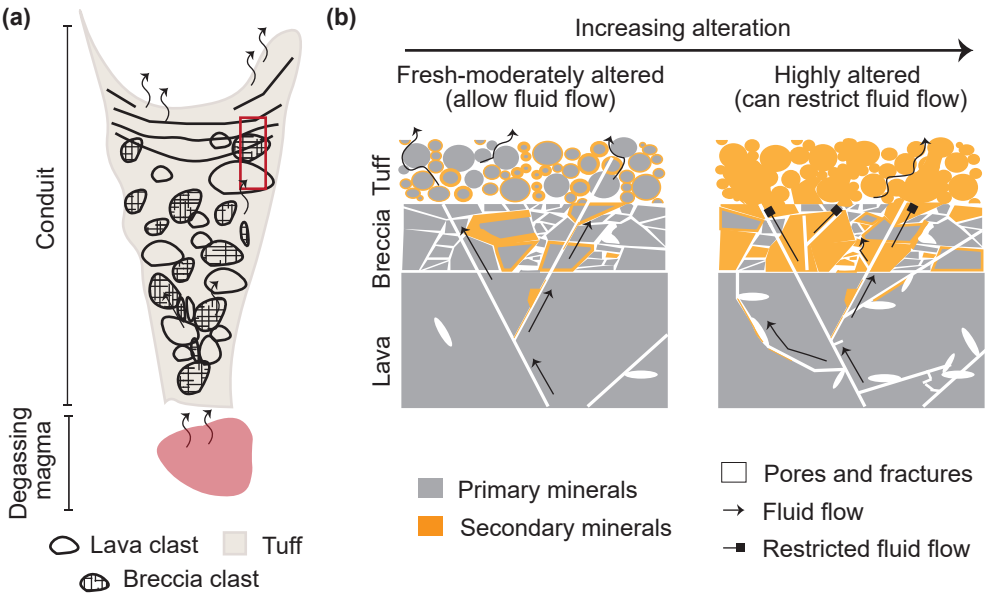

Figure 2.5: (a) Schematic of a volcanic conduit. A schematic of lithologies within the red box is shown in part (b). (b) Schematic showing the evolution of fluid pathways through tuff, breccia, and lava with hydrothermal alteration. Fresh to slightly altered lithologies would allow fluid flow. With increasing alteration, lavas undergo net dissolution and tuffs, net secondary mineral precipitation. Highly altered tuff can form zones of low porosity and low permeability, restricting fluid flow.

Subsurface pressures further control the fluid pathways within the conduit. Crack closure due to lithologic pressure will reduce fluid pathways, especially in lithologies with high aspect ratio pores, like altered lavas and breccias (Kennedy et al., 2020). The compaction of macropores in tuffs under pressure will also reduce the overall fluid pathways within the conduit (Figure 2.2). The inelastic compaction is more prominent in highly porous tuffs, irrespective of the alteration intensities, for effective pressures as low as 14 MPa, representing < 1 km depth (Figure 2.2). Cataclastic deformation can trigger pore collapse and shear-enhanced compaction resulting in reduced fluid pathways (Baud et al., 2000; Zhu & Wong, 1997; Wong & Baud, 2012). We propose that first, the fresh to moderately altered tuffs compact at shallow depths (< 1 km). Over time, enhanced sealing due to secondary mineral precipitation develops in the tuffs. Although lavas undergo net dissolution, precipitation of secondary minerals in their fractures and microcracks, as well as the closure of many of these compressible pores at subsurface pressure, aid in the overall reduction in fluid pathways in the conduit.

Other sealing mechanisms, such as high temperatures, typical of volcanic settings, could also aid in sealing the hydrothermal system by promoting compactant behavior of the conduit rocks (M. J. Heap et al., 2017b; Kennedy et al., 2010). Elemental sulfur likely

also plays a role in reducing fluid flow as it accumulates in isolated zones near fumaroles and beneath the crater floor from the condensation of SO_2 and H_2S (Christenson et al., 2017). Increasing temperature melts the sulfur, making it flow and clog porosity, with a complex viscous behavior (Scolamacchia & Cronin, 2016). Such processes have played a role in pressurizing Mt. Ruapehu (Christenson et al., 2010).

Overall, acid sulfate alteration and compaction, particularly of tuffs, can create a partially sealed hydrothermal system. Fluids in this system would flow through any unsealed macro fractures and secondary pathways developed by the dissolution of altered lavas and breccias. The existence of a partially sealed system is in agreement with the persistent degassing observed at Whakaari (Burton et al., 2021; Werner et al., 2008). A minor change in the permeability or overpressure of this partially sealed system could trigger an eruption (Burton et al., 2021), especially given the lower fragmentation threshold of tuffs (Spieler et al., 2004). Such changes can occur days to hours before the eruption. If fluids flow into the conduit at a higher rate, they can fracture the rocks and resonate in the lower conduit, generating accelerating trends in seismic tremors observed before eruptions (Chardot et al., 2015; Dempsey et al., 2020; Chouet, 1996; Chouet et al., 1994; Ogiso et al., 2015; Kato et al., 2015). The partially sealed hydrothermal system and ductile nature of the tuffs (M. J. Heap et al., 2015) could then lead to fluid pressurization. Werner et al. (2008) observed that earthquakes occurred preferentially when the gas pathways were open, with seismicity being shallow in the upper conduit. We suggest that the observed decrease in seismicity that follows a high tremor as seen in many eruptions at Whakaari (Chardot et al., 2015; Dempsey et al., 2020) and other volcanoes (Chouet et al., 1994; Ogiso et al., 2015) could be indicative of fluid pressurization in the upper conduit in part due to the development and possibly further compaction of a seal.

Throughout the process of alteration and compaction-related sealing of the volcanic conduit, the elasticity of the conduit rocks also changes. Ground uplift regularly observed at Whakaari is considered to be shallow and driven by hydrothermal processes (Fournier & Chardot, 2012; Peltier et al., 2009; Werner et al., 2008). We suggest that the increased fluid pressure build-up resulting from tuffs sealing and the continuous magmatic fluid sourcing drives the uplift. Such ground inflation, however, can also be compensated by the compaction of tuffs in the upper conduit (Figure 2.2). Our estimates of variably altered conduit rocks show that the young's moduli can vary between 5 GPa and 63 GPa (Figure 2.4). In particular, for tuffs (E=5 GPa-22 GPa), literature estimates significantly underestimate young's moduli for dynamic hydrothermal conduits, commonly reported in the range of 0.7 GPa-8.7 GPa at Whakaari (M. J. Heap et al., 2020a). We thus recommend the use of our data to constrain field geophysical inversions in acid-sulfate

altered conduits.

2.4 Concluding Remarks

We conclude that SO_2-rich fluids alter lava and tuff in volcanic conduits differently. In lava, they create fluid pathways by dissolving primary minerals, while in tuffs, they reduce fluid pathways by sealing them with secondary minerals. The divergent evolution of these conduit-filling lithologies with alteration can be responsible for partial sealing and further pressurization of volcanic conduits. Over time, compaction due to subsurface pressures in highly altered tuffs can further seal the conduit. Based on our findings, identifying tuffs and their type and degree of hydrothermal alteration using geophysical methods would help develop forecasting tools for phreatic and phreatomagmatic eruptions.

Chapter 3

High remanent magnetization measured in hydrothermally altered lavas

3.1 Introduction

In volcanic settings, results from aeromagnetic surveys are often used to indicate whether the underlying rocks are fresh or hydrothermally altered, for example, to assess slope-stability hazards (Finn et al., 2001; Fujii et al., 2015; Kereszturi et al., 2020; Reid et al., 2001). Fe-Ti oxides are one of the main magnetic phases in volcanic rocks. As hydrothermal fluids alter the host rocks, they dissolve and replace the primary minerals, including ferrimagnetic Fe-Ti oxides, usually reducing both magnetic susceptibility and the remanent magnetization of the rock (Fujimoto & Kikawa, 1989; Oliva-Urcia et al., 2011). This, along with thermal demagnetization within hot hydrothermal zones (Szitkar et al., 2014), has led several studies to link reduced magnetization intensities with hydrothermal alteration. Here we report a contrasting observation from Whakaari (White Island) volcano in New Zealand, in which some hydrothermally altered lavas show an order of magnitude higher remanent magnetization than fresh lavas.

Evidence of how hydrothermal alteration influences magnetic properties of volcanic rocks mainly comes from mid-ocean ridge basalts (Xu et al., 1997; Wang et al., 2020), seafloor hydrothermal systems (Fujii et al., 2015, 2018), geothermal fields (Pandarinath et al., 2019), and mineralized porphyry systems (Byrne et al., 2019). All these studies associate hydrothermal alteration with reduced magnetization. Almost all alteration types, except potassic, which involves magnetite creation, are commonly associated with

reduced magnetization (Clark, 2014; Riveros et al., 2014; Tapia et al., 2016). In some cases, the effect of alteration on the magnetic properties of fresh and altered rocks is derived by measuring only magnetic susceptibility, from which induced magnetization is calculated, and this is used to constrain field-scale magnetic data (Byrne et al., 2019; Caratori Tontini et al., 2012; Kereszturi et al., 2020; Nicolosi et al., 2016). But, the total magnetization of volcanic rocks is the vector sum of their induced (magnetic susceptibility multiplied by the local Earth's magnetic field) and remanent magnetization (Tauxe, 2010).

Thus, if natural remanent magnetization dominates the overall magnetization as observed at Whakaari volcano (Woodward & Mumme, 1993), it is important to understand how changes with alteration in the composition, concentration, and grain size distribution of ferrimagnetic minerals contribute to both components of magnetization (Gee & Kent, 1997; Moskowitz, 1980). In hydrothermal settings, the primary ferrimagnetic minerals are likely titanomagnetite or magnetite, which are progressively dissolved (Channell & Hawthorne, 1990; Wang et al., 2020) or oxidized to titanomaghemite or maghemite (Johnson & Merrill, 1973). In the presence of SO_2-rich fluids, ferrimagnetic or paramagnetic Fe-sulfides could also be formed depending on the hydrothermal conditions (Benning et al., 2000).

Here we investigate the magnetic properties of variably altered volcanic lithologies from Whakaari (White Island) volcano. Whakaari is New Zealand's most active volcano with a history of phreatic and phreatomagmatic eruptions (Dempsey et al., 2020; Kilgour et al., 2019, 2021). A magma source 0.8-1 km deep (Jolly et al., 2018) drives the circulation of hydrothermal fluids through the various conduit-filling lithologies (Christenson et al., 2017; Giggenbach et al., 2003). The resulting hydrothermal alteration dissolves the primary minerals of these lithologies and precipitates secondary minerals (Kennedy et al., 2020) (Chapter 2). In this study, we investigate the induced and remanent magnetization of variably altered conduit-filling and surficial lithologies at Whakaari and provide plausible causes for the high remanent magnetization observed in the hydrothermally altered lavas.

3.2 Materials and Methods

3.2.1 Sample description

The sample set consists of forty-two variably altered conduit-filling lithologies: lavas, tuffs, and breccias ejected as ballistics during the 2016 eruption and vesicular lavas

and sulfur flow from surface outcrops. Sample collection, as well as characterization of hydrothermal alteration mineralogy and intensity using X-ray diffraction, petrography, backscattered-electron imaging (BSE), and energy dispersive spectroscopy (EDS), is reported in Chapter 2. Overall, these samples underwent acid-sulfate alteration in which their primary minerals (plagioclase, pyroxene, volcanic glass, and Fe-Ti oxides) were consumed to different extents and replaced by a secondary mineral assemblage of alunite ± cristobalite ± tridymite ± anhydrite ± clays ± pyrite ± amorphous phases (silica/aluminosilicates) (Chapter 2). Based on the secondary mineral assemblage, it is inferred that the samples were altered by hot acidic (pH<2-6) fluids at temperatures less than 400^{o}C (Hedenquist et al., 1993; Pirajno, 2009; Zimbelman et al., 2005). The samples were classified based on the proportion of secondary phases as fresh to slightly altered (0-5%), moderately altered (5-40%), and highly altered (>40%). A list of reference IDs for the measured samples is provided in the Appendices (Table A.2).

3.2.2 Magnetic properties

The intensity of natural remanent magnetization (NRM) and magnetic susceptibility of the samples were measured using the Agico JR-6A spinner magnetometer and Bartington MS2B dual-frequency sensor, respectively. The Bartington MS2B dual-frequency sensor was calibrated using a 10 cm^3 sample of 1% Fe_3O_4. The low field reversible magnetic susceptibility was measured at low (0.46 kHz) and high (4.6 kHz) frequencies. Temperature dependence of magnetic susceptibility between room temperature and 700^o C was also measured on select, powdered samples (2-3 g), representative of the lavas, using a Bartington MS2 magnetic susceptibility system and furnace.

The (in-situ) intensity of induced magnetization (M_i) was then computed as $M_i = \chi \times H$, where χ is the bulk magnetic susceptibility calculated as the average of the low and high-frequency volume-specific susceptibilities and H is the local geomagnetic field intensity (H = 42.552 A/m at Whakaari, corresponding to B = 53472.7 nT in 2019 (Alken et al., 2021)). Total magnetization (M) was computed as the scalar sum of NRM and M_i. Due to the nature of ballistics, the orientations in which the samples originally cooled could not be retrieved, so vector addition is not possible. Data from low and high frequency magnetic susceptibility measurements, intensities of induced, remanent, and total magnetizations of all samples, and the associated standard deviations are provided in the Appendices (Tables E.9 and E.10).

Both induced and remanent magnetization depend primarily on the composition and concentration of the constituent magnetic minerals. The bulk magnetic susceptibilities

of ferro- and ferri-magnetic minerals such as titanomagnetite, magnetite, maghemite, greigite, and pyrrhotite are orders of magnitude stronger than those of paramagnetic minerals such as pyrite. Ferro- or ferri-magnetic minerals are essential for a remanent magnetization. Grain size also plays a crucial role in the division between remanent and induced magnetization in a rock, specifically the balance between superparamagnetic (SPM), stable single domain (SD), and multi-domain (MD) grains, since this affects the stability of the grain-scale magnetic moments.

The stability of the magnetization carried by an assemblage of identical uniformly magnetized (i.e., SPM or SD) grains is conventionally described by a relaxation time, τ, that increases with grain volume and decreases with temperature (Néel, 1949). At any temperature, e.g., ambient temperature, there is a "blocking" grain volume below which the overall magnetization decays rapidly (τ <100 s), and the grains are defined as superparamagnetic (SPM). The magnetic moments of larger grains are stable over longer time periods, and these grains are termed stable single domain (SD). SD grains become more stable with increasing volume until it finally becomes energetically favorable to split into two or more "domains" with different directions of magnetization. Domain walls move relatively easily in an imposed magnetic field, allowing the total grain moment to change. It follows that susceptibility (and induced magnetization), which requires rapid response to an imposed field, is strongest in SPM grains, moderate in MD grains, and lower in SD grain assemblages. Conversely, remanence is held most strongly in SD grains, is less stable in MD grains, and SPM grains cannot retain a remanent magnetization.

In this study, susceptibility has been measured using an alternating magnetic field, which requires the induced magnetization of the sample to alternate with the signal. The maximum frequency at which a SPM grain moment can alternate decreases with increasing volume (and relaxation time). Hence, the difference between the low frequency and high-frequency susceptibility measurements is a measure of the SPM grains in a specific size range close to the SPM/SD boundary (≈ 0.03 μm for spherical magnetite grains). Grains of other ferrimagnetic minerals should behave similarly, although the SPM/SD grain size boundary will differ slightly. Frequency dependence of susceptibility, χ_{FD}, (the difference between susceptibilities measured at low and high frequencies expressed as a percentage of the low-frequency value) has been used extensively in environmental magnetism to detect SPM grains formed by secondary processes such as pedogenesis, microbial activity, and burning (Dearing et al., 1996; Torrent et al., 2010). In such cases, values rarely exceed 14%, with values greater than 10% being taken to indicate a predominance of SPM grains, while values less than 2% indicate primarily SD and/or MD grains (Dearing et al., 1996). χ_{FD} was computed only for samples with magnetic susceptibility

greater than 0.0001 SI, which can provide reliable dual-frequency data.

To determine the coercivity (ability to withstand demagnetization) spectra of ferrimagnetic minerals present in the lavas, a fresh to slightly altered, moderately altered, and highly altered lava were demagnetized using a Molspin alternating field demagnetizer. The demagnetization was conducted progressively using peak alternating field steps starting at 5 mT, then 10 mT, followed by increments of 10 mT up to 80 mT. At each step, the demagnetization was performed along three perpendicular axes. After each step, the remaining NRM was measured using the Agico JR-6A spinner magnetometer. Data from the alternating field demagnetization experiments are provided in the appendices (Table E.11).

3.2.3 Compositional imaging

The composition of magnetic minerals was identified by analyzing elemental X-ray maps, BSE, and EDS data. The data were acquired using the JEOL Field Emission Electron Probe Microanalyser System 8530F at the University of Auckland on eight thin sections of variably altered lavas, tuffs, and breccias from Chapter 2. X-ray maps of elements Si, Al, Fe, S, Ti, Na, Mg, P, O, K, Ca and Mn, were acquired for a representative 1.5 $\times$ 1.5 mm area of the thin section. Color composite of Fe-Ti-S maps was then created using Fiji software (Schindelin et al., 2012) to identify the magnetic phases present in these samples (Fe-oxides, Fe-Ti oxides, or Fe-sulfides). The BSE images and X-ray maps were also used to estimate the grain size of magnetic phases in the samples. EDS was used to verify the composition of some grains imaged using BSE and approximate their Fe/Ti ratio. The raw X-ray map data are available in the data repository (see Data Availability).

3.3 Results and Discussion

3.3.1 Magnetization intensity

Natural remanent magnetization (NRM) dominates over induced magnetization in all sampled lithologies (Koenigsberger ratio, Q>1; Figure 3.1a). Overall, we observe a decrease in magnetic susceptibility and, therefore, induced magnetization, with increasing alteration in lavas and tuffs. NRM, on the other hand, varies by about five orders of magnitude among different lithologies. The surficial, fresh to slightly altered sulfur flows have low NRM ($\leq$0.01 A/m). As these flows are primarily composed of native sulfur and detrital silica (Chapter 2), we attribute this to the very low concentrations of ferri-

magnetic minerals. In surficial vesicular lavas, we observe low ($\leq$0.08 A/m) to moderate NRM (2.73 A/m - 4.04A/m), the variability of which we attribute to porosity variations. Vesicular lavas that have lower NRM are highly porous (ϕ = 61% to 75%) while those with moderate NRM have a lower porosity (ϕ = 53% to 62%, porosity values from Chapter 2).

Among the conduit-filling lithologies, lavas have higher NRM compared to tuffs (Figure 3.1a). All except one fresh to slightly altered lava also have higher NRM compared to breccias. In breccias, there is no correlation between NRM and increasing alteration intensity. Highly altered breccias (0.01-2.48 A/m) can have a higher or lower NRM than moderately altered breccia (1.13 A/m). For tuffs, however, NRM decreases with increasing alteration intensity. Highly altered tuffs have lower NRM ($\leq$0.20 A/m) than moderately altered tuffs (0.76 A/m - 1.42 A/m). In contrast to tuffs, lavas show the opposite trend between NRM and alteration intensity. Highly and moderately altered lavas have higher NRM (3.00 A/m - 66.12 A/m) than fresh to slightly altered lavas (1.94 A/m - 3.00 A/m).

The altered lavas have 1-2 orders of magnitude higher NRM even compared to previously studied fresh lavas from Whakaari by Woodward and Mumme (1993) (Figure 3.1b). Furthermore, their NRM is also higher compared to the total magnetization of Whakaari rocks (3.7 to 10.1 A/m) measured by Hurst and Christoffel (1973). Highly magnetized rocks in Whakaari's crater were previously interpreted as fresh andesitic flows and sills (Woodward & Mumme, 1993), but could these instead be altered lavas in the conduit similar to our samples? Next, we study the magnetic phases within the samples.

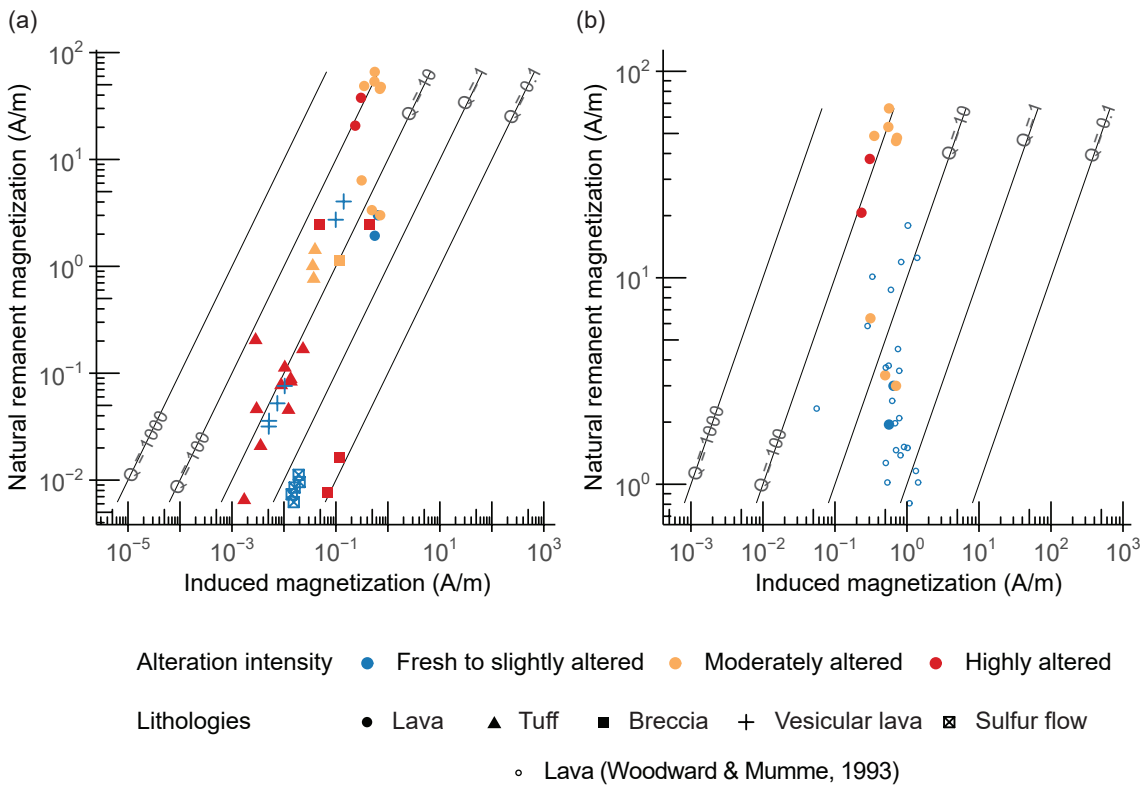

Figure 3.1: Natural remanent and induced (in a field of 42.552 A/m) magnetizations of (a) all variably altered lithologies sampled from Whakaari (b) only variably altered lavas shown together with fresh andesitic lavas from Whakaari from Woodward and Mumme (1993). Grey lines are the Koenigsberger ratios (Q), the ratio of natural remanent to induced magnetization. The symbols and colors represent the lithologies and alteration intensity of the samples, respectively. Measurement uncertainties are within the size of the symbols.

3.3.2 Magnetic phases in conduit-filling lithologies

Different magnetic phases in lavas, tuffs, and breccias are observed from X-ray maps (Figure 3.2). Fe-Ti oxides and pyroxene are the primary Fe-bearing phases in lavas with minor traces of Fe-oxides and Fe-sulfides. As pyroxene is paramagnetic, the Fe-Ti oxides, likely titanomagnetite with some magnetite, are the primary NRM carriers in lavas, irrespective of the degree of alteration. The presence of titanomagnetite and magnetite in Whakaari rocks is inferred by Hurst et al. (2004) and also supported by the observed decrease in magnetic susceptibility of the studied lavas from 390-500^{o}C to close to zero at 580^{o}C, the Curie temperature of magnetite (Figure D.1). Tuffs and breccias mainly have Fe-sulfides, likely pyrite, pyrrhotite, or greigite rather than Fe-Ti oxides. Fe-Ti oxides are only observed in one of the investigated highly altered tuffs. The presence of Fe-Ti oxides and Fe-sulfides in these lithologies indicates complex redox conditions within the

conduit (Benning et al., 2000; Shi, 1992).

In terms of magnetic phase composition alone, hydrothermal alteration has affected lavas less than tuffs and breccias. Unlike in lavas, alteration processes have consumed the primary Fe-Ti oxides in most tuffs and breccias. This might be attributed to the inherently high hydraulic permeability of tuffs and breccias, which allows hydrothermal fluids to readily consume the Fe-Ti oxides and precipitate Fe-sulfides, whereas lavas with low inherent permeability instead undergo net dissolution (Chapter 2).

As the primary minerals in these lavas dissolve, the grain size distribution of Fe-Ti oxides changes with increasing alteration. The fresh to slightly altered and moderately altered lavas have Fe-Ti oxides as both phenocrysts and groundmass phases (Figure 3.2). In comparison, the highly altered lavas only have groundmass Fe-Ti oxides (Figure 3.2). As a result, the NRM of these variably altered lavas could differ considerably depending on the Fe-Ti oxide grain size and their ability to retain a remanent magnetization.

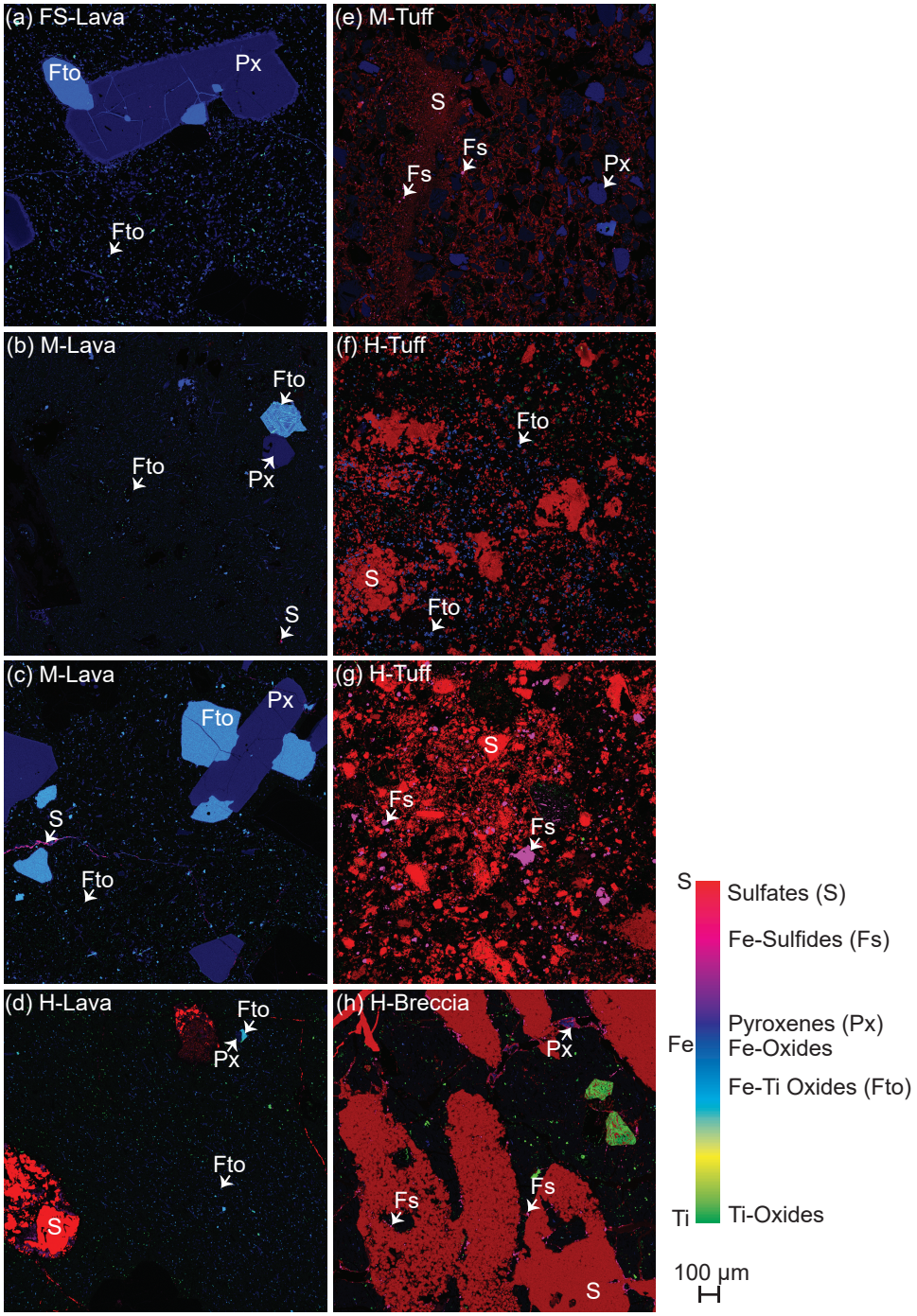

Figure 3.2: X-ray color composite maps of Fe-Ti-S bearing minerals. All maps have the same scale. The prefixes indicate fresh to slightly altered (FS-), moderately altered (M-), and highly altered (H-). Fe-Ti oxides (cyan) are the primary magnetic phase in lavas (a-d). In tuffs, one of the highly altered samples (f) has Fe-Ti oxides as its primary magnetic phase, while the others (e and g) have Fe-sulfides (pink) as the primary magnetic phase.

The lavas, tuffs, and breccias show an unusually broad range of frequency dependence of magnetic susceptibility (χ_{FD}) (Figure 3.3), indicating significant differences in

the grain size distributions of the ferrimagnetic phases. Overall the highest values of χ_{FD} (>10%) are found in some highly altered breccia samples, which have variable bulk magnetic properties, and in highly altered tuffs, which have relatively weak bulk susceptibilities and NRM (Figures 3.1 and 3.3). The high χ_{FD} of tuffs is noteworthy since, although both bulk susceptibility and NRM are low compared with the lavas, observations show they contain mainly Fe-sulfides (Figure 3.2). We interpret the high χ_{FD} of the tuffs as being largely due to ferrimagnetic sulfides, greigite, or pyrrhotite, in a SPM state.

In lavas, the fresh to slightly altered and moderately altered samples have the highest bulk susceptibilities and very low χ_{FD} (<2%) (Figure 3.3), which, together with X-ray imaging (Figure 3.2), indicates high concentrations of ferrimagnetic Fe-Ti oxides in the SD-MD grain size range that carry the moderate to high NRM (Figures 3.1 and 3.3). The highly altered lavas, despite having a lower bulk susceptibility, retain a strong NRM and have a markedly higher χ_{FD} (≈8%) (Figures 3.1 and 3.3). This indicates that the highly altered lavas have ferrimagnetic Fe-Ti oxides in the SD-SPM grain size range. These observations are consistent with the observed decrease in the overall grain size distribution, from fresh and moderately altered lavas to highly altered lavas (Figure 3.2). The NRM in highly altered lavas would be carried by the remaining SD grains with the SPM fraction producing the high χ_{FD}. Next, we further discuss the plausible causes of high NRM in hydrothermally altered lavas.

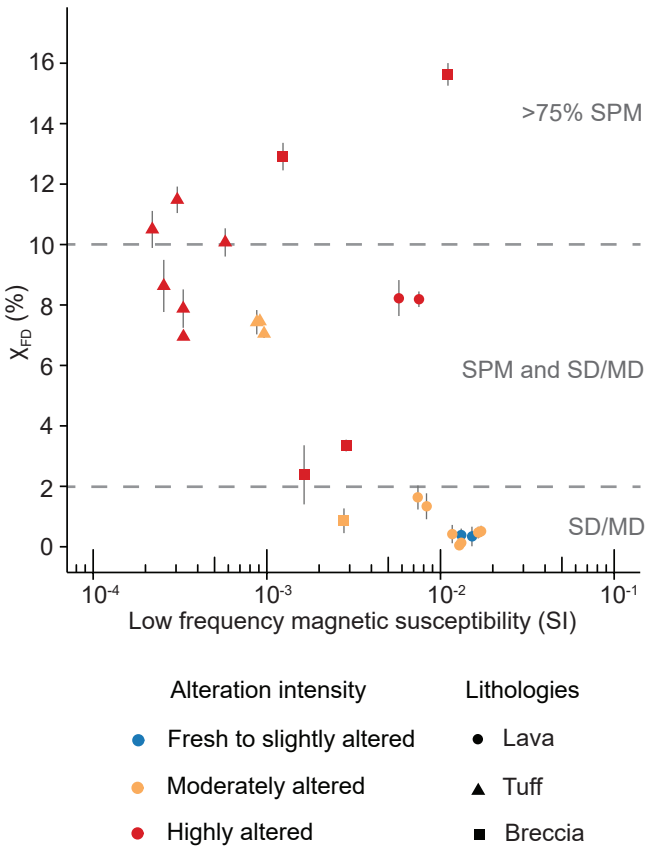

Figure 3.3: Frequency dependence of magnetic susceptibility (χ_{FD}) plotted against low-frequency susceptibility for variably altered samples of conduit-filling lithologies, lavas, tuffs, and breccias. Measurement uncertainties are shown as grey bars. Frequency dependence up to 2% indicates that the magnetic grains present are mainly single domain (SD) or multi-domain (MD), up to 10% indicates that some of the grains are superparamagnetic (SPM), greater than 10% indicates that more than 75% of the magnetic grains are SPM.

3.3.3 Plausible causes of high remanent magnetization in hydrothermally altered lavas

Although hydrothermal alteration is often assumed to dissolve primary ferrimagnetic minerals and reduce both the remanent and induced magnetization of rocks, our results show that the assumption of altered lavas having lower magnetization than fresh lavas may not always be true. Altered lavas could carry higher remanent magnetization than fresh lavas due to one or more of the following: (a) they had equal or higher remanent magnetization in their initial fresh state due to ferrimagnetic grains that were efficient and stable NRM carriers, (b) their ferrimagnetic grains were shielded from being consumed by alteration processes and (c) alteration-related enhancement of ferrimagnetic grains.

We discuss the feasibility of these in detail below.

High initial remanent magnetization can occur in lavas with a high concentration of ferrimagnetic Fe-Ti oxides, many of which are fine single-domain grains capable of carrying stable NRM (Fujii et al., 2018). From our alternating field demagnetization data and BSE images (Figure 3.4), we observe a difference in both the magnetic coercivity spectra (ability to withstand demagnetization) and size of Fe-Ti oxide grains between fresh and altered lavas. Fresh to slightly altered lavas contain mainly large (>1 μm) Fe-Ti oxide grains with relatively low coercivity and a median destructive field (MDF) below 10 mT (Figure 3.4a and b). Moderately and highly altered lavas, on the other hand, contain Fe-Ti oxide grains with higher coercivities and MDFs between 20-25 mT (Figure 3.4a). The higher coercivity of altered lavas suggests the predominance of fine sub-micrometer scale, single-domain (SD) Fe-Ti oxide grains in addition to large grains as observed in the BSE images (Figure 3.4c and d). The presence of SD grains in altered lavas is also consistent with the observed low to moderate frequency dependence of magnetic susceptibility (Figure 3.3). Furthermore, a reduction in the effective magnetic grain size due to the zoning of Fe-Ti oxide phenocrysts in moderately altered lavas could also contribute to the increased coercivity (Figure 3.4e). Depending on the shape and Ti content of the fine Fe-Ti oxide grains in altered lavas, they could act as single-domain (or pseudo-single domain or single vortex) grains at sizes less than 0.1 μm for magnetite and less than 1-2 μm for titanomagnetite (Butler & Banerjee, 1975; Day et al., 1977). Such single-domain (and SD-like) grains can be efficient and stable carriers of NRM as also observed, for example, in fresh lavas from the Okinawa Trough (Fujii et al., 2018). Due to these efficient NRM carriers, the now altered lavas at Whakaari could have had equal or higher magnetization in their initial fresh state. When altered, these lavas would have a higher magnetization than other fresh lavas composed primarily of multi-domain Fe-Ti oxides and lacking such efficient NRM carriers.

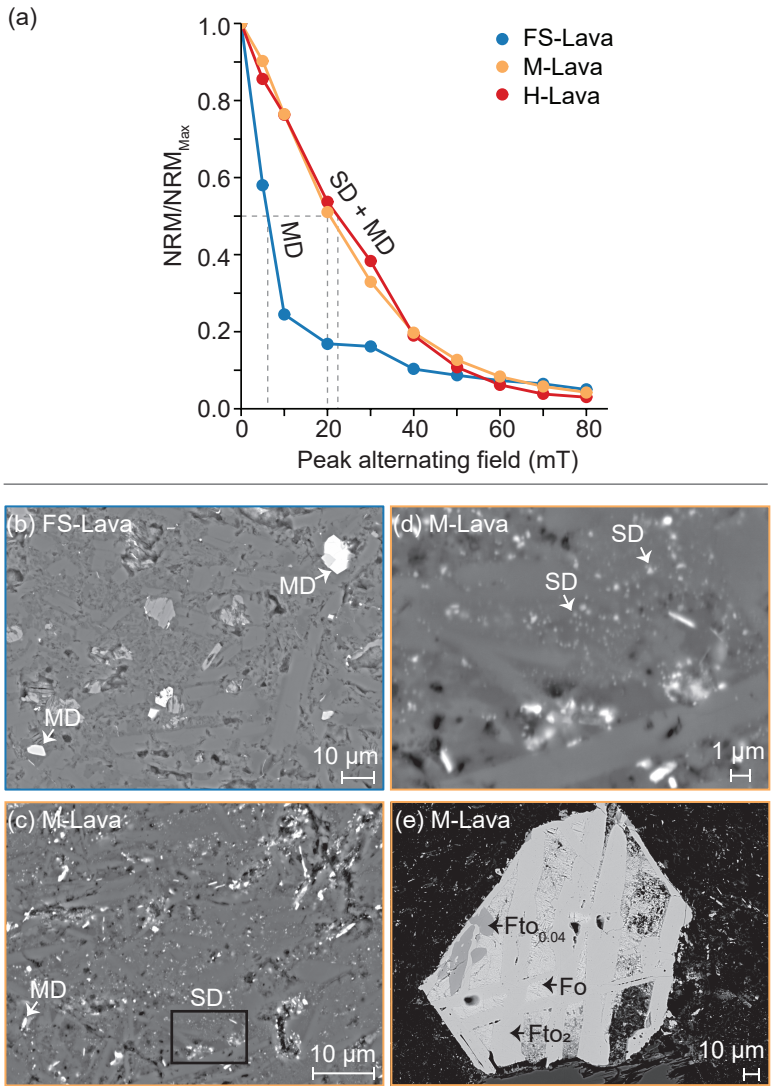

Figure 3.4: Alternating field demagnetization behavior of variably altered lavas. (a) NRM/NRM$_{max}$ decays faster in fresh-slightly altered (FS) lava compared to moderately (M) and highly altered (H) lavas. Corresponding Zijderveld diagrams are provided in the supporting information Figure D.2. Grey dotted lines indicate the median destructive field. (b) Representative backscattered electron images showing that the fresh-slightly altered lava has mainly multi-domain (MD) Fe-Ti oxide grains (white in images). (c) Moderately altered lava has a combination of multi-domain and sub-micron scale single-domain (SD) grains. A zoomed view of the area in the black box is provided in (d). (e) A zoned texture with varying Fe/Ti content is also observed in some grains, reducing the effective magnetic grain size. Fto: Fe-Ti oxides (subscript indicates the EDS Fe/Ti ratio), Fo: Fe-oxides.

Altered lavas could also retain their high remanent magnetization if their ferrimagnetic grains carrying the NRM were protected from alteration processes. From BSE images (Figure 3.5), we observe that large Fe-Ti oxide phenocrysts appear to be con-

sumed by dissolution, but the fine Fe-Ti oxide grains in the groundmass remain relatively unaffected. As dissolution has been thought to consume fine titanomagnetite grains faster than larger grains (Channell & Hawthorne, 1990; Xu et al., 1997), our contrasting observation indicates that the fine Fe-Ti oxide grains may have been shielded from dissolution. Zhou et al. (2001) support our observations, where sub-micron-sized titanomagnetite grains in mid-ocean ridge basalts are shielded from oxidation by the surrounding interstitial glass. We, therefore, suggest that interstitial glass, given its low reactivity compared to pyroxene and plagioclase (G. Rowe & Brantley, 1993), protects fine-grained Fe-Ti oxides in the groundmass from dissolving (Figure 3.5). Furthermore, if the groundmass Fe-Ti oxide grains were distant from fluid pathways, this would also prevent them from being dissolved by hydrothermal fluids.

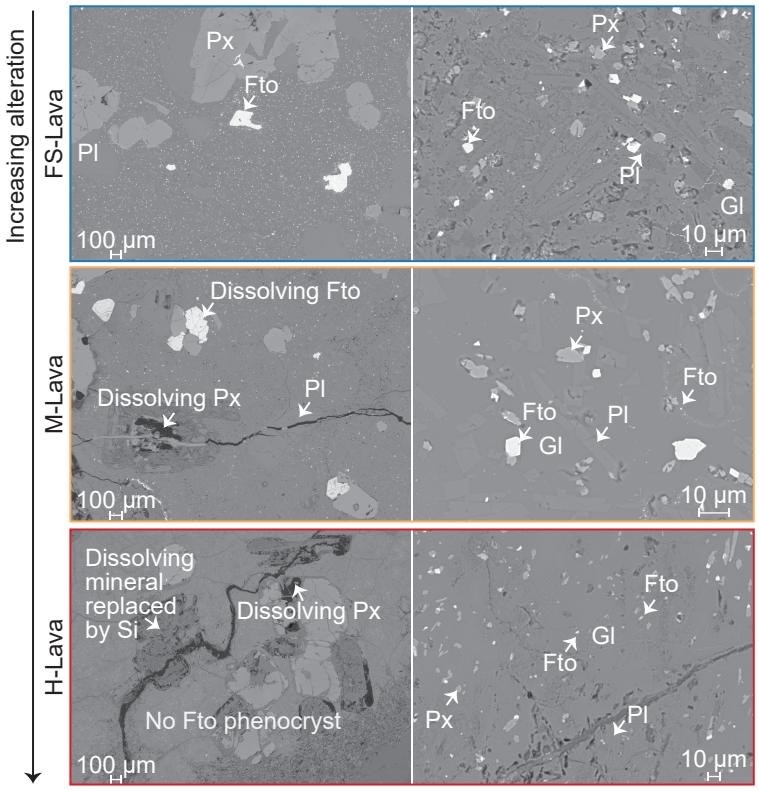

Figure 3.5: Backscattered electron images of phenocrysts (left) and groundmass (right) of variably altered lavas. With increasing alteration, the phenocrysts of pyroxene (Px), plagioclase (Pl), and Fe-Ti oxides (Fto) are dissolved and replaced by secondary silica (Si). In contrast, small Fe-Ti oxide grains that carry most of the stable NRM remain unaffected in the groundmass, likely due to interstitial glass (Gl) acting like a protective layer. The prefixes indicate fresh to slightly altered (FS-), moderately altered (M-), and highly altered (H-).

A third explanation for the high magnetization could also be an alteration-related

enhancement in magnetization. While we do not see evidence for this in our data, ferrimagnetic greigite or pyrrhotite could have precipitated with sulfates in the moderately and highly altered lavas (Figure 3.2). NRM intensities from 6.8 A/m to as high as 953 A/m have been measured in samples containing pyrrhotite (Honsho et al., 2016). An oxidizing environment could also enhance titanomagnetite (Johnson & Merrill, 1973). Compositional iron enrichment is also thought to be a cause for strong crustal magnetization on the Terra Cimmeria-Sirenum region of Mars (AlHantoobi et al., 2020; Ojha et al., 2021). Alteration-related enhancement in magnetization is also thought to have played a role at the Haughton impact structure where post-impact hydrothermal alteration led to the crystallization of magnetite (Zylberman et al., 2017). Such enrichment may not be evident in our X-ray maps (Figure 3.2) due to inherent scale limitations (1.5 mm X 1.5 mm area on thin sections) compared to the sample volume used for the magnetization measurements (25.4 mm X 22 mm cylindrical cores).

3.4 Concluding remarks

Irrespective of the most likely cause, our data shows that hydrothermally altered regions may not always be associated with reduced magnetization. In particular, lavas could form areas of strong magnetization in volcanic conduits, even when highly altered. Given that aeromagnetic data is widely used to identify hydrothermally altered regions in volcanoes, we urge caution in assuming that only areas of reduced magnetization could represent hydrothermal alteration. We also urge caution in using only trends in magnetic susceptibility, and thereby induced magnetization, to constrain field-scale magnetic data, especially in volcanoes like Whakaari, where NRM dominates over induced magnetization.

Chapter 4

Petrophysical and corresponding geophysical properties of variably altered lavas from Mt. Taranaki

4.1 Introduction

Hydrothermal alteration is known to change petrophysical properties such as mineralogy, porosity, and permeability of volcanic rocks (Farquharson et al., 2015; M. J. Heap et al., 2019; Mordensky et al., 2019). Such alteration-related changes can often promote volcano instability by weakening the edifice (Ball et al., 2015; M. J. Heap et al., 2021a; López & Williams, 1993) or by allowing pore-pressure augmentation (M. J. Heap et al., 2021b). The resulting destabilization of the volcano poses significant hazards ranging from the collapse of parts of individual lava domes generating block and ash flows (M. J. Heap et al., 2019; Ball et al., 2013; Charbonnier & Gertisser, 2008; Rodríguez-Elizarrarás et al., 1991) to major sector collapses generating debris avalanches (Reid et al., 2001, 2010a; Voight & Elsworth, 1997; Voight et al., 1983). Collapse-related sudden depressurization of the system can also trigger explosive eruptions such as that observed at Te Maari, Tongariro, wherein collapse of hydrothermally altered breccia triggered the 2012 eruption (Procter et al., 2014). Mt. Taranaki, an andesitic stratovolcano in New Zealand, has a long-standing history of lava dome and sector collapses (Platz et al., 2012; Zernack et al., 2012). But the lack of petrophysical properties on altered rocks from Mt. Taranaki limits the assessment of the role hydrothermal alteration may have played in its instability. Here we study the petrophysical and geophysical properties of variably altered lavas from Mt. Taranaki to assess the role hydrothermal alteration may have played in its slope failures,

mainly lava dome collapses.

Factors affecting the stability of lava domes, including hydrothermal alteration, have been studied at several volcanoes (Ball et al., 2013; Coats et al., 2018; M. J. Heap et al., 2019; Harnett et al., 2019a). Gravitational loading, internal gas overpressures, topography, rainfall, change in extrusion direction are some of the most common mechanisms attributed to promoting instability (Harnett et al., 2019b). More intrinsic factors such as crystallinity and porosity of the dome-forming lavas are thought to control the overall dome strength (Harnett et al., 2019a; Zorn et al., 2018). The role of hydrothermal alteration in promoting instability is complex to understand due to the contrasting effects of dissolution and secondary mineral precipitation on the petrophysical properties of the rocks (Farquharson et al., 2019; Mordensky et al., 2018).

Mt. Taranaki's eruptive history of effusive and explosive volcanic activity (Damaschke et al., 2018; Torres-Orozco et al., 2017) is interspersed with cycles of edifice collapse and regrowth (Zernack et al., 2009, 2011, 2012). This cyclic destruction has resulted in a young upper edifice (above 1200 m) composed of lavas and pyroclastic flow units surrounded by a 15-times larger ring of older volcaniclastic deposits (Cronin et al., 2021; Zernack et al., 2009). In the upper edifice, the summit currently hosts a half-sectioned lava dome formed by the collapse of the western flank with a surrounding crater basin (Platz et al., 2012; Zorn et al., 2018). Almost all of the eruptive periods of Mt. Taranaki involved pyroclastic density currents, mostly related to summit dome emplacement and collapse generating block and ash flows that went up to 5 to more than 13 km from the source (Cronin et al., 2021; Platz et al., 2007; Procter et al., 2010). The dome collapses are considered to have ranged from syn-eruptive in nature to post-eruptive events (Platz et al., 2012; Lerner et al., 2019a, 2019b). Downslope the edifice consists of a ring of debris-avalanche deposits caused by large edifice failures intercalated by lahar deposits (Zernack et al., 2009; Lerner et al., 2019b).

Several past studies on Mt. Taranaki have focused on one or more of the petrophysical properties, magnetic properties, and strength of fresh lavas from the summit dome area and fresh lava clasts from the distal block and ash flow deposits (Higgins, 1996; Lerner et al., 2019a; G. Turner et al., 2018; Zorn et al., 2018). However, to our knowledge, no study has thus far investigated the properties of altered lavas at Mt. Taranaki. Given its history of collapses and the extensive evidence of hydrothermal weakening at other volcanoes (e.g., (Kereszturi et al., 2021; Norini et al., 2020; Opfergelt et al., 2006; Reid et al., 2001, 2010b)), it is vital to determine how hydrothermal alteration affects both the petrophysical and corresponding geophysical properties of rocks from Mt. Taranaki and the role that may have played in its past collapses.

4.2 Materials and Methods

4.2.1 Samples

The sample-set consists variably altered lavas collected from Mt. Taranaki (Figure 4.1). These include lavas mainly from the summit dome area and from block and ash flow deposits resulting from the collapse of the lava dome. A few samples were also collected from debris-avalanche deposits resulting from a sector collapse. Overall, twenty-four large sample blocks were collected in the field targeting potentially altered lavas from (a) outcrops near the summit dome (n=13) (b) clasts from block and ash flow deposits in Maero stream (n=8) (c) clasts from road-side debris-avalanche deposits on the western side of Mt. Taranaki (n=3). In addition, we also used fresh lavas collected by Zorn et al. (2018) from (a) outcrops on the summit dome (n=1) (b) clasts from block and ash flow deposits in Maero stream (n=8) and in Pyramid Stream (n=1). Details on each sample's location are provided in the Appendices (Table E.2). The large blocks were sub-sampled to thirty-four cylindrical cores (2.54 cm diameter $\times$ 2.2 cm length). Representative sections of each sample were also cut and polished to prepare thin sections and powdered for X-ray diffraction (XRD) analysis.

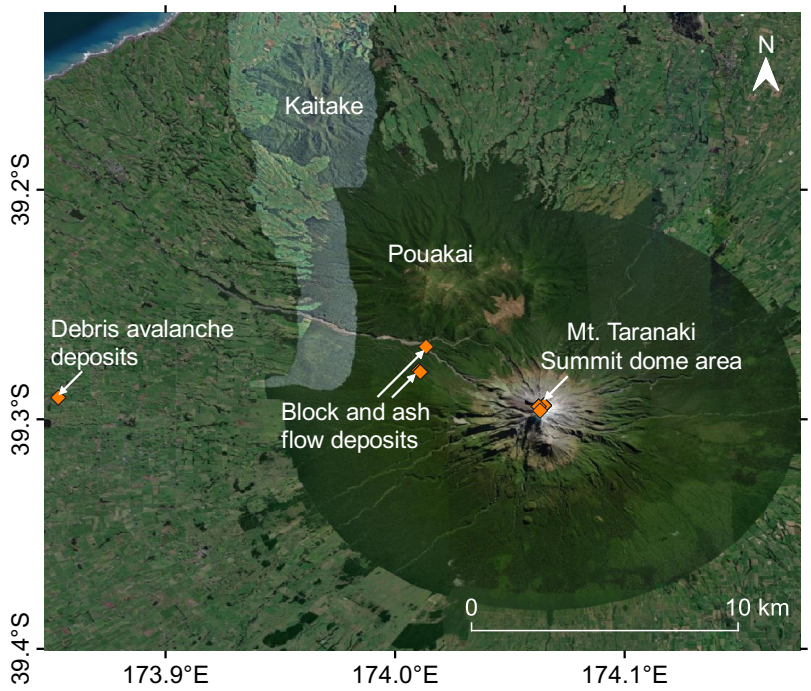

Figure 4.1: Sampling locations of variably altered lavas from Mt. Taranaki. Nearby relict andesitic volcanoes, Pouakai and Kaitake, of the Taranaki Volcanic Lineament are also shown. Note that the bright zone near Kaitake does not represent any particular feature. Map source: (ESRI basemap, 2021a).

4.2.2 Hydrothermal alteration intensity

The hydrothermal alteration mineralogy and intensity of each sample were characterized using XRD and petrographic analysis following the workflow provided in the Appendices (Figure B.3). The XRD data were collected on powdered samples using PANalytical Empyrean X-ray Diffractometer. The instrument and measurement conditions used were: Cu Kα, 45 kV, 40 mA, 0.5^o fixed divergence slit, in step-scan mode from an angular range of 5^o to 70^o 2θ, step size 0.013^o 2θ, time per step 97.92s. The raw XRD data were used to identify minerals by comparing the patterns to reference patterns in the Crystallography Open Database (COD) (Gražulis et al., 2020) using HighScore Plus software (Panalytical, 2012). The identified minerals were constrained by petrographic analysis. The mineral composition was then quantified using Rietveld refinement. The refinement quality was determined by visual examination of the peaks explained and the goodness of fit statistic. Rietveld refinement with the goodness of fit statistic less than four and all major peaks explained was considered good. A goodness of fit less than 5.5 was also considered acceptable in five samples as long as the selected phases explained all major peaks. The mineralogy of select samples was verified by backscattered-electron imaging (BSE) and

energy dispersive spectroscopy (EDS). Apart from the crystalline mineral phases, the amorphous phase content of each sample was also quantified. The AMORPH program (M. Rowe & Brewer, 2018) was used to determine the relative content of amorphous phases. These were converted into actual amorphous phase contents by calibrating with known volcanic glass calibration standards (Figure B.1). The amorphous phase-type of the samples was classified as either primary, secondary, or a mixture of both, based on the skewness results of the low-intensity amorphous curve from AMORPH (Figure B.2). Samples with a gaussian amorphous curve were classified to have primary volcanic glass. Whereas samples whose amorphous curves skewed at 22^o 2θ with skewness above 0.2 were considered to have secondary amorphous silica/aluminosilicates. The samples were then categorized based on the amount of secondary minerals as fresh to slightly altered (0-5%), moderately altered (5-40%), and highly altered (>40%). Data containing raw XRD patterns and results from phase quantification for all samples are available in the data repository (see Data Availability) and appendices (Table E.6), respectively. The crystallinity of the samples, that is the volume percent of crystalline mineral phases detectable by XRD, was also computed using the relation below:

$$Crystallinity(\%) = 100 - Actual\ amorphous\ phase\ content(\%). \tag{4.1}$$

4.2.3 Fluid pathways

The fluid pathways through each sample were quantified by measuring their porosity and hydraulic permeability. The connected porosities of all dry samples were first measured at atmospheric pressure using a nitrogen gas porosimeter from Vinci Technologies (Poroperm). Then, to determine how these fluid pathways would evolve within the lava dome under subsurface pressures up to 500 m, the porosity and permeability of each sample (dry) were also measured under effective pressures from 1.5 MPa to 5.5 MPa. These measurements were performed using a porosimeter and permeameter AP608 from CoreTest by pycnometer for porosity and pulse-decay method for permeability. The porosity and permeability data and associated standard deviations for all samples are available in the appendices (Table E.8).

4.2.4 Elastic properties

Elastic properties of the samples were quantified in terms of their stiffness using dynamic Young's and shear moduli. These moduli are a measure of the rock stiffness to an applied stress. P-and S-wave travel-time data were acquired on dry samples using ultrasonic

transducers (0.5 - 1 MHz) at atmospheric conditions. P-(V_p) and S-wave (V_s) speeds were computed by dividing the sample length by the P- and S- wave arrival times, respectively. These wave speeds and the bulk density (ρ) of the samples were then used to compute the dynamic Young's (E) and shear (G) moduli using equations 4.1 and 4.2, respectively. The V_p, V_s, E and G data and associated standard deviations for all samples are available in the appendices (Table E.15).

$$E = \frac{\rho {V_s}^2 (3{V_p}^2 - 4{V_s}^2)}{({V_p}^2 - {V_s}^2)} \tag{4.2}$$

$$G = \rho {V_s}^2 \tag{4.3}$$

4.2.5 Magnetization

The magnetization intensity of the samples was quantified by measuring their natural remanent magnetization (NRM) and magnetic susceptibility. NRM was measured using the Agico JR-6A spinner magnetometer. Volume-specific magnetic susceptibility of the samples was measured using the Bartington MS2B dual-frequency sensor. The sensor was first calibrated using a 1% Fe_3O_4, 10 cm^3 sample. Each sample's volume-specific magnetic susceptibility was then measured at both low and high frequencies, 0.46 kHz and 4.6 kHz, respectively. Induced magnetization intensity of the samples was computed from these measurements as follows: $M_i = \chi \times H$, where χ is the average of low and high-frequency volume-specific magnetic susceptibility (SI units) and H is the intensity of the local geomagnetic field ($H = 43.797$ A/m at Mt. Taranaki since the magnetic flux density, $B = 55038.1$ ηT in 2019 (Alken et al., 2021)). The induced magnetization and NRM were summed to compute the samples' total magnetization intensity (M). Due to sampling limitations and flank collapse transport, the samples measured were unoriented. Therefore, a scalar addition is performed, and the magnetization is discussed in terms of its intensity. The data on low and high frequency magnetic susceptibility, intensities of remanent, induced, and total magnetization, and the associated standard deviations for all samples are available in the appendices (Tables E.12 and E.13).

4.3 Results and discussion

4.3.1 Petrophysical properties

Mineralogy

For our samples, lavas range from fresh to slightly altered (n=20), through moderately altered (n=13), to highly altered (n=1) (Figure 4.2). Field sampling targeted potentially altered rocks, and as a result, most of the lavas sampled near the summit dome are moderately to highly altered (n = 12), except one which was fresh to slightly altered. But in contrast, only two of the eleven lava clasts sampled from the block and ash flow and debris avalanche deposits are moderately altered. The lava from the summit area (n=1) and lava clasts (n=9) from the block and ash flow deposits collected by Zorn et al. (2018) are also fresh to slightly altered.

The fresh to slightly altered lavas mainly consist of primary feldspars, pyroxenes, amphiboles, Fe-Ti oxides, and amorphous phase (volcanic glass). Secondary minerals ($\leq$5% in total volume) include silica mainly in the form of cristobalite, with some tridymite. In moderately altered lavas, the proportion of primary minerals decreases and gets increasingly replaced by secondary alunite and silica (cristobalite) (up to 27%). The highly altered lava has none of its primary feldspar, pyroxene, and amphiboles preserved and is composed of secondary alunite, silica (quartz and cristobalite), amorphous phases, and some remanent Fe-Ti oxides. The amorphous phases are classified as primary volcanic glass (see Section 4.2.2). However, it could also be partially of secondary origin, especially in the highly altered lavas.

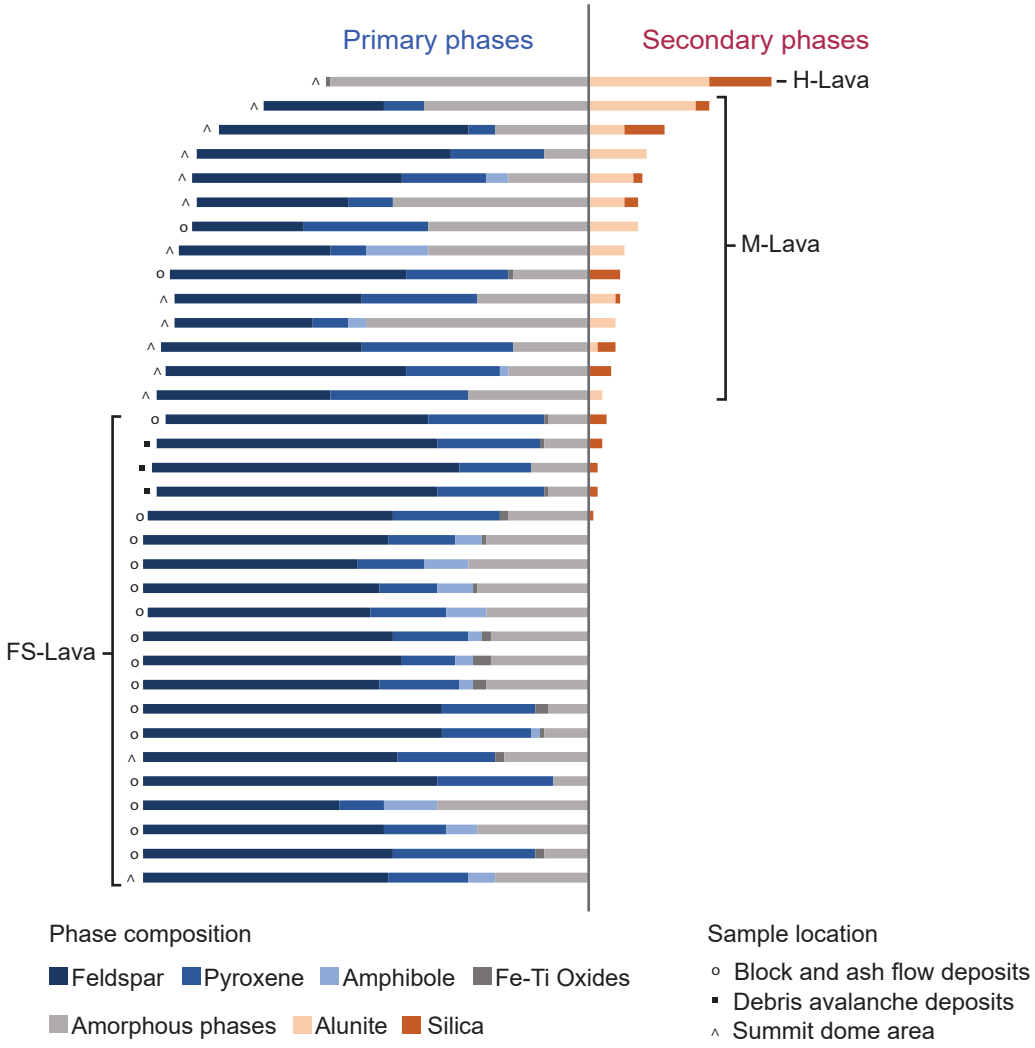

Figure 4.2: Phase composition of variably altered lavas determined by X-ray diffraction analysis. Bars represent major volumetric phase compositions, adding to 100%. Fresh to slightly altered samples (FS) are mainly composed of primary phases. Secondary phases increasingly replace primary phases in moderately (M) and highly (H) altered samples. Underlying data for all samples are provided in a tabular form in the appendices (Table E.6).

The presence of only silica (primarily cristobalite) as a secondary mineral in fresh to slightly altered lavas indicates alteration in a low-pH environment (pH<2), which upon subsequent neutralization (pH<4) would have added alunite to the mineral assemblage in moderately and highly altered lavas (Hemley et al., 1969; Stoffregen, 1987). Given their surficial occurrence and secondary mineral assemblage, we interpret that the lavas have undergone acid-sulfate alteration at low temperatures ($<250^oC$) characteristic of shallow environments (Zimbelman et al., 2005). Similar alteration to alunite and silica, often in association with clays, is also observed at exposed edifices and collapse deposits

of several other volcanoes worldwide (Frank, 1995; M. J. Heap et al., 2019; Norini et al., 2020; Zimbelman et al., 2004). No clays are, however, observed in the lavas from Mt. Taranaki studied here.

Fluid pathways

Our porosity and permeability data show a wide range of porosity (ϕ=5%-38%) and eight orders of magnitude variation in permeability of the lavas (Figure 4.3). While altered lavas have a slightly narrower range of porosity and permeability than fresh to slightly altered lavas, there is no systematic correlation between changes in fluid pathways and alteration intensity. As expected, lavas with high porosity are more permeable. However, some lavas with similar porosity (e.g. ϕ=11.1%-11.8%) show 1-2 orders of magnitude difference in permeability ($\kappa = 10^{-14} - 10^{-16}$ m^2). Similar differences in permeability for comparable porosities are common in volcanic rocks (Farquharson et al., 2015; M. J. Heap et al., 2017a; Mordensky et al., 2019) and can be associated with differences in pore shape, pore connectivity, or alteration-related changes. Fresh to slightly altered lava clasts from the debris avalanche deposits have low porosity and permeability (κ=$\leq 10^{-17}$ m^2). These clasts show the largest porosity and permeability reduction with effective pressure for our sample set. This is attributed to the closure of intra and inter-grain micro-fractures (cracks) and micro-pores (Mavko & Nur, 1978), as shown in the BSE image (Figure 4.3). Samples with higher porosity show little to no pressure dependence of porosity and permeability, attributed to relatively stiff large pores (Adam & Otheim, 2013) (Figure 4.3).

In accordance with Zorn et al. (2018), the porosity of fresh to slightly altered lavas has a significant inverse correlation (R^2=0.485, p-value<0.001) with their crystallinity. Zorn et al. (2018) interpret that the development of fluid pathways through these fresh lavas at Mt. Taranaki is mainly controlled by magma decompression and ascent rates, volatile exsolution, and crystallization (Cashman & Blundy, 2000; Calder et al., 2015; Zorn et al., 2018). Simplistically, fast ascending magmas have little time for outgassing, cooling, and crystallisation resulting in extrusion of lava with high porosity and low crystallinity (M. Heap et al., 2016; Zorn et al., 2018). Whereas, magmas ascending slowly, have had a greater opportunity to outgas, allowing more time for cooling for crystallisation of the melt prior to extrusion resulting in lavas with low porosity and high crystallinity (M. Heap et al., 2016; Zorn et al., 2018). At intermediate ascent rates, there may be some variations in this trend. As many of the fresh to slightly altered lavas used in this study are from Zorn et al. (2018) we see the inverse correlation between porosity and crystallinity as expected.

However, this correlation decreases and is insignificant in altered lavas (R^2=0.077, p-value$\not<$0.001) (Figure 4.4) indicating that the fluid pathways and crystallinity of the lavas are further controlled by alteration processes. The scattering of the porosity-crystallinity data for altered lavas is interpreted to be due to competing effects between dissolution and secondary mineral precipitation, by which the relative amount of crystalline minerals and fluid pathways change. The highly altered lava, for example, has low crystallinity and high porosity. Based on the XRD analysis and porosity data, we interpret that for this sample, primary minerals (pyroxene, feldspar, and amphibole) were mostly dissolved, creating new fluid pathways. However, alteration also results in the precipitation of secondary alunite and silica (mainly cristobalite), which relatively increased its crystallinity and decreased the fluid pathways (Figure 4.2). The observed petrophysical properties of variably altered lavas influence their geophysical signatures.

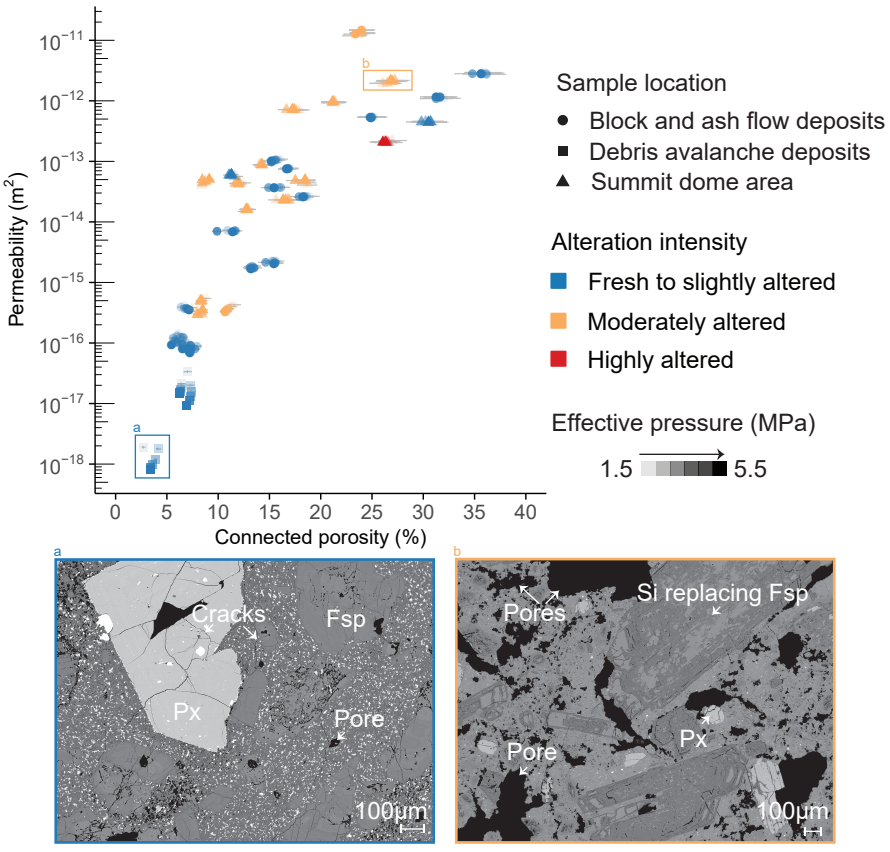

Figure 4.3: Porosity and permeability of variably altered lavas. Pore structures of select samples (boxes) are shown using BSE images. The letters on top of the boxes and border of BSE images correspond with each other. Px: pyroxene, Fsp: feldspar, and Si: silica. Underlying data for all samples are provided in a tabular form in the appendices (Table E.8)

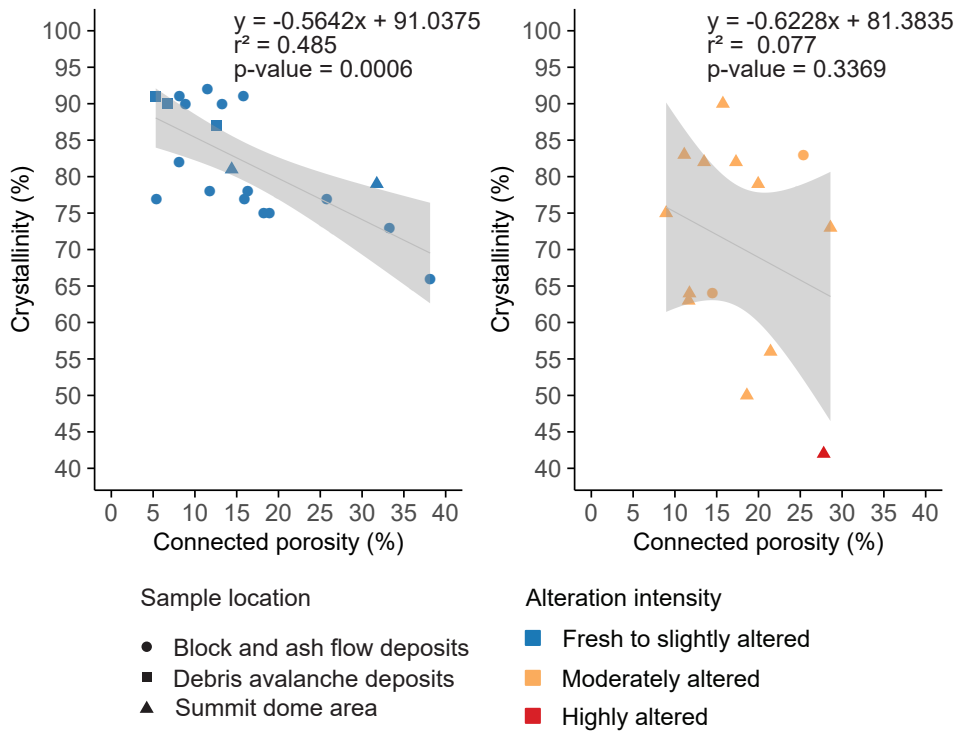

Figure 4.4: Correlation between crystallinity and connected porosity of fresh to slightly altered lavas (left) and moderately and highly altered lavas (right). Errors in porosity and crystallinity are less than 3%. The grey line is the linear regression fit, and the grey shaded regions around show 95% confidence intervals for the regression. The regression equation, coefficient of determination (r^2), and p-values are also shown. p-value <0.05 indicates a statistically significant correlation.

4.3.2 Lab-scale geophysical data

Magnetic properties

Magnetization data (Figure 4.5) show that the natural remanent magnetization intensity (NRM) of the lavas varies from 0.22 A/m to 30.6 A/m and their induced magnetization intensity (M_i) from 0.02 A/m to 3.97 A/m. Overall, NRM dominates induced magnetization in most samples (Q>1) except for some lava clasts (n=6) from the block and ash flow and debris avalanche deposits in which induced magnetization is equal or higher than NRM (Q<1). Fresh to slightly altered lavas have NRM from 0.86 A/m to 22.94 A/m and M_i from 0.15 A/m to 3.97 A/m. These values are in agreement with NRM intensities previously reported on fresh lavas from Mt. Taranaki (Cox, 1971; Downey et al., 1994; Locke et al., 1994; Lerner et al., 2019a; G. Turner et al., 2018). Moderately altered lavas, however, have a wider range of magnetization (NRM = 0.22 A/m-30.64 A/m, M_i=0.04-2.02 A/m) both lower and higher compared to fresh to slightly altered

lavas. In contrast, the highly altered lava has low magnetization (NRM = 0.34 A/m, M_i=0.02 A/m).

BSE-EDS and XRD data show that the primary magnetic carriers in the lavas are Fe-Ti oxides. Given the ability of these Fe-Ti oxides to carry strong NRM and based on previous observations (Cronin et al., 2021; Lerner et al., 2019a; M. Turner et al., 2011), we interpret these to be titanomagnetites. BSE-EDS data performed on select lavas also show different magnetic grain textures (Figure 4.5). A fresh to slightly altered lava (NRM = 1.29 A/m, M_i=3.97 A/m) has Fe-Ti oxides as phenocrysts and in the groundmass throughout the sample. One of the moderately altered lava (NRM = 3.53 A/m, M_i=0.75 A/m) has limited Fe-Ti oxides phenocrysts with secondary alunite and silica associated with decomposition of Fe-Ti oxides. Such decomposition reduces their effective magnetic grain size. As discussed in Chapter 3, reduction in effective magnetic grain size, high initial magnetization when the lavas were fresh, presence of single-domain magnetic grains, and secondary iron enrichment are plausible reasons for the relatively high NRM intensity of some of the moderately altered lavas compared to fresh to slightly altered lavas. As these NRM intensities are not anomalously high (e.g., 170-520 A/m as observed by Downey et al. (1994)), we disregard lightning strikes to have played any role. In the highly altered lava, the low magnetization (NRM = 0.34 A/m, M_i=0.02 A/m) is plausibly a result of remanent Fe-Ti oxides and secondary Fe-oxide precipitation in pores (Figure 4.5).

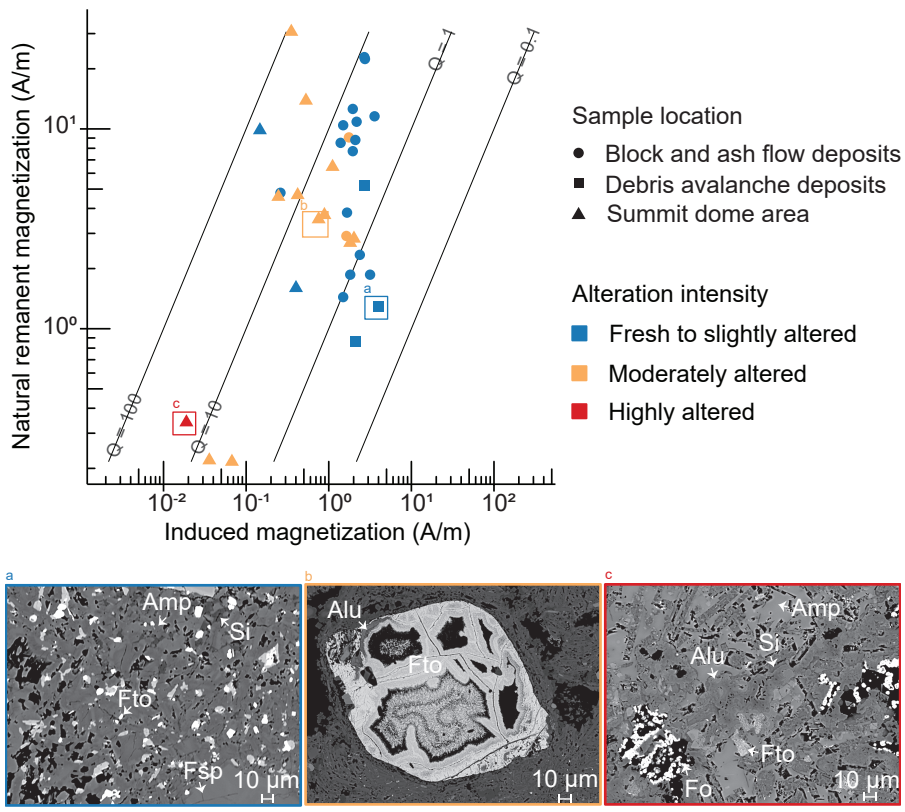

Figure 4.5: Natural remanent and induced magnetization of variably altered lavas. The grey lines are Koenigsberger (Q) ratios, the ratio of natural remanent and induced magnetizations. The letters on top of the boxes and the border of BSE images correspond with each other. BSE images of three samples (boxes) show the different magnetic grains in the samples. The magnetic minerals are whites in the BSE images. Fsp: feldspar, Amp: amorphous phase, Si: silica, Alu: alunite, Fto: Fe-Ti oxide, and Fo: Fe-oxide.

Elastic properties

The dynamic Young's (E) and shear moduli (G) of the lavas vary from 8 GPa to 57 GPa and 3 GPa to 22 GPa, respectively. Both Young's and shear moduli decrease with increasing porosity, as expected (Figure 4.6). These observations are consistent with other studies (Al-Harthi et al., 1999; Baud et al., 2014; Coats et al., 2018; Harnett et al., 2019a; Zorn et al., 2018) wherein porosity is the primary control on rock strength. The data, however, are scattered for porosities less than 20% porosity. Although limited in samples (n=3) fresh to slightly altered lava clasts from the debris-avalanche deposit have relatively high Young's (>40 GPa) and shear moduli (>16 GPa) and low porosities. In the 5-20% range, the moderately altered summit dome lavas have overall higher Young's and shear moduli than the fresh to slightly altered lava clasts from the block and ash flow deposits. Moreover, the largest scattering in elastic parameters for a constant porosity

value occurs in this porosity range.

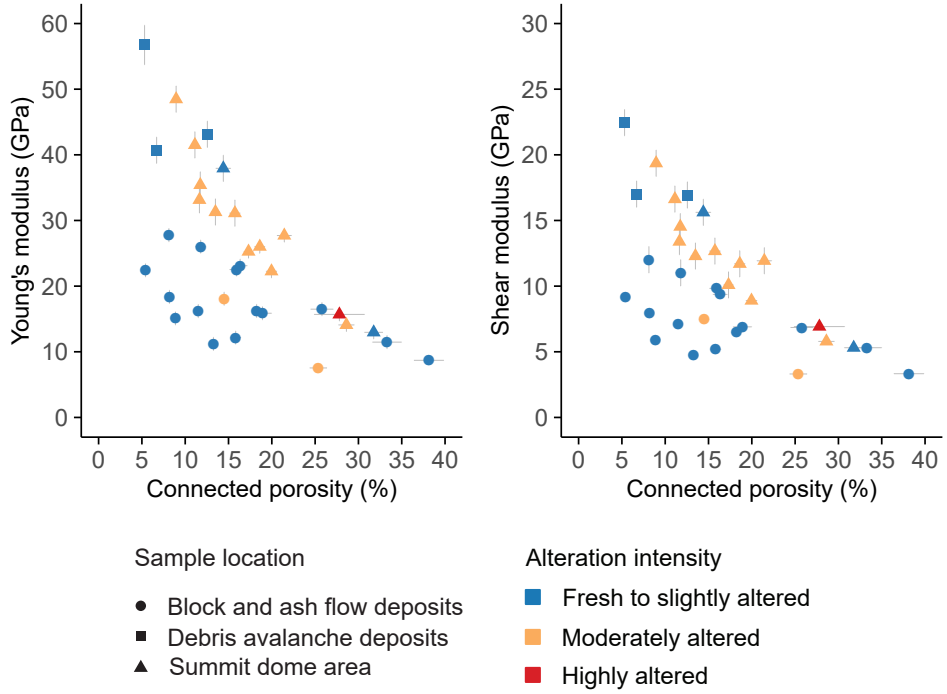

Figure 4.6: Dynamic Young's and shear moduli with porosity for variably altered lavas from Mt. Taranaki.

Overall, alteration dissolves stiff primary minerals and replaces them with secondary minerals (alunite and cristobalite) with lower or similar elastic moduli (Table 4.1). Our data shows that for constant porosity, altered samples with secondary minerals have higher elastic moduli than unaltered lavas (Figure 4.6). The effective shear moduli (Voigt-Reuss-Hill average) of these lavas computed based on the phase composition of the lavas alone (i.e., assuming zero porosity), shows that the altered lavas have similar or slightly lower effective shear moduli than the fresh lavas (Figure 4.7). Therefore, mineral replacement due to alteration is probably not the cause for the observed stiffening of lavas with similar porosity (Figure 4.6). We thus attribute the differences in stiffness of fresh and altered lavas of similar porosity to pore shape (David & Zimmerman, 2011). The reduced stiffness of lava clasts from the block and ash flow deposits could be due to the creation of secondary cracks during the lava dome collapse event from fragmentation and other frictional and collisional processes during transport (Roverato et al., 2015). As these cracks are compressible (Durán et al., 2019a; Walsh, 1965), they lower the Young's and shear moduli of the lavas compared to lavas with similar porosity likely containing a high proportion of stiffer pores.

Mineral	G (GPa)	Reference
Plagioclase*	28-38	Saxena et al. (2018)
Pyroxene*	67-84	Anderson (1989)
		Collins and Brown (1998)
Amphibole*	54-57	J. M. Brown and Abramson (2016)
		Hacker et al. (2003)
Alunite^	46-53	Majzlan et al. (2006)
Cristobalite^	33-46	Saxena et al. (2018)
		Yeganeh-Haeri et al. (1992)

Table 4.1: Shear moduli (G) of primary* and secondary^ minerals in the variably altered lavas

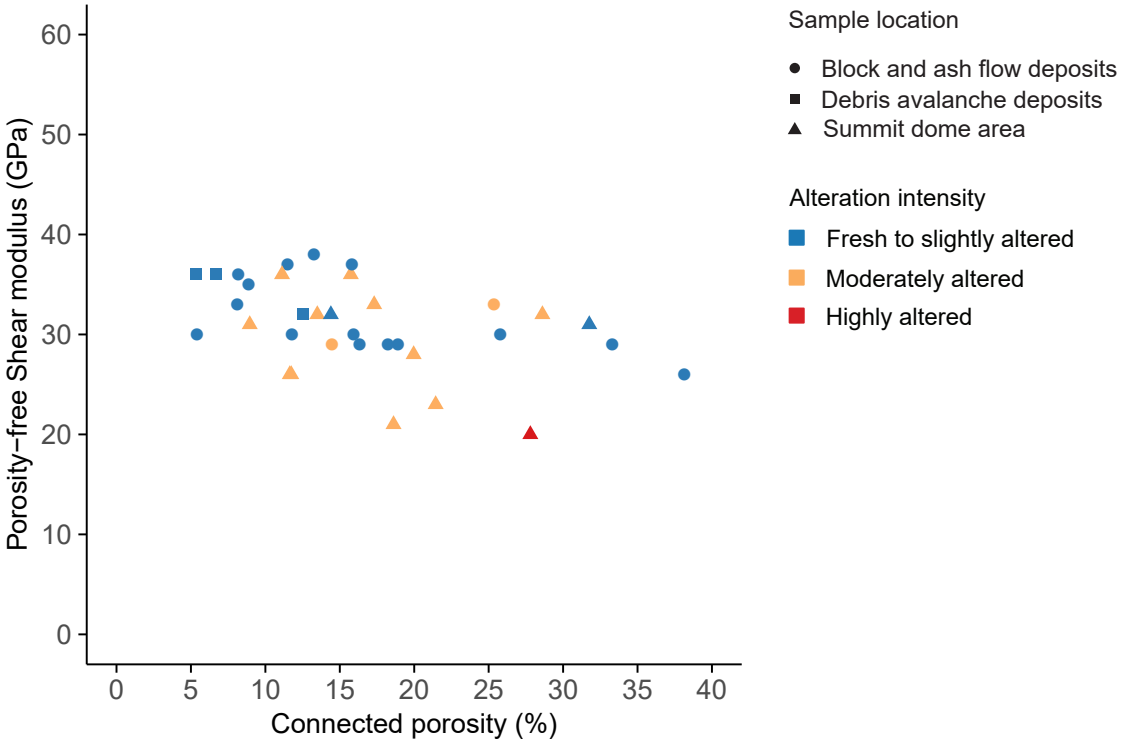

Figure 4.7: Mineral Voigt-Reuss-Hill effective shear moduli based on XRD phases and volumes (Table E.6). Moduli are plotted versus porosity to compare to Figure 4.6, showing that the moduli variability for constant porosity is not due to mineral assemblages, but rather fractures.

4.3.3 Implications for volcano slope stability

Hydrothermal alteration-related rock strength reduction can occur in lavas by intense dissolution, which increases the fluid pathways, and by replacement of stiffer primary minerals with weak secondary minerals (Ball et al., 2015; Farquharson et al., 2019; López & Williams, 1993; Varekamp et al., 2001), predisposing the volcano to slope failures (Ball et al., 2015; Carrasco-Núñez et al., 1993; Reid et al., 2001). However, based on the limited evidence of pervasive alteration, low volume of altered material in the block and ash flow deposits, and the relatively stiff secondary mineral assemblage, we infer that hydrothermal alteration-related weakening did not play a key role in past lava dome collapses at Mt. Taranaki.

Exposed hydrothermally altered regions are limited and localized at Mt. Taranaki (Platz et al., 2012). From the near summit lavas, only one of the lavas shows evidence of pervasive alteration. The rest are either fresh to slightly- or moderately altered. Together with the low proportion of altered material observed in the block and ash flow and debris avalanche deposits in this and previous studies (Cronin et al., 2021; Lerner et al., 2019b; Platz et al., 2007; Torres-Orozco et al., 2017), it is possible that parts of the dome and edifice of Mt. Taranaki that collapsed in the past 130 k.y. were not pervasively altered. According to Ball et al. (2015), the longevity and intensity of alteration depend on the availability of persistent heat supply and just enough fluid pathways to allow infiltration of water without cooling the system quickly. The alteration may have been localized and limited at Mt. Taranaki due to an intermittent heat source and relatively quick cooling. Another possible reason could be a short time gap between dome emplacement and collapse (Platz et al., 2012).

Furthermore, while we observe changes in the fluid pathways of lavas due to acid-sulfate alteration (Figure 4.3 and Figure 4.4), we do not observe a systematic dissolution-related reduction in strength. Only the highly altered lava, where primary crystalline minerals have been dissolved and replaced by secondary minerals, shows evidence of intense dissolution (i.e., increased fluid pathways). This sample has the lowest crystallinity, high porosity, and low strength (elastic moduli). This is consistent with observations by Harnett et al. (2019a) and Zorn et al. (2018) wherein lava dome rocks with low crystallinity and high porosity, have low strength. Moderately altered lavas show no systematic increase in fluid pathways from dissolution compared to fresh to slightly altered lavas. A partial cause for this is the difficulty in decoupling increased fluid pathways due to dissolution from the initial porosity and permeability of the lava during emplacement. But, given that the moderately altered lavas have a large volume of their primary min-

erals preserved (Figure 4.2), it is safe to say that they have undergone lesser dissolution than the highly altered lava, preventing a substantial decrease in stiffness, and thus, rock strength (Figure 4.6).

The type of secondary mineral assemblage shows that replacement of primary minerals by secondary alunite and cristobalite is unlikely to reduce the lavas' strength substantially. The shear moduli of these secondary minerals are similar or slightly lower compared to the primary pyroxene, amphibole, and plagioclase (Table 4.1). We did not find evidence of weak secondary minerals like clays, which have a much lower shear moduli (Kaolinite: G=1-32 GPa, montmorillonite and smectite: G=4-26 GPa), in the altered lavas from Mt. Taranaki (Saxena et al., 2018). These lavas likely underwent alteration in a highly acidic environment (Pirajno, 2009), which prevented the precipitation of clays. Our findings imply that the type of secondary mineral assemblage can be an important controlling factor in determining the rock strength and its reduction with increasing alteration intensity. Work on altered volcanic rocks and soils by del Potro and Hürlimann (2009) support our conclusion in that the type of alteration mineralogy might play a bigger role in controlling rock shear strength than the degree of alteration. Their fully altered soils, composed mainly of alunite, had higher shear strength than partially altered soil composed of similar proportions of clay (kaolinite) and alunite (del Potro & Hürlimann, 2009). Thus, we cannot generalize that hydrothermal alteration alone will weaken zones within volcanoes to the extent necessary to cause slope failures.

Our findings show that hydrothermal alteration-related weakening is unlikely to have predisposed the lava dome of Mt. Taranaki to collapses. Instead, hydrothermal alteration-related precipitation of relatively stiff secondary minerals may have promoted dome instability by blocking fluid pathways and causing pore pressurization (M. J. Heap et al., 2021b). For example, dome collapse at Soufrière Hills Volcano, Montserrat is thought to be linked to pressurized gas and magma extrusion (Calder et al., 2002). Other factors likely to have predisposed the lava dome to failures include dome emplacement on the volcano's steep topography, extrusion rate, gravitational loading, fractured zones, heavy rainfall, tectonic activity, or magmatic processes (Harnett et al., 2019b; Cronin et al., 2021; Harnett et al., 2019b; Zernack et al., 2009).

Note that here we mainly study surficial lavas from the summit dome area and deposits from past lava dome collapses. The debris avalanche deposits related to more deep-seated sector collapses were very sparsely sampled. Thus further study with extensive sampling of the debris avalanche deposits is needed to assess the role of hydrothermal alteration in the sector collapses at Mt. Taranaki. Particularly, if hydrothermal processes pervasively altered the core of the edifice, as speculated by Platz et al. (2012) and Zernack et al.

(2009), either by intense dissolution or precipitation of weak clay minerals, they could have weakened the edifice internally and predisposed Mt. Taranaki to collapses. It should also be noted that the lack of evidence for alteration-related weakening in dome-forming lavas and their collapse deposits in the past does not preclude such a possibility in the future.

4.4 Concluding remarks

We conclude that acid-sulfate alteration changes the petrophysical and geophysical properties of lavas at Mt. Taranaki. But given the limited dissolution and precipitation of relatively strong secondary minerals like alunite and cristobalite, hydrothermal alteration does not substantially decrease the stiffness and thus strength of these lavas. The role of hydrothermal alteration in weakening volcanic rocks and causing slope instability depends not only on the degree of alteration but also on the type.

Chapter 5

Discussion

In this thesis, I endeavored to determine the geophysical signatures of hydrothermal alteration for volcano monitoring. This involved studying conduit-filling and surficial lithologies from Whakaari, a stratovolcano with a dynamically active hydrothermal system and a history of phreatic and phreatomagmatic eruptions as well as studying lavas from the dome and collapse deposits of Mt. Taranaki, a stratovolcano lacking surface expression of a dynamic hydrothermal system but with a long-standing history of dome and edifice collapses. The specific aims were to (a) Determine how hydrothermal alteration changes the petrophysical properties of volcanic rocks, (b) Understand how these petrophysical changes can affect volcanic dynamics (c) determine the corresponding geophysical signatures of variably altered volcanic rocks to inform volcano monitoring. I now summarize (Figure 5.1) and discuss the key findings from the previous three Chapters to address these aims.

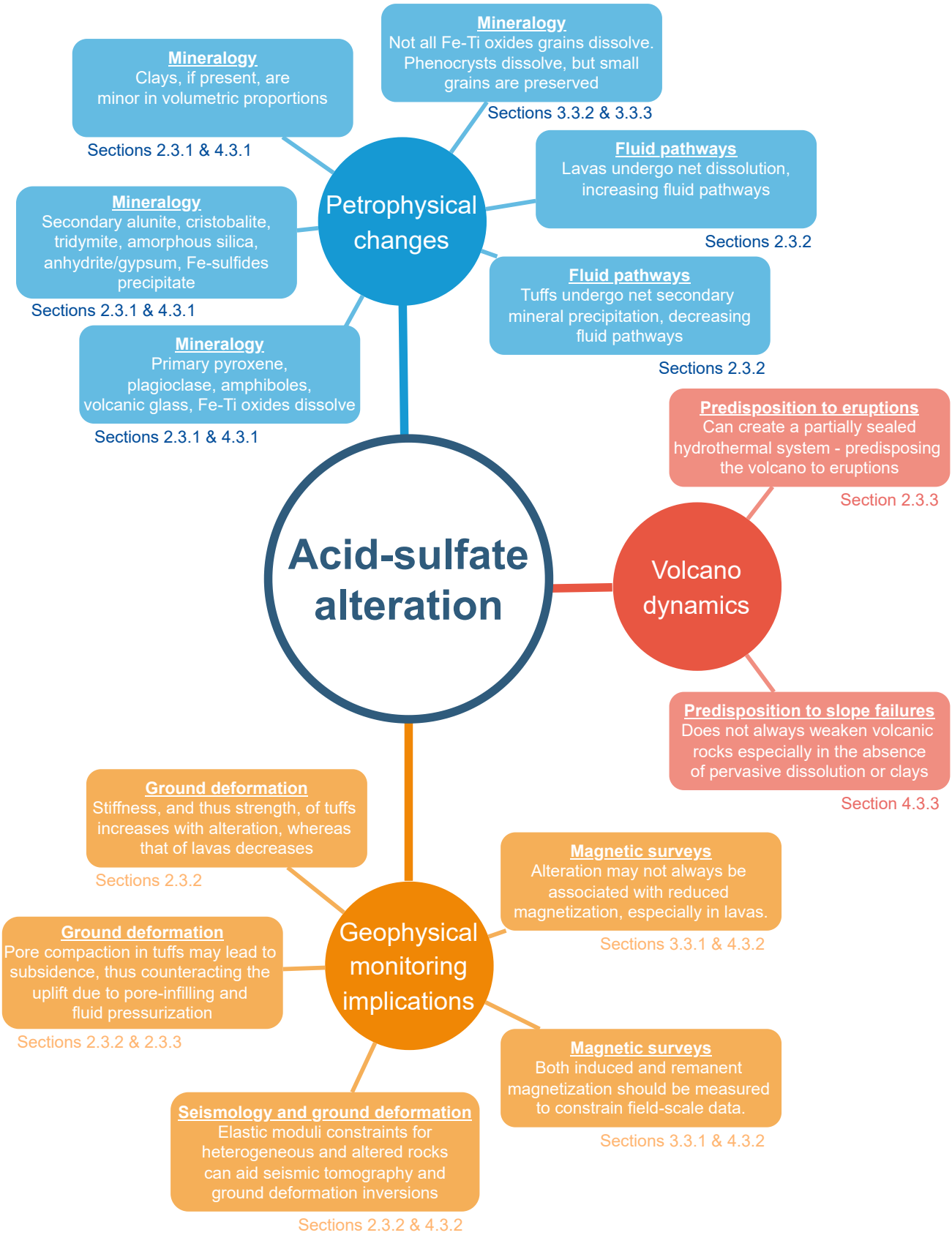

Figure 5.1: Summary of the key findings of this thesis.

5.1 Changes in petrophysical properties of volcanic rocks due to hydrothermal alteration

Hydrothermal alteration changes the petrophysical properties of volcanic rocks, such as their mineralogy and fluid pathways. In terms of mineralogy, alteration processes dissolve the primary minerals in these rocks and precipitate secondary minerals that are stable at the conditions of alteration (Figure 5.2). The observed secondary mineral assemblage at both Whakaari and Mt. Taranaki are consistent with acid-sulfate alteration. However, the secondary mineral assemblage observed at Whakaari is more diverse than that observed at Mt.Taranaki, as discussed below.

5.1.1 Changes in mineralogy due to hydrothermal alteration

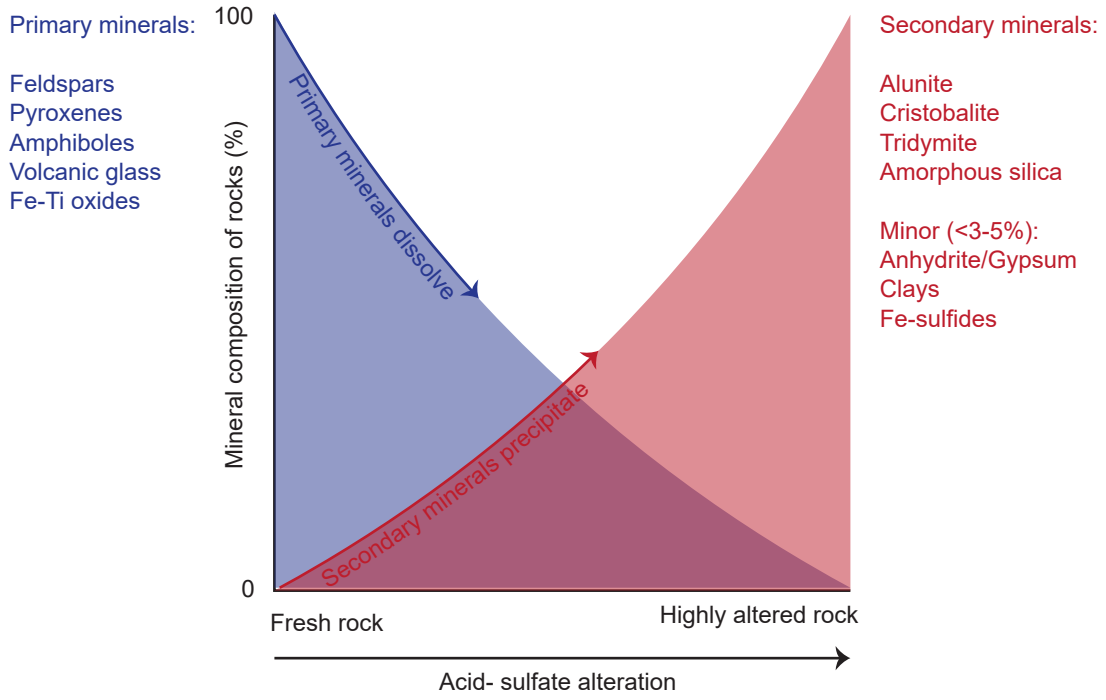

Figure 5.2: Schematic summarizing changes in the mineralogy of the studied volcanic rocks from Whakaari and Mt. Taranaki due to acid-sulfate alteration.

At Whakaari, the primary phases in conduit-filling lavas, tuffs, and breccias, include plagioclase, pyroxene, Fe-Ti oxides, and amorphous volcanic glass (Figure 2.1b). These minerals were progressively dissolved and replaced by secondary minerals to different extents in these lithologies (Figure 2.1b). Common secondary phases observed are alunite, silica

(cristobalite/tridymite), and amorphous phases (likely amorphous silica). Secondary anhydrite/gypsum and clays are observed only in one of the highly altered tuffs and lavas, respectively. In other instances, secondary anhydrite, clays, pyrite occur only in minor proportions (< 3-5%) detected during BSE-EDS analysis (Appendix E.5). Kennedy et al. (2020) observed similar secondary minerals in ballistics from Whakaari. They, however, lacked quantitative data to evaluate the relative mineralogical changes and estimate the degree of alteration. This thesis contributes the first quantitative data on alteration-related changes in mineralogy within Whakaari's conduit. This thesis also contributes a methodology to classify alteration intensity based on quantitative mineralogical analysis, which encompasses the first attempt at distinguishing primary and secondary amorphous phases (following Appendix B). The results obtained by following this methodology are cross-verified independently by BSE-EDS analysis. So far, quantitative data on alteration-related mineralogy changes in lavas, tuffs, and breccias at Whakaari were based on six surficial samples collected from the scree near Shark Bay and from collapse debris of the north-eastern crater wall (M. J. Heap et al., 2015, 2017a).

M. J. Heap et al. (2015) interpret that hydrothermal alteration changed the primary mineralogy of tuffs to mainly amorphous phases (66%-92%, assumed to be Opal-A) and alunite (1%-32%), sometimes with minor (<1%-5%) jarosite, gypsum, cristobalite, quartz, and clays. M. J. Heap et al. (2017a) interpret that the lava breccia is also altered mainly to amorphous silica (≈72%) and clays (10%) with minor (<1%-3%) jarosite, anhydrite, cristobalite, and quartz. The ballistics from Whakaari studied here, however, show that hydrothermal alteration changes the mineralogy of tuffs and breccia from the conduit with a comparatively much lower volume of amorphous silica (39%-52%) and instead a high volume of crystallized secondary minerals (Figure 2.1b). Furthermore, no K-feldspar is observed in any of the studied lavas as has been observed by M. J. Heap et al. (2015). The surficial sulfur flows studied here are primarily composed of native sulfur (85%-92%) similar to the sulfur flow in M. J. Heap et al. (2017a), but also have 8%-15% detrital amorphous silica. The mineralogy of vesicular lavas from Whakaari has not been previously studied, and thus no comparative samples exist for the surficial vesicular lavas studied here. Together, the mineralogical data presented in this thesis and previous studies provide a better picture of how hydrothermal alteration changes the mineralogy of rocks at Whakaari both within the conduit and away from the conduit in a relatively surficial environment.

While there is extensive geochemical data (Stewart et al., 1996; Lerner et al., 2019b, 2019a; Platz et al., 2012) on rocks from Mt. Taranaki, to our knowledge, no quantitative mineralogical data exists, especially on hydrothermally altered rocks. This thesis provides

the first quantitative data on alteration-related changes in mineralogy in lavas from Mt. Taranaki (Figure 4.2). The primary phases in these lavas include feldspars, pyroxene, amphiboles, Fe-Ti oxides, and amorphous volcanic glass (Figure 4.2). This is consistent with qualitative mineralogy observations by other studies (Stewart et al., 1996; Platz et al., 2007; Zorn et al., 2018). K-feldspars are observed in some samples due to groundmass devitrification. Hydrothermal alteration progressively dissolves these primary phases and precipitates secondary alunite and silica (Figure 4.2). Although similar to Whakaari, the secondary mineral assemblage of lavas from Mt. Taranaki is less diverse, with no secondary amorphous phases, anhydrite/gypsum, or clays. This difference could arise from variable alteration environments. For example, secondary silica (e.g., cristobalite) would precipitate in a highly acidic environment (pH<2), alunite in a relatively less acidic environment (pH<4), and clays and anhydrite (pH<6) in acidic-near neutral environment (Zimbelman et al., 2005). The absence of low-temperature clays in surficial samples from Mt. Taranaki further indicates that these rocks had not undergone surface weathering, but rather the observed secondary mineralogy is due to hydrothermal alteration.

Overall, the changes in mineralogy observed at both Whakaari and Mt. Taranaki are consistent with acid sulfate alteration (Zimbelman et al., 2005). Similar alteration is evident in the conduits of several other volcanoes based on the secondary minerals observed in their phreatic or phreatomagmatic ejecta (e.g., Ontake (Ikehata & Maruoka, 2016), Stromboli (Del Moro et al., 2011), Soufriere Hills (Boudon et al., 1998)). Therefore, the findings of this thesis can be extended to understand hydrothermal alteration at other volcanoes in New Zealand and around the world. So far, mineralogical changes due to hydrothermal alteration in other volcanoes in New Zealand (e.g., Mt. Ruapehu) have been studied on surficial exposures (Mordensky et al., 2018), or indirectly using hyperspectral data (Kereszturi et al., 2020, 2021). They find that the primary mineralogy of the rocks is replaced by clays which can also have an overprint of surface weathering. This thesis provides a deeper insight into the diverse changes in mineralogy that can occur due to hydrothermal alteration in the subsurface of active volcanoes. Hydrothermal alteration also affects fluid pathways in volcanic rocks. This depends on the proportion of primary minerals dissolved versus secondary minerals precipitated and where these secondary minerals precipitate (pores, fractures, replacing minerals) as discussed next.

5.1.2 Changes in fluid pathways due to hydrothermal alteration

At Whakaari, distinct trends are observed on how acid-sulfate alteration affects the fluid pathways in conduit-filling lavas, tuffs, and breccias (Figure 2.2). In lavas, which inher-

ently have low porosity and permeability mainly from fractures, acid-sulfate alteration creates new fluid pathways by net dissolution of primary minerals. In contrast, in the inherently porous and permeable tuffs, acid-sulfate alteration reduces fluid pathways by net secondary mineral precipitation. In breccias, similar to tuffs, high precipitation of secondary minerals and almost complete destruction of primary minerals is observed. The highly altered breccias have lower porosity than moderately altered breccia. However, breccias are inherently highly fractured and thus likely to allow fluid flow. Furthermore, given the heterogeneous nature of breccias, it would be ill-conceived to generalize how alteration would affect their fluid pathways. It is worth acknowledging that the differences in initial porosity of these lithologies would also play a role in the observed relations between alteration and fluid pathways. However, BSE images (Figure 2.3 and Appendix E.5) show a clear effect of alteration-related changes in these fluid pathways by dissolution and secondary mineral precipitation.

Net dissolution in lavas due to hydrothermal alteration is also supported by the experimental observation of an increase in porosity due to alteration in andesites from Mt. Ruapehu (Farquharson et al., 2015). It is also supported by the higher porosity of altered lava compared to relatively less altered lava from Whakaari (Kennedy et al., 2020). So far, fluid pathways through tuffs at Whakaari have been studied on limited surficial samples (M. J. Heap et al., 2015, 2017a) and ballistics (Kennedy et al., 2020). However, these studies did not have the range of alteration and microstructural data needed to determine the effect of increasing alteration on fluid pathways in tuffs. This thesis provides evidence of a reduction in fluid pathways in tuffs due to alteration. As the alteration intensity of tuffs increases, fluid pathways are reduced by extensive pore-filling secondary mineral precipitation and complete replacement of primary minerals, turning the granular structure of tuffs into a massive coherent structure.

In contrast to lavas from Whakaari, lavas from Mt. Taranaki show no distinct trend on how hydrothermal alteration changes their fluid pathways (Figure 4.3). This is at least partially because the effects of alteration are hidden within the wide range of initial porosity of dome-forming lavas depending on the magma decompression and ascent rates, volatile exsolution, and crystallization (Cashman & Blundy, 2000; Calder et al., 2015; Zorn et al., 2018). A wide range of porosity and permeability is also observed in unaltered rocks from the lava dome of Merapi volcano (Kushnir et al., 2016). The fluid pathways of collapse deposits would further have an overprint of fractures from frictional and collisional processes during transport. However, the changes in the relation between crystallinity and porosity with alteration (Figure 4.4) confirm that the fluid pathways were affected by acid-sulfate alteration. The high porosity (Figure 4.3) and dissolution of

most primary minerals (Figure 4.2) in the highly altered lava further support the trend of net dissolution in lavas with increasing alteration similar to that observed at Whakaari. This is consistent with experimental observations from the lava dome of Merapi volcano, where highly altered lavas have higher porosity compared to many fresh and slightly altered lavas (M. J. Heap et al., 2019).

Overall, the petrophysical changes in mineralogy and fluid pathways due to hydrothermal alteration show a potential coupling with the initial fluid pathways available in different lithologies in their fresh state. Rocks with low initial porosity and permeability, like conduit-filling lavas from Whakaari, undergo net dissolution. While those with high porosity and permeability, like tuffs and some breccias, undergo more intense alteration with almost all primary minerals dissolved and extensive secondary mineral precipitation. This coupling between initial porosity and alteration may partially be due to the amount of fluids in relation to the rock in these lithologies during alteration (Pirajno, 2009). A high surface area, pore connectivity, and fluid-rock ratio can allow more intense alteration with extensive secondary mineral precipitation. This is consistent with observations from the drill cores of the Newberry Volcano, where Bargar and Keith (1999) find pervasive secondary mineral precipitation in interflow breccias and volcaniclastic layers where initial permeability was highest.

Furthermore, the degree to which the petrophysical properties of the volcanic rocks are affected by alteration would also depend on the duration of fluid-rock interactions. This duration would depend on the availability of a persistent heat supply and just enough fluid pathways to allow infiltration of water without cooling the system quickly (Ball et al., 2015). It should be noted that this thesis explores alteration-related petrophysical changes in two different hydrothermal environments. At Whakaari, alteration-related changes are studied mainly from conduit-filling rocks. The long-lived and persistent hydrothermal system (Giggenbach et al., 2003; Kilgour et al., 2021) at Whakaari exposes these rocks to continuous reactions with circulating hydrothermal fluids. Whereas, at Mt. Taranaki, the alteration-related changes are studied in dome-forming lavas at the top of the vent and their collapse deposits. The alteration in these rocks results from intermittent interaction with fluids during and shortly after emplacement or periods of heightened volcanic unrest. The extent of alteration-related changes in collapse deposits would also depend on the gap between dome emplacement and collapse. How the observed alteration-related petrophysical changes in rocks from Whakaari and Mt. Taranaki can affect their volcano dynamics is discussed next.

5.2 Effect of alteration-related petrophysical changes on volcano dynamics

Alteration-related petrophysical changes can affect volcano dynamics by controlling fluid flow and degassing at the surface. Persistent degassing observations (Burton et al., 2021; Werner et al., 2008) and geochemical monitoring (Christenson et al., 2017) at Whakaari suggest the existence of a partially sealed hydrothermal system. But little experimental evidence exists from conduit-filling rocks on how such a seal develops. This thesis provides mineralogical and microimaging evidence of how alteration-related petrophysical changes can help form a partially sealed hydrothermal system. The conduit-filling lithologies, in general, have a lower porosity at depth due to pore compaction under subsurface pressures (Figure 2.2). Pore compaction is particularly pronounced in porous tuffs, with inelastic compaction beginning at effective pressures as low as 14 MPa, representing $<$ 1 km depth (Figure 2.2). This thesis suggests that the fluid pathways through the conduit are first reduced under subsurface pressures due to pore compaction and the closure of microfractures. Overtime as hydrothermal alteration reduces fluid pathways in tuffs by precipitating secondary minerals (Figure 2.2 and Figure 2.3), the compacted and highly altered tuffs form zones of low porosity and low permeability within the conduit. Secondary mineral precipitation and pore compaction also affect lavas and breccias, further restricting fluid flow within the conduit. Still, the net dissolution of lavas and unfilled macrofractures simultaneously help fluids flow and degas at the surface. These processes together can create a partially sealed hydrothermal system (Figure 2.5).

Until now, the permeability of Whakaari's conduit was considered to be controlled by pressure-related opening and closure of cracks in altered rocks allowing variable fluid advection (Kennedy et al., 2020), a carapace of elemental sulfur on the crater lake floor forming a semi-permeable seal (Christenson et al., 2017) or generalized to be related to alteration (M. J. Heap et al., 2017a). This thesis provides evidence for an additional mechanism by which subsurface pressures and different alteration-related petrophysical changes in conduit-filling lithologies together help form a partially sealed hydrothermal system. Future modeling studies can incorporate this mechanism, observed at a micro-scale, together with macro features typical in a volcanic setting (e.g. fluid flow through macrofractures or pathways in broken pieces of wall rock that may have been incorporated into the conduit) to further characterize hydrothermal sealing. When fluid injection rates are high, the reduced fluid pathways between the conduit and surface can aid pressurization and predispose the volcano to phreatic and phreatomagmatic eruptions.

Hydrothermal sealing driven by acid-sulfate alteration has also been thought to play a role in predisposing several other volcanoes to phreatic and phreatomagmatic eruptions (e.g., Soufrière Hills (Edmonds et al., 2003), Ontake (Stix & de Moor, 2018), Poás (de Moor et al., 2019).

Alteration-related petrophysical changes can also affect volcano dynamics by changing the strength of volcanic edifices and lava domes. At Whakaari, net dissolution in lavas reduces their stiffness, while the stiffness of tuffs increases due to net secondary mineral precipitation (Figure 2.4). The stiffness of breccia is low to moderate (Figure 2.4). At Mt. Taranaki, the stiffness variations due to alteration are more challenging to separate due to the high variability in the initial porosity of dome-forming lavas and their collapse deposits. But overall, the moderately altered lavas from near the summit are stiffer than the fresh to slightly altered lavas from collapse deposits (Figure 4.6). Although it might sound counterintuitive that fresh to slightly altered lavas have lower stiffness than moderately altered lavas, this relation is plausible due to the creation of secondary cracks from fragmentation and other frictional and collisional processes during transport (Roverato et al., 2015). The highly altered lava has low stiffness, likely due to extensive dissolution as previously discussed (Figure 4.6). These stiffness data can be considered representative of the strength of these lithologies.

Hydrothermal alteration has been commonly linked to weakening volcanoes and predisposing them to slope failures (Ball et al., 2015; López & Williams, 1993). This thesis shows that alteration and weakening of volcanic rocks do not have a simple direct link but is rather dependent on both the degree and type of alteration. For example, intense dissolution can reduce the stiffness of host rocks as observed in highly altered lavas from both Whakaari (Figure 2.4) and Mt. Taranaki (Figure 4.6). Such reduction in stiffness can weaken edifices and lava domes, predisposing them to slope failures. But if secondary mineral precipitation dominates, the type of secondary mineral assemblage is also important in controlling the stiffness and thus strength of the host rocks. Precipitation of alunite and silica in place of the primary minerals is unlikely to reduce the strength of host rocks substantially due to the similar elastic moduli of these secondary minerals and primary minerals (Section 4.3.3). Precipitation of clays, which have much lower elastic moduli, may, however, weaken the rocks.

At most volcanoes, hydrothermal alteration-related slope failures have been attributed to the reduction in strength with the formation of secondary clay minerals (Kereszturi et al., 2021; López & Williams, 1993; Norini et al., 2020; Opfergelt et al., 2006; Reid et al., 2001, 2010b). At Whakaari, as well, hydrothermally altered rocks with a high amount of clay minerals have been considered to play a role in sector collapses (Moon et al., 2005).

However, extensive clays are not observed in this study in samples from Whakaari's conduit and altered rocks from near the summit dome of Mt. Taranaki. It should be noted that the debris avalanche deposits related to deep-seated sector collapses at Mt. Taranaki were very sparsely sampled in this thesis. Thus further study with extensive sampling of the debris avalanche deposits is needed to assess the role of hydrothermal alteration in the sector collapses at Mt. Taranaki. Clays have been observed at other regions in the Taupo Volcanic Zone (Mordensky et al., 2018, 2019; Wyering et al., 2014) and may occur at Whakaari and Mt. Taranaki in areas that have been altered in a lower pH environment away from the main vent as described in the conceptual model of near-surface high-sulfidation alteration by Mayer et al. (2016). Overall, alteration-related extensive dissolution and precipitation of clay minerals can weaken edifices and lava domes, predisposing them to collapses. Studies on altered rocks that have undergone dissolution (Farquharson et al., 2019) and are clay-rich (Mayer et al., 2017) have also observed the rocks to have lower strength. However, the edifice and lava domes would strengthen due to alteration if net secondary mineral precipitation replaces primary minerals with stiffer secondary minerals while simultaneously in-filling pore spaces. A recent study on altered rhyodacites from the Lassen volcanic center also suggests that pore- and crack-filling mineral precipitation increases their strength (M. J. Heap et al., 2021b). Knowing how the alteration-related petrophysical changes would manifest in geophysical data is vital to monitor the effect of hydrothermal alteration on volcano dynamics. Next discussed are the corresponding geophysical signatures of variably altered rocks from Whakaari and Mt. Taranaki to inform volcano monitoring.

5.3 Geophysical signatures of variably altered volcanic rocks and implications for volcano monitoring

The corresponding geophysical signatures of variably altered volcanic rocks studied in this thesis can help advance the interpretation of geophysical data used for volcano monitoring.

5.3.1 Implications for ground deformation

Ground deformation is regularly monitored at Whakaari through the leveling network on the crater floor and remotely using Interferometric Synthetic Aperture Radar (InSAR)

(Hamling, 2021; Kilgour et al., 2021). Analysis of leveling data between 1967-2008 indicated shallow pressure sources (200-600 m deep) causing episodes of uplift before eruptions or resurgence of eruptive activity, accompanied or followed by subsidence episodes (Peltier et al., 2009). They suggest that the uplift episodes resulted from an increase in fluid pore pressure within the shallow volcano-hydrothermal system in response to heat and gas flux changes due to a magmatic intrusion at depth rather than directly by magma intrusion at a shallow depth (Peltier et al., 2009). Fournier and Chardot (2012) also attribute the observed ground uplift at Whakaari to injection of hot magmatic fluids into the shallow hydrothermal system (100-200 m deep). Furthermore, analysis of InSAR data also supports a shallow pressure source originating (about 100 m deep) in the vicinity of the crater lake, coinciding with the shallow hydrothermal system (Hamling, 2017). From the results of this thesis, it is inferred that increased fluid pressure build-up resulting from tuffs sealing the conduit and the continuous magmatic fluid sourcing drives the uplift (Section 2.3.3).

The numerical model inversions used to analyze the leveling data so far assume that the deforming medium is elastic, homogenous, and isotropic with Young's modulus of 30 GPa (Fournier & Chardot, 2012; Peltier et al., 2009) or 2.5 GPa (Fournier & Chardot, 2012). The elastic properties data presented in this thesis (Figure 2.4) show that Young's modulus for different lithologies, alteration intensity, and effective pressures at Whakaari ranges from 3-63 GPa, up to double the value of previously modeled elastic parameters. The elastic properties data also highlight the heterogeneity in Whakaari's subsurface. Fournier and Chardot (2012) observed that while the source location may not be affected, the retrieved rates of overpressure and source radii vary significantly based on the values of the elastic properties used for the inversions. A recent review by M. J. Heap et al. (2020a) provides a wealth of laboratory data on Young's moduli to help numerical model inversions. But they too highlight the lack of such data on variably altered volcanic rocks, which are often acquired on surficial samples at atmospheric conditions (e.g., Mordensky et al. (2018)). Thus, using the elastic moduli data from this thesis is suggested for constraining numerical model inversions of ground deformation in acid-sulfate altered volcanic environments. Given these data are acquired on ballistics, and at realistic subsurface conditions (variable confining pressures, dry and saturated conditions, and at varying fluid pressures for one of the highly altered tuffs), they provide calibrated constraints on the elastic properties of the deforming medium. These laboratory data suggest an average dynamic Young's modulus of 21 GPa for Whakaari's subsurface. For a field-scale estimate, it is recommended to upscale the moduli values with the help of the porosity data presented in this thesis (Figure 2.2) and the method described in

M. J. Heap et al. (2020a).

Furthermore, the results of this thesis show that within the conduit, pore compaction occurs under subsurface pressures, especially in tuffs (Figure 2.2). Such compaction of conduit-filling lithologies could compensate for ground deformation, especially if the effective pressure exceeds the rock's elastic limit. This effect would be most prominent in tuffs, in which inelastic compaction can begin as low as 14 MPa (<1 km) (Figure 2.2). Given the shallow nature of pressure sources interpreted at Whakaari (Fournier & Chardot, 2012; Peltier et al., 2009), the assumption of an elastic medium is likely to be valid. But, as it has been highlighted by studies on deformation at Mt. Etna (Currenti et al., 2010; Del Negro et al., 2009), assuming an elastic medium can often be an over-simplification. Suppose the pressure sources were deeper or related to a direct magmatic intrusion in the future. In that case, it is recommended to incorporate heterogeneity and use viscoelastic or elastoplastic models, which would provide more accurate inversions for monitoring (Currenti et al., 2010; Del Negro et al., 2009).

5.3.2 Implications for magnetic surveys

Magnetic surveys have been used to identify collapse-prone hydrothermally altered regions on several volcanoes (Finn et al., 2001; Kereszturi et al., 2020). At Whakaari, regular measurements were acquired using a magnetic survey network from 1968 to 2000 (Hurst & Christoffel, 1973; Hurst et al., 2004). These were used to constraint heating and cooling at depth and were successfully deployed as a forecasting tool for eruptions in the 1976-2000 eruptive period (Hurst et al., 2004; Kilgour et al., 2021). Aeromagnetic surveys have also been employed at Whakaari (Woodward & Caldwell, 1992; Woodward & Mumme, 1993) and relict volcanoes in the Taranaki Volcanic Lineament (Locke et al., 1994). Although such surveys have not been focused on identifying altered regions on Whakaari or Mt. Taranaki, aeromagnetic surveys are widely used at other volcanoes and hydrothermal systems for that purpose (Finn et al., 2001; Fujii et al., 2015; Kereszturi et al., 2020).

The results of these surveys are often interpreted with the assumption that altered regions would manifest as areas of reduced magnetization (Finn et al., 2001). The results of this thesis show that this may not always be the case. Some of the altered lavas from both Whakaari (Figure 3.1) and Mt. Taranaki (Figure 4.5) have higher remanent magnetization than fresh lavas. Plausible causes for the high remanent magnetization in altered lavas include one or more of the following: equal or higher magnetization in their initial fresh state due to efficient and stable NRM carriers, shielding of NRM

carriers from being consumed by alteration processes, or alteration-related secondary compositional iron enhancement (Section 3.3.3). Irrespective of the underlying cause, this thesis suggests that regions of strong magnetization should be scrutinized as they could also be hydrothermally altered.

Furthermore, lab-based magnetization measurements on a representative suite of samples should be used as constraints for interpreting field-scale surveys. Although the magnetic properties data presented in this thesis are limited due to their acquisition on un-oriented samples, they emphasize the need to measure both components of magnetization, induced (computed from magnetic susceptibility) and remanent (NRM) for deriving these constraints. At Whakaari, it is observed that altered lavas have similar or lower magnetic susceptibility and thus induced magnetization than fresh lavas (Figure 3.1). In contrast, the NRM of some altered lavas is higher than fresh lavas (Figure 3.1). At Mt. Taranaki, the magnetic properties are scattered, from which the relation between alteration intensity and magnetization cannot be drawn (Figure 4.5). Some fresh lavas have lower induced and remanent magnetization than altered lavas, some have higher induced and remanent magnetization. In contrast, others have one of the magnetization components higher. Using magnetic susceptibility without NRM to aid field magnetic data analysis (e.g., (Byrne et al., 2019; Caratori Tontini et al., 2012; Kereszturi et al., 2020; Nicolosi et al., 2016)) may lead to inaccurate constraints and interpretations.

These implications for volcano monitoring not only apply to Whakaari and Mt. Taranaki but also other stratovolcanoes with acid sulfate alteration where ground deformation and magnetic surveys are regularly employed. Furthermore, the results of this thesis can also aid in constraining other geophysical data used to monitor volcanoes like field-scale electrical resistivity surveys, induced polarization, seismic tomography surveys which depend on knowledge of subsurface porosity, mineralogy, wave speeds, and elastic moduli for accurate inversions.

Chapter 6

Concluding remarks and future work

Hydrothermal alteration, in particular acid-sulfate alteration, changes the physical and chemical properties of stratovolcanoes worldwide. But how these changes affect volcano dynamics and manifest themselves in geophysical data used to monitor and study the internal structure of volcanoes is challenging to determine. This thesis endeavored to address this challenge with systematic laboratory measurements of both the petrophysical and geophysical properties of 79 variably altered volcanic rocks from Whakaari (White Island) and Mt. Taranaki, New Zealand. These measurements include mineralogy, porosity, permeability, elastic, and magnetic properties of conduit-filling lavas, tuffs, and breccias ejected as ballistics; surficial sulfur flows, and vesicular lavas; dome-forming lavas and their collapse deposits.

Some of the key results show how inherently porous and permeable tuffs can play a role in sealing volcanic conduits (Chapter 2), how altered regions are not always associated with reduced magnetization (Chapter 3), and how both the type and degree of alteration are vital in determining if the altered regions are weaker (Chapter 4). The data and findings presented in this thesis advance the current understanding of hydrothermal alteration-related petrophysical changes in host rocks, their geophysical signatures and provide constraints and recommendations to help invert geophysical data used for volcano monitoring. They further advance current knowledge on the effect of alteration-related changes in rock properties on volcano dynamics. Future studies can employ the methodologies used and designed in this thesis to study how alteration by less acidic fluids or in a deeper environment would play a role in volcano dynamics and manifest in geophysical data. Another avenue for future research is to explore how temperature can aid the compaction of tuffs and affect the corresponding geophysical signatures.

Appendices

A Sample reference IDs

Table A.1: Reference ID for samples used in Chapter 2. Block ID: ID of the block collected from Whakaari, n: no. of cores analyzed from each block, Sample ID: ID of cylindrical core samples used for porosity, P- and S- wave velocity measurements. Permeability measurements were performed on select samples(*). Powder ID: ID of powder sample used for XRD analysis, Thin section ID: ID of thin section used for petrographic analysis. ^Thins sections on which BSE-EDS analysis was performed. Alteration intensities of the samples are shown by FS-Fresh to slightly altered, M-moderately altered, and H-highly altered.

Block ID	Sample type	Alteration intensity	n	Sample ID	Powder ID	Thin section ID
W1	Lava	FS	2	W1-1 W1-2	W1-1c	W1-1c^
W2	Sulfur flow	FS	2	W2-1 W2-2	W2-2c	W2-2c^
W3	Sulfur flow	FS	4	W3-1 W3-2 W3-3 W3-4	W3-2c	W3-2c^
W4	Breccia	H	1	W4-1	W4-1c	W4-1c^
W4	Lava	H	2	W4-2 W4-3	W4-23c	W4-23c^
W5	Tuff	M	5	W5-1 W5-2 W5-3 W5-5 W5-6*	W5-1c	W5-1c^
W6	Lava	M	5	W6-1 W6-2 W6-3* W6-4 W6-5*	W6-1c W6-2c W6-3c W6-4c W6-5c	W6-1c^ W6-2c W6-3c W6-4c W6-5c
W7	Lava	M	3	W7-1 W7-2	W7-2c	W7-2c^

Continued on next page

Table A.1 – continued from previous page

Block ID	Sample type	Alteration intensity	n	Sample ID	Powder ID	Thin section ID
				W7-3		
W8	Tuff	H	2	W8-1	W8-12c	W8-12c^
				W8-2		
W9	Breccia	H	2	W9-1	W9-1c	W9-1c^
				W9-2	W9-2c	W9-2c
W11	Tuff	H	5	W11-1	W11-1c	W11-1c
				W11-2	W11-2c	W11-2c^
				W11-3	W11-45c	W11-45c
				W11-4		
				W11-5		
W12	Breccia	H	1	W12-1	W12-1c	W12-1c^
W13	Tuff	H	2	W13-1	W13-1c	W13-1c^
				W13-2*	W13-2c	W13-2c
W14	Breccia	M	1	W14-1	W14-1c	W14-1c^
W15	Tuff	H	1	W15-1*	W15-1c	W15-1c^
W18	Vesicular lava	FS	3	W18-1	W18-1c	W18-1c^
				W18-3	W18-4c	W18-4c
				W18-4		
W19	Vesicular lava	FS	2	W19-1	W19-1c	W19-1c^
				W19-2		
W20	Vesicular lava	FS	1	W20-1	W20-1c	W20-1c^
WS	Sulfur flow	FS	1	WS-1	WS-1c	

Table A.2: Reference ID for samples used in Chapter 3 from Chapter 2. Sample ID: ID of cylindrical core samples used for magnetic susceptibility and natural remanent magnetization measurements, X-ray map ID: ID of thin section from Chapter 2 used for X-ray map analysis, χ_{temp}: ID of powder sample from Chapter 2 used for measurement of magnetic susceptibility with temperature, *Samples used for alternating field demagnetization experiments. Alteration intensities of the samples are shown by FS-Fresh to slightly altered, M-moderately altered, and H-highly altered.

Sample ID	Sample type	Alteration intensity	X-ray map ID	χ_{temp} ID
W1-1*	Lava	FS	W1-1c	W1-1c
W1-2	Lava	FS		
W6-1	Lava	M	W6-1c	W6-1c
W6-2	Lava	M		
W6-3	Lava	M		
W6-4*	Lava	M		
W6-5	Lava	M		
W7-1	Lava	M		
W7-2	Lava	M	W7-2c	W7-2c
W7-3	Lava	M		
W4-2*	Lava	H	W4-23c	W4-23c
W4-3	Lava	H		
W5-1	Tuff	M	W5-1c	
W5-2	Tuff	M		
W5-3	Tuff	M		
W8-1	Tuff	H		
W8-2	Tuff	H		
W11-1	Tuff	H		
W11-2	Tuff	H	W11-2c	
W11-3	Tuff	H		
W11-4	Tuff	H		
W11-5	Tuff	H		
W13-1	Tuff	H		
W13-2	Tuff	H		
W15-1	Tuff	H	W15-1c	
W12-1	Breccia	H		

Continued on next page

Table A.2 – continued from previous page

Sample ID	Sample type	Alteration intensity	X-ray map ID	χ_{temp} ID
W4-1	Breccia	H		
W9-1	Breccia	H	W9-1c	
W9-2	Breccia	H		
W14-1	Breccia	M		
W18-1	Vesicular lava	FS		
W18-3	Vesicular lava	FS		
W18-4	Vesicular lava	FS		
W19-1	Vesicular lava	FS		
W19-2	Vesicular lava	FS		
W20-1	Vesicular lava	FS		
W2-1	Sulfur flow	FS		
W2-2	Sulfur flow	FS		
W3-1	Sulfur flow	FS		
W3-2	Sulfur flow	FS		
W3-3	Sulfur flow	FS		
WS-1	Sulfur flow	FS		

Table A.3: Reference ID for samples used in Chapter 4. Block ID: ID of the block collected from Mt. Taranaki, n: no. of cores analyzed from each block, Sample ID: ID of cylindrical core samples used for porosity, permeability, magnetic susceptibility, natural remanent magnetization, P- and S- wave velocity measurements, Powder ID: ID of powder sample used for XRD analysis, Thin section ID: ID of thin section used for petrographic analysis. ^Samples on which BSE-EDS analysis was performed. *Samples collected by (Zorn et al., 2018). Alteration intensities of the samples are shown by FS-Fresh to slightly altered, M-moderately altered, and H-highly altered.

Block ID	Sample type	Sampling locality	Alteration intensity	n	Sample ID	Powder ID	Thin section ID
T1	Lava	Near summit	M	1	T1-1	T1-1c	T1-1c^
T2	Lava	Near summit	M	1	T2-1	T2-1c	T2-1c
T3	Lava	Near summit	M	1	T3-1	T3-1c	T3-1c
T4	Lava	Near summit	FS	1	T4-1	T4-1c	T4-1c
T5	Lava	Near summit	M	1	T5-1	T5-1c	T5-1c
T6	Lava	Maero stream	FS	1	T6-1	T6-1c	T6-1c
T7	Lava	Maero stream	FS	1	T7-1	T7-1c	T7-1c
T8	Lava	Maero stream	FS	1	T8-1	T8-1c	T8-1c
T9	Lava	Maero stream	M	1	T9-1	T9-1c	T9-1c
T10	Lava	Maero stream	FS	1	T10-1	T10-1c	T10-1c
T11	Lava	Maero stream	FS	1	T11-1	T11-1c	T11-1c
T12	Lava	Maero stream	M	1	T12-1	T12-1c	T12-1c
T13	Lava	Maero stream	FS	1	T13-1	T13-1c	T13-1c
T14	Lava	Debris avalanche deposit	FS	1	T14-1	T14-1c	T14-1c
T15	Lava	Debris avalanche deposit	FS	1	T15-1	T15-1c	T15-1c^

Continued on next page

Table A.3 – continued from previous page

Block ID	Sample type	Sampling locality	Alteration intensity	n	Sample ID	Powder ID	Thin section ID
T16	Lava	Debris avalanche deposit	FS	1	T16-1	T16-1c	T16-1c
T17	Lava	Near summit	M	1	T17-1	T17-1c	T17-1c
T18	Lava	Near summit	M	1	T18-1	T18-1c	T18-1c
T19	Lava	Near summit	M	1	T19-1	T19-1c	T19-1c
T20	Lava	Near summit	H	1	T20-1	T20-1c	T20-1c^
T21	Lava	Near summit	M	1	T21-1	T21-1c	T21-1c^
T22	Lava	Near summit	M	1	T22-1	T22-1c	T22-1c
T23	Lava	Near summit	M	1	T23-1	T23-1c	T23-1c
T24	Lava	Near summit	M	1	T24-1	T24-1c	T24-1c
T25	Lava	Summit	FS	1	T25-1*	T25-1c	T25-1c
T26	Lava	Maero stream	FS	1	T26-1*	T26-1c	T26-1c
T27	Lava	Pyramid stream	FS	1	T27-1*	T27-1c	T27-1c
T28	Lava	Maero stream	FS	1	T28-1*	T28-1c	T28-1c
T29	Lava	Maero stream	FS	1	T29-1*	T29-1c	T29-1c
T30	Lava	Maero stream	FS	1	T30-1*	T30-1c	T30-1c
T31	Lava	Maero stream	FS	1	T31-1*	T31-1c	T31-1c
T32	Lava	Maero stream	FS	1	T32-1*	T32-1c	T32-1c
T33	Lava	Maero stream	FS	1	T33-1*	T33-1c	T33-1c
T34	Lava	Maero stream	FS	1	T34-1*	T34-1c	T34-1c

B Quantification of hydrothermal alteration intensity

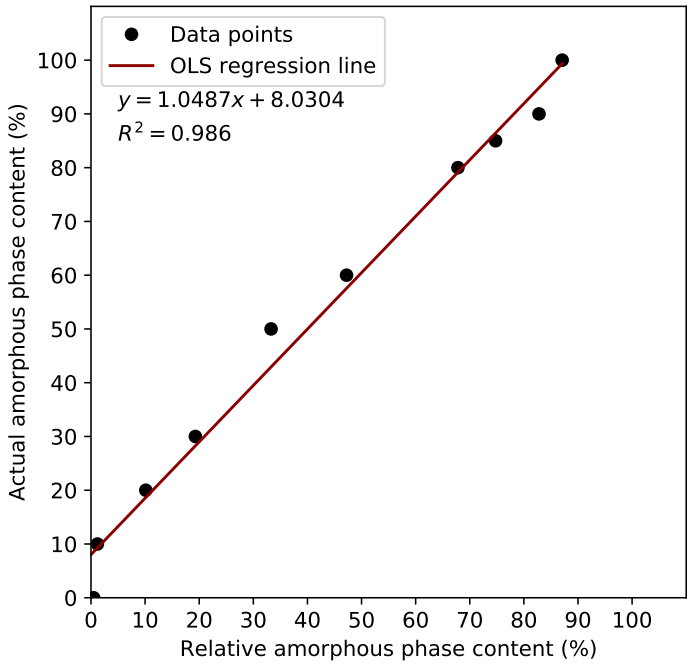

Figure B.1: Amorphous phase calibration curve used for this study. The black circles show the relative amorphous phase content, determined using AMORPH (M. Rowe & Brewer, 2018), plotted against the sample's known amorphous phase content. The known amorphous phase content was determined by mixing different proportions of gabbro and glass. The calibration curve was computed by Ordinary Least Squares (OLS) regression.

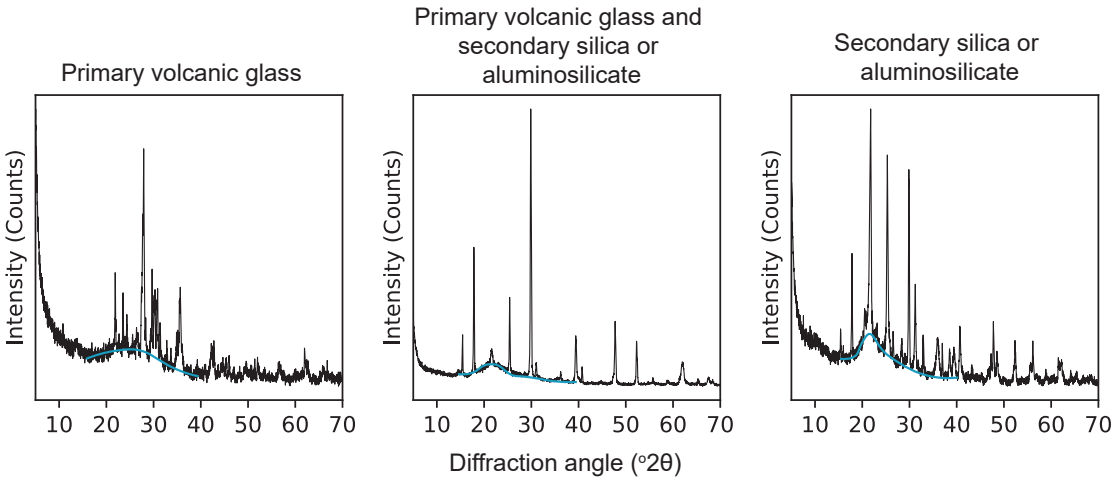

Figure B.2: X-ray diffraction patterns of representative samples with mixed crystalline and amorphous phases showing different shapes of low-intensity amorphous curve (highlighted in blue). Amorphous phase-type present in the samples was classified as primary volcanic glass, secondary silica/aluminosilicate, or a combination of both based on the skewness of the amorphous curve and overall mineralogy of the sample. The skewness of the amorphous curve of each sample was computed using AMORPH (M. Rowe & Brewer, 2018).

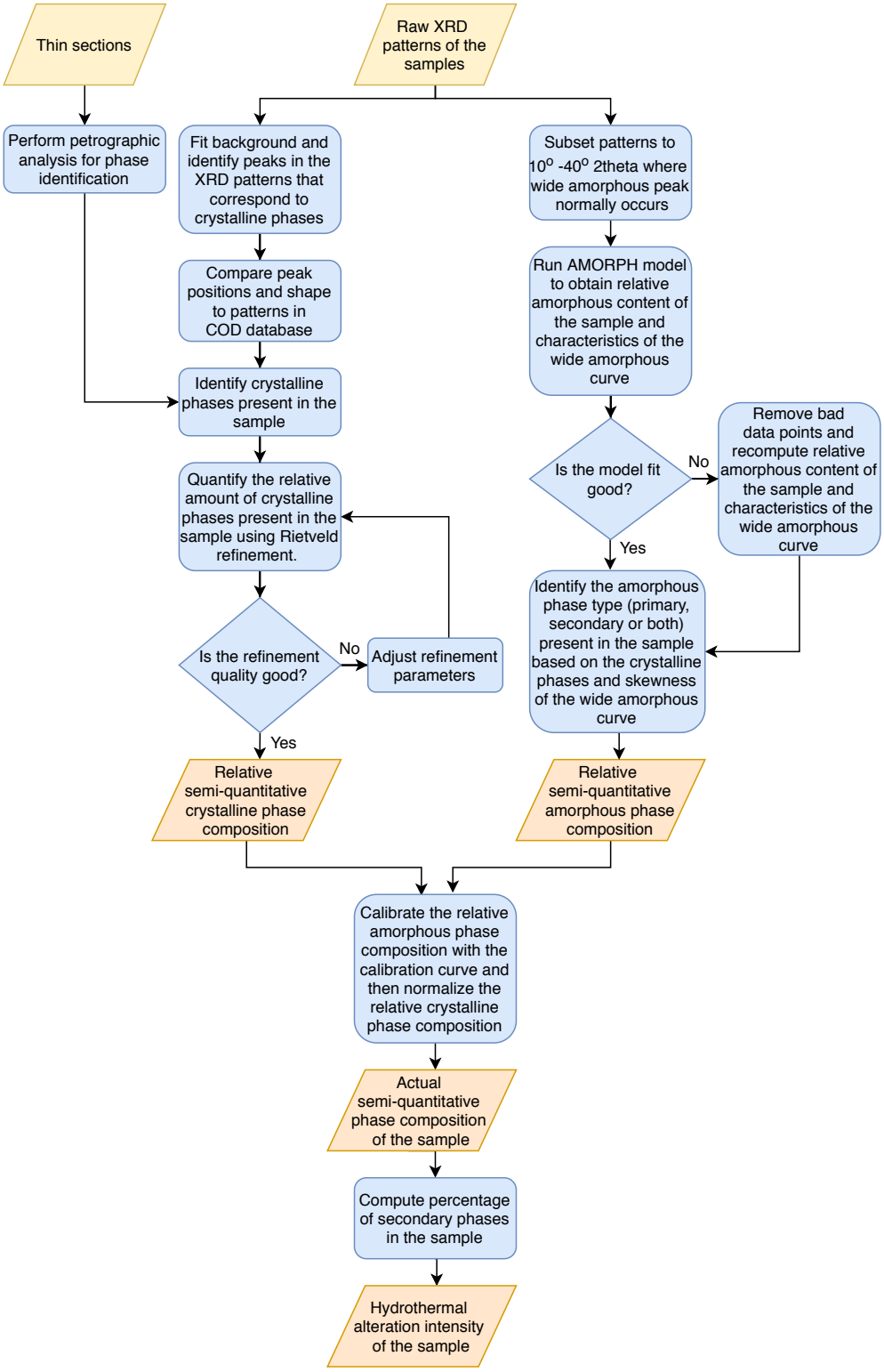

Figure B.3: Summary of the procedure followed to determine the hydrothermal alteration intensity of the samples based on the percentage of secondary phases in the samples. Yellow parallelograms represent data input or output, rounded blue rectangles represent processes, and blue diamonds indicate decisions made during the process.

C Stress path for multi-stage porosity experiments

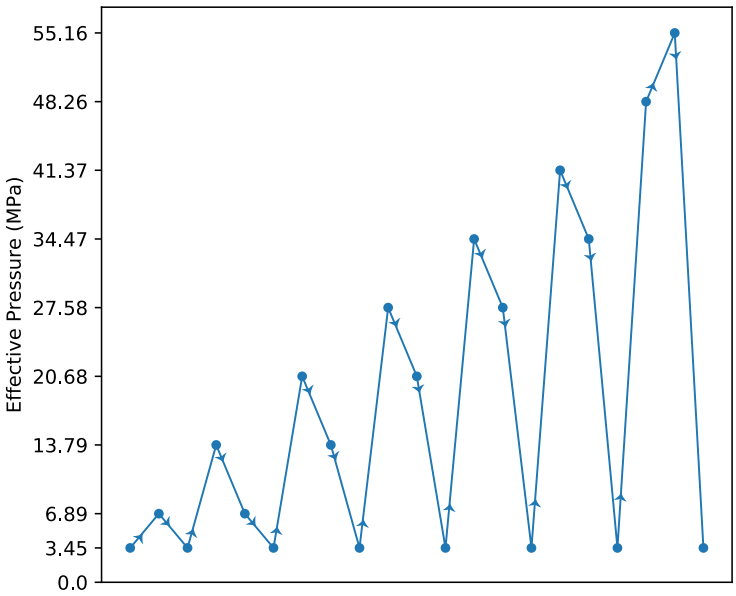

Figure C.1: Stress-path followed for multi-stage porosity measurements under hydrostatic effective pressure. The x-axis (not shown) is the time of porosity measurement. An effective pressure was considered to have exceeded the elastic limit of the sample if upon unloading to 3 MPa, more than 2% absolute porosity difference was observed compared to the initial porosity at 3 MPa. The threshold 2% was selected to ensure that the computed porosity difference was not due to measurement uncertainty.

D Magnetic properties

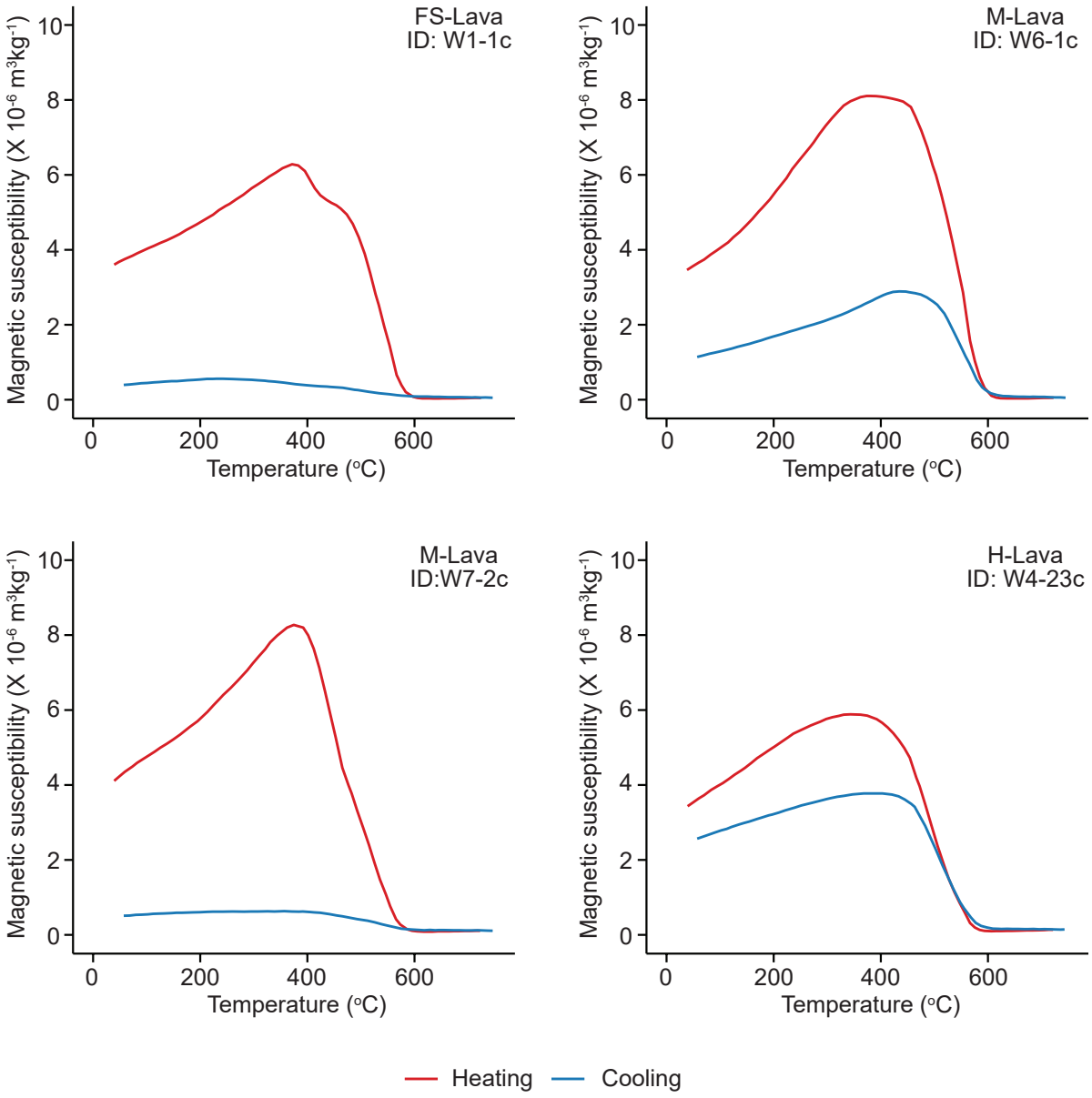

Figure D.1: Variation in magnetic susceptibility of fresh to slightly altered (FS), moderately altered (M), and highly altered (H) lavas with temperature during heating and cooling. The magnetic susceptibility of these lavas decrease from 390-500^{o}C to close to zero at 580^{o}C, the Curie temperature of magnetite.

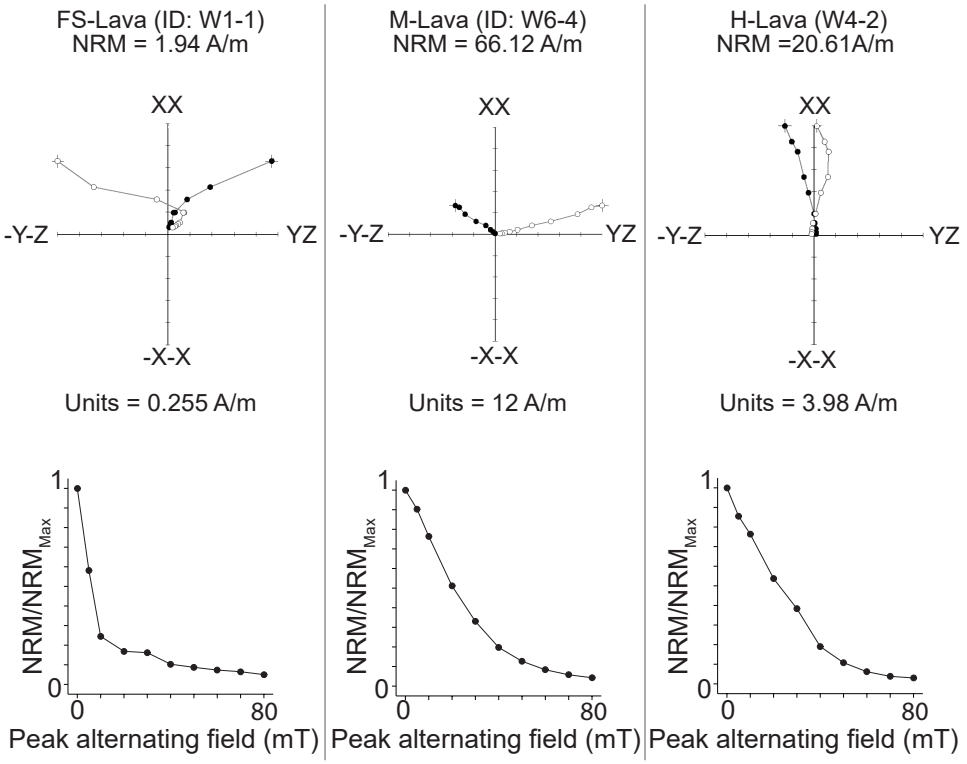

Figure D.2: (Top) Zijderveld diagrams (bottom) magnetization intensity decay curves during alternating field demagnetization of fresh to slightly altered (FS), moderately altered (M), and highly altered (H) lavas. As the samples are not oriented, each sample's corresponding orthogonal vector projections are on an arbitrary X-Y-Z plane. Closed and open circles indicate Y vs. X and Z vs. X projections in the Zijderveld diagrams, respectively. The scale of axis ticks (Units) in the Zijderveld diagrams is provided at the bottom.

E Data

E.1 Data Availability

All data supporting the findings of this study are available in the thesis figures and the following appendices. They will also be available for download via the online open-access repository - figshare.

- Data for Chapter 2: (Kanakiya, 2021a)
- Data for Chapter 3: (Kanakiya, 2021b)
- Data for Chapter 4: (Kanakiya, 2022)

E.2 Sampling locations

Table E.1: Sampling locations for samples used in Chapter 2 and Chapter 3 from Whakaari.

Block ID	Sample ID	Sample type	Latitude (DD-WGS84)	Longitude (DD-WGS84)
W1	W1-1	Lava	-37.52471722	177.1897081
W1	W1-2	Lava	-37.52471722	177.1897081
W2	W2-1	Sulfur flow	-37.52344778	177.1875728
W2	W2-2	Sulfur flow	-37.52344778	177.1875728
W3	W3-1	Sulfur flow	-37.52344778	177.1875728
W3	W3-2	Sulfur flow	-37.52344778	177.1875728
W3	W3-3	Sulfur flow	-37.52344778	177.1875728
W3	W3-4	Sulfur flow	-37.52344778	177.1875728
W4	W4-1	Breccia	-37.52312611	177.1872667
W4	W4-2	Lava	-37.52312611	177.1872667
W4	W4-3	Lava	-37.52312611	177.1872667
W5	W5-1	Tuff	-37.523075	177.1872247
W5	W5-2	Tuff	-37.523075	177.1872247
W5	W5-3	Tuff	-37.523075	177.1872247
W5	W5-5	Tuff	-37.523075	177.1872247
W5	W5-6	Tuff	-37.523075	177.1872247
W6	W6-1	Lava	-37.5230075	177.1872561
W6	W6-2	Lava	-37.5230075	177.1872561
W6	W6-3	Lava	-37.5230075	177.1872561
W6	W6-4	Lava	-37.5230075	177.1872561
W6	W6-5	Lava	-37.5230075	177.1872561
W7	W7-1	Lava	-37.52314056	177.1872722
W7	W7-2	Lava	-37.52314056	177.1872722
W7	W7-3	Lava	-37.52314056	177.1872722
W8	W8-1	Tuff	-37.52298028	177.1873194
W8	W8-2	Tuff	-37.52298028	177.1873194
W9	W9-1	Breccia	-37.52308194	177.1872567

Continued on next page

Table E.1 – continued from previous page

Block ID	Sample ID	Sample type	Latitude (DD-WGS84)	Longitude (DD-WGS84)
W9	W9-2	Breccia	-37.52308194	177.1872567
W11	W11-1	Tuff	-37.52289028	177.1866317
W11	W11-2	Tuff	-37.52289028	177.1866317
W11	W11-3	Tuff	-37.52289028	177.1866317
W11	W11-4	Tuff	-37.52289028	177.1866317
W11	W11-5	Tuff	-37.52289028	177.1866317
W12	W12-1	Breccia	-37.52262278	177.1866086
W13	W13-1	Tuff	-37.52262972	177.1867028
W13	W13-2	Tuff	-37.52262972	177.1867028
W14	W14-1	Breccia	-37.52263667	177.1867992
W15	W15-1	Tuff	-37.52256194	177.1871403
W18	W18-1	Vesicular lava	-37.52552167	177.1934581
W18	W18-3	Vesicular lava	-37.52552167	177.1934581
W18	W18-4	Vesicular lava	-37.52552167	177.1934581
W19	W19-1	Vesicular lava	-37.52552167	177.1934581
W19	W19-2	Vesicular lava	-37.52552167	177.1934581
W20	W20-1	Vesicular lava	-37.52552167	177.1934581
WS	WS-1	Sulfur flow	-37.52344778	177.1875728

Table E.2: Sampling locations for samples used in Chapter 4 from Mt.Taranaki.

Block ID	Sample ID	Sample type	Latitude (DD-WGS84)	Longitude (DD-WGS84)	Sampling locality
T1	T1-1	Lava	-39.294533	174.062547	Near summit
T2	T2-1	Lava	-39.294533	174.062547	Near summit
T3	T3-1	Lava	-39.294533	174.062547	Near summit
T4	T4-1	Lava	-39.294533	174.062547	Near summit
T5	T5-1	Lava	-39.294533	174.062547	Near summit
T6	T6-1	Lava	-39.27877083	174.0103731	Maero stream
T7	T7-1	Lava	-39.27877083	174.0103731	Maero stream

Continued on next page

Table E.2 – continued from previous page

Block ID	Sample ID	Sample type	Latitude (DD-WGS84)	Longitude (DD-WGS84)	Sampling locality
T8	T8-1	Lava	-39.27877083	174.0103731	Maero stream
T9	T9-1	Lava	-39.27877083	174.0103731	Maero stream
T10	T10-1	Lava	-39.27877083	174.0103731	Maero stream
T11	T11-1	Lava	-39.27877083	174.0103731	Maero stream
T12	T12-1	Lava	-39.27877083	174.0103731	Maero stream
T13	T13-1	Lava	-39.27877083	174.0103731	Maero stream
T14	T14-1	Lava	-39.29059444	173.8532075	Debris avalanche deposit
T15	T15-1	Lava	-39.29059444	173.8532075	Debris avalanche deposit
T16	T16-1	Lava	-39.29059444	173.8532075	Debris avalanche deposit
T17	T17-1	Lava	-39.29401083	174.06488	Near summit
T18	T18-1	Lava	-39.29401083	174.06488	Near summit
T19	T19-1	Lava	-39.29401083	174.06488	Near summit
T20	T20-1	Lava	-39.29401083	174.06488	Near summit
T21	T21-1	Lava	-39.29401083	174.06488	Near summit
T22	T22-1	Lava	-39.29401083	174.06488	Near summit
T23	T23-1	Lava	-39.294533	174.062547	Near summit
T24	T24-1	Lava	-39.294533	174.062547	Near summit
T25	T25-1	Lava	-39.296292	174.06315	Summit
T26	T26-1	Lava	-39.278883	174.010308	Maero stream
T27	T27-1	Lava	-39.268453	174.013453	Pyramid stream
T28	T28-1	Lava	-39.279444	174.010942	Maero stream
T29	T29-1	Lava	-39.279444	174.010942	Maero stream
T30	T30-1	Lava	-39.279444	174.010942	Maero stream
T31	T31-1	Lava	-39.279444	174.010942	Maero stream
T32	T32-1	Lava	-39.279444	174.010942	Maero stream
T33	T33-1	Lava	-39.279444	174.010942	Maero stream
T34	T34-1	Lava	-39.279444	174.010942	Maero stream

E.3 Sample dimensions

Table E.3: Dimensions of samples used in Chapters 2 and 3 from Whakaari. The length (l), diameter (d), weight (w), volume (v), and dry bulk density (ρ) of the samples are provided with their respective standard deviations ($_{sd}$).

Sample ID	l (cm)	d (cm)	w (g)	v (cm^3)	ρ (kg/m^3)	l_{sd} (cm)	d_{sd} (cm)	w_{sd} (g)	v_{sd} (cm^3)	ρ_{sd} (kg/m^3)
W1-1	2.195	2.5	28.17	10.77	2615.6	0.003	0.003	0.01	0.03	7.34
W1-2	2.206	2.501	28.4	10.84	2619.93	0.006	0.004	0.01	0.05	12.12
W2-1	2.205	2.505	20.97	10.87	1929.16	0.003	0.004	0.01	0.04	7.16
W2-2	2.058	2.498	19.1	10.09	1892.96	0.01	0.005	0.01	0.06	11.3
W3-1	2.217	2.503	20.79	10.91	1905.59	0.01	0.003	0	0.06	10.48
W3-2	2.204	2.5	20.08	10.82	1855.82	0.004	0.004	0.01	0.04	6.92
W3-3	2.199	2.503	20.32	10.82	1878	0.008	0.003	0.01	0.05	8.73
W3-4	2.189	2.501	19.61	10.75	1824.19	0.022	0.005	0.01	0.12	20.38
W4-1	2.211	2.504	17.18	10.89	1577.59	0.008	0.006	0.01	0.07	10.18
W4-2	2.136	2.502	21.58	10.5	2055.24	0.013	0.003	0	0.07	13.7
W4-3	2.113	2.503	22.85	10.4	2197.12	0.005	0.003	0.01	0.04	8.5
W5-1	2.203	2.498	16.43	10.8	1521.3	0.005	0.001	0.01	0.03	4.33
W5-2	2.202	2.502	16.51	10.83	1524.47	0.004	0.003	0.01	0.03	4.32
W5-3	2.205	2.5	16.62	10.82	1536.04	0.008	0.004	0.01	0.05	7.16
W5-5	3.18	2.499	24.14	15.6	1547.44	0.008	0.002	0.03	0.05	5.32
W5-6	4.073	2.499	31.15	19.98	1559.06	0.008	0.002	0.02	0.05	4.03
W6-1	2.2	2.503	24.28	10.83	2241.92	0.009	0.003	0	0.05	10.35
W6-2	2.207	2.503	24.15	10.86	2223.76	0.004	0.003	0.01	0.03	6.21

Continued on next page

Table E.3 – continued from previous page

Sample ID	l (cm)	d (cm)	w (g)	v (cm^3)	ρ (kg/m^3)	l_{sd} (cm)	d_{sd} (cm)	w_{sd} (g)	v_{sd} (cm^3)	ρ_{sd} (kg/m^3)
W6-3	2.202	2.502	26.67	10.83	2462.6	0.005	0.003	0.01	0.04	9.14
W6-4	2.201	2.502	26.9	10.82	2486.14	0.003	0.002	0	0.02	4.6
W6-5	2.195	2.502	26.41	10.79	2447.64	0.004	0.002	0.01	0.03	6.87
W7-1	2.212	2.503	25.39	10.88	2333.64	0.032	0.003	0.01	0.16	34.33
W7-2	2.199	2.504	25	10.83	2308.4	0.003	0.002	0.01	0.02	4.36
W7-3	2.18	2.502	24.66	10.72	2300.37	0.008	0.002	0.01	0.04	8.63
W8-1	2.212	2.502	19.94	10.88	1832.72	0.017	0.005	0	0.09	15.16
W8-2	2.165	2.502	18.63	10.64	1750.94	0.007	0.003	0.01	0.04	6.65
W9-1	2.185	2.502	22.84	10.74	2126.63	0.009	0.003	0.01	0.05	9.94
W9-2	2.193	2.502	22.15	10.78	2054.73	0.004	0.003	0	0.03	5.72
W11-1	2.191	2.497	14.92	10.73	1390.49	0.021	0.005	0.01	0.11	14.29
W11-2	2.18	2.496	15.36	10.67	1439.55	0.016	0.006	0.01	0.09	12.18
W11-3	2.205	2.503	18.4	10.85	1695.85	0.007	0.004	0.01	0.05	7.87
W11-4	2.203	2.464	15.37	10.5	1463.81	0.004	0.014	0.01	0.12	16.76
W11-5	2.213	2.503	17.27	10.89	1585.86	0.014	0.005	0.01	0.08	11.69
W12-1	2.203	2.503	19.02	10.84	1754.61	0.019	0.003	0	0.1	16.19
W13-1	2.146	2.503	19.03	10.56	1802.08	0.037	0.003	0.01	0.18	30.73
W13-2	2.165	2.502	17.96	10.64	1687.97	0.007	0.003	0.01	0.04	6.41
W14-1	2.198	2.499	17.34	10.78	1608.53	0.013	0.002	0.01	0.07	10.49
W15-1	2.199	2.502	16.85	10.81	1558.74	0.01	0.003	0.01	0.06	8.7
W18-1	2.177	2.491	9.69	10.61	913.29	0.005	0.009	0	0.08	6.89

Continued on next page

Table E.3 – continued from previous page

Sample ID	l (cm)	d (cm)	w (g)	v (cm^3)	ρ (kg/m^3)	l_{sd} (cm)	d_{sd} (cm)	w_{sd} (g)	v_{sd} (cm^3)	ρ_{sd} (kg/m^3)
W18-3	2.205	2.493	7.25	10.76	673.79	0.008	0.007	0.01	0.07	4.48
W18-4	2.197	2.495	11.54	10.74	1074.49	0.008	0.005	0.01	0.06	6.07
W19-1	2.202	2.501	11.34	10.82	1048.06	0.003	0.002	0	0.02	1.94
W19-2	2.202	2.503	13.63	10.83	1258.54	0.006	0.003	0.01	0.04	4.74
W20-1	2.197	2.493	7.51	10.72	700.56	0.008	0.007	0.01	0.07	4.67
WS-1	2.194	2.499	20.27	10.76	1883.83	0.003	0.005	0.01	0.05	8.8

Table E.4: Dimensions of samples used in Chapter 4 from Mt. Taranaki. The length (l), diameter (d), weight (w), volume (v), and dry bulk density (ρ) of the samples are provided with their associated standard deviations ($_{sd}$).

Sample ID	l (cm)	d (cm)	w (g)	v (cm^3)	ρ (kg/m^3)	l_{sd} (cm)	d_{sd} (cm)	w_{sd} (g)	v_{sd} (cm^3)	ρ_{sd} (kg/m^3)
T1-1	2.204	2.502	23.64	10.84	2180.81	0.006	0.003	0.00	0.04	8.05
T2-1	2.192	2.502	21.63	10.78	2006.49	0.014	0.003	0.01	0.07	13.06
T3-1	2.196	2.502	24.01	10.80	2223.15	0.002	0.002	0.01	0.02	4.22
T4-1	2.193	2.498	19.99	10.75	1859.53	0.023	0.002	0.02	0.11	19.12
T5-1	2.205	2.503	25.42	10.85	2342.86	0.002	0.003	0.01	0.03	6.54
T6-1	2.139	2.503	26.11	10.53	2479.58	0.010	0.003	0.01	0.06	14.16
T7-1	2.201	2.502	24.21	10.82	2237.52	0.004	0.002	0.01	0.03	6.27
T8-1	2.200	2.503	27.60	10.83	2548.48	0.004	0.003	0.01	0.03	7.12
T9-1	2.194	2.501	23.77	10.78	2205.01	0.008	0.003	0.01	0.05	10.27
T10-1	2.150	2.503	17.25	10.58	1630.43	0.006	0.004	0.01	0.04	6.24

Continued on next page

Table E.4 – continued from previous page

Sample ID	l (cm)	d (cm)	w (g)	v (cm^3)	ρ (kg/m^3)	l_{sd} (cm)	d_{sd} (cm)	w_{sd} (g)	v_{sd} (cm^3)	ρ_{sd} (kg/m^3)
T11-1	2.202	2.502	26.59	10.83	2455.22	0.003	0.003	0.01	0.03	6.86
T12-1	2.197	2.502	22.88	10.80	2118.52	0.011	0.003	0.01	0.06	11.81
T13-1	2.198	2.503	25.35	10.82	2342.88	0.004	0.003	0.01	0.03	6.56
T14-1	2.172	2.504	26.39	10.70	2466.36	0.007	0.002	0.01	0.04	9.27
T15-1	2.205	2.503	29.37	10.85	2706.91	0.003	0.003	0.01	0.03	7.54
T16-1	2.205	2.504	29.09	10.86	2678.64	0.007	0.002	0.01	0.04	9.91
T17-1	2.201	2.504	23.79	10.84	2194.65	0.003	0.002	0.01	0.02	4.15
T18-1	2.194	2.504	26.37	10.80	2441.67	0.005	0.002	0.03	0.03	7.33
T19-1	2.185	2.502	22.30	10.74	2076.35	0.005	0.002	0.01	0.03	5.87
T20-1	2.174	2.493	18.18	10.61	1713.48	0.056	0.020	0.02	0.32	51.71
T21-1	2.198	2.501	19.97	10.80	1849.07	0.007	0.002	0.01	0.04	6.91
T22-1	2.249	2.500	27.07	11.04	2451.99	0.012	0.002	0.02	0.06	13.45
T23-1	2.191	2.501	22.22	10.76	2065.06	0.014	0.002	0.01	0.07	13.47
T24-1	2.242	2.500	25.79	11.01	2342.42	0.008	0.002	0.02	0.04	8.70
T25-1	2.199	2.495	25.23	10.75	2346.98	0.005	0.007	0.02	0.07	15.40
T26-1	2.158	2.486	26.49	10.47	2530.09	0.006	0.007	0.02	0.07	17.02
T27-1	2.199	2.492	28.09	10.73	2617.89	0.003	0.005	0.01	0.05	12.23
T28-1	2.194	2.492	24.31	10.70	2271.96	0.016	0.005	0.01	0.09	19.13
T29-1	2.256	2.495	25.09	11.03	2274.71	0.009	0.005	0.01	0.06	12.41
T30-1	2.205	2.493	25.88	10.76	2405.20	0.006	0.005	0.01	0.05	11.22
T31-1	2.208	2.491	27.82	10.76	2585.50	0.010	0.003	0.01	0.06	14.45

Continued on next page

Table E.4 – continued from previous page

Sample ID	l (cm)	d (cm)	w (g)	v (cm^3)	ρ (kg/m^3)	l_{sd} (cm)	d_{sd} (cm)	w_{sd} (g)	v_{sd} (cm^3)	ρ_{sd} (kg/m^3)
T32-1	2.251	2.493	24.19	10.99	2201.09	0.016	0.006	0.01	0.09	18.05
T33-1	2.203	2.495	19.12	10.77	1775.30	0.005	0.005	0.01	0.05	8.29
T34-1	2.210	2.494	21.38	10.80	1979.63	0.004	0.005	0.01	0.05	9.21

E.4 Phase composition - X-ray diffraction analysis

Table E.5: Semi-quantitative phase composition of 45 samples used in Chapter 2 from Whakaari. Here, Pl-Plagioclase, Px-pyroxene, Fto-Fe-Ti oxides, Alu-alunite, Crs-cristobalite, Trd-tridymite, S-Sulfur, Py-pyrite, Kln-clays, Anh-anhydrite, Gp-Gypsum, Si-silica, Brt-barite, Amo-amorphous phases. Amorphous phase types are classified as primary (P), secondary (S), or a combination of both (PS). Alteration intensities of the samples are shown by FS-Fresh to slightly altered, M-moderately altered, and H-highly altered. Note that sample W14-1 was classified as moderately altered based on visual examination during BSE imaging.

Sample ID	Sample type	Pl (%)	Px (%)	Fto (%)	Alu (%)	Crs (%)	Trd (%)	S (%)	Py (%)	Kln (%)	Anh (%)	Amo (%)	Amo type	Other phases	Alteration intensity
W1-1	Lava	67	20	0	0	0	0	0	0	0	0	13	P	Anh/Gp, Fto	FS
W1-2	Lava	67	20	0	0	0	0	0	0	0	0	13	P	Anh/Gp, Fto	FS
W2-1	Sulfur flow	0	0	0	0	0	0	85	0	0	0	15	P	Detrital Si, Anh/Gp	FS
W2-2	Sulfur flow	0	0	0	0	0	0	85	0	0	0	15	P	Detrital Si, Anh/Gp	FS
W3-1	Sulfur flow	0	0	0	0	0	0	85	0	0	0	15	P	Detrital Si, Brt	FS
W3-2	Sulfur flow	0	0	0	0	0	0	85	0	0	0	15	P	Detrital Si, Brt	FS
W3-3	Sulfur flow	0	0	0	0	0	0	85	0	0	0	15	P	Detrital Si, Brt	FS
W3-4	Sulfur flow	0	0	0	0	0	0	85	0	0	0	15	P	Detrital Si, Brt	FS
W4-1	Breccia	0	0	0	46	3	0	0	0	0	0	50	S		H
W4-2	Lava	22	12	0	8	3	0	0	0	9	0	45	PS	Fto	H
W4-3	Lava	22	12	0	8	3	0	0	0	9	0	45	PS	Fto	H
W5-1	Tuff	24	20	0	13	0	0	0	0	0	0	44	P	Si, Py	M
W5-2	Tuff	24	20	0	13	0	0	0	0	0	0	44	P	Si, Py	M

Continued on next page

Table E.5 – continued from previous page

Sample ID	Sample type	Pl (%)	Px (%)	Fto (%)	Alu (%)	Crs (%)	Trd (%)	S (%)	Py (%)	Kln (%)	Anh (%)	Amo (%)	Amo type	Other phases	Alteration intensity
W5-3	Tuff	24	20	0	13	0	0	0	0	0	0	44	P	Si, Py	M
W5-5	Tuff	24	20	0	13	0	0	0	0	0	0	44	P	Si, Py	M
W5-6	Tuff	24	20	0	13	0	0	0	0	0	0	44	P	Si, Py	M
W6-1	Lava	60	17	0	0	9	6	0	0	0	0	8	P	Fto, Kln	M
W6-2	Lava	43	15	0	0	8	6	0	0	0	0	28	P	Fto, Kln	M
W6-3	Lava	62	17	0	0	10	1	0	0	0	0	10	P	Fto, Kln	M
W6-4	Lava	62	18	0	0	11	1	0	0	0	0	9	P	Fto, Kln	M
W6-5	Lava	62	18	0	0	10	1	0	0	0	0	9	P	Fto, Kln	M
W7-1	Lava	58	13	0	0	13	0	0	0	0	0	15	P	Anh/Gp, Fto	M
W7-2	Lava	58	13	0	0	13	0	0	0	0	0	15	P	Anh/Gp, Fto	M
W7-3	Lava	58	13	0	0	13	0	0	0	0	0	15	P	Anh/Gp, Fto	M
W8-1	Tuff	0	0	0	28	1	17	1	1	0	0	52	S		H
W8-2	Tuff	0	0	0	28	1	17	1	1	0	0	52	S		H
W9-1	Breccia	0	15	0	54	5	0	0	0	0	0	26	PS	Anh/Gp, Py	H
W9-2	Breccia	0	2	0	63	0	0	0	0	0	0	34	PS	Anh/Gp, Py, Si	H
W11-1	Tuff	0	0	0	49	3	0	0	0	0	0	48	S	Fto, Kln	H
W11-2	Tuff	0	0	4	37	7	0	0	0	0	0	52	S	Kln	H
W11-3	Tuff	0	0	4	37	7	0	0	0	0	0	52	S	Kln	H
W11-4	Tuff	0	0	0	49	3	0	0	0	0	0	48	S	Fto, Kln	H
W11-5	Tuff	0	0	0	49	3	0	0	0	0	0	48	S	Fto, Kln	H

Continued on next page

Table E.5 – continued from previous page

Sample ID	Sample type	Pl (%)	Px (%)	Fto (%)	Alu (%)	Crs (%)	Trd (%)	S (%)	Py (%)	Kln (%)	Anh (%)	Amo (%)	Amo type	Other phases	Alteration intensity
W12-1	Breccia	0	0	0	40	3	0	0	0	0	0	57	S	Py	H
W13-1	Tuff	0	0	0	50	1	0	0	0	0	0	49	S		H
W13-2	Tuff	0	0	0	50	0	0	0	0	0	0	50	S		H
W14-1	Breccia	27	26	1	0	0	0	0	0	0	0	46	P	Si, Py	M
W15-1	Tuff	0	0	0	18	18	6	0	3	0	16	39	S		H
W18-1	Vesicular lava	42	24	0	0	0	0	0	0	0	0	35	P		FS
W18-3	Vesicular lava	42	24	0	0	0	0	0	0	0	0	35	P		FS
W18-4	Vesicular lava	41	23	0	0	0	0	0	0	0	0	36	P	Fto	FS
W19-1	Vesicular lava	41	27	0	0	0	0	0	0	0	0	32	P	Kln	FS
W19-2	Vesicular lava	41	27	0	0	0	0	0	0	0	0	32	P	Kln	FS
W20-1	Vesicular lava	27	25	1	0	0	0	0	0	0	0	47	P	Kln, Anh/Gp	FS
WS-1	Sulfur flow	0	0	0	0	0	0	92	0	0	0	8	P		FS

Table E.6: Semi-quantitative phase composition of 34 samples used in Chapter 4 from Mt. Taranaki. Here, Fsp-feldspar, Px-pyroxene, Amp-amphibole, Fto-Fe-Ti oxides, Alu-alunite, Si-silica (mainly cristobalite), Amo-amorphous phases. Amorphous phase types are classified as primary (P), secondary (S), or a combination of both (PS). Alteration intensities of the samples are shown by FS-Fresh to slightly altered, M-moderately altered, and H-highly altered. Sampling locality is represented by S-summit dome area, BAF-block and ash flow deposits, and DA-debris avalanche deposits. Note that sample T21-1 was classified as moderately altered based on visual examination during BSE imaging.

Sample ID	Sample type	Sampling locality	Fsp (%)	Px (%)	Amp (%)	Fto (%)	Alu (%)	Si (%)	Amo (%)	Amo type	Other phases	Alteration intensity
T1-1	Lava	S	57	21	0	0	13	0	10	P	Si, Amp, Fto	M
T2-1	Lava	S	34	10	0	0	8	3	44	P	Amp	M
T3-1	Lava	S	47	19	5	0	10	2	18	P		M
T4-1	Lava	S	55	18	6	0	0	0	21	P		FS
T5-1	Lava	S	54	21	2	0	0	5	18	P		M
T6-1	Lava	BAF	56	32	0	2	0	0	10	P		FS
T7-1	Lava	BAF	54	14	7	0	0	0	25	P		FS
T8-1	Lava	BAF	55	24	0	2	0	1	18	P	Amp	FS
T9-1	Lava	BAF	25	28	0	0	11	0	36	P		M
T10-1	Lava	BAF	44	10	12	0	0	0	34	P		FS
T11-1	Lava	BAF	66	26	0	0	0	0	8	P	Amp	FS
T12-1	Lava	BAF	53	23	0	1	0	7	17	P		M
T13-1	Lava	BAF	59	26	0	1	0	4	9	P	Amp	FS
T14-1	Lava	DA	69	16	0	0	0	2	13	P		FS
T15-1	Lava	DA	63	24	0	1	0	2	9	P		FS

Continued on next page

Table E.6 – continued from previous page

Sample ID	Sample type	Sampling locality	Fsp (%)	Px (%)	Amp (%)	Fto (%)	Alu (%)	Si (%)	Amo (%)	Amo type	Other phases	Alteration intensity
T16-1	Lava	DA	63	23	0	1	0	3	10	P	Amp	FS
T17-1	Lava	S	27	9	0	0	24	3	37	P		M
T18-1	Lava	S	45	34	0	0	2	4	17	P		M
T19-1	Lava	S	56	6	0	0	8	9	21	P		M
T20-1	Lava	S	0	0	0	1	27	14	58	P	Px, Fsp	H
T21-1	Lava	S	39	31	0	0	3	0	27	P	Amp, Si, Fto	M
T22-1	Lava	S	42	26	0	0	6	1	25	P	Amp	M
T23-1	Lava	S	31	8	4	0	6	0	50	P		M
T24-1	Lava	S	34	8	14	0	8	0	36	P		M
T25-1	Lava	S	57	22	0	2	0	0	19	P	Amp	FS
T26-1	Lava	BAF	67	20	2	1	0	0	10	P		FS
T27-1	Lava	BAF	67	21	0	3	0	0	9	P	Amp	FS
T28-1	Lava	BAF	53	18	3	3	0	0	23	P		FS
T29-1	Lava	BAF	58	12	4	4	0	0	22	P		FS
T30-1	Lava	BAF	56	17	3	2	0	0	22	P		FS
T31-1	Lava	BAF	50	17	9	0	0	0	23	P		FS
T32-1	Lava	BAF	53	13	8	1	0	0	25	P		FS
T33-1	Lava	BAF	48	15	10	0	0	0	27	P		FS
T34-1	Lava	BAF	55	15	6	1	0	0	23	P		FS

E.5 Phase composition - Backscattered-electron imaging and energy disperse spectroscopy

This section consists of backscattered-electron images for samples used in Chapter 2. The phases were identified using energy dispersive spectroscopy.

Lavas

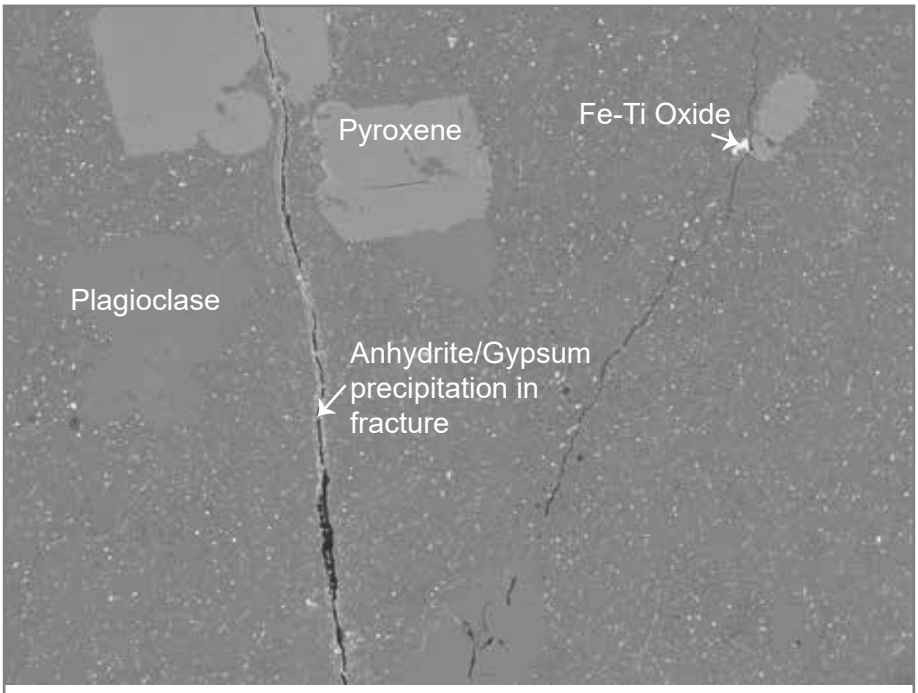

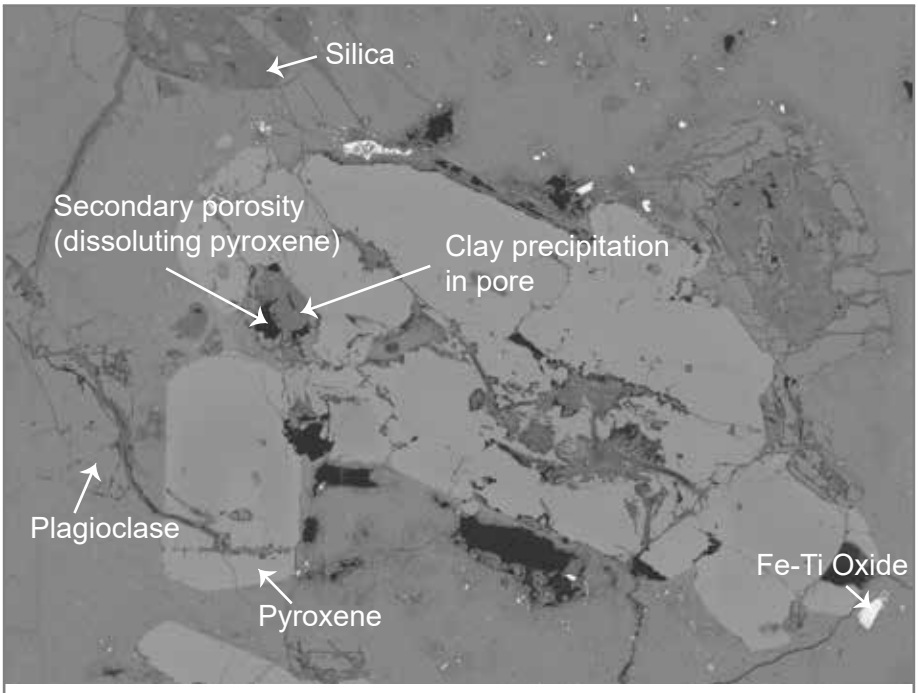

Block ID: W6 Sample ID: W6-1c
Sample type: Lava
Alteration intensity: Moderately altered
100 µm

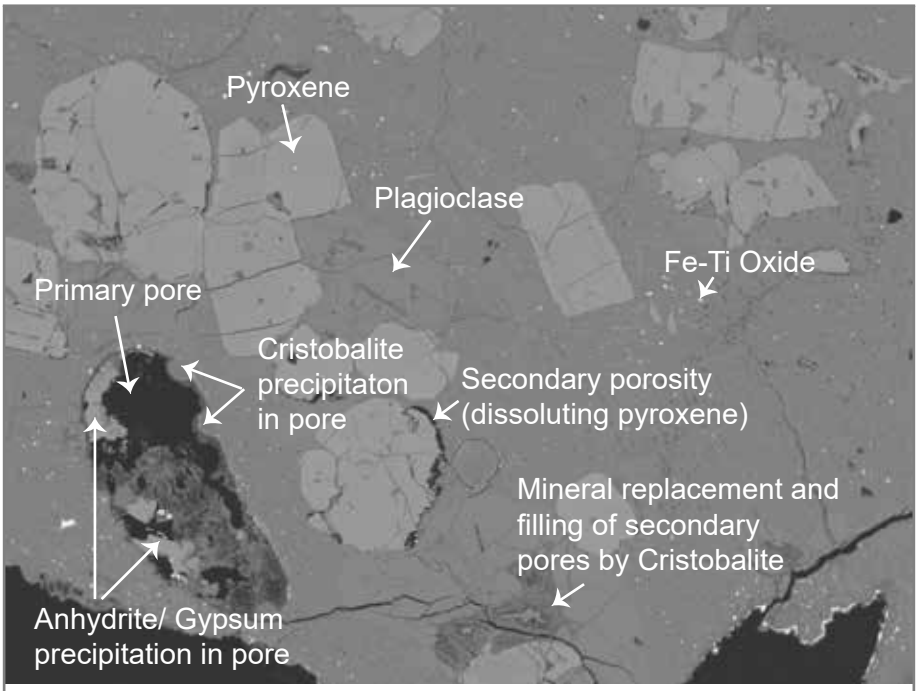

Block ID: W7 Sample ID: W7-2c
Sample type: Lava
Alteration intensity: Moderately altered
100 µm

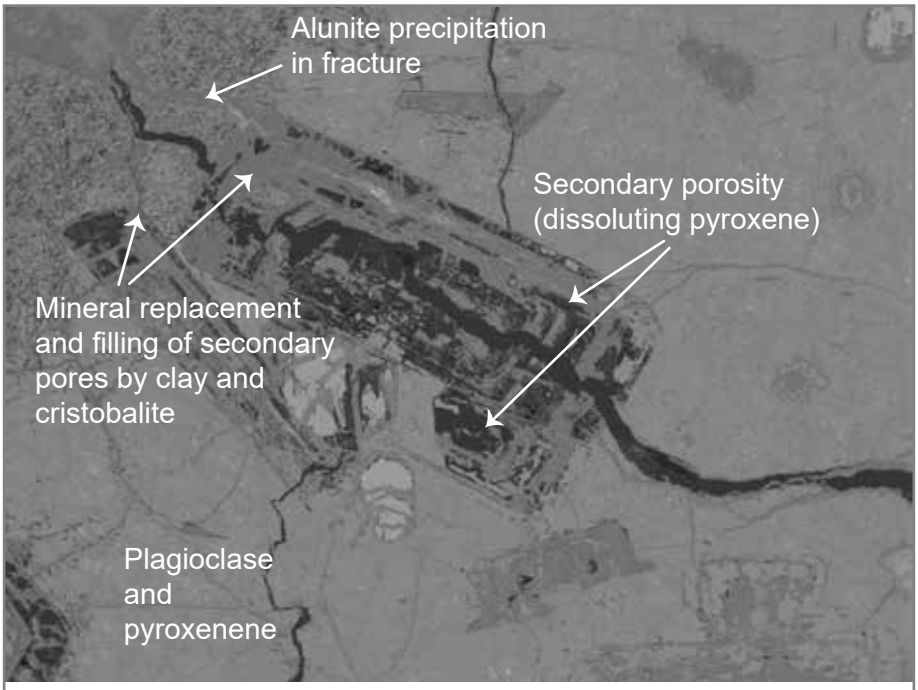

Block ID: W4 Sample ID: W4-23c
Sample type: Lava
Alteration intensity: Highly altered

100 µm

Tuffs

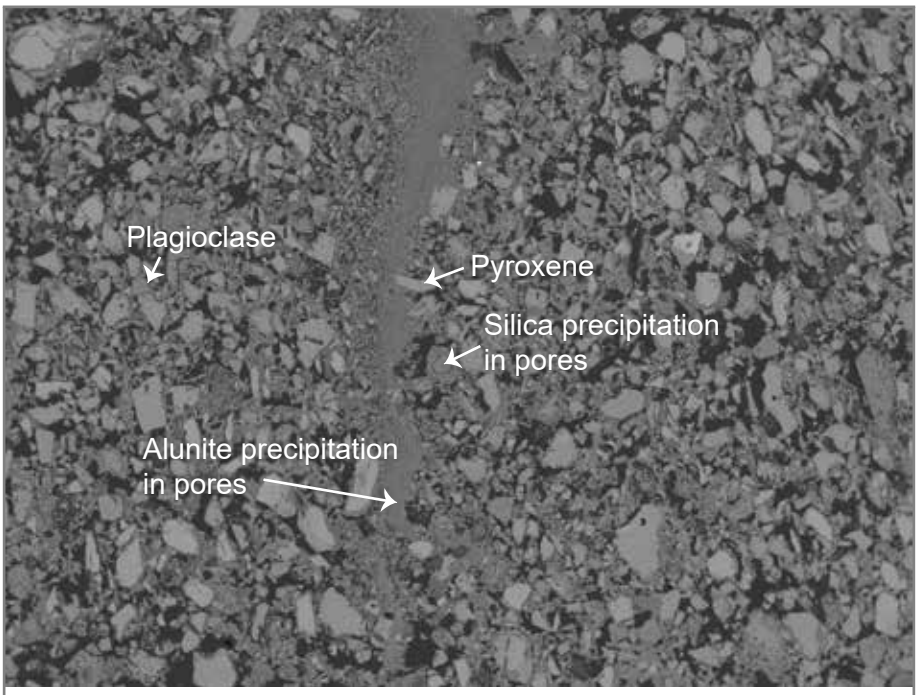

Block ID: W5 Sample ID: W5-1c
Sample type: Tuff
Alteration intensity: Moderately altered

100 µm

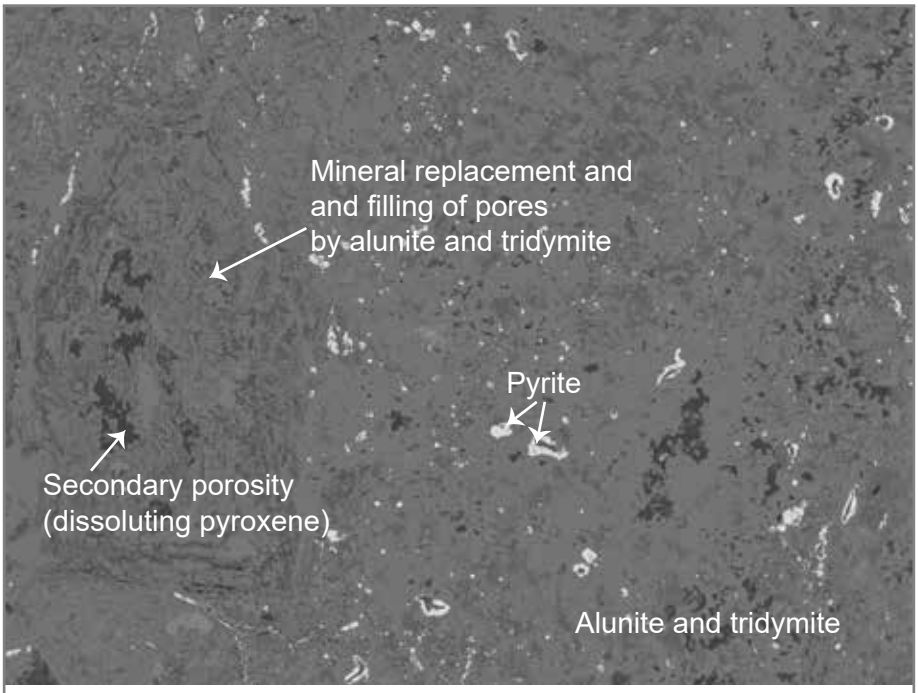

Block ID: W8 Sample ID: W8-1c
Sample type: Tuff
Alteration intensity: Highly altered
100 µm

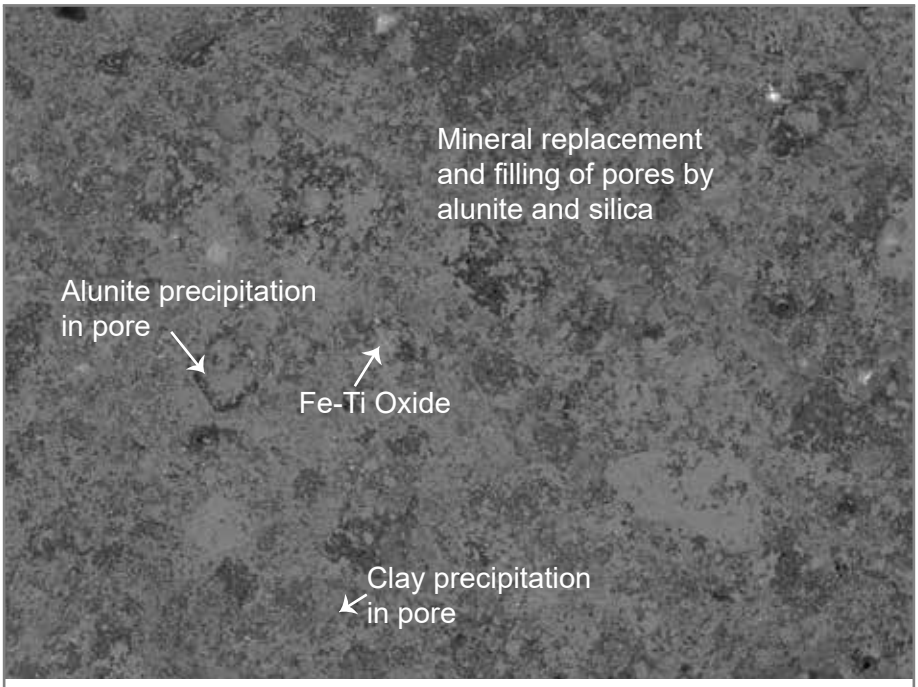

Block ID: W11 Sample ID: W11-2c
Sample type: Tuff
Alteration intensity: Highly altered
100 µm

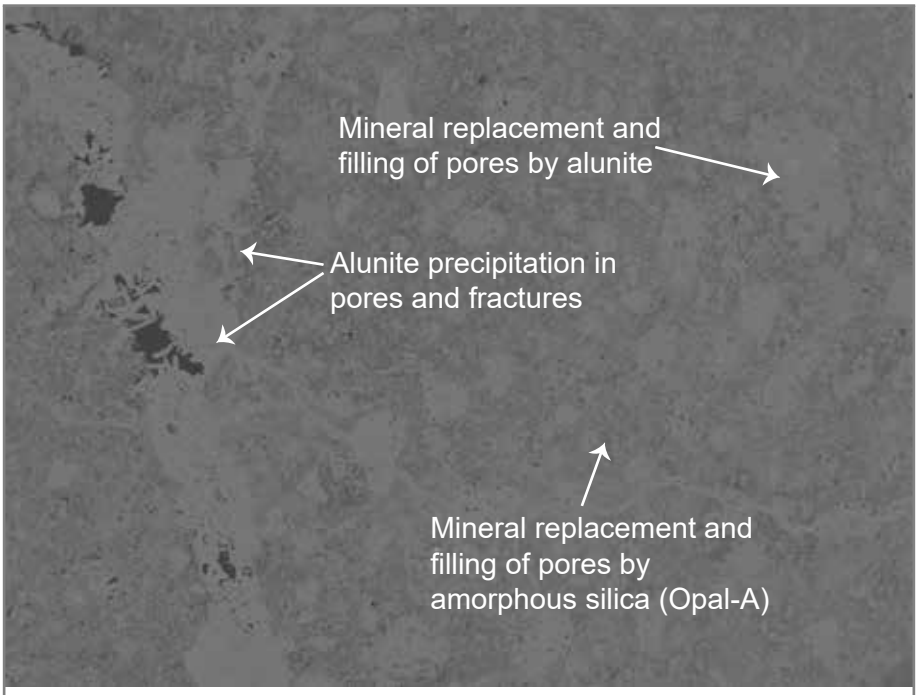

Block ID: W13 Sample ID: W13-1c
Sample type: Tuff
Alteration intensity: Highly altered

100 µm

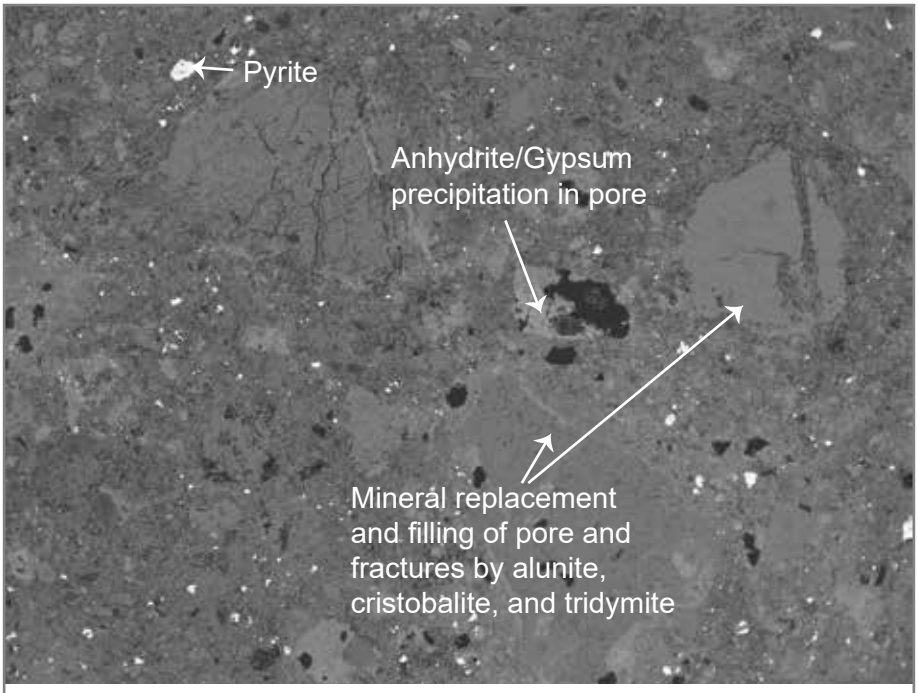

Block ID: W15 Sample ID: W15-1c
Sample type: Tuff
Alteration intensity: Highly altered

100 µm

Breccias

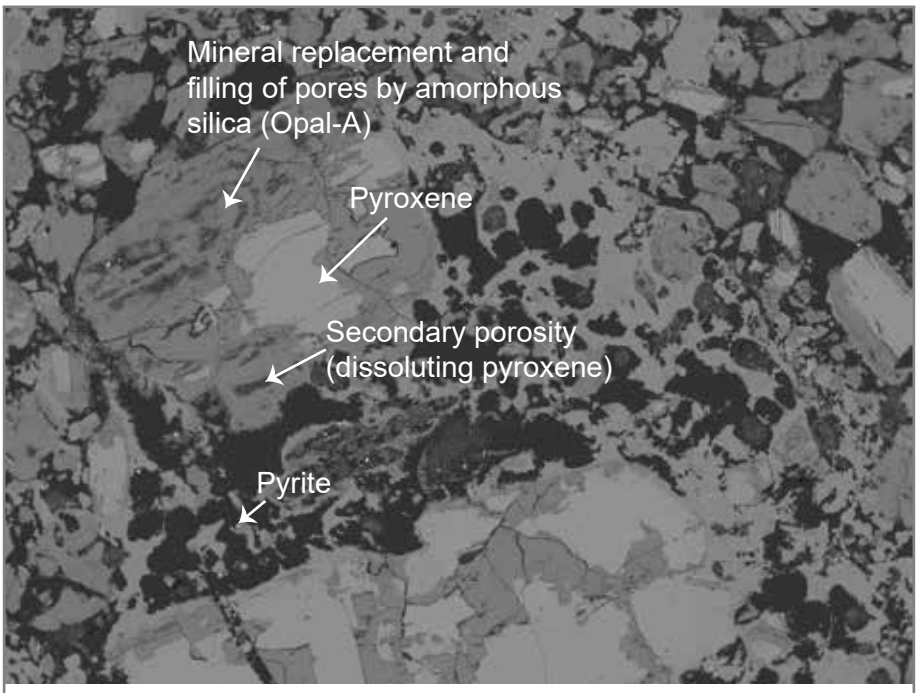

Block ID: W14 Sample ID: W14-1c
Sample type: Breccia
Alteration intensity: Moderately altered

100 µm

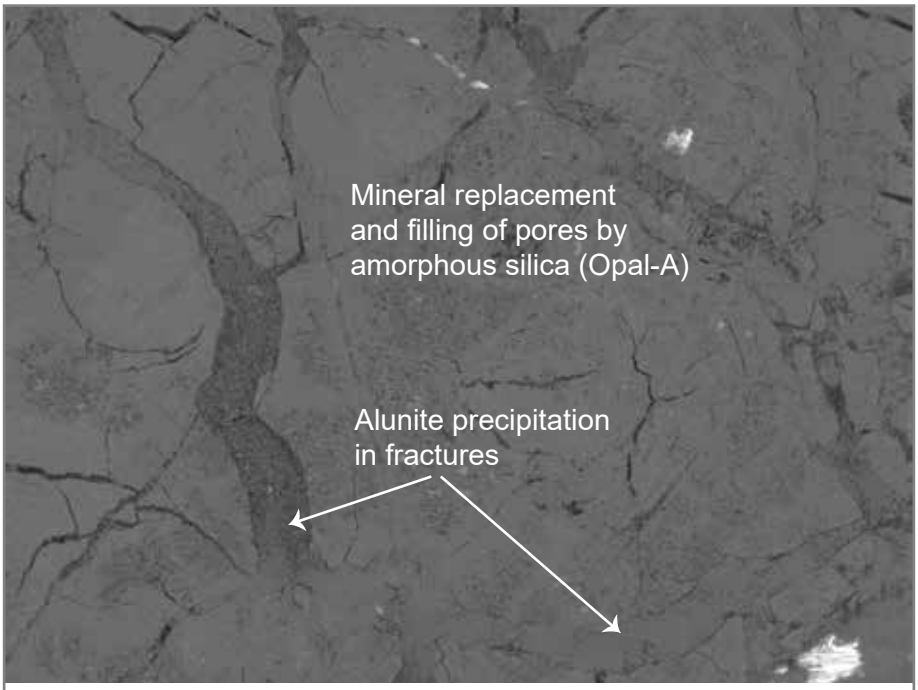

Block ID: W4 Sample ID: W4-1c
Sample type: Breccia
Alteration intensity: Highly altered

100 µm

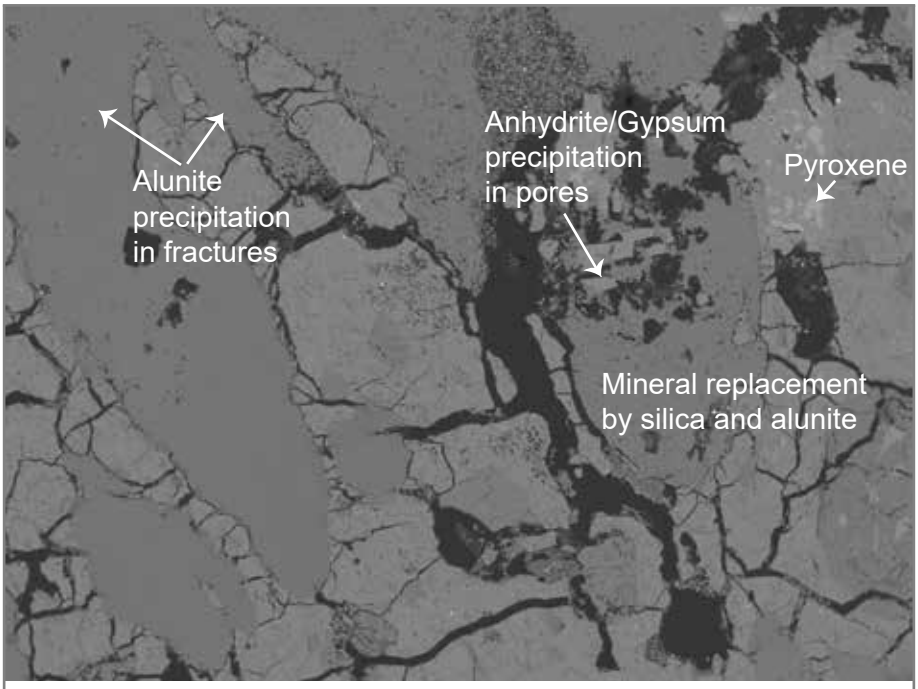

Block ID: W9 Sample ID: W9-1c
Sample type: Breccia
Alteration intensity: Highly altered

100 µm

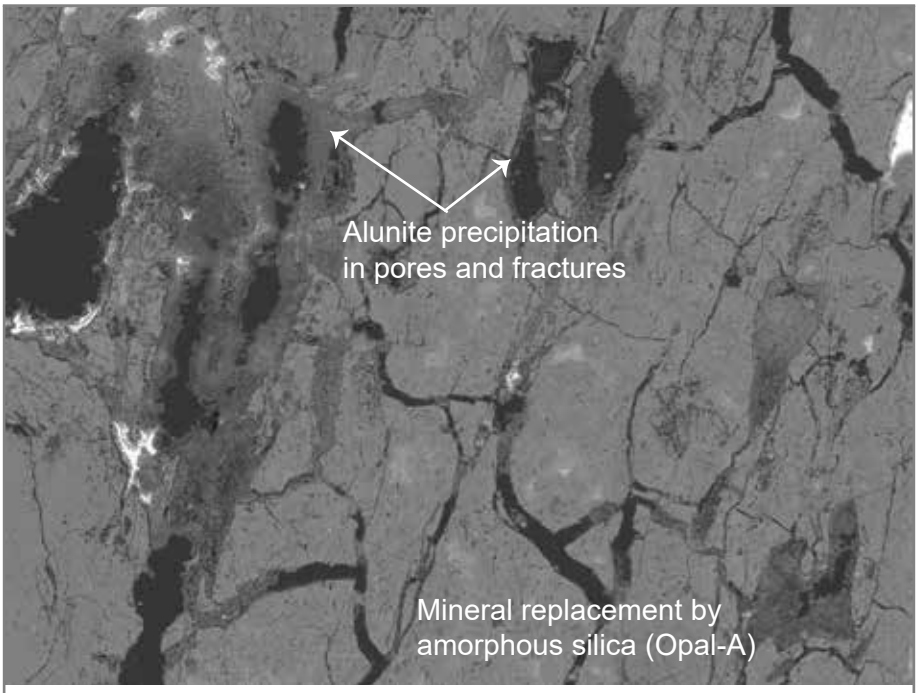

Block ID: W12 Sample ID: W12-1c
Sample type: Breccia
Alteration intensity: Highly altered

100 µm

Vesicular lavas

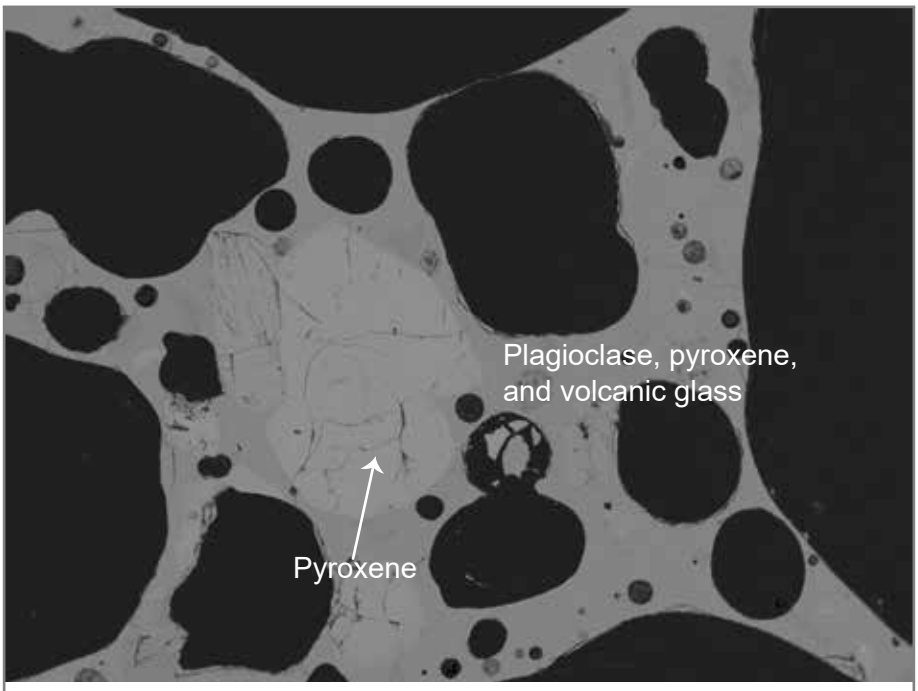

Block ID: W18 Sample ID: W18-1c
Sample type: Vesicular lava
Alteration intensity: Fresh-slightly altered

100 µm

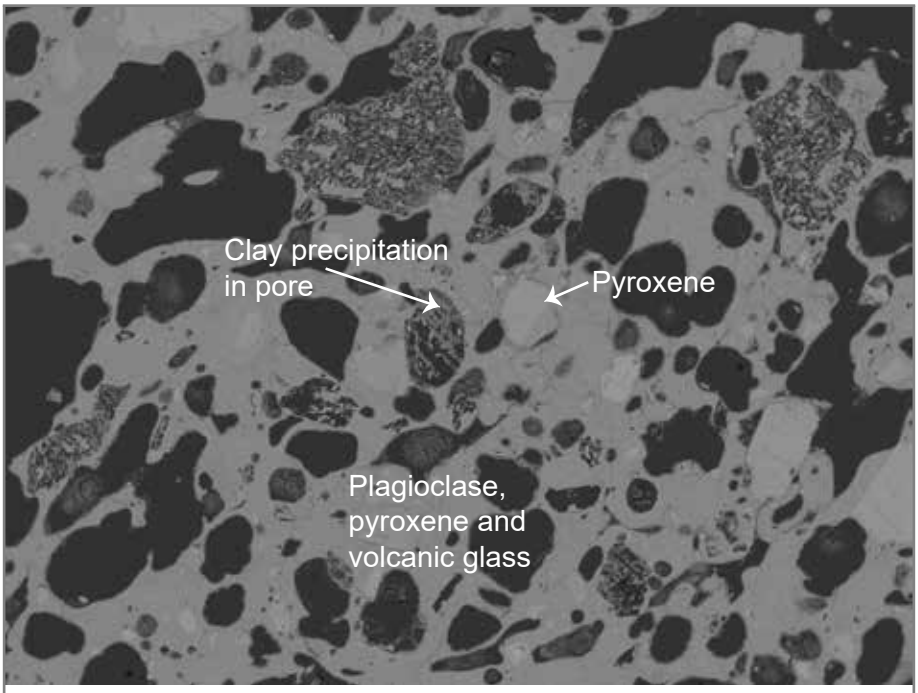

Block ID: W19 Sample ID: W19-1c
Sample type: Vesicular lava
Alteration intensity: Fresh-slightly altered

100 µm

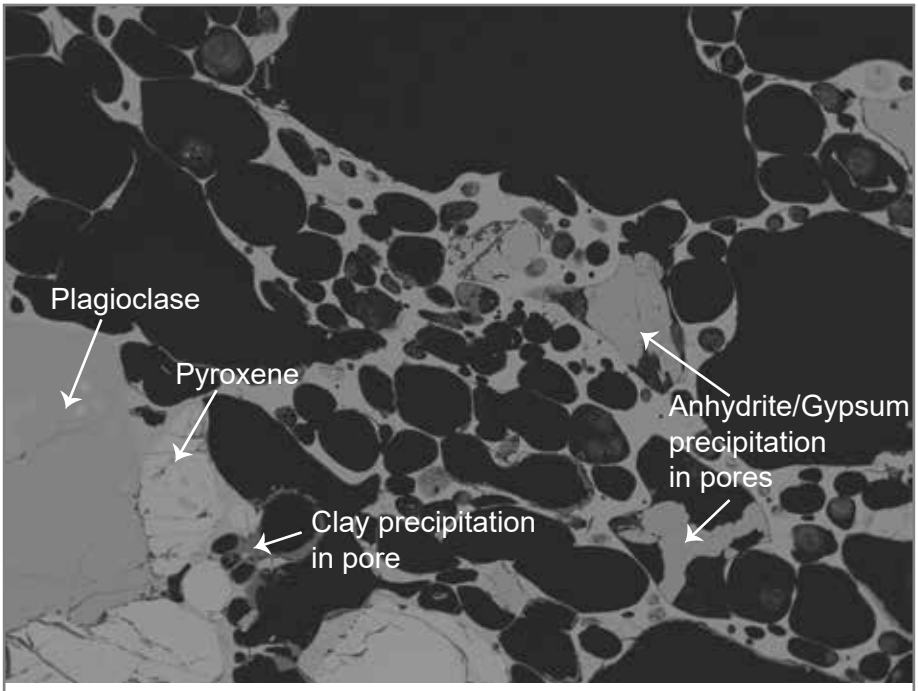

Block ID: W20 Sample ID: W20-1c
Sample type: Vesicular lava
Alteration intensity: Fresh-slightly altered

100 µm

Sulfur flows

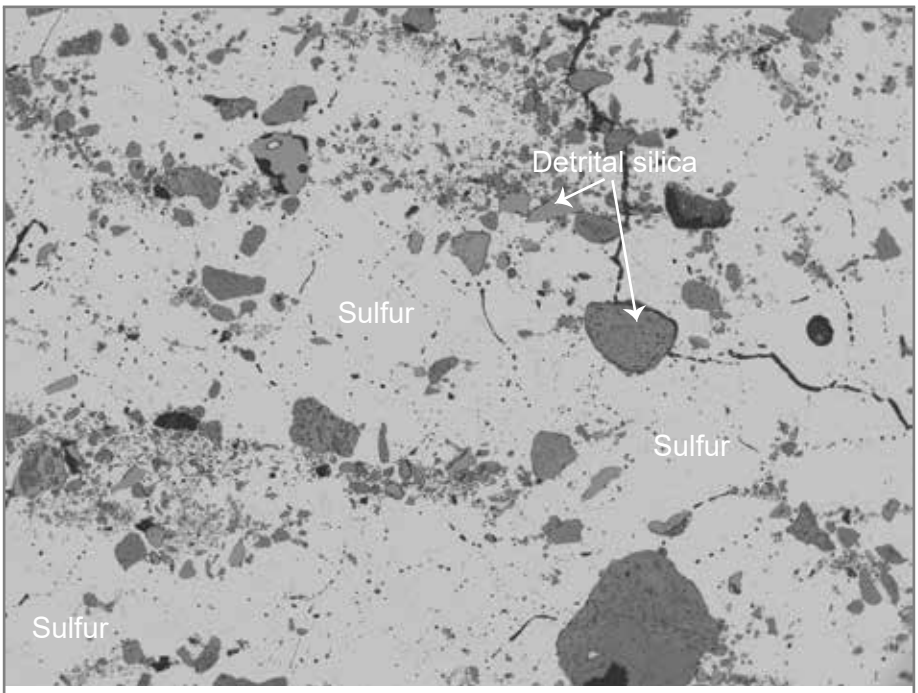

Block ID: W2 Sample ID: W2-2c
Sample type: Sulfur flow
Alteration intensity: Fresh-slightly altered

100 µm

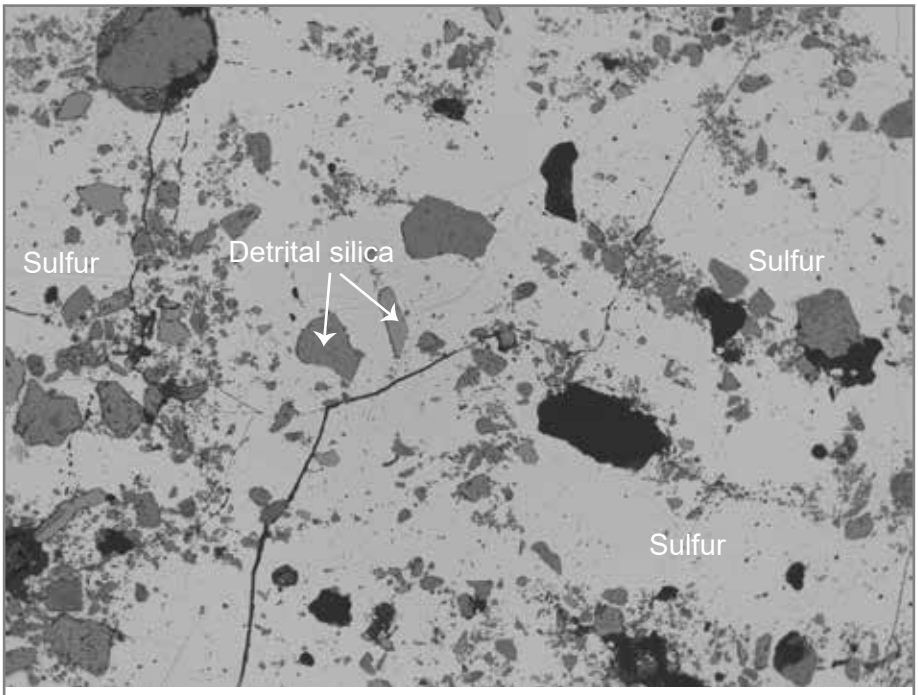

Block ID: W3 Sample ID: W3-2c
Sample type: Sulfur flow
Alteration intensity: Fresh-slightly altered

100 µm

E.6 Porosity and permeability

Table E.7: Porosity and permeability of samples used in Chapter 2 from Whakaari. Here, P_{eff}-effective hydrostatic pressure, ϕ-porosity, ϕ_{SD} -standard deviation of porosity, κ-permeability. Error on permeability is less than 5%. Alteration intensities of the samples are shown by FS-Fresh to slightly altered, M-moderately altered, and H-highly altered. In samples with (a) in notes, porosity is not directly measured but instead are computed from an average of porosities of samples W5-1, W5-2, and W5-3; with (b) in notes porosity was below the detection limit; with * in notes standard deviation of porosity was estimated based on atmospheric pressure measurements.

Sample ID	Sample type	Alteration Intensity	P_{eff} (MPa)	ϕ (%)	ϕ_{SD} (%)	κ (m^2)	Notes
W1-1	Lava	FS	0	2	0		
W11-1	Tuff	H	0	44	2		
W11-2	Tuff	H	0	45	3		
W11-3	Tuff	H	0	32	1		
W11-4	Tuff	H	0	41	4		
W11-5	Tuff	H	0	34	2		
W1-2	Lava	FS	0	2	0		
W12-1	Breccia	H	0	25	1		
W13-1	Tuff	H	0	21	1		
W13-2	Tuff	H	0	28	1		
W14-1	Breccia	M	0	37	1		
W15-1	Tuff	H	0	33	1		
W18-1	Vesicular lava	FS	0	67	5		
W18-3	Vesicular lava	FS	0	76	5		
W18-4	Vesicular lava	FS	0	61	3		
W19-1	Vesicular lava	FS	0	62	2		
W19-2	Vesicular lava	FS	0	54	2		
W20-1	Vesicular lava	FS	0	73	4		
W2-1	Sulfur flow	FS	0	7	0		
W2-2	Sulfur flow	FS	0	8	0		
W3-1	Sulfur flow	FS	0	6	0		
W3-2	Sulfur flow	FS	0	9	0		
W3-3	Sulfur flow	FS	0	8	0		

Continued on next page

Table E.7 – continued from previous page

Sample ID	Sample type	Alteration Intensity	P_{eff} (MPa)	ϕ (%)	ϕ_{SD} (%)	κ (m^2)	Notes
W3-4	Sulfur flow	FS	0	9	0		
W4-1	Breccia	H	0	36	2		
W4-2	Lava	H	0	16	1		
W4-3	Lava	H	0	12	0		
W5-1	Tuff	M	0	41	1		
W5-2	Tuff	M	0	40	2		
W5-3	Tuff	M	0	39	2		
W5-5	Tuff	M	0	40	1		*a
W6-1	Lava	M	0	11	0		
W6-2	Lava	M	0	10	0		
W6-3	Lava	M	0	7	0		
W6-4	Lava	M	0	7	0		
W6-5	Lava	M	0	7	0		
W7-1	Lava	M	0	12	1		
W7-2	Lava	M	0	13	0		
W7-3	Lava	M	0	13	0		
W8-1	Tuff	H	0	21	1		
W8-2	Tuff	H	0	24	1		
W9-1	Breccia	H	0	18	1		
W9-2	Breccia	H	0	19	1		
WS-1	Sulfur flow	FS	0	7	0		
W5-6	Tuff	M	1.89	31	1	6.11×10^{-14}	*
W5-6	Tuff	M	5.4	29	1	5.82×10^{-14}	*
W5-6	Tuff	M	12.29	29	1	5.72×10^{-14}	*
W5-6	Tuff	M	19.07	29	1	5.52×10^{-14}	*
W5-6	Tuff	M	25.73	29	1	5.58×10^{-14}	*
W5-6	Tuff	M	32.51	29	1	5.43×10^{-14}	*
W5-6	Tuff	M	39.49	29	1	5.33×10^{-14}	*
W5-6	Tuff	M	46.64	28	1	5.12×10^{-14}	*
W5-6	Tuff	M	53.64	28	1	4.89×10^{-14}	*
W6-3	Lava	M	1.94	6	0	7.38×10^{-17}	*

Continued on next page

Table E.7 – continued from previous page

Sample ID	Sample type	Alteration Intensity	P_{eff} (MPa)	ϕ (%)	ϕ_{SD} (%)	κ (m^2)	Notes
W6-3	Lava	M	5.38	5	0	4.25×10^{-17}	*
W6-3	Lava	M	12.16	5	0	2.73×10^{-17}	*
W6-3	Lava	M	19.17	5	0	1.9×10^{-17}	*
W6-3	Lava	M	25.99	4	0	1.37×10^{-17}	*
W6-3	Lava	M	32.85	4	0	1.05×10^{-17}	*
W6-3	Lava	M	39.85	4	0	8.48×10^{-18}	*
W6-3	Lava	M	46.71	4	0	6.43×10^{-18}	*
W6-3	Lava	M	53.76	3	0	5.01×10^{-18}	*
W6-5	Lava	M	2.04	3	0	2.78×10^{-16}	*
W6-5	Lava	M	5.53	3	0	1.84×10^{-16}	*
W6-5	Lava	M	12.28	2	0	8.1×10^{-17}	*
W6-5	Lava	M	19.01	2	0	4.14×10^{-17}	*
W6-5	Lava	M	25.77	2	0	2.49×10^{-17}	*
W6-5	Lava	M	32.51	2	0	1.46×10^{-17}	*
W6-5	Lava	M	39.9	2	0	8.29×10^{-18}	*
W6-5	Lava	M	46.57	1	0	4.92×10^{-18}	*
W6-5	Lava	M	53.85	1	0	3.38×10^{-18}	*
W13-2	Tuff	H	1.85	27	1	2.63×10^{-16}	*
W13-2	Tuff	H	5.36	27	1	2.49×10^{-16}	*
W13-2	Tuff	H	19.07	26	1	2.14×10^{-16}	*
W13-2	Tuff	H	26.1	26	1	1.68×10^{-16}	*
W13-2	Tuff	H	33.05	26	1	1.66×10^{-16}	*
W13-2	Tuff	H	39.62	25	1	1.5×10^{-16}	*
W13-2	Tuff	H	46.6	25	1	1.61×10^{-16}	*
W13-2	Tuff	H	53.57	25	1	1.44×10^{-16}	*
W15-1	Tuff	H	1.77	32	1	1.57×10^{-15}	*
W15-1	Tuff	H	5.37	32	1	1.41×10^{-15}	*
W15-1	Tuff	H	12.18	31	1	1.23×10^{-15}	*
W15-1	Tuff	H	19.15	31	1	1.09×10^{-15}	*
W15-1	Tuff	H	25.83	30	1	9.48×10^{-16}	*
W15-1	Tuff	H	32.68	30	1	9.05×10^{-16}	*

Continued on next page

Table E.7 – continued from previous page

Sample ID	Sample type	Alteration Intensity	P_{eff} (MPa)	ϕ (%)	ϕ_{SD} (%)	κ (m^2)	Notes
W15-1	Tuff	H	39.89	30	1	8.32×10^{-16}	*
W15-1	Tuff	H	46.69	30	1	7.8×10^{-16}	*
W15-1	Tuff	H	53.64	29	1	3.65×10^{-16}	*
W5-1	Tuff	M	3.45	37	1		*
W5-1	Tuff	M	6.89	37	1		*
W5-1	Tuff	M	13.79	37	1		*
W5-1	Tuff	M	20.68	36	1		*
W5-1	Tuff	M	27.58	36	1		*
W5-1	Tuff	M	34.47	35	1		*
W5-1	Tuff	M	41.37	33	1		*
W5-1	Tuff	M	48.26	32	1		*
W5-1	Tuff	M	55.16	30	1		*
W7-2	Lava	M	3.45	11	0		*
W7-2	Lava	M	6.89	10	0		*
W7-2	Lava	M	13.79	9	0		*
W7-2	Lava	M	20.68	8	0		*
W7-2	Lava	M	27.58	8	0		*
W7-2	Lava	M	34.47	8	0		*
W7-2	Lava	M	41.37	7	0		*
W7-2	Lava	M	48.26	6	0		*
W7-2	Lava	M	55.16	6	0		*
W1-2	Lava	FS	3.45	1	0		*
W1-2	Lava	FS	6.89	0	0		*
W1-2	Lava	FS	13.79	0	0		*
W1-2	Lava	FS	20.68	0	0		*
W1-2	Lava	FS	27.58	0	0		*b
W1-2	Lava	FS	34.47	0	0		*b
W1-2	Lava	FS	41.37	0	0		*
W1-2	Lava	FS	48.26	0	0		*b
W1-2	Lava	FS	55.16	0	0		*
W9-2	Breccia	H	3.45	15	1		*

Continued on next page

Table E.7 – continued from previous page

Sample ID	Sample type	Alteration Intensity	P_{eff} (MPa)	ϕ (%)	ϕ_{SD} (%)	κ (m^2)	Notes
W9-2	Breccia	H	6.89	14	1		*
W9-2	Breccia	H	13.79	14	1		*
W9-2	Breccia	H	20.68	13	1		*
W9-2	Breccia	H	27.58	13	1		*
W9-2	Breccia	H	34.47	13	1		*
W9-2	Breccia	H	41.37	13	1		*
W9-2	Breccia	H	48.26	13	1		*
W9-2	Breccia	H	55.16	13	1		*
W6-2	Lava	M	3.45	9	0		*
W6-2	Lava	M	6.89	8	0		*
W6-2	Lava	M	13.79	7	0		*
W6-2	Lava	M	20.68	6	0		*
W6-2	Lava	M	27.58	7	0		*
W6-2	Lava	M	34.47	4	0		*
W6-2	Lava	M	41.37	4	0		*
W6-2	Lava	M	48.26	3	0		*
W6-2	Lava	M	55.16	3	0		*
W11-2	Tuff	H	3.45	44	3		*
W11-2	Tuff	H	6.89	42	3		*
W11-2	Tuff	H	13.79	40	3		*
W11-2	Tuff	H	20.68	39	3		*
W11-2	Tuff	H	27.58	38	3		*
W11-2	Tuff	H	34.47	35	3		*
W11-2	Tuff	H	41.37	33	3		*
W11-2	Tuff	H	48.26	32	3		*
W11-2	Tuff	H	55.16	31	3		*
W11-5	Tuff	H	3.45	31	2		*
W11-5	Tuff	H	6.89	30	2		*
W11-5	Tuff	H	13.79	30	2		*
W11-5	Tuff	H	20.68	29	2		*
W11-5	Tuff	H	27.58	29	2		*

Continued on next page

Table E.7 – continued from previous page

Sample ID	Sample type	Alteration Intensity	P_{eff} (MPa)	ϕ (%)	ϕ_{SD} (%)	κ (m^2)	Notes
W11-5	Tuff	H	34.47	29	2		*
W11-5	Tuff	H	41.37	29	2		*
W11-5	Tuff	H	48.26	28	2		*
W11-5	Tuff	H	55.16	28	2		*
W2-1	Sulfur flow	FS	3.45	5	0		*
W2-1	Sulfur flow	FS	6.89	4	0		*
W2-1	Sulfur flow	FS	13.79	4	0		*
W2-1	Sulfur flow	FS	20.68	4	0		*
W2-1	Sulfur flow	FS	27.58	4	0		*
W2-1	Sulfur flow	FS	34.47	3	0		*
W2-1	Sulfur flow	FS	41.37	4	0		*
W2-1	Sulfur flow	FS	48.26	3	0		*
W2-1	Sulfur flow	FS	55.16	3	0		*
W13-1	Tuff	H	3.45	22	1		*
W13-1	Tuff	H	6.89	22	1		*
W13-1	Tuff	H	13.79	22	1		*
W13-1	Tuff	H	20.68	21	1		*
W13-1	Tuff	H	27.58	21	1		*
W13-1	Tuff	H	34.47	21	1		*
W13-1	Tuff	H	41.37	21	1		*
W13-1	Tuff	H	48.26	20	1		*
W13-1	Tuff	H	55.16	20	1		*
W4-2	Lava	H	3.45	16	1		*
W4-2	Lava	H	6.89	15	1		*
W4-2	Lava	H	13.79	14	1		*
W4-2	Lava	H	20.68	14	1		*
W4-2	Lava	H	27.58	14	1		*
W4-2	Lava	H	34.47	13	1		*
W4-2	Lava	H	41.37	12	1		*
W4-2	Lava	H	48.26	12	1		*
W4-2	Lava	H	55.16	12	1		*

Continued on next page

Table E.7 – continued from previous page

Sample ID	Sample type	Alteration Intensity	P_{eff} (MPa)	ϕ (%)	ϕ_{SD} (%)	κ (m^2)	Notes
W18-1	Vesicular lava	FS	3.45	43	5		*
W18-1	Vesicular lava	FS	6.89	35	5		*
W18-1	Vesicular lava	FS	13.79	30	5		*
W18-1	Vesicular lava	FS	20.68	24	5		*
W18-1	Vesicular lava	FS	27.58	15	5		*
W18-1	Vesicular lava	FS	34.47	13	5		*
W19-1	Vesicular lava	FS	3.45	58	2		*
W19-1	Vesicular lava	FS	6.89	57	2		*
W19-1	Vesicular lava	FS	13.79	55	2		*
W19-1	Vesicular lava	FS	20.68	53	2		*
W19-1	Vesicular lava	FS	27.58	50	2		*
W19-1	Vesicular lava	FS	34.47	19	2		*

Table E.8: Porosity and permeability of samples used in Chapter 4 from Mt. Taranaki. Here, P_{eff}-effective hydrostatic pressure, ϕ-porosity, ϕ_{SD} -standard deviation of porosity, κ-permeability. Error on porosity, where not specified, and permeability is less than 5%. Alteration intensities of the samples are shown by FS-Fresh to slightly altered, M-moderately altered, and H-highly altered. Sampling locality is represented by S-summit dome area, BAF-block and ash flow deposits, and DA-debris avalanche deposits.

Sample ID	Sample type	Sampling locality	Alteration Intensity	P_{eff} (MPa)	ϕ (%)	ϕ_{SD} (%)	κ (m^2)
T1-1	Lava	S	M	0	16	1	
T1-1	Lava	S	M	1.79	14		8.74×10^{-14}
T1-1	Lava	S	M	2.45	14		8.80×10^{-14}
T1-1	Lava	S	M	3.2	14		8.77×10^{-14}
T1-1	Lava	S	M	3.82	14		8.83×10^{-14}
T1-1	Lava	S	M	4.54	14		8.80×10^{-14}
T1-1	Lava	S	M	5.22	14		8.83×10^{-14}
T2-1	Lava	S	M	0	21	1	
T2-1	Lava	S	M	2	21		9.32×10^{-13}

Continued on next page

Table E.8 – continued from previous page

Sample ID	Sample type	Sampling locality	Alteration Intensity	P_{eff} (MPa)	ϕ (%)	ϕ_{SD} (%)	κ (m^2)
T2-1	Lava	S	M	2.51	21		9.29×10^{-13}
T2-1	Lava	S	M	3.15	21		9.59×10^{-13}
T2-1	Lava	S	M	3.87	21		9.52×10^{-13}
T2-1	Lava	S	M	4.51	21		9.55×10^{-13}
T2-1	Lava	S	M	5.23	21		9.67×10^{-13}
T3-1	Lava	S	M	0	17	1	
T3-1	Lava	S	M	1.86	17		2.33×10^{-14}
T3-1	Lava	S	M	2.59	16		2.31×10^{-14}
T3-1	Lava	S	M	3.16	17		2.31×10^{-14}
T3-1	Lava	S	M	3.97	17		2.31×10^{-14}
T3-1	Lava	S	M	4.65	17		2.31×10^{-14}
T3-1	Lava	S	M	5.35	16		2.30×10^{-14}
T4-1	Lava	S	FS	0	32	1	
T4-1	Lava	S	FS	1.57	30		4.62×10^{-13}
T4-1	Lava	S	FS	2.44	31		4.42×10^{-13}
T4-1	Lava	S	FS	3.17	30		4.53×10^{-13}
T4-1	Lava	S	FS	3.82	30		4.47×10^{-13}
T4-1	Lava	S	FS	4.57	31		4.52×10^{-13}
T4-1	Lava	S	FS	5.19	31		4.41×10^{-13}
T5-1	Lava	S	M	0	13	1	
T5-1	Lava	S	M	1.74	12		4.42×10^{-14}
T5-1	Lava	S	M	2.38	12		4.41×10^{-14}
T5-1	Lava	S	M	3.1	12		4.37×10^{-14}
T5-1	Lava	S	M	3.75	12		4.30×10^{-14}
T5-1	Lava	S	M	4.57	12		4.21×10^{-14}
T5-1	Lava	S	M	5.21	12		4.40×10^{-14}
T6-1	Lava	BAF	FS	0	13	1	
T6-1	Lava	BAF	FS	1.92	13		1.90×10^{-15}
T6-1	Lava	BAF	FS	2.44	13		1.84×10^{-15}
T6-1	Lava	BAF	FS	3.17	13		1.81×10^{-15}
T6-1	Lava	BAF	FS	3.86	13		1.75×10^{-15}

Continued on next page

Table E.8 – continued from previous page

Sample ID	Sample type	Sampling locality	Alteration Intensity	P_{eff} (MPa)	ϕ (%)	ϕ_{SD} (%)	κ (m^2)
T6-1	Lava	BAF	FS	4.52	14		1.74×10^{-15}
T6-1	Lava	BAF	FS	5.34	13		1.69×10^{-15}
T7-1	Lava	BAF	FS	0	18	1	
T7-1	Lava	BAF	FS	1.61	17		7.74×10^{-14}
T7-1	Lava	BAF	FS	2.16	17		7.61×10^{-14}
T7-1	Lava	BAF	FS	2.8	17		7.63×10^{-14}
T7-1	Lava	BAF	FS	3.61	17		7.55×10^{-14}
T7-1	Lava	BAF	FS	4.21	17		7.55×10^{-14}
T7-1	Lava	BAF	FS	5.01	17		7.48×10^{-14}
T8-1	Lava	BAF	FS	0	8	0	
T8-1	Lava	BAF	FS	1.86	8		8.82×10^{-17}
T8-1	Lava	BAF	FS	2.3	8		8.86×10^{-17}
T8-1	Lava	BAF	FS	3.12	7		8.05×10^{-17}
T8-1	Lava	BAF	FS	3.91	8		7.96×10^{-17}
T8-1	Lava	BAF	FS	4.58	7		9.15×10^{-17}
T8-1	Lava	BAF	FS	5.36	7		7.89×10^{-17}
T9-1	Lava	BAF	M	0	14	1	
T9-1	Lava	BAF	M	1.84	12		4.27×10^{-16}
T9-1	Lava	BAF	M	2.49	11		4.00×10^{-16}
T9-1	Lava	BAF	M	3.13	11		3.74×10^{-16}
T9-1	Lava	BAF	M	3.83	11		3.57×10^{-16}
T9-1	Lava	BAF	M	4.61	11		3.38×10^{-16}
T9-1	Lava	BAF	M	5.19	11		3.27×10^{-16}
T10-1	Lava	BAF	FS	0	38	2	
T10-1	Lava	BAF	FS	1.86	36		2.94×10^{-12}
T10-1	Lava	BAF	FS	2.48	36		2.88×10^{-12}
T10-1	Lava	BAF	FS	3.25	36		2.74×10^{-12}
T10-1	Lava	BAF	FS	3.88	35		2.81×10^{-12}
T10-1	Lava	BAF	FS	4.59	36		2.82×10^{-12}
T10-1	Lava	BAF	FS	5.41	36		2.78×10^{-12}
T11-1	Lava	BAF	FS	0	12	0	

Continued on next page

Table E.8 – continued from previous page

Sample ID	Sample type	Sampling locality	Alteration Intensity	P_{eff} (MPa)	ϕ (%)	ϕ_{SD} (%)	κ (m^2)
T11-1	Lava	BAF	FS	1.89	7		4.13×10^{-16}
T11-1	Lava	BAF	FS	2.48	6		3.91×10^{-16}
T11-1	Lava	BAF	FS	3.17	7		3.70×10^{-16}
T11-1	Lava	BAF	FS	3.85	7		3.74×10^{-16}
T11-1	Lava	BAF	FS	4.56	7		3.63×10^{-16}
T11-1	Lava	BAF	FS	5.21	7		3.58×10^{-16}
T12-1	Lava	BAF	M	0	25	1	
T12-1	Lava	BAF	M	1.88	23		1.19×10^{-11}
T12-1	Lava	BAF	M	2.53	24		1.30×10^{-11}
T12-1	Lava	BAF	M	3.17	24		1.34×10^{-11}
T12-1	Lava	BAF	M	3.89	24		1.49×10^{-11}
T12-1	Lava	BAF	M	4.56	24		1.46×10^{-11}
T12-1	Lava	BAF	M	5.37	23		1.27×10^{-11}
T13-1	Lava	BAF	FS	0	16	1	
T13-1	Lava	BAF	FS	1.91	15		2.30×10^{-15}
T13-1	Lava	BAF	FS	2.48	16		2.26×10^{-15}
T13-1	Lava	BAF	FS	3.14	15		2.22×10^{-15}
T13-1	Lava	BAF	FS	4.02	15		2.15×10^{-15}
T13-1	Lava	BAF	FS	4.73	16		2.11×10^{-15}
T13-1	Lava	BAF	FS	5.36	15		2.07×10^{-15}
T14-1	Lava	DA	FS	0	13	0	
T14-1	Lava	DA	FS	1.89	7		3.37×10^{-17}
T14-1	Lava	DA	FS	2.42	7		2.01×10^{-17}
T14-1	Lava	DA	FS	3.05	7		1.58×10^{-17}
T14-1	Lava	DA	FS	3.82	7		1.31×10^{-17}
T14-1	Lava	DA	FS	4.73	7		1.10×10^{-17}
T14-1	Lava	DA	FS	5.35	7		9.26×10^{-18}
T15-1	Lava	DA	FS	0	5	0	
T15-1	Lava	DA	FS	1.9	3		1.90×10^{-18}
T15-1	Lava	DA	FS	2.48	4		1.79×10^{-18}
T15-1	Lava	DA	FS	3.3	4		1.19×10^{-18}

Continued on next page

Table E.8 – continued from previous page

Sample ID	Sample type	Sampling locality	Alteration Intensity	P_{eff} (MPa)	ϕ (%)	ϕ_{SD} (%)	κ (m^2)
T15-1	Lava	DA	FS	4	4		9.97×10^{-19}
T15-1	Lava	DA	FS	4.63	3		8.83×10^{-19}
T15-1	Lava	DA	FS	5.37	3		7.99×10^{-19}
T16-1	Lava	DA	FS	0	7	0	
T16-1	Lava	DA	FS	1.8	6		2.12×10^{-17}
T16-1	Lava	DA	FS	2.41	6		1.84×10^{-17}
T16-1	Lava	DA	FS	3.17	6		1.69×10^{-17}
T16-1	Lava	DA	FS	3.96	6		1.58×10^{-17}
T16-1	Lava	DA	FS	4.62	6		1.52×10^{-17}
T16-1	Lava	DA	FS	5.42	6		1.45×10^{-17}
T17-1	Lava	S	M	0	12	0	
T17-1	Lava	S	M	1.72	9		4.29×10^{-14}
T17-1	Lava	S	M	2.43	8		4.07×10^{-14}
T17-1	Lava	S	M	3.09	8		4.43×10^{-14}
T17-1	Lava	S	M	3.86	9		4.65×10^{-14}
T17-1	Lava	S	M	4.55	8		4.97×10^{-14}
T17-1	Lava	S	M	5.5	9		5.05×10^{-14}
T18-1	Lava	S	M	0	11	0	
T18-1	Lava	S	M	1.78	7		3.84×10^{-16}
T18-1	Lava	S	M	2.32	8		3.35×10^{-16}
T18-1	Lava	S	M	3.17	8		2.97×10^{-16}
T18-1	Lava	S	M	4.06	8		3.00×10^{-16}
T18-1	Lava	S	M	4.64	8		2.93×10^{-16}
T18-1	Lava	S	M	5.32	8		3.54×10^{-16}
T19-1	Lava	S	M	0	20	1	
T19-1	Lava	S	M	1.87	19		4.07×10^{-14}
T19-1	Lava	S	M	2.46	19		4.42×10^{-14}
T19-1	Lava	S	M	3.2	18		4.75×10^{-14}
T19-1	Lava	S	M	4.01	18		4.84×10^{-14}
T19-1	Lava	S	M	4.72	18		4.83×10^{-14}
T19-1	Lava	S	M	5.4	18		4.94×10^{-14}

Continued on next page

Table E.8 – continued from previous page

Sample ID	Sample type	Sampling locality	Alteration Intensity	P_{eff} (MPa)	ϕ (%)	ϕ_{SD} (%)	κ (m^2)
T20-1	Lava	S	H	0	28	3	
T20-1	Lava	S	H	1.99	27		2.21×10^{-13}
T20-1	Lava	S	H	2.57	26		2.07×10^{-13}
T20-1	Lava	S	H	3.22	27		2.04×10^{-13}
T20-1	Lava	S	H	3.84	26		2.10×10^{-13}
T20-1	Lava	S	H	4.63	26		2.08×10^{-13}
T20-1	Lava	S	H	5.26	26		2.08×10^{-13}
T21-1	Lava	S	M	0	29	1	
T21-1	Lava	S	M	1.78	27		2.11×10^{-12}
T21-1	Lava	S	M	2.58	26		1.95×10^{-12}
T21-1	Lava	S	M	3.13	26		1.95×10^{-12}
T21-1	Lava	S	M	3.94	27		2.17×10^{-12}
T21-1	Lava	S	M	4.61	27		2.09×10^{-12}
T21-1	Lava	S	M	5.33	27		2.17×10^{-12}
T22-1	Lava	S	M	0	9	0	
T22-1	Lava	S	M	1.9	9		5.45×10^{-16}
T22-1	Lava	S	M	2.44	8		5.02×10^{-16}
T22-1	Lava	S	M	3.26	8		5.04×10^{-16}
T22-1	Lava	S	M	3.9	8		4.99×10^{-16}
T22-1	Lava	S	M	4.6	8		4.89×10^{-16}
T22-1	Lava	S	M	5.38	8		4.95×10^{-16}
T23-1	Lava	S	M	0	19	1	
T23-1	Lava	S	M	1.89	18		7.05×10^{-13}
T23-1	Lava	S	M	2.46	18		7.10×10^{-13}
T23-1	Lava	S	M	3.18	17		7.16×10^{-13}
T23-1	Lava	S	M	3.99	17		7.15×10^{-13}
T23-1	Lava	S	M	4.73	17		7.16×10^{-13}
T23-1	Lava	S	M	5.45	17		7.22×10^{-13}
T24-1	Lava	S	M	0	12	0	
T24-1	Lava	S	M	1.78	13		1.49×10^{-14}
T24-1	Lava	S	M	2.36	13		1.60×10^{-14}

Continued on next page

Table E.8 – continued from previous page

Sample ID	Sample type	Sampling locality	Alteration Intensity	P_{eff} (MPa)	ϕ (%)	ϕ_{SD} (%)	κ (m^2)
T24-1	Lava	S	M	3.23	13		1.60×10^{-14}
T24-1	Lava	S	M	3.91	13		1.59×10^{-14}
T24-1	Lava	S	M	4.44	13		1.63×10^{-14}
T24-1	Lava	S	M	5.26	13		1.61×10^{-14}
T25-1	Lava	S	FS	0	14	1	
T25-1	Lava	S	FS	1.63	12		5.65×10^{-14}
T25-1	Lava	S	FS	2.03	12		5.59×10^{-14}
T25-1	Lava	S	FS	2.82	11		5.97×10^{-14}
T25-1	Lava	S	FS	3.33	11		5.87×10^{-14}
T25-1	Lava	S	FS	4.5	11		5.94×10^{-14}
T25-1	Lava	S	FS	5.33	11		6.06×10^{-14}
T26-1	Lava	BAF	FS	0	9	1	
T26-1	Lava	BAF	FS	1.94	6		8.94×10^{-17}
T26-1	Lava	BAF	FS	2.57	7		8.84×10^{-17}
T26-1	Lava	BAF	FS	3.27	7		7.87×10^{-17}
T26-1	Lava	BAF	FS	3.85	7		7.95×10^{-17}
T26-1	Lava	BAF	FS	4.45	7		7.20×10^{-17}
T26-1	Lava	BAF	FS	5.12	7		7.00×10^{-17}
T27-1	Lava	BAF	FS	0	8	0	
T27-1	Lava	BAF	FS	1.98	7		1.00×10^{-16}
T27-1	Lava	BAF	FS	2.35	7		1.04×10^{-16}
T27-1	Lava	BAF	FS	3.12	6		1.23×10^{-16}
T27-1	Lava	BAF	FS	3.72	7		1.24×10^{-16}
T27-1	Lava	BAF	FS	4.6	7		9.53×10^{-17}
T27-1	Lava	BAF	FS	5.16	7		8.07×10^{-17}
T28-1	Lava	BAF	FS	0	16	1	
T28-1	Lava	BAF	FS	1.91	16		3.72×10^{-14}
T28-1	Lava	BAF	FS	2.46	16		3.72×10^{-14}
T28-1	Lava	BAF	FS	3.1	16		3.70×10^{-14}
T28-1	Lava	BAF	FS	3.93	15		3.70×10^{-14}
T28-1	Lava	BAF	FS	4.58	15		3.68×10^{-14}

Continued on next page

Table E.8 – continued from previous page

Sample ID	Sample type	Sampling locality	Alteration Intensity	P_{eff} (MPa)	ϕ (%)	ϕ_{SD} (%)	κ (m^2)
T28-1	Lava	BAF	FS	5.35	15		3.69×10^{-14}
T29-1	Lava	BAF	FS	0	16	1	
T29-1	Lava	BAF	FS	1.92	16		1.09×10^{-13}
T29-1	Lava	BAF	FS	2.48	16		1.05×10^{-13}
T29-1	Lava	BAF	FS	3.09	16		1.05×10^{-13}
T29-1	Lava	BAF	FS	3.83	16		1.06×10^{-13}
T29-1	Lava	BAF	FS	4.65	15		9.75×10^{-14}
T29-1	Lava	BAF	FS	5.26	15		1.02×10^{-13}
T30-1	Lava	BAF	FS	0	12	1	
T30-1	Lava	BAF	FS	1.82	12		7.27×10^{-15}
T30-1	Lava	BAF	FS	2.48	11		7.26×10^{-15}
T30-1	Lava	BAF	FS	3.26	12		7.12×10^{-15}
T30-1	Lava	BAF	FS	3.96	12		7.13×10^{-15}
T30-1	Lava	BAF	FS	4.61	10		7.01×10^{-15}
T30-1	Lava	BAF	FS	5.31	11		6.97×10^{-15}
T31-1	Lava	BAF	FS	0	5	0	
T31-1	Lava	BAF	FS	1.87	6		1.43×10^{-16}
T31-1	Lava	BAF	FS	2.47	6		1.32×10^{-16}
T31-1	Lava	BAF	FS	3.14	6		1.21×10^{-16}
T31-1	Lava	BAF	FS	4.02	6		1.10×10^{-16}
T31-1	Lava	BAF	FS	4.68	6		1.04×10^{-16}
T31-1	Lava	BAF	FS	5.41	5		9.48×10^{-17}
T32-1	Lava	BAF	FS	0	19	1	
T32-1	Lava	BAF	FS	1.83	19		2.65×10^{-14}
T32-1	Lava	BAF	FS	2.44	19		2.64×10^{-14}
T32-1	Lava	BAF	FS	3.16	18		2.64×10^{-14}
T32-1	Lava	BAF	FS	3.86	18		2.62×10^{-14}
T32-1	Lava	BAF	FS	4.61	18		2.59×10^{-14}
T32-1	Lava	BAF	FS	5.31	18		2.59×10^{-14}
T33-1	Lava	BAF	FS	0	33	2	
T33-1	Lava	BAF	FS	1.88	32		1.10×10^{-12}

Continued on next page

Table E.8 – continued from previous page

Sample ID	Sample type	Sampling locality	Alteration Intensity	P_{eff} (MPa)	ϕ (%)	ϕ_{SD} (%)	κ (m^2)
T33-1	Lava	BAF	FS	2.49	32		1.11×10^{-12}
T33-1	Lava	BAF	FS	3.14	32		1.15×10^{-12}
T33-1	Lava	BAF	FS	4.82	31		1.09×10^{-12}
T33-1	Lava	BAF	FS	4.17	32		1.16×10^{-12}
T33-1	Lava	BAF	FS	4.8	31		1.16×10^{-12}
T34-1	Lava	BAF	FS	0	26	1	
T34-1	Lava	BAF	FS	1.81	25		5.40×10^{-13}
T34-1	Lava	BAF	FS	2.51	25		5.43×10^{-13}
T34-1	Lava	BAF	FS	3.22	25		5.36×10^{-13}
T34-1	Lava	BAF	FS	3.91	25		5.37×10^{-13}
T34-1	Lava	BAF	FS	4.71	25		5.37×10^{-13}
T34-1	Lava	BAF	FS	5.33	25		5.35×10^{-13}

E.7 Magnetic properties

Table E.9: Magnetic susceptibility of samples used in Chapter 3 from Whakaari. Here, χ_{lf}-volume-specific magnetic susceptibility measured at low frequency 0.46 kHz, χ_{hf}-volume-specific magnetic susceptibility measured at high frequency 4.6 kHz, χ_{lf-SD} and χ_{hf-SD} are the standard deviations of susceptibility measurements at low and high frequencies, respectively. Alteration intensities of the samples are shown by FS-Fresh to slightly altered, M-moderately altered, and H-highly altered.

Sample ID	Sample type	Alteration intensity	χ_{lf} (SI)	χ_{lf-SD} (SI)	χ_{hf} (SI)	χ_{hf-SD} (SI)
W1-1	Lava	FS	1.32×10^{-2}	2.20×10^{-5}	1.31×10^{-2}	1.70×10^{-5}
W1-2	Lava	FS	1.52×10^{-2}	3.90×10^{-5}	1.51×10^{-2}	3.00×10^{-5}
W2-1	Sulfur flow	FS	4.75×10^{-4}	2.00×10^{-6}	4.27×10^{-4}	1.00×10^{-6}
W2-2	Sulfur flow	FS	4.95×10^{-4}	1.00×10^{-6}	4.45×10^{-4}	1.00×10^{-6}
W3-1	Sulfur flow	FS	3.98×10^{-4}	2.00×10^{-6}	3.56×10^{-4}	1.00×10^{-6}
W3-2	Sulfur flow	FS	3.83×10^{-4}	2.00×10^{-6}	3.44×10^{-4}	0.00
W3-3	Sulfur flow	FS	3.50×10^{-4}	1.00×10^{-6}	3.13×10^{-4}	1.00×10^{-6}
W4-1	Breccia	H	1.24×10^{-3}	3.00×10^{-6}	1.08×10^{-3}	5.00×10^{-6}
W4-2	Lava	H	5.76×10^{-3}	1.80×10^{-5}	5.29×10^{-3}	3.00×10^{-5}
W4-3	Lava	H	7.51×10^{-3}	1.80×10^{-5}	6.89×10^{-3}	1.00×10^{-5}
W5-1	Tuff	M	9.64×10^{-4}	1.00×10^{-6}	8.96×10^{-4}	1.00×10^{-6}
W5-2	Tuff	M	9.12×10^{-4}	1.00×10^{-6}	8.44×10^{-4}	0.00
W5-3	Tuff	M	8.75×10^{-4}	2.00×10^{-6}	8.10×10^{-4}	3.00×10^{-6}
W6-1	Lava	M	8.31×10^{-3}	3.50×10^{-5}	8.20×10^{-3}	9.00×10^{-6}
W6-2	Lava	M	7.41×10^{-3}	1.40×10^{-5}	7.29×10^{-3}	2.60×10^{-5}

Continued on next page

Table E.9 – continued from previous page

Sample ID	Sample type	Alteration intensity	χ_{lf} (SI)	χ_{lf-SD} (SI)	χ_{hf} (SI)	χ_{hf-SD} (SI)
W6-3	Lava	M	1.29×10^{-2}	1.30×10^{-5}	1.29×10^{-2}	5.00×10^{-5}
W6-4	Lava	M	1.32×10^{-2}	2.00×10^{-5}	1.32×10^{-2}	1.50×10^{-5}
W6-5	Lava	M	1.17×10^{-2}	2.30×10^{-5}	1.16×10^{-2}	2.70×10^{-5}
W7-1	Lava	M	1.71×10^{-2}	2.40×10^{-5}	1.70×10^{-2}	1.80×10^{-5}
W7-2	Lava	M	1.65×10^{-2}	2.50×10^{-5}	1.64×10^{-2}	2.00×10^{-5}
W7-3	Lava	M	1.67×10^{-2}	2.30×10^{-5}	1.66×10^{-2}	1.70×10^{-5}
W8-1	Tuff	H	8.40×10^{-5}	1.00×10^{-6}	8.30×10^{-5}	0.00
W8-2	Tuff	H	4.00×10^{-5}	1.00×10^{-6}	4.10×10^{-5}	1.00×10^{-6}
W9-1	Breccia	H	1.64×10^{-3}	8.00×10^{-6}	1.60×10^{-3}	1.40×10^{-5}
W9-2	Breccia	H	2.86×10^{-3}	4.00×10^{-6}	2.77×10^{-3}	4.00×10^{-6}
W11-1	Tuff	H	3.30×10^{-4}	2.00×10^{-6}	3.04×10^{-4}	1.00×10^{-6}
W11-2	Tuff	H	3.05×10^{-4}	1.00×10^{-6}	2.70×10^{-4}	1.00×10^{-6}
W11-3	Tuff	H	3.31×10^{-4}	0.00	3.08×10^{-4}	0.00
W11-4	Tuff	H	2.19×10^{-4}	1.00×10^{-6}	1.96×10^{-4}	1.00×10^{-6}
W11-5	Tuff	H	2.55×10^{-4}	1.00×10^{-6}	2.33×10^{-4}	2.00×10^{-6}
W12-1	Breccia	H	1.10×10^{-2}	2.40×10^{-5}	9.31×10^{-3}	3.60×10^{-5}
W13-1	Tuff	H	7.30×10^{-5}	1.00×10^{-6}	6.10×10^{-5}	1.00×10^{-6}
W13-2	Tuff	H	7.50×10^{-5}	1.00×10^{-6}	6.50×10^{-5}	1.00×10^{-6}
W14-1	Breccia	M	2.78×10^{-3}	7.00×10^{-6}	2.76×10^{-3}	9.00×10^{-6}
W15-1	Tuff	H	5.76×10^{-4}	2.00×10^{-6}	5.18×10^{-4}	2.00×10^{-6}

Continued on next page

Table E.9 – continued from previous page

Sample ID	Sample type	Alteration intensity	χ_{lf} (SI)	χ_{lf-SD} (SI)	χ_{hf} (SI)	χ_{hf-SD} (SI)
W18-1	Vesicular lava	FS	1.78×10^{-4}	1.00×10^{-6}	1.73×10^{-4}	1.00×10^{-6}
W18-3	Vesicular lava	FS	1.23×10^{-4}	1.00×10^{-6}	1.20×10^{-4}	1.00×10^{-6}
W18-4	Vesicular lava	FS	2.48×10^{-4}	1.00×10^{-6}	2.38×10^{-4}	1.00×10^{-6}
W19-1	Vesicular lava	FS	2.39×10^{-3}	1.30×10^{-5}	2.28×10^{-3}	1.20×10^{-5}
W19-2	Vesicular lava	FS	3.39×10^{-3}	1.70×10^{-5}	3.24×10^{-3}	2.00×10^{-5}
W20-1	Vesicular lava	FS	1.21×10^{-4}	0.00	1.19×10^{-4}	1.00×10^{-6}
WS-1	Sulfur flow	FS	-1.10×10^{-5}	0.00	-1.10×10^{-5}	0.00

Table E.10: Magnetization of samples used in Chapter 3 from Whakaari. Here, NRM-natural remanent magnetization intensity, M_i-induced magnetization intensity computed from magnetic susceptibility, and M- total magnetization intensity of the samples. NRM_{SD}, M_{i-SD}, and M_{SD} are the respective standard deviations in magnetization. Alteration intensities of the samples are shown by FS-Fresh to slightly altered, M-moderately altered, and H-highly altered.

Sample ID	Sample type	Alteration intensity	NRM (A/m)	NRM_{SD} (A/m)	M_i (A/m)	M_{i-SD} (A/m)	M (A/m)	M_{SD} (A/m)
W1-1	Lava	FS	1.94	0.02	0.56	0.00	2.50	0.02
W1-2	Lava	FS	3.00	0.03	0.64	0.00	3.64	0.03
W2-1	Sulfur flow	FS	0.01	0.00	0.02	0.00	0.03	0.00
W2-2	Sulfur flow	FS	0.01	0.00	0.02	0.00	0.03	0.00

Continued on next page

Table E.10 – continued from previous page

Sample ID	Sample type	Alteration intensity	NRM (A/m)	NRM_{SD} (A/m)	M_i (A/m)	M_{i-SD} (A/m)	M (A/m)	M_{SD} (A/m)
W3-1	Sulfur flow	FS	0.01	0.00	0.02	0.00	0.02	0.00
W3-2	Sulfur flow	FS	0.01	0.00	0.02	0.00	0.02	0.00
W3-3	Sulfur flow	FS	0.01	0.00	0.01	0.00	0.02	0.00
W4-1	Breccia	H	2.47	0.02	0.05	0.00	2.52	0.02
W4-2	Lava	H	20.61	0.00	0.23	0.00	20.84	0.00
W4-3	Lava	H	37.71	0.00	0.31	0.00	38.02	0.00
W5-1	Tuff	M	1.42	0.01	0.04	0.00	1.46	0.01
W5-2	Tuff	M	0.76	0.00	0.04	0.00	0.80	0.00
W5-3	Tuff	M	1.01	0.01	0.04	0.00	1.04	0.01
W6-1	Lava	M	48.74	0.49	0.35	0.00	49.09	0.49
W6-2	Lava	M	6.38	0.06	0.31	0.00	6.69	0.06
W6-3	Lava	M	53.68	0.00	0.55	0.00	54.22	0.00
W6-4	Lava	M	66.12	0.66	0.56	0.00	66.68	0.66
W6-5	Lava	M	3.37	0.00	0.50	0.00	3.86	0.00
W7-1	Lava	M	47.70	0.00	0.73	0.00	48.42	0.00
W7-2	Lava	M	45.83	0.92	0.70	0.00	46.53	0.92
W7-3	Lava	M	3.00	0.00	0.71	0.00	3.70	0.00
W8-1	Tuff	H	0.02	0.00	0.00	0.00	0.02	0.00
W8-2	Tuff	H	0.01	0.00	0.00	0.00	0.01	0.00
W9-1	Breccia	H	0.01	0.00	0.07	0.00	0.08	0.00

Continued on next page

Table E.10 – continued from previous page

Sample ID	Sample type	Alteration intensity	NRM (A/m)	NRM_{SD} (A/m)	M_i (A/m)	M_{i-SD} (A/m)	M (A/m)	M_{SD} (A/m)
W9-2	Breccia	H	0.02	0.00	0.12	0.00	0.14	0.00
W11-1	Tuff	H	0.09	0.00	0.01	0.00	0.10	0.00
W11-2	Tuff	H	0.05	0.00	0.01	0.00	0.06	0.00
W11-3	Tuff	H	0.08	0.00	0.01	0.00	0.10	0.00
W11-4	Tuff	H	0.08	0.00	0.01	0.00	0.09	0.00
W11-5	Tuff	H	0.11	0.00	0.01	0.00	0.12	0.00
W12-1	Breccia	H	2.48	0.00	0.43	0.00	2.91	0.00
W13-1	Tuff	H	0.20	0.00	0.00	0.00	0.21	0.00
W13-2	Tuff	H	0.05	0.00	0.00	0.00	0.05	0.00
W14-1	Breccia	M	1.13	0.01	0.12	0.00	1.24	0.01
W15-1	Tuff	H	0.17	0.00	0.02	0.00	0.19	0.00
W18-1	Vesicular lava	FS	0.05	0.00	0.01	0.00	0.06	0.00
W18-3	Vesicular lava	FS	0.04	0.00	0.01	0.00	0.04	0.00
W18-4	Vesicular lava	FS	0.08	0.00	0.01	0.00	0.09	0.00
W19-1	Vesicular lava	FS	2.73	0.00	0.10	0.00	2.83	0.00
W19-2	Vesicular lava	FS	4.04	0.00	0.14	0.00	4.18	0.00
W20-1	Vesicular lava	FS	0.03	0.00	0.01	0.00	0.04	0.00
WS-1	Sulfur flow	FS	0.00	0.00	0.00	0.00	0.00	0.00

Table E.11: Alternating field demagnetization of variably altered lavas used in Chapter 3 from Whakaari. Here, NRM-natural remanent magnetization intensity, NRM/NRM$_{max}$-the ratio of remaining natural remanent magnetization of the sample after demagnetization to its initial natural remanent magnetization. Alteration intensities of the samples are shown by FS-Fresh to slightly altered, M-moderately altered, and H-highly altered.

Sample ID	Sample type	Alteration intensity	Peak alternating field (mT)	NRM (A/m)	NRM/NRM$_{max}$
W1-1	Lava	FS	0	1.94	1.00
W1-1	Lava	FS	5	1.13	0.58
W1-1	Lava	FS	10	0.48	0.24
W1-1	Lava	FS	20	0.33	0.17
W1-1	Lava	FS	30	0.31	0.16
W1-1	Lava	FS	40	0.20	0.10
W1-1	Lava	FS	50	0.17	0.09
W1-1	Lava	FS	60	0.14	0.07
W1-1	Lava	FS	70	0.13	0.06
W1-1	Lava	FS	80	0.10	0.05
W4-2	Lava	H	0	20.61	1.00
W4-2	Lava	H	5	17.63	0.86
W4-2	Lava	H	10	15.73	0.76
W4-2	Lava	H	20	11.07	0.54
W4-2	Lava	H	30	7.90	0.38
W4-2	Lava	H	40	3.92	0.19
W4-2	Lava	H	50	2.22	0.11

Continued on next page

Table E.11 – continued from previous page

Sample ID	Sample type	Alteration intensity	Peak alternating field (mT)	NRM (A/m)	NRM/NRM$_{max}$
W4-2	Lava	H	60	1.28	0.06
W4-2	Lava	H	70	0.79	0.04
W4-2	Lava	H	80	0.62	0.03
W6-4	Lava	M	0	66.12	1.00
W6-4	Lava	M	5	59.68	0.90
W6-4	Lava	M	10	50.53	0.76
W6-4	Lava	M	20	33.78	0.51
W6-4	Lava	M	30	21.83	0.33
W6-4	Lava	M	40	13.05	0.20
W6-4	Lava	M	50	8.38	0.13
W6-4	Lava	M	60	5.51	0.08
W6-4	Lava	M	70	3.83	0.06
W6-4	Lava	M	80	2.83	0.04

Table E.12: Magnetic susceptibility of samples used in Chapter 4 from Mt. Taranaki. Here, χ_{lf}-volume-specific magnetic susceptibility measured at low frequency 0.46 kHz, χ_{hf}-volume-specific magnetic susceptibility measured at high frequency 4.6 kHz, χ_{lf-SD} and χ_{hf-SD} are the standard deviations of susceptibility measurements at low and high frequencies, respectively. Alteration intensities of the samples are shown by FS-Fresh to slightly altered, M-moderately altered, and H-highly altered. Sampling locality is represented by S-summit dome area, BAF-block and ash flow deposits, and DA-debris avalanche deposits.

Sample ID	Sample type	Sampling location	Alteration intensity	χ_{lf} (SI)	χ_{lf-SD} (SI)	χ_{hf} (SI)	χ_{hf-SD} (SI)
T1-1	Lava	S	M	1.72×10^{-2}	9.00×10^{-6}	1.72×10^{-2}	4.20×10^{-5}
T2-1	Lava	S	M	8.06×10^{-3}	3.50×10^{-5}	8.02×10^{-3}	4.20×10^{-5}
T3-1	Lava	S	M	2.02×10^{-2}	5.50×10^{-5}	2.02×10^{-2}	3.70×10^{-5}
T4-1	Lava	S	FS	9.18×10^{-3}	2.20×10^{-5}	9.14×10^{-3}	2.30×10^{-5}
T5-1	Lava	S	M	1.21×10^{-2}	1.90×10^{-5}	1.20×10^{-2}	2.90×10^{-5}
T6-1	Lava	BAF	FS	4.46×10^{-2}	5.60×10^{-5}	4.43×10^{-2}	1.10×10^{-5}
T7-1	Lava	BAF	FS	3.25×10^{-2}	7.20×10^{-5}	3.13×10^{-2}	4.50×10^{-5}
T8-1	Lava	BAF	FS	7.19×10^{-2}	2.12×10^{-4}	7.15×10^{-2}	3.50×10^{-5}
T9-1	Lava	BAF	M	3.72×10^{-2}	5.70×10^{-5}	3.71×10^{-2}	6.40×10^{-5}
T10-1	Lava	BAF	FS	6.07×10^{-3}	1.40×10^{-5}	5.89×10^{-3}	2.30×10^{-5}
T11-1	Lava	BAF	FS	3.42×10^{-2}	5.20×10^{-5}	3.40×10^{-2}	6.20×10^{-5}
T12-1	Lava	BAF	M	4.01×10^{-2}	5.50×10^{-5}	3.96×10^{-2}	4.00×10^{-5}
T13-1	Lava	BAF	FS	6.24×10^{-2}	1.26×10^{-4}	6.20×10^{-2}	1.01×10^{-4}
T14-1	Lava	DA	FS	4.81×10^{-2}	3.70×10^{-5}	4.79×10^{-2}	4.60×10^{-5}
T15-1	Lava	DA	FS	9.08×10^{-2}	1.45×10^{-4}	9.04×10^{-2}	1.65×10^{-4}
T16-1	Lava	DA	FS	6.14×10^{-2}	7.10×10^{-5}	6.14×10^{-2}	1.98×10^{-4}

Continued on next page

Table E.12 – continued from previous page

Sample ID	Sample type	Sampling location	Alteration intensity	χ_{lf} (SI)	χ_{lf-SD} (SI)	χ_{hf} (SI)	χ_{hf-SD} (SI)
T17-1	Lava	S	M	8.28×10^{-4}	4.00×10^{-6}	8.09×10^{-4}	1.00×10^{-6}
T18-1	Lava	S	M	4.61×10^{-2}	6.00×10^{-5}	4.61×10^{-2}	7.10×10^{-5}
T19-1	Lava	S	M	1.54×10^{-3}	1.10×10^{-5}	1.53×10^{-3}	8.00×10^{-6}
T20-1	Lava	S	H	4.42×10^{-4}	2.00×10^{-6}	4.22×10^{-4}	1.00×10^{-6}
T21-1	Lava	S	M	5.62×10^{-3}	1.40×10^{-5}	5.59×10^{-3}	3.00×10^{-5}
T22-1	Lava	S	M	4.15×10^{-2}	6.60×10^{-5}	4.15×10^{-2}	8.30×10^{-5}
T23-1	Lava	S	M	9.59×10^{-3}	1.30×10^{-5}	9.60×10^{-3}	5.20×10^{-5}
T24-1	Lava	S	M	2.54×10^{-2}	7.50×10^{-5}	2.54×10^{-2}	7.70×10^{-5}
T25-1	Lava	S	FS	3.36×10^{-3}	4.00×10^{-6}	3.34×10^{-3}	7.00×10^{-6}
T26-1	Lava	BAF	FS	6.15×10^{-2}	3.70×10^{-5}	6.14×10^{-2}	9.00×10^{-5}
T27-1	Lava	BAF	FS	8.23×10^{-2}	1.08×10^{-4}	8.18×10^{-2}	2.29×10^{-4}
T28-1	Lava	BAF	FS	4.50×10^{-2}	3.90×10^{-5}	4.48×10^{-2}	3.30×10^{-5}
T29-1	Lava	BAF	FS	5.02×10^{-2}	7.50×10^{-5}	4.97×10^{-2}	3.60×10^{-5}
T30-1	Lava	BAF	FS	4.78×10^{-2}	9.30×10^{-5}	4.75×10^{-2}	8.80×10^{-5}
T31-1	Lava	BAF	FS	5.46×10^{-2}	1.21×10^{-4}	5.43×10^{-2}	5.80×10^{-5}
T32-1	Lava	BAF	FS	3.78×10^{-2}	7.50×10^{-5}	3.76×10^{-2}	7.80×10^{-5}
T33-1	Lava	BAF	FS	3.44×10^{-2}	1.90×10^{-5}	3.38×10^{-2}	2.80×10^{-5}
T34-1	Lava	BAF	FS	4.20×10^{-2}	5.70×10^{-5}	4.16×10^{-2}	7.60×10^{-5}

Table E.13: Magnetization of samples used in Chapter 4 from Mt. Taranaki. Here, NRM-natural remanent magnetization intensity, M_i-induced magnetization intensity computed from magnetic susceptibility, and M- total magnetization intensity of the samples. NRM_{SD}, M_{i-SD}, and M_{SD} are the respective standard deviations in magnetization. Alteration intensities of the samples are shown by FS-Fresh to slightly altered, M-moderately altered, and H-highly altered. Sampling locality is represented by S-near summit dome, BAF-block and ash flows, and DA-debris avalanche deposits.

Sample ID	Sample type	Sampling location	Alteration intensity	NRM (A/m)	NRM_{SD} (A/m)	M_i (A/m)	M_{i-SD} (A/m)	M (A/m)	M_{SD} (A/m)
T1-1	Lava	S	M	3.53	0.00	0.75	0.00	4.28	0.00
T2-1	Lava	S	M	30.64	0.31	0.35	0.00	30.99	0.31
T3-1	Lava	S	M	3.71	0.04	0.89	0.00	4.59	0.04
T4-1	Lava	S	FS	1.60	0.02	0.40	0.00	2.00	0.02
T5-1	Lava	S	M	13.86	0.14	0.53	0.00	14.39	0.14
T6-1	Lava	BAF	FS	7.72	0.08	1.95	0.00	9.67	0.08
T7-1	Lava	BAF	FS	8.50	0.00	1.40	0.00	9.90	0.00
T8-1	Lava	BAF	FS	1.86	0.02	3.14	0.01	5.00	0.02
T9-1	Lava	BAF	M	2.91	0.00	1.63	0.00	4.54	0.00
T10-1	Lava	BAF	FS	4.78	0.00	0.26	0.00	5.04	0.00
T11-1	Lava	BAF	FS	10.43	0.00	1.49	0.00	11.92	0.00
T12-1	Lava	BAF	M	9.06	0.09	1.74	0.00	10.81	0.09
T13-1	Lava	BAF	FS	22.39	0.00	2.72	0.00	25.11	0.00
T14-1	Lava	DA	FS	0.86	0.01	2.10	0.00	2.97	0.01
T15-1	Lava	DA	FS	1.29	0.01	3.97	0.01	5.26	0.01
T16-1	Lava	DA	FS	5.19	0.00	2.69	0.01	7.88	0.01

Continued on next page

Table E.13 – continued from previous page

Sample ID	Sample type	Sampling location	Alteration intensity	NRM (A/m)	NRM_{SD} (A/m)	M_i (A/m)	M_{i-SD} (A/m)	M (A/m)	M_{SD} (A/m)
T17-1	Lava	S	M	0.22	0.00	0.04	0.00	0.26	0.00
T18-1	Lava	S	M	2.83	0.00	2.02	0.00	4.85	0.00
T19-1	Lava	S	M	0.22	0.00	0.07	0.00	0.28	0.00
T20-1	Lava	S	H	0.34	0.00	0.02	0.00	0.36	0.00
T21-1	Lava	S	M	4.57	0.05	0.25	0.00	4.82	0.05
T22-1	Lava	S	M	2.69	0.03	1.82	0.00	4.51	0.03
T23-1	Lava	S	M	4.67	0.05	0.42	0.00	5.09	0.05
T24-1	Lava	S	M	6.46	0.07	1.11	0.00	7.57	0.07
T25-1	Lava	S	FS	9.85	0.10	0.15	0.00	10.00	0.10
T26-1	Lava	BAF	FS	22.94	0.23	2.69	0.00	25.63	0.23
T27-1	Lava	BAF	FS	11.58	0.12	3.59	0.01	15.17	0.12
T28-1	Lava	BAF	FS	12.58	0.00	1.97	0.00	14.55	0.00
T29-1	Lava	BAF	FS	10.87	0.00	2.19	0.00	13.06	0.00
T30-1	Lava	BAF	FS	8.80	0.09	2.09	0.00	10.88	0.09
T31-1	Lava	BAF	FS	2.34	0.00	2.39	0.00	4.72	0.00
T32-1	Lava	BAF	FS	3.82	0.04	1.65	0.00	5.47	0.04
T33-1	Lava	BAF	FS	1.44	0.01	1.50	0.00	2.94	0.01
T34-1	Lava	BAF	FS	1.87	0.02	1.83	0.00	3.70	0.02

E.8 Elastic properties

Table E.14: Elastic properties of samples used in Chapter 2 from Whakaari. Here, P_c-confining pressure, P_p-pore pressure,P_{eff}-effective hydrostatic pressure, V_p-P-wave velocity, V_s-S-wave velocity, and E-Young's modulus. V_{p-SD}, V_{s-SD}, and E_{SD} are standard deviations in P-wave velocity, S-wave velocity, and Young's modulus. Alteration intensities of the samples are shown by FS-Fresh to slightly altered, M-moderately altered, and H-highly altered.

Sample ID	Sample type	Alteration intensity	P_c (MPa)	P_p (MPa)	P_{eff} (MPa)	V_p (km/s)	V_{p-SD} (km/s)	V_s (km/s)	V_{s-SD} (km/s)	E (GPa)	E_{SD} (GPa)
W1-1	Lava	FS	0.0	0.0	0.0	5.15	0.01	3.08	0.02	60.6	3
W1-2	Lava	FS	0.0	0.0	0.0	5.25	0.01	3.10	0.01	62.1	3
W2-1	Sulfur flow	FS	0.0	0.0	0.0	2.66	0.00	1.56	0.00	11.6	1
W2-2	Sulfur flow	FS	0.0	0.0	0.0	2.56	0.01	1.51	0.01	10.7	1
W3-1	Sulfur flow	FS	0.0	0.0	0.0	2.85	0.01	1.66	0.01	13.1	1
W3-2	Sulfur flow	FS	0.0	0.0	0.0	2.58	0.00	1.54	0.00	10.8	1
W3-3	Sulfur flow	FS	0.0	0.0	0.0	2.79	0.01	1.75	0.01	13.5	1
W3-4	Sulfur flow	FS	0.0	0.0	0.0	2.48	0.03	1.40	0.01	9.1	0
W4-1	Breccia	H	0.0	0.0	0.0	2.22	0.01	1.31	0.01	6.7	0
W4-2	Lava	H	0.0	0.0	0.0	3.76	0.02	2.13	0.01	23.6	1
W4-3	Lava	H	0.0	0.0	0.0	4.30	0.01	2.38	0.01	31.8	2
W5-1	Tuff	M	0.0	0.0	0.0	2.39	0.01	1.49	0.00	8.0	0
W5-2	Tuff	M	0.0	0.0	0.0	2.42	0.00	1.55	0.00	8.4	0
W5-3	Tuff	M	0.0	0.0	0.0	2.61	0.01	1.61	0.01	9.5	0
W5-5	Tuff	M	0.0	0.0	0.0	2.59	0.01	1.62	0.00	9.5	0

Continued on next page

Table E.14 – continued from previous page

Sample ID	Sample type	Alteration intensity	P_c (MPa)	P_p (MPa)	P_{eff} (MPa)	V_p (km/s)	V_{p-SD} (km/s)	V_s (km/s)	V_{s-SD} (km/s)	E (GPa)	E_{SD} (GPa)
W5-6	Tuff	M	0.0	0.0	0.0	2.83	0.01	1.78	0.00	13.3	1
W6-1	Lava	M	0.0	0.0	0.0	4.33	0.02	2.51	0.01	35.3	2
W6-2	Lava	M	0.0	0.0	0.0	4.28	0.01	2.55	0.00	35.4	2
W6-3	Lava	M	0.0	0.0	0.0	4.43	0.01	2.56	0.01	40.3	2
W6-4	Lava	M	0.0	0.0	0.0	4.63	0.01	3.04	0.01	51.5	3
W6-5	Lava	M	0.0	0.0	0.0	4.30	0.01	2.60	0.01	40.1	2
W7-1	Lava	M	0.0	0.0	0.0	4.08	0.06	2.47	0.04	34.5	2
W7-2	Lava	M	0.0	0.0	0.0	4.43	0.01	2.71	0.00	40.7	2
W7-3	Lava	M	0.0	0.0	0.0	4.37	0.02	2.67	0.01	39.4	2
W8-1	Tuff	H	0.0	0.0	0.0	3.18	0.03	1.90	0.01	16.2	1
W8-2	Tuff	H	0.0	0.0	0.0	3.41	0.01	2.19	0.01	19.3	1
W9-1	Breccia	H	0.0	0.0	0.0	3.04	0.01	1.88	0.01	17.9	1
W9-2	Breccia	H	0.0	0.0	0.0	2.41	0.00	1.50	0.00	10.9	1
W11-1	Tuff	H	0.0	0.0	0.0	2.97	0.03	1.85	0.02	11.3	1
W11-2	Tuff	H	0.0	0.0	0.0	2.00	0.01	1.24	0.01	5.3	0
W11-3	Tuff	H	0.0	0.0	0.0	3.44	0.01	2.12	0.01	18.2	1
W11-4	Tuff	H	0.0	0.0	0.0	3.39	0.01	1.72	0.00	11.5	1
W11-5	Tuff	H	0.0	0.0	0.0	3.40	0.02	1.99	0.01	15.6	1
W12-1	Breccia	H	0.0	0.0	0.0	2.95	0.03	1.71	0.01	12.8	1
W13-1	Tuff	H	0.0	0.0	0.0	3.54	0.06	2.16	0.04	20.2	1

Continued on next page

Table E.14 – continued from previous page

Sample ID	Sample type	Alteration intensity	P_c (MPa)	P_p (MPa)	P_{eff} (MPa)	V_p (km/s)	V_{p-SD} (km/s)	V_s (km/s)	V_{s-SD} (km/s)	E (GPa)	E_{SD} (GPa)
W13-2	Tuff	H	0.0	0.0	0.0	3.86	0.01	2.33	0.01	22.2	1
W14-1	Breccia	M	0.0	0.0	0.0	2.54	0.02	1.67	0.01	10.0	1
W15-1	Tuff	H	0.0	0.0	0.0	2.55	0.01	1.58	0.01	9.3	0
W18-1	Vesicular lava	FS	0.0	0.0	0.0	2.57	0.01	1.61	0.00	5.6	0
W18-3	Vesicular lava	FS	0.0	0.0	0.0	2.21	0.02	1.36	0.01	3.0	0
W18-4	Vesicular lava	FS	0.0	0.0	0.0	2.70	0.01	1.58	0.01	6.7	0
W19-1	Vesicular lava	FS	0.0	0.0	0.0	3.83	0.01	2.13	0.00	12.2	1
W19-2	Vesicular lava	FS	0.0	0.0	0.0	3.90	0.01	2.22	0.01	15.6	1
W20-1	Vesicular lava	FS	0.0	0.0	0.0	2.35	0.01	1.41	0.01	3.4	0
WS-1	Sulfur flow	FS	0.0	0.0	0.0	2.34	0.00	1.48	0.00	9.6	0
W1-1	Lava	FS	6.9	0.0	6.9	5.33	0.01	3.08	0.00	62.8	3
W1-1	Lava	FS	5.2	0.0	5.2	5.33	0.01	3.07	0.01	62.5	3
W1-1	Lava	FS	3.4	0.0	3.4	5.34	0.01	3.06	0.00	62.1	3
W1-1	Lava	FS	1.7	0.0	1.7	5.32	0.01	3.06	0.01	61.9	3
W1-1	Lava	FS	55.2	3.4	51.7	5.43	0.01	3.09	0.01		
W1-1	Lava	FS	48.3	3.4	44.8	5.43	0.01	3.09	0.01		
W1-1	Lava	FS	41.4	3.4	37.9	5.42	0.01	3.08	0.00		
W1-1	Lava	FS	34.5	3.4	31.0	5.40	0.01	3.07	0.01		
W1-1	Lava	FS	27.6	3.4	24.1	5.41	0.01	3.07	0.01	63.14	3
W1-1	Lava	FS	24.1	3.4	20.7	5.41	0.01	3.07	0.00	63.14	3

Continued on next page

Table E.14 – continued from previous page

Sample ID	Sample type	Alteration intensity	P_c (MPa)	P_p (MPa)	P_{eff} (MPa)	V_p (km/s)	V_{p-SD} (km/s)	V_s (km/s)	V_{s-SD} (km/s)	E (GPa)	E_{SD} (GPa)
W1-1	Lava	FS	20.7	3.4	17.2	5.40	0.01	3.07	0.00	63.08	3
W1-1	Lava	FS	17.2	3.4	13.8	5.39	0.01	3.06	0.00	62.72	3
W1-1	Lava	FS	13.8	3.4	10.3	5.39	0.01	3.05	0.00	62.42	3
W1-1	Lava	FS	10.3	3.4	6.9	5.37	0.01	3.05	0.00	62.29	3
W1-1	Lava	FS	6.9	3.4	3.4	5.37	0.01	3.04	0.00	61.86	3
W1-1	Lava	FS	5.2	3.4	1.7	5.35	0.01	3.03	0.01	61.43	3
W6-1	Lava	M	6.9	0.0	6.9	4.38	0.02	2.58	0.01	38.21	2
W6-1	Lava	M	3.4	0.0	3.4	4.34	0.03	2.54	0.01	36.78	2
W6-1	Lava	M	55.2	3.4	51.7	4.86	0.02	2.52	0.01		
W6-1	Lava	M	51.7	3.4	48.3	4.84	0.02	2.52	0.01		
W6-1	Lava	M	44.8	3.4	41.4	4.84	0.02	2.51	0.01		
W6-1	Lava	M	37.9	3.4	34.5	4.81	0.02	2.49	0.01		
W6-1	Lava	M	31.0	3.4	27.6	4.78	0.02	2.48	0.01	38.87	2
W6-1	Lava	M	24.1	3.4	20.7	4.77	0.02	2.46	0.01	38.33	2
W6-1	Lava	M	17.2	3.4	13.8	4.74	0.02	2.42	0.01	37.23	2
W6-1	Lava	M	10.3	3.4	6.9	4.66	0.02	2.37	0.01	35.76	2
W6-1	Lava	M	6.9	3.4	3.4	4.62	0.02	2.35	0.01	34.93	2
W4-3	Lava	H	6.9	0.0	6.9	4.39	0.02	2.50	0.01	34.61	2
W4-3	Lava	H	3.4	0.0	3.4	4.31	0.01	2.42	0.01	32.68	2
W4-3	Lava	H	55.2	3.4	51.7	4.96	0.01	2.57	0.01		

Continued on next page

Table E.14 – continued from previous page

Sample ID	Sample type	Alteration intensity	P_c (MPa)	P_p (MPa)	P_{eff} (MPa)	V_p (km/s)	V_{p-SD} (km/s)	V_s (km/s)	V_{s-SD} (km/s)	E (GPa)	E_{SD} (GPa)
W4-3	Lava	H	51.7	3.4	48.3	4.95	0.01	2.55	0.01		
W4-3	Lava	H	44.8	3.4	41.4	4.92	0.01	2.52	0.01		
W4-3	Lava	H	37.9	3.4	34.5	4.92	0.01	2.49	0.01		
W4-3	Lava	H	31.0	3.4	27.6	4.86	0.01	2.46	0.01	37.31	2
W4-3	Lava	H	24.1	3.4	20.7	4.80	0.01	2.45	0.01	36.9	2
W4-3	Lava	H	17.2	3.4	13.8	4.78	0.01	2.41	0.01	35.86	2
W4-3	Lava	H	10.3	3.4	6.9	4.69	0.01	2.44	0.01	36.34	2
W4-3	Lava	H	6.9	3.4	3.4	4.64	0.01	2.41	0.01	35.47	2
W5-5	Tuff	M	6.9	0.0	6.9	2.67	0.01	1.64	0.00	10.31	1
W5-5	Tuff	M	5.2	0.0	5.2	2.67	0.01	1.64	0.00	10.31	1
W5-5	Tuff	M	3.4	0.0	3.4	2.66	0.01	1.64	0.00	10.25	1
W5-5	Tuff	M	1.7	0.0	1.7	2.65	0.01	1.63	0.00	10.15	1
W5-5	Tuff	M	55.2	3.4	51.7	2.86	0.01	1.39	0.00		
W5-5	Tuff	M	48.3	3.4	44.8	2.83	0.01	1.39	0.00		
W5-5	Tuff	M	41.4	3.4	37.9	2.84	0.01	1.45	0.00		
W5-5	Tuff	M	34.5	3.4	31.0	2.85	0.01	1.47	0.00		
W5-5	Tuff	M	27.6	3.4	24.1	2.86	0.01	1.48	0.00		
W5-5	Tuff	M	24.1	3.4	20.7	2.86	0.01	1.48	0.00		
W5-5	Tuff	M	20.7	3.4	17.2	2.87	0.01	1.47	0.00		
W5-5	Tuff	M	17.2	3.4	13.8	2.86	0.01	1.47	0.00	11.26	1

Continued on next page

Table E.14 – continued from previous page

Sample ID	Sample type	Alteration intensity	P_c (MPa)	P_p (MPa)	P_{eff} (MPa)	V_p (km/s)	V_{p-SD} (km/s)	V_s (km/s)	V_{s-SD} (km/s)	E (GPa)	E_{SD} (GPa)
W5-5	Tuff	M	13.8	3.4	10.3	2.86	0.01	1.47	0.00	11.26	1
W5-5	Tuff	M	10.3	3.4	6.9	2.86	0.01	1.47	0.00	11.26	1
W5-5	Tuff	M	6.9	3.4	3.4	2.84	0.01	1.46	0.00	11.09	1
W5-5	Tuff	M	5.2	3.4	1.7	2.82	0.01	1.46	0.00	11.06	1
W11-4	Tuff	H	6.9	0.0	6.9	3.55	0.01	2.11	0.00	15.99	1
W11-4	Tuff	H	5.2	0.0	5.2	3.54	0.01	2.04	0.01	15.24	1
W11-4	Tuff	H	3.4	0.0	3.4	3.47	0.01	2.00	0.01	14.65	1
W11-4	Tuff	H	1.7	0.0	1.7	3.43	0.01	1.95	0.01	14.04	1
W11-4	Tuff	H	55.2	3.4	51.7	3.78	0.01	1.82	0.01		
W11-4	Tuff	H	48.3	3.4	44.8	3.74	0.01	1.83	0.01		
W11-4	Tuff	H	41.4	3.4	37.9	3.74	0.01	1.81	0.00		
W11-4	Tuff	H	34.5	3.4	31.0	3.73	0.01	1.80	0.01		
W11-4	Tuff	H	27.6	3.4	24.1	3.71	0.01	1.80	0.00		
W11-4	Tuff	H	24.1	3.4	20.7	3.72	0.01	1.80	0.01		
W11-4	Tuff	H	20.7	3.4	17.2	3.71	0.01	1.78	0.00		
W11-4	Tuff	H	17.2	3.4	13.8	3.66	0.01	1.76	0.00	15.66	1
W11-4	Tuff	H	13.8	3.4	10.3	3.65	0.01	1.74	0.00	15.35	1
W11-4	Tuff	H	10.3	3.4	6.9	3.59	0.01	1.71	0.00	14.82	1
W11-4	Tuff	H	6.9	3.4	3.4	3.50	0.01	1.68	0.01	14.28	1
W11-4	Tuff	H	5.2	3.4	1.7	3.51	0.04	1.63	0.00	13.56	1

Continued on next page

Table E.14 – continued from previous page

Sample ID	Sample type	Alteration intensity	P_c (MPa)	P_p (MPa)	P_{eff} (MPa)	V_p (km/s)	V_{p-SD} (km/s)	V_s (km/s)	V_{s-SD} (km/s)	E (GPa)	E_{SD} (GPa)
W11-3	Tuff	H	6.9	0.0	6.9	3.69	0.01	2.17	0.01	20.43	1
W11-3	Tuff	H	5.2	0.0	5.2	3.58	0.01	2.16	0.01	19.88	1
W11-3	Tuff	H	3.4	0.0	3.4	3.58	0.01	2.16	0.01	19.69	1
W11-3	Tuff	H	1.7	0.0	1.7	3.56	0.01	2.15	0.01	19.5	1
W11-3	Tuff	H	55.2	1.7	53.4	3.88	0.01	1.98	0.01		
W11-3	Tuff	H	48.3	1.7	46.5	3.86	0.01	1.96	0.01		
W11-3	Tuff	H	41.4	1.7	39.6	3.84	0.01	1.96	0.01		
W11-3	Tuff	H	34.5	1.7	32.8	3.84	0.01	1.95	0.01		
W11-3	Tuff	H	27.6	1.7	25.9	3.81	0.01	1.93	0.01		
W11-3	Tuff	H	24.1	1.7	22.4	3.78	0.02	1.92	0.01		
W11-3	Tuff	H	20.7	1.7	19.0	3.79	0.01	1.90	0.01		
W11-3	Tuff	H	17.2	1.7	15.5	3.81	0.01	1.89	0.01		
W11-3	Tuff	H	13.8	1.7	12.1	3.77	0.01	1.88	0.01	19.38	1
W11-3	Tuff	H	10.3	1.7	8.6	3.73	0.01	1.87	0.01	19.14	1
W11-3	Tuff	H	6.9	1.7	5.2	3.67	0.01	1.86	0.01	18.86	1
W11-3	Tuff	H	5.2	1.7	3.4	3.65	0.01	1.85	0.01	18.57	1
W11-3	Tuff	H	3.4	1.7	1.7	3.61	0.01	1.85	0.01	18.5	1
W11-3	Tuff	H	27.6	3.4	24.1	3.80	0.01	1.94	0.01		
W11-3	Tuff	H	24.1	3.4	20.7	3.79	0.01	1.92	0.01		
W11-3	Tuff	H	20.7	3.4	17.2	3.80	0.01	1.90	0.01		

Continued on next page

Table E.14 – continued from previous page

Sample ID	Sample type	Alteration intensity	P_c (MPa)	P_p (MPa)	P_{eff} (MPa)	V_p (km/s)	V_{p-SD} (km/s)	V_s (km/s)	V_{s-SD} (km/s)	E (GPa)	E_{SD} (GPa)
W11-3	Tuff	H	17.2	3.4	13.8	3.71	0.02	1.89	0.01	19.44	1
W11-3	Tuff	H	13.8	3.4	10.3	3.65	0.01	1.88	0.01	19.16	1
W11-3	Tuff	H	10.3	3.4	6.9	3.72	0.02	1.87	0.01	19.12	1
W11-3	Tuff	H	6.9	3.4	3.4	3.67	0.01	1.85	0.01	18.61	1
W11-3	Tuff	H	5.2	3.4	1.7	3.65	0.01	1.84	0.01	18.4	1
W11-3	Tuff	H	27.6	5.2	22.4	3.81	0.01	1.94	0.01		
W11-3	Tuff	H	24.1	5.2	19.0	3.78	0.01	1.91	0.01		
W11-3	Tuff	H	20.7	5.2	15.5	3.78	0.01	1.88	0.01		
W11-3	Tuff	H	17.2	5.2	12.1	3.68	0.01	1.88	0.01	19.22	1
W11-3	Tuff	H	13.8	5.2	8.6	3.67	0.01	1.87	0.01	19.03	1
W11-3	Tuff	H	10.3	5.2	5.2	3.65	0.01	1.85	0.01	18.66	1
W11-3	Tuff	H	6.9	5.2	1.7	3.64	0.02	1.84	0.01	18.39	1
W11-3	Tuff	H	27.6	6.9	20.7	3.79	0.01	1.94	0.01		
W11-3	Tuff	H	24.1	6.9	17.2	3.74	0.02	1.90	0.01		
W11-3	Tuff	H	20.7	6.9	13.8	3.73	0.02	1.87	0.01	19.14	1
W11-3	Tuff	H	17.2	6.9	10.3	3.71	0.01	1.88	0.01	19.27	1
W11-3	Tuff	H	13.8	6.9	6.9	3.69	0.01	1.86	0.01	18.9	1
W11-3	Tuff	H	10.3	6.9	3.4	3.69	0.01	1.85	0.01	18.64	1
W11-3	Tuff	H	27.6	10.3	17.2	3.78	0.01	1.90	0.01		
W11-3	Tuff	H	24.1	10.3	13.8	3.73	0.01	1.89	0.01	19.48	1

Continued on next page

Table E.14 – continued from previous page

Sample ID	Sample type	Alteration intensity	P_c (MPa)	P_p (MPa)	P_{eff} (MPa)	V_p (km/s)	V_{p-SD} (km/s)	V_s (km/s)	V_{s-SD} (km/s)	E (GPa)	E_{SD} (GPa)
W11-3	Tuff	H	20.7	10.3	10.3	3.73	0.02	1.87	0.01	19.14	1
W11-3	Tuff	H	17.2	10.3	6.9	3.68	0.02	1.85	0.01	18.71	1
W11-3	Tuff	H	13.8	10.3	3.4	3.67	0.01	1.85	0.01	18.61	1
W11-3	Tuff	H	27.6	13.8	13.8	3.77	0.01	1.88	0.01	19.38	1
W11-3	Tuff	H	24.1	13.8	10.3	3.70	0.01	1.87	0.01	19.09	1
W11-3	Tuff	H	20.7	13.8	6.9	3.68	0.02	1.86	0.01	18.88	1
W11-3	Tuff	H	17.2	13.8	3.4	3.64	0.01	1.84	0.01	18.39	1
W11-3	Tuff	H	27.6	17.2	10.3	3.74	0.01	1.87	0.01	19.16	1
W11-3	Tuff	H	24.1	17.2	6.9	3.74	0.01	1.86	0.01	18.98	1
W11-3	Tuff	H	20.7	17.2	3.4	3.64	0.01	1.85	0.01	18.55	1
W11-3	Tuff	H	27.6	20.7	6.9	3.71	0.02	1.86	0.01	18.93	1
W11-3	Tuff	H	24.1	20.7	3.4	3.68	0.02	1.85	0.01	18.62	1

Table E.15: Elastic properties of samples used in Chapter 4 from Mt.Taranaki. Here, P_{eff}-effective hydrostatic pressure, V_p-P-wave velocity, V_s-S-wave velocity, E-Young's modulus, and G-shear modulus.V_{p-SD}, V_{s-SD}, E_{SD}, and G_{SD} are standard deviations in P-wave velocity, S-wave velocity, Young's modulus, and shear modulus, respectively. Alteration intensities of the samples are shown by FS-Fresh to slightly altered, M-moderately altered, and H-highly altered. Sampling locality is represented by S-summit dome area, BAF-block and ash flow deposits, and DA-debris avalanche deposits.

Sample ID	Sample type	Sampling locality	Alteration intensity	P_{eff} (MPa)	V_p (km/s)	V_{p-SD} (km/s)	V_s (km/s)	V_{s-SD} (km/s)	E (GPa)	E_{SD} (GPa)	G (GPa)	G_{SD} (GPa)
T1-1	Lava	S	M	0	4.06	0.01	2.41	0.01	31.12	2	12.67	1
T2-1	Lava	S	M	0	3.84	0.03	2.44	0.02	27.71	1	11.93	1
T3-1	Lava	S	M	0	3.7	0	2.13	0	25.26	1	10.09	1
T4-1	Lava	S	FS	0	2.82	0.03	1.69	0.02	12.96	1	5.31	0
T5-1	Lava	S	M	0	4.1	0.01	2.29	0	31.29	2	12.29	1
T6-1	Lava	BAF	FS	0	2.22	0.01	1.38	0.01	11.2	1	4.72	0
T7-1	Lava	BAF	FS	0	2.96	0.01	1.7	0	16.22	1	6.47	0
T8-1	Lava	BAF	FS	0	3.4	0.01	2.17	0.01	27.77	1	12.01	1
T9-1	Lava	BAF	M	0	3.04	0.01	1.84	0.01	18.08	1	7.47	0
T10-1	Lava	BAF	FS	0	2.7	0.01	1.43	0.01	8.7	0	3.33	0
T11-1	Lava	BAF	FS	0	2.63	0.01	1.7	0	16.2	1	7.1	0
T12-1	Lava	BAF	M	0	1.93	0.01	1.25	0.01	7.54	0	3.31	0
T13-1	Lava	BAF	FS	0	2.36	0.01	1.49	0	12.16	1	5.2	0
T14-1	Lava	DA	FS	0	4.69	0.02	2.62	0.01	43.13	2	16.94	1
T15-1	Lava	DA	FS	0	5.08	0.01	2.88	0	56.73	3	22.45	1
T16-1	Lava	DA	FS	0	4.1	0.02	2.52	0.01	40.7	2	17.01	1

Continued on next page

Table E.15 – continued from previous page

Sample ID	Sample type	Sampling locality	Alteration intensity	P_{eff} (MPa)	V_p (km/s)	V_{p-SD} (km/s)	V_s (km/s)	V_{s-SD} (km/s)	E (GPa)	E_{SD} (GPa)	G (GPa)	G_{SD} (GPa)
T17-1	Lava	S	M	0	4.21	0.02	2.47	0.01	33.14	2	13.39	1
T18-1	Lava	S	M	0	4.51	0.02	2.61	0.01	41.51	2	16.63	1
T19-1	Lava	S	M	0	3.59	0.02	2.07	0.01	22.26	1	8.9	0
T20-1	Lava	S	H	0	3.09	0.08	2.01	0.05	15.69	1	6.92	0
T21-1	Lava	S	M	0	2.94	0.01	1.77	0.01	14.09	1	5.79	0
T22-1	Lava	S	M	0	4.88	0.03	2.81	0.02	48.48	2	19.36	1
T23-1	Lava	S	M	0	3.6	0.03	2.38	0.02	26.01	1	11.7	1
T24-1	Lava	S	M	0	4.15	0.02	2.49	0.01	35.41	2	14.53	1
T25-1	Lava	S	FS	0	4.28	0.01	2.58	0.01	37.94	2	15.62	1
T26-1	Lava	BAF	FS	0	2.74	0.02	1.53	0	15.08	1	5.92	0
T27-1	Lava	BAF	FS	0	2.73	0.01	1.74	0	18.36	1	7.93	0
T28-1	Lava	BAF	FS	0	3.23	0.03	2.08	0.02	22.53	1	9.83	0
T29-1	Lava	BAF	FS	0	3.44	0.02	2.03	0.01	23.11	1	9.37	0
T30-1	Lava	BAF	FS	0	3.43	0.02	2.14	0.01	26.02	1	11.01	1
T31-1	Lava	BAF	FS	0	3.16	0.02	1.88	0.01	22.41	1	9.14	0
T32-1	Lava	BAF	FS	0	2.76	0.02	1.77	0.01	15.87	1	6.9	0
T33-1	Lava	BAF	FS	0	2.56	0.01	1.73	0.01	11.47	1	5.31	0
T34-1	Lava	BAF	FS	0	3.05	0.01	1.86	0.01	16.49	1	6.85	0

References

Adam, L., & Otheim, T. (2013). Elastic laboratory measurements and modeling of saturated basalts. *Journal of Geophysical Research: Solid Earth*, *118*(3), 840–851. doi: 10.1002/jgrb.50090

Adelinet, M., Fortin, J., Guéguen, Y., Schubnel, A., & Geoffroy, L. (2010). Frequency and fluid effects on elastic properties of basalt: Experimental investigations. *Geophysical Research Letters*, *37*(2). doi: 10.1029/2009GL041660

Airo, M.-L. (2002). Aeromagnetic and aeroradiometric response to hydrothermal alteration. *Surveys in Geophysics*, *23*(4), 273–302. doi: 10.1023/A:1015556614694

AlHantoobi, A., Buz, J., O'Rourke, J., Langlais, B., & Edwards, C. (2020). Compositional Enhancement of Crustal Magnetization on Mars. *Geophysical Research Letters*, e2020GL090379. doi: 10.1029/2020GL090379

Al-Harthi, A., Al-Amri, R., & Shehata, W. (1999). The porosity and engineering properties of vesicular basalt in Saudi Arabia. *Engineering Geology*, *54*(3-4), 313–320. doi: 10.1016/S0013-7952(99)00050-2

Alken, P., Thébault, E., Beggan, C. D., Amit, H., Aubert, J., Baerenzung, J., ... others (2021). International geomagnetic reference field: the thirteenth generation. *Earth, Planets and Space*, *73*(1), 1–25. doi: 10.1186/s40623-020-01288-x

Allis, R., Armstrong, P., & Funnell, R. (1995). Implications of a high heat flow anomaly around New Plymouth, North Island, New Zealand. *New Zealand Journal of Geology and Geophysics*, *38*(2), 121–130. doi: 10.1080/00288306.1995.9514644

Alloway, B., McComb, P., Neall, V., Vucetich, C., Gibb, J., Sherburn, S., & Stirling, M. (2005). Stratigraphy, age, and correlation of voluminous debris-avalanche events from an ancestral Egmont Volcano: implications for coastal plain construction and regional hazard assessment. *Journal of the Royal Society of New Zealand*, *35*(1-2), 229–267. doi: 10.1080/03014223.2005.9517782

Anderson, D. L. (1989). *Theory of the Earth*. Blackwell Scientific Publications.

Ball, J. L., Calder, E., Hubbard, B. E., & Bernstein, M. L. (2013). An assessment of hydrothermal alteration in the Santiaguito lava dome complex, Guatemala: im-

plications for dome collapse hazards. *Bulletin of Volcanology*, *75*(1), 1–18. doi: 10.1007/s00445-012-0676-z

Ball, J. L., Stauffer, P. H., Calder, E., & Valentine, G. A. (2015). The hydrothermal alteration of cooling lava domes. *Bulletin of Volcanology*, *77*(12), 102. doi: 10.1007/s00445-015-0986-z

Bargar, K. E., & Keith, T. E. (1999). *Hydrothermal mineralogy of core from geothermal drill holes at Newberry volcano, Oregon* (No. 1578 - U.S. Geological Survey professional paper). US Geological Survey. `https://pubs.usgs.gov/pp/pp1578/`.

Baud, P., Schubnel, A., & Wong, T.-f. (2000). Dilatancy, compaction, and failure mode in Solnhofen limestone. *Journal of Geophysical Research: Solid Earth*, *105*(B8), 19289–19303. doi: 10.1029/2000JB900133

Baud, P., Wong, T.-f., & Zhu, W. (2014). Effects of porosity and crack density on the compressive strength of rocks. *International Journal of Rock Mechanics and Mining Sciences*, *67*, 202–211. doi: 10.1016/j.ijrmms.2013.08.031

Bazargan, M., & Gudmundsson, A. (2019). Dike-induced stresses and displacements in layered volcanic zones. *Journal of Volcanology and Geothermal Research*, *384*, 189–205. doi: 10.1016/j.jvolgeores.2019.07.010

Benning, L. G., Wilkin, R. T., & Barnes, H. (2000). Reaction pathways in the Fe–S system below 100 C. *Chemical Geology*, *167*(1-2), 25–51. doi: 10.1016/S0009-2541(99)00198-9

Berger, B. R. (1998). Hydrothermal alteration. In C. P. Marshall & R. W. Fairbridge (Eds.), *Encyclopedia of geochemistry* (pp. 331–333). Springer Netherlands. doi: 10.1007/1-4020-4496-8_162

Black, P. (1970). Observations on White Island volcano, New Zealand. *Bulletin volcanologique*, *34*(1), 158–167. doi: 10.1007/BF02597783

Blake, O., Faulkner, D., & Tatham, D. (2019). The role of fractures, effective pressure and loading on the difference between the static and dynamic Poisson's ratio and Young's modulus of Westerly granite. *International Journal of Rock Mechanics and Mining Sciences*, *116*, 87–98. doi: 10.1016/j.ijrmms.2019.03.001

Boudon, G., Villemant, B., Komorowski, J.-C., Ildefonse, P., & Semet, M. P. (1998). The hydrothermal system at Soufriere Hills Volcano, Montserrat (West Indies): Characterization and role in the on-going eruption. *Geophysical Research Letters*, *25*(19), 3693–3696. doi: 10.1029/98GL00985

Brown, J. M., & Abramson, E. H. (2016). Elasticity of calcium and calcium-sodium amphiboles. *Physics of the Earth and Planetary Interiors*, *261*, 161–171. doi: 10.1016/j.pepi.2016.10.010

Brown, L., & McEnroe, S. (2011). Remanent Magnetism. In H. K. Gupta (Ed.), *Encyclopedia of solid earth geophysics* (pp. 1024–1030). Dordrecht: Springer Netherlands. doi: 10.1007/978-90-481-8702-7_126

Burton, M., Hayer, C., Miller, C., & Christenson, B. (2021). Insights into the 9 December 2019 eruption of Whakaari/White Island from analysis of TROPOMI SO_2 imagery. *Science Advances*, *7*(25), eabg1218. doi: 10.1126/sciadv.abg1218

Butler, R. F., & Banerjee, S. K. (1975). Theoretical single-domain grain size range in magnetite and titanomagnetite. *Journal of Geophysical Research*, *80*(29), 4049–4058. doi: 10.1029/JB080i029p04049

Byrne, K., Lesage, G., Morris, W., Enkin, R., Gleeson, S., & Lee, R. (2019). Variability of outcrop magnetic susceptibility and its relationship to the porphyry Cu centers in the Highland Valley Copper district. *Ore geology reviews*, *107*, 201–217. doi: 10.1016/j.oregeorev.2019.02.015

Calder, E., Lavallée, Y., Kendrick, J. E., & Bernstein, M. (2015). Lava dome eruptions. In *The encyclopedia of volcanoes* (pp. 343–362). Elsevier. doi: 10.1016/B978-0-12-385938-9.00018-3

Calder, E., Luckett, R., Sparks, R., & Voight, B. (2002). Mechanisms of lava dome instability and generation of rockfalls and pyroclastic flows at Soufriere Hills Volcano, Montserrat. *Geological Society, London, Memoirs*, *21*(1), 173–190. doi: 10.1144/GSL.MEM.2002.021.01.08

Caratori Tontini, F., Davy, B., De Ronde, C., Embley, R., Leybourne, M., & Tivey, M. (2012). Crustal magnetization of Brothers volcano, New Zealand, measured by autonomous underwater vehicles: Geophysical expression of a submarine hydrothermal system. *Economic Geology*, *107*(8), 1571–1581. doi: 10.2113/econgeo.107.8.1571

Carrasco-Núñez, G., Vallance, J. W., & Rose, W. I. (1993). A voluminous avalanche-induced lahar from Citlaltépetl volcano, Mexico: implications for hazard assessment. *Journal of Volcanology and Geothermal Research*, *59*(1-2), 35–46. doi: 10.1016/0377-0273(93)90076-4

Cashman, K., & Blundy, J. (2000). Degassing and crystallization of ascending andesite and dacite. *Philosophical Transactions of the Royal Society of London. Series A: Mathematical, Physical and Engineering Sciences*, *358*(1770), 1487–1513. doi: 10.1098/rsta.2000.0600

Channell, J., & Hawthorne, T. (1990). Progressive dissolution of titanomagnetites at ODP Site 653 (Tyrrhenian Sea). *Earth and planetary science letters*, *96*(3-4), 469–480. doi: 10.1016/0012-821X(90)90021-O

Charbonnier, S. J., & Gertisser, R. (2008). Field observations and surface characteristics of pristine block-and-ash flow deposits from the 2006 eruption of Merapi Volcano, Java, Indonesia. *Journal of Volcanology and Geothermal Research*, *177*(4), 971–982. doi: 10.1016/j.jvolgeores.2008.07.008

Chardot, L., Jolly, A. D., Kennedy, B. M., Fournier, N., & Sherburn, S. (2015). Using volcanic tremor for eruption forecasting at White Island volcano (Whakaari), New Zealand. *Journal of Volcanology and Geothermal Research*, *302*, 11–23. doi: 10 .1016/j.jvolgeores.2015.06.001

Chouet, B. A. (1996). Long-period volcano seismicity: Its source and use in eruption forecasting. *Nature*, *380*(6572), 309–316. doi: 10.1038/380309a0

Chouet, B. A., Page, R. A., Stephens, C. D., Lahr, J. C., & Power, J. A. (1994). Precursory swarms of long-period events at Redoubt Volcano (1989–1990), Alaska: their origin and use as a forecasting tool. *Journal of Volcanology and Geothermal Research*, *62*(1-4), 95–135. doi: 10.1016/0377-0273(94)90030-2

Christenson, B., Reyes, A., Young, R., Moebis, A., Sherburn, S., Cole-Baker, J., & Britten, K. (2010). Cyclic processes and factors leading to phreatic eruption events: Insights from the 25 September 2007 eruption through Ruapehu Crater Lake, New Zealand. *Journal of Volcanology and Geothermal Research*, *191*(1-2), 15–32. doi: 10.1016/j.jvolgeores.2010.01.008

Christenson, B., White, S., Britten, K., & Scott, B. (2017). Hydrological evolution and chemical structure of a hyper-acidic spring-lake system on Whakaari/White Island, NZ. *Journal of Volcanology and Geothermal Research*, *346*, 180–211. doi: 10.1016/j.jvolgeores.2017.06.017

Clark, D. A. (2014). Magnetic effects of hydrothermal alteration in porphyry copper and iron-oxide copper–gold systems: A review. *Tectonophysics*, *624*, 46–65. doi: 10.1016/j.tecto.2013.12.011

Coats, R., Kendrick, J. E., Wallace, P. A., Miwa, T., Hornby, A. J., Ashworth, J. D., ... Lavallée, Y. (2018). Failure criteria for porous dome rocks and lavas: a study of Mt. Unzen, Japan. *Solid Earth*, *9*(6), 1299–1328. doi: 10.5194/se-9-1299-2018

Cole, J., & Lewis, K. (1981). Evolution of the Taupo-Hikurangi subduction system. *Tectonophysics*, *72*(1-2), 1–21. doi: 10.1016/0040-1951(81)90084-6

Cole, J., Thordarson, T., & Burt, R. (2000). Magma origin and evolution of White Island (Whakaari) volcano, Bay of plenty, New Zealand. *Journal of Petrology*, *41*(6), 867–895. doi: 10.1093/petrology/41.6.867

Collins, M., & Brown, J. (1998). Elasticity of an upper mantle clinopyroxene. *Physics and chemistry of minerals*, *26*(1), 7–13. doi: 10.1007/s002690050156

Cox, A. (1971). Remanent magnetization and susceptibility of late Cenozoic rocks from New Zealand. *New Zealand journal of geology and geophysics*, *14*(1), 192–207. doi: 10.1080/00288306.1971.10422470

Cronin, S. J., Zernack, A., Ukstins, I. A., Turner, M., Torres-Orozco, R., Stewart, R. B., ... others (2021). The geological history and hazards of a long-lived stratovolcano, Mt. Taranaki, New Zealand. *New Zealand Journal of Geology and Geophysics*, 1–23. doi: 10.1080/00288306.2021.1895231

Currenti, G., Bonaccorso, A., Del Negro, C., Scandura, D., & Boschi, E. (2010). Elasto-plastic modeling of volcano ground deformation. *Earth and Planetary Science Letters*, *296*(3-4), 311–318. doi: 10.1016/j.epsl.2010.05.013

Damaschke, M., Cronin, S. J., & Bebbington, M. S. (2018). A volcanic event forecasting model for multiple tephra records, demonstrated on Mt. Taranaki, New Zealand. *Bulletin of Volcanology*, *80*(1), 1–14. doi: 10.1007/s00445-017-1184-y

David, E., & Zimmerman, R. W. (2011). Elastic moduli of solids containing spheroidal pores. *International Journal of Engineering Science*, *49*(7), 544–560. doi: 10.1016/j.ijengsci.2011.02.001

Day, R., Fuller, M., & Schmidt, V. (1977). Hysteresis properties of titanomagnetites: grain-size and compositional dependence. *Physics of the Earth and planetary interiors*, *13*(4), 260–267. doi: 10.1016/0031-9201(77)90108-X

Dearing, J. A. (1994). *Environmental magnetic susceptibility: using the Bartington MS2 system*. Chi Pub.

Dearing, J. A., Dann, R., Hay, K., Lees, J., Loveland, P., Maher, B. A., & O'grady, K. (1996). Frequency-dependent susceptibility measurements of environmental materials. *Geophysical Journal International*, *124*(1), 228–240. doi: 10.1111/j.1365-246X.1996.tb06366.x

Del Moro, S., Renzulli, A., & Tribaudino, M. (2011). Pyrometamorphic processes at the magma–hydrothermal system interface of active volcanoes: Evidence from buchite ejecta of Stromboli (Aeolian Islands, Italy). *Journal of Petrology*, *52*(3), 541–564. doi: 10.1093/petrology/egq090

Del Negro, C., Currenti, G., & Scandura, D. (2009). Temperature-dependent viscoelastic modeling of ground deformation: Application to Etna volcano during the 1993–1997 inflation period. *Physics of the Earth and Planetary Interiors*, *172*(3-4), 299–309. doi: 10.1016/j.pepi.2008.10.019

del Potro, R., & Hürlimann, M. (2009). The decrease in the shear strength of volcanic materials with argillic hydrothermal alteration, insights from the summit region of Teide stratovolcano, Tenerife. *Engineering Geology*, *104*(1-2), 135–143. doi:

10.1016/j.enggeo.2008.09.005

de Moor, J., Stix, J., Avard, G., Muller, C., Corrales, E., Diaz, J., ... others (2019). Insights on hydrothermal-magmatic interactions and eruptive processes at Poás Volcano (Costa Rica) from high-frequency gas monitoring and drone measurements. *Geophysical Research Letters*, *46*(3), 1293–1302. doi: 10.1029/2018GL080301

Dempsey, D., Cronin, S., Mei, S., & Kempa-Liehr, A. (2020). Automatic precursor recognition and real-time forecasting of sudden explosive volcanic eruptions at Whakaari, New Zealand. *Nature Communications*, *11*(1), 1–8. doi: 10.1038/s41467-020-17375-2

Dentith, M., & Mudge, S. T. (2014). *Geophysics for the mineral exploration geoscientist.* Cambridge University Press. doi: 10.1017/CBO9781139024358

Dobson, P. F., Kneafsey, T. J., Hulen, J., & Simmons, A. (2003). Porosity, permeability, and fluid flow in the Yellowstone geothermal system, Wyoming. *Journal of Volcanology and Geothermal Research*, *123*(3-4), 313–324. doi: 10.1016/S0377-0273(03)00039-8

Downey, W., Kellett, R., Smith, I., Price, R., & Stewart, R. (1994). New palaeomagnetic evidence for the recent eruptive activity of Mt. Taranaki, New Zealand. *Journal of volcanology and geothermal research*, *60*(1), 15–27. doi: 10.1016/0377-0273(94)90095-7

Durán, E. L., Adam, L., & Wallis, I. C. (2019b). A robust methodology for time picking and error analysis of ultrasonic waveforms and rock densities in the laboratory. *Geophysics*, *84*(2), MR85–MR97. doi: 10.1190/geo2018-0331.1

Durán, E. L., Adam, L., Wallis, I. C., & Barnhoorn, A. (2019a). Mineral alteration and fracture influence on the elastic properties of volcaniclastic rocks. *Journal of Geophysical Research: Solid Earth*, *124*(5), 4576–4600.

Edmonds, M., Oppenheimer, C., Pyle, D. M., Herd, R. A., & Thompson, G. (2003). SO_2 emissions from Soufrière Hills Volcano and their relationship to conduit permeability, hydrothermal interaction and degassing regime. *Journal of Volcanology and Geothermal Research*, *124*(1-2), 23–43. doi: 10.1016/S0377-0273(03)00041-6

ESRI basemap. (2021a). *ESRI Satellite.* Retrieved from `https://server.arcgisonline.com/ArcGIS/rest/services/World_Imagery/MapServer/tile/%7Bz%7D/%7By%7D/%7Bx%7D&zmax=20&zmin=0`

ESRI basemap. (2021b). *ESRI Shaded Relief.* Retrieved from `https://server.arcgisonline.com/ArcGIS/rest/services/World_Shaded_Relief/MapServer/tile/%7Bz%7D/%7By%7D/%7Bx%7D&zmax=20&zmin=0`

Farquharson, J., Heap, M. J., Varley, N. R., Baud, P., & Reuschlé, T. (2015). Perme-

ability and porosity relationships of edifice-forming andesites: a combined field and laboratory study. *Journal of Volcanology and Geothermal Research*, *297*, 52–68. doi: 10.1016/j.jvolgeores.2015.03.016

Farquharson, J., Wild, B., Kushnir, A. R., Heap, M. J., Baud, P., & Kennedy, B. (2019). Acid-induced dissolution of andesite: Evolution of permeability and strength. *Journal of Geophysical Research: Solid Earth*, *124*(1), 257–273. doi: 10.1029/2018JB016130

Finn, C. A., Sisson, T. W., & Deszcz-Pan, M. (2001). Aerogeophysical measurements of collapse-prone hydrothermally altered zones at Mount Rainier volcano. *Nature*, *409*(6820), 600. doi: 10.1038/35054533

Fournier, N., & Chardot, L. (2012). Understanding volcano hydrothermal unrest from geodetic observations: Insights from numerical modeling and application to White Island volcano, New Zealand. *Journal of Geophysical Research: Solid Earth*, *117*(B11). doi: 10.1029/2012JB009469

Frank, D. (1995). Surficial extent and conceptual model of hydrothermal system at Mount Rainier, Washington. *Journal of Volcanology and Geothermal Research*, *65*(1-2), 51–80. doi: 10.1016/0377-0273(94)00081-Q

Fujii, M., Okino, K., Honsho, C., Dyment, J., Szitkar, F., Mochizuki, N., & Asada, M. (2015). High-resolution magnetic signature of active hydrothermal systems in the back-arc spreading region of the southern Mariana Trough. *Journal of Geophysical Research: Solid Earth*, *120*(5), 2821–2837. doi: 10.1002/2014JB011714

Fujii, M., Sato, H., Togawa, E., Shimada, K., & Ishibashi, J.-i. (2018). Seafloor hydrothermal alteration affecting magnetic properties of abyssal basaltic rocks: insights from back-arc lavas of the Okinawa Trough. *Earth, Planets and Space*, *70*(1), 1–14. doi: 10.1186/s40623-018-0958-6

Fujimoto, K., & Kikawa, E. (1989). Alteration of titanomagnetites and its related magnetic properties in the Noya Geothermal Area, Central Kyushu, Japan. *Journal of geomagnetism and geoelectricity*, *41*(1), 39–64. doi: 10.5636/jgg.41.39

Gee, J., & Kent, D. V. (1997). Magnetization of axial lavas from the southern East Pacific Rise (14–23 S): Geochemical controls on magnetic properties. *Journal of Geophysical Research: Solid Earth*, *102*(B11), 24873–24886. doi: 10.1029/97JB02544

Ghorbani, A., Revil, A., Coperey, A., Soueid Ahmed, A., Roque, S., Heap, M., ... Viveiros, F. (2018). Complex conductivity of volcanic rocks and the geophysical mapping of alteration in volcanoes. *Journal of Volcanology and Geothermal Research*, *357*, 106 - 127. doi: 10.1016/j.jvolgeores.2018.04.014

Giggenbach, W. F., Shinohara, H., Kusakabe, M., & Ohba, T. (2003, 01). Formation of

Acid Volcanic Brines through Interaction of Magmatic Gases, Seawater, and Rock within the White Island Volcanic-Hydrothermal System, New Zealand. In *Volcanic, Geothermal, and Ore-Forming Fluids: Rulers and Witnesses of Processes within the Earth* (Vol. 10, pp. 19–40). Society of Economic Geologists. doi: 10.5382/SP.10.02

Gražulis, S., Merkys, A., & Vaitkus, A. (2020). Crystallography Open Database (COD). *Handbook of Materials Modeling: Methods: Theory and Modeling*, 1863–1881.

Hacker, B. R., Abers, G. A., & Peacock, S. M. (2003). Subduction factory 1. Theoretical mineralogy, densities, seismic wave speeds, and H_2O contents. *Journal of Geophysical Research: Solid Earth*, *108*(B1). doi: 10.1029/2001JB001127

Hamling, I. J. (2017). Crater lake controls on volcano stability: Insights from White Island, New Zealand. *Geophysical Research Letters*, *44*(22), 11–311. doi: 10.1002/2017GL075572

Hamling, I. J. (2021). InSAR observations over the Taupō Volcanic Zone's cone volcanoes: insights and challenges from the New Zealand volcano supersite. *New Zealand Journal of Geology and Geophysics*, 3347-357. doi: 10.1080/00288306.2020.1721545

Harnett, C. E., Kendrick, J. E., Lamur, A., Thomas, M. E., Stinton, A., Wallace, P. A., ... Lavallée, Y. (2019a). Evolution of mechanical properties of lava dome rocks across the 1995–2010 eruption of Soufrière Hills volcano, Montserrat. *Frontiers in Earth Science*, *7*, 7. doi: 10.3389/feart.2019.00007

Harnett, C. E., Thomas, M. E., Calder, E., Ebmeier, S. K., Telford, A., Murphy, W., & Neuberg, J. (2019b). Presentation and analysis of a worldwide database for lava dome collapse events: the Global Archive of Dome Instabilities (GLADIS). *Bulletin of Volcanology*, *81*(3), 1–17. doi: 10.1007/s00445-019-1276-y

Heap, M., Russell, J., & Kennedy, L. (2016). Mechanical behaviour of dacite from Mount St. Helens (USA): A link between porosity and lava dome extrusion mechanism (dome or spine)? *Journal of Volcanology and Geothermal Research*, *328*, 159–177. doi: 10.1016/j.jvolgeores.2016.10.015

Heap, M. J., Baud, P., Meredith, P., Vinciguerra, S., & Reuschlé, T. (2014). The permeability and elastic moduli of tuff from Campi Flegrei, Italy: Implications for ground deformation modelling. *Solid Earth*, *5*(1), 25–44. doi: 10.5194/se-5-25-2014

Heap, M. J., Baumann, T., Gilg, H. A., Kolzenburg, S., Ryan, A. G., Villeneuve, M., ... Clynne, M. A. (2021b). Hydrothermal alteration can result in pore pressurization and volcano instability. *Geology*. doi: 10.1130/G49063.1

Heap, M. J., Baumann, T. S., Rosas-Carbajal, M., Komorowski, J.-C., Gilg, H. A., Villeneuve, M., ... others (2021a). Alteration-induced volcano instability at La

Soufrière de Guadeloupe (Eastern Caribbean). *Journal of Geophysical Research: Solid Earth*, e2021JB022514. doi: 10.1029/2021JB022514

Heap, M. J., Gravley, D. M., Kennedy, B. M., Gilg, H. A., Bertolett, E., & Barker, S. L. (2020b). Quantifying the role of hydrothermal alteration in creating geothermal and epithermal mineral resources: the Ohakuri ignimbrite (Taupō Volcanic Zone, New Zealand). *Journal of Volcanology and Geothermal Research*, *390*, 106703. doi: 10.1016/j.jvolgeores.2019.106703

Heap, M. J., Kennedy, B. M., Farquharson, J., Ashworth, J., Mayer, K., Letham-Brake, M., ... others (2017a). A multidisciplinary approach to quantify the permeability of the Whakaari/White Island volcanic hydrothermal system (Taupo Volcanic Zone, New Zealand). *Journal of Volcanology and Geothermal Research*, *332*, 88–108. doi: 10.1016/j.jvolgeores.2016.12.004

Heap, M. J., Kennedy, B. M., Pernin, N., Jacquemard, L., Baud, P., Farquharson, J., ... others (2015). Mechanical behaviour and failure modes in the Whakaari (White Island volcano) hydrothermal system, New Zealand. *Journal of Volcanology and Geothermal Research*, *295*, 26–42. doi: 10.1016/j.jvolgeores.2015.02.012

Heap, M. J., Troll, V. R., Kushnir, A. R., Gilg, H. A., Collinson, A. S., Deegan, F. M., ... Walter, T. R. (2019). Hydrothermal alteration of andesitic lava domes can lead to explosive volcanic behaviour. *Nature Communications*, *10*(1), 1–10. doi: 10.1038/s41467-019-13102-8

Heap, M. J., Villeneuve, M., Albino, F., Farquharson, J., Brothelande, E., Amelung, F., ... Baud, P. (2020a). Towards more realistic values of elastic moduli for volcano modelling. *Journal of Volcanology and Geothermal Research*, *390*, 106684. doi: 10.1016/j.jvolgeores.2019.106684

Heap, M. J., Violay, M., Wadsworth, F. B., & Vasseur, J. (2017b). From rock to magma and back again: The evolution of temperature and deformation mechanism in conduit margin zones. *Earth and Planetary Science Letters*, *463*, 92–100. doi: 10.1016/j.epsl.2017.01.021

Hedenquist, J. W., & Lowenstern, J. B. (1994). The role of magmas in the formation of hydrothermal ore deposits. *Nature*, *370*(6490), 519-527. doi: 10.1038/370519a0

Hedenquist, J. W., Simmons, S. F., Giggenbach, W. F., & Eldridge, C. S. (1993). White Island, New Zealand, volcanic-hydrothermal system represents the geochemical environment of high-sulfidation Cu and Au ore deposition. *Geology*, *21*(8), 731–734. doi: 10.1130/0091-7613(1993)021<0731:WINZVH>2.3.CO;2

Hemley, J., Hostetler, P., Gude, A., & Mountjoy, W. (1969). Some stability relations of alunite. *Economic Geology*, *64*(6), 599–612. doi: 10.2113/gsecongeo.64.6.599

Hemley, J., & Jones, W. R. (1964). Chemical aspects of hydrothermal alteration with emphasis on hydrogen metasomatism. *Economic Geology*, *59*(4), 538–569. doi: 10.2113/gsecongeo.59.4.538

Higgins, M. D. (1996). Crystal size distributions and other quantitative textural measurements in lavas and tuff from Egmont volcano (Mt. Taranaki), New Zealand. *Bulletin of Volcanology*, *58*(2), 194–204. doi: 10.1007/s004450050135

Honsho, C., Yamazaki, T., Ura, T., Okino, K., Morozumi, H., & Ueda, S. (2016). Magnetic anomalies associated with abundant production of pyrrhotite in a sulfide deposit in the Okinawa Trough, Japan. *Geochemistry, Geophysics, Geosystems*, *17*(11), 4413–4424. doi: 10.1002/2016GC006480

Hurst, A., & Christoffel, D. (1973). Surveillance of White Island volcano, 1968–1972: Part 3âĂŤThermo-magnetic effects due to volcanic activity. *New Zealand journal of geology and geophysics*, *16*(4), 965–972. doi: 10.1080/00288306.1973.10555236

Hurst, A., Rickerby, P., Scott, B., & Hashimoto, T. (2004). Magnetic field changes on White Island, New Zealand, and the value of magnetic changes for eruption forecasting. *Journal of volcanology and geothermal research*, *136*(1-2), 53–70. doi: 10.1016/j.jvolgeores.2004.03.017

Ikehata, K., & Maruoka, T. (2016). Sulfur isotopic characteristics of volcanic products from the September 2014 Mount Ontake eruption, Japan. *Earth, Planets and Space*, *68*(1), 1–7. doi: 10.1186/s40623-016-0496-z

Johnson, H., & Merrill, R. (1973). Low-temperature oxidation of a titanomagnetite and the implications for paleomagnetism. *Journal of Geophysical Research*, *78*(23), 4938–4949. doi: 10.1029/JB078i023p04938

Jolly, A., Chardot, L., Neuberg, J., Fournier, N., Scott, B., & Sherburn, S. (2012). High impact mass drops from helicopter: A new active seismic source method applied in an active volcanic setting. *Geophysical Research Letters*, *39*(12). doi: 10.1029/2012GL051880

Jolly, A., Lokmer, I., Christenson, B., & Thun, J. (2018). Relating gas ascent to eruption triggering for the April 27, 2016, White Island (Whakaari), New Zealand eruption sequence. *Earth, Planets and Space*, *70*(1), 1–15. doi: 10.1186/s40623-018-0948-8

Julia, F., Vladimir, L., Sergey, R., & David, Z. (2014). Effects of hydrothermal alterations on physical and mechanical properties of rocks in the Kuril–Kamchatka island arc. *Engineering Geology*, *183*, 80–95. doi: 10.1016/j.enggeo.2014.10.011

Kanakiya, S. (2021a). *Physicochemical and corresponding elastic properties of hydrothermally altered rocks from Whakaari (White Island) volcano, New Zealand.* doi: 10.17608/k6.auckland.13619297

Kanakiya, S. (2021b). *Magnetic properties of hydrothermally altered rocks from Whakaari (White Island) volcano, New Zealand.* doi: 10.17608/k6.auckland.14614599

Kanakiya, S. (2022). *Petrophysical and corresponding elastic and magnetic properties of hydrothermally altered lavas from Mt. Taranaki, New Zealand.* doi: 10.17608/k6.auckland.14706930

Kanakiya, S., Adam, L., Esteban, L., Rowe, M., & Shane, P. (2017). Dissolution and secondary mineral precipitation in basalts due to reactions with carbonic acid. *Journal of Geophysical Research: Solid Earth*, *122*(6), 4312–4327. doi: 10.1002/2017JB014019

Kanakiya, S., Adam, L., Rowe, M. C., Lindsay, J. M., & Esteban, L. (2021a). The role of tuffs in sealing volcanic conduits. *Geophysical Research Letters*, *48*, e2021GL095175. doi: 10.1029/2021GL095175

Kanakiya, S., Turner, G. M., Rowe, M. C., Adam, L., & Lindsay, J. M. (2021b). High remanent magnetization measured in hydrothermally altered lavas. *Geophysical Research Letters*, *48*(23), e2021GL095732. doi: 10.1029/2021GL095732

Kato, A., Terakawa, T., Yamanaka, Y., Maeda, Y., Horikawa, S., Matsuhiro, K., & Okuda, T. (2015). Preparatory and precursory processes leading up to the 2014 phreatic eruption of Mount Ontake, Japan. *Earth, Planets and Space*, *67*(1), 1–11. doi: 10.1186/s40623-015-0288-x

Kennedy, B., Farquhar, A., Hilderman, R., Villeneuve, M. C., Heap, M. J., Mordensky, S., ... Reuschlé, T. (2020). Pressure controlled permeability in a conduit filled with fractured hydrothermal breccia reconstructed from ballistics from Whakaari (White Island), New Zealand. *Geosciences*, *10*(4), 138. doi: 10.3390/geosciences10040138

Kennedy, B., Jellinek, A., Russell, J., Nichols, A., & Vigouroux, N. (2010). Time-and temperature-dependent conduit wall porosity: A key control on degassing and explosivity at Tarawera volcano, New Zealand. *Earth and Planetary Science Letters*, *299*(1-2), 126–137. doi: 10.1016/j.epsl.2010.08.028

Kereszturi, G., Schaefer, L., Mead, S., Miller, C., Procter, J., & Kennedy, B. (2021). Synthesis of hydrothermal alteration, rock mechanics and geophysical mapping to constrain failure and debris avalanche hazards at Mt. Ruapehu (New Zealand). *New Zealand Journal of Geology and Geophysics*, 1–22. doi: 10.1080/00288306.2021.1885048

Kereszturi, G., Schaefer, L. N., Miller, C., & Mead, S. (2020). Hydrothermal Alteration on Composite Volcanoes: Mineralogy, Hyperspectral Imaging, and Aeromagnetic Study of Mt Ruapehu, New Zealand. *Geochemistry, Geophysics, Geosystems*, *21*(9), e2020GC009270. doi: 10.1029/2020GC009270

Kilgour, G., Gates, S., Kennedy, B., Farquhar, A., McSporran, A., & Asher, C. (2019). Phreatic eruption dynamics derived from deposit analysis: A case study from a small, phreatic eruption from Whakaari/White Island, New Zealand. *Earth, Planets and Space*, *71*(1), 36. doi: 10.1186/s40623-019-1008-8

Kilgour, G., Kennedy, B., Scott, B., Christenson, B., Jolly, A., Asher, C., ... Saunders, K. (2021). Whakaari/White Island: A review of New Zealand's most active volcano. *New Zealand Journal of Geology and Geophysics*, 1–23. doi: 10.1080/00288306.2021.1918186

Kushnir, A. R., Martel, C., Bourdier, J.-L., Heap, M. J., Reuschlé, T., Erdmann, S., ... Cholik, N. (2016). Probing permeability and microstructure: unravelling the role of a low-permeability dome on the explosivity of Merapi (Indonesia). *Journal of Volcanology and Geothermal Research*, *316*, 56–71. doi: 10.1016/j.jvolgeores.2016.02.012

Large, R. R., Gemmell, J. B., Paulick, H., & Huston, D. L. (2001). The alteration box plot: A simple approach to understanding the relationship between alteration mineralogy and lithogeochemistry associated with volcanic-hosted massive sulfide deposits. *Economic geology*, *96*(5), 957–971. doi: 10.2113/gsecongeo.96.5.957

Leonard, G. S., Cole, R. P., Christenson, B. W., Conway, C. E., Cronin, S. J., Gamble, J. A., ... others (2021). Ruapehu and Tongariro stratovolcanoes: a review of current understanding. *New Zealand Journal of Geology and Geophysics*, 1–32. doi: 10.1080/00288306.2021.1909080

Lerner, G. A., Cronin, S. J., Bebbington, M. S., & Platz, T. (2019b). The characteristics of a multi-episode volcanic regime: the post-AD 960 Maero Eruptive Period of Mt. Taranaki (New Zealand). *Bulletin of Volcanology*, *81*(11), 1–24. doi: 10.1007/s00445-019-1327-4

Lerner, G. A., Cronin, S. J., Turner, G., & Rowe, M. (2019a). Paleomagnetic determination of the age and properties of the 1780–1800 AD dome effusion/collapse episode of Mt. Taranaki, New Zealand. *Bulletin of Volcanology*, *81*(3), 15. doi: 10.1007/s00445-019-1275-z

Letham-Brake, M. (2013). *Geological constraints on fluid flow at Whakaari volcano (White Island)* (Master's thesis, University of Canterbury). doi: 10.26021/7415

LINZ. (2021). *LINZ New Zealand Aerial Imagery.* Retrieved from `https://basemaps.linz.govt.nz/#@-41.8899962,174.0492437,z5`

Locke, C., Cassidy, J., & MacDonald, A. (1994). Constraints on the evolution of the Taranaki volcanoes, New Zealand, based on aeromagnetic data. *Bulletin of volcanology*, *56*(6-7), 552–560. doi: 10.1007/BF00302835

López, D. L., & Williams, S. N. (1993). Catastrophic volcanic collapse: Relation to hydrothermal processes. *Science*, *260*(5115), 1794–1796. doi: 10.1126/science.260.5115.1794

Majzlan, J., Speziale, S., Duffy, T. S., & Burns, P. (2006). Single-crystal elastic properties of alunite, KAl 3 (SO 4) 2 (OH) 6. *Physics and Chemistry of Minerals*, *33*(8), 567–573. doi: 10.1007/s00269-006-0104-z

Mas, A., Guisseau, D., Mas, P. P., Beaufort, D., Genter, A., Sanjuan, B., & Girard, J. (2006). Clay minerals related to the hydrothermal activity of the Bouillante geothermal field (Guadeloupe). *Journal of Volcanology and Geothermal Research*, *158*(3), 380 - 400. doi: 10.1016/j.jvolgeores.2006.07.010

Mavko, G. M., & Nur, A. (1978). The effect of nonelliptical cracks on the compressibility of rocks. *Journal of Geophysical Research: Solid Earth*, *83*(B9), 4459–4468. doi: 10.1029/JB083iB09p04459

Mayer, K., Scheu, B., Gilg, H. A., Heap, M. J., Kennedy, B. M., Lavallée, Y., ... Dingwell, D. B. (2015). Experimental constraints on phreatic eruption processes at Whakaari (White Island volcano). *Journal of Volcanology and Geothermal Research*, *302*, 150–162. doi: 10.1016/j.jvolgeores.2015.06.014

Mayer, K., Scheu, B., Montanaro, C., Yilmaz, T. I., Isaia, R., Aßbichler, D., & Dingwell, D. B. (2016). Hydrothermal alteration of surficial rocks at Solfatara (Campi Flegrei): Petrophysical properties and implications for phreatic eruption processes. *Journal of Volcanology and Geothermal Research*, *320*, 128–143. doi: 10.1016/j.jvolgeores.2016.04.020

Mayer, K., Scheu, B., Yilmaz, T. I., Montanaro, C., Gilg, H. A., Rott, S., ... Dingwell, D. B. (2017). Phreatic activity and hydrothermal alteration in the Valley of Desolation, Dominica, Lesser Antilles. *Bulletin of Volcanology*, *79*(12), 82. doi: 10.1007/s00445-017-1166-0

Miller, C. A., Christenson, B. W., Byrdina, S., Vandemeulebrouck, J., Brakenrig, T., Britten, K., ... Epstein, G. (2020). Snapshot of a magmatic/hydrothermal system from electrical resistivity tomography and fumarolic composition, Whakaari/White Island, New Zealand. *Journal of Volcanology and Geothermal Research*, 106909. doi: 10.1016/j.jvolgeores.2020.106909

Moon, V., Bradshaw, J., & de Lange, W. (2009). Geomorphic development of White Island Volcano based on slope stability modelling. *Engineering Geology*, *104*(1-2), 16–30. doi: 10.1016/j.enggeo.2008.08.003

Moon, V., Bradshaw, J., Smith, R., & de Lange, W. (2005). Geotechnical characterisation of stratocone crater wall sequences, White Island Volcano, New Zealand.

Engineering geology, *81*(2), 146–178. doi: 10.1016/j.enggeo.2005.07.014

Mordensky, S., Heap, M., Kennedy, B., Gilg, H., Villeneuve, M., Farquharson, J., & Gravley, D. (2019). Influence of alteration on the mechanical behaviour and failure mode of andesite: Implications for shallow seismicity and volcano monitoring. *Bulletin of Volcanology*, *81*(8), 44. doi: 10.1007/s00445-019-1306-9

Mordensky, S., Villeneuve, M., Kennedy, B., Heap, M., Gravley, D., Farquharson, J., & Reuschlé, T. (2018). Physical and mechanical property relationships of a shallow intrusion and volcanic host rock, Pinnacle Ridge, Mt. Ruapehu, New Zealand. *Journal of Volcanology and Geothermal Research*, *359*, 1–20. doi: 10.1016/j.jvolgeores.2018.05.020

Moskowitz, B. M. (1980). Theoretical grain size limits for single-domain, pseudo-single-domain and multi-domain behavior in titanomagnetite (x= 0.6) as a function of low-temperature oxidation. *Earth and Planetary Science Letters*, *47*(2), 285–293. doi: 10.1016/0012-821X(80)90045-X

Navelot, V., Géraud, Y., Favier, A., Diraison, M., Corsini, M., Lardeaux, J.-M., ... Beauchamps, G. (2018). Petrophysical properties of volcanic rocks and impacts of hydrothermal alteration in the Guadeloupe Archipelago (West Indies). *Journal of Volcanology and Geothermal Research*, *360*, 1–21. doi: 10.1016/j.jvolgeores.2018.07.004

Néel, L. (1949). Théorie du traînage magnétique des ferromagnétiques en grains fins avec application aux terres cuites. *Annales de géophysique*, *5*, 99–136. Retrieved from `https://hal.archives-ouvertes.fr/hal-03070532`

Nicolosi, I., Caracciolo, F. D., Branca, S., Ferlito, C., & Chiappini, M. (2016). The earliest open conduit eruptive center of the Etnean region: evidence from aeromagnetic, geophysical, and geological data. *Bulletin of volcanology*, *78*(7), 1–11. doi: 10.1007/s00445-016-1042-3

Norini, G., Bustos, E., Arnosio, M., Baez, W., Zuluaga, M. C., & Roverato, M. (2020). Unusual volcanic instability and sector collapse configuration at Chimpa volcano, central Andes. *Journal of Volcanology and Geothermal Research*, *393*, 106807. doi: 10.1016/j.jvolgeores.2020.106807

Ogiso, M., Matsubayashi, H., & Yamamoto, T. (2015). Descent of tremor source locations before the 2014 phreatic eruption of Ontake volcano, Japan. *Earth, Planets and Space*, *67*(1), 1–12. doi: 10.1186/s40623-015-0376-y

Ojha, L., Karunatillake, S., Karimi, S., & Buffo, J. (2021). Amagmatic hydrothermal systems on Mars from radiogenic heat. *Nature communications*, *12*(1), 1–11. doi: 10.1038/s41467-021-21762-8

Oliva-Urcia, B., Kontny, A., Vahle, C., & Schleicher, A. M. (2011). Modification of the magnetic mineralogy in basalts due to fluid–rock interactions in a high-temperature geothermal system (Krafla, Iceland). *Geophysical Journal International*, *186*(1), 155–174. doi: 10.1111/j.1365-246X.2011.05029.x

Opfergelt, S., Delmelle, P., Boivin, P., & Delvaux, B. (2006). The 1998 debris avalanche at Casita volcano, Nicaragua: Investigation of the role of hydrothermal smectite in promoting slope instability. *Geophysical Research Letters*, *33*(15). doi: 10.1029/2006GL026661

Panalytical, B. (2012). *HighScore Plus Version 3.0.5.* PANalytical B.V. (Almelo, The Netherlands)

Pandarinath, K., Shankar, R., Santoyo, E., Shetty, S. B., García-Soto, A. Y., & Gonzalez-Partida, E. (2019). A rock magnetic fingerprint of hydrothermal alteration in volcanic rocks-An example from the Los Azufres Geothermal Field, Mexico. *Journal of South American Earth Sciences*, *91*, 260–271. doi: 10.1016/j.jsames.2019.02.018

Peltier, A., Scott, B., & Hurst, T. (2009). Ground deformation patterns at White Island volcano (New Zealand) between 1967 and 2008 deduced from levelling data. *Journal of volcanology and geothermal research*, *181*(3-4), 207–218. doi: 10.1016/j.jvolgeores.2009.01.020

Pirajno, F. (2009). Hydrothermal processes and wall rock alteration. In *Hydrothermal processes and mineral systems* (pp. 73–164). Springer Netherlands. doi: 10.1007/978-1-4020-8613-7

Platz, T., Cronin, S. J., Cashman, K. V., Stewart, R. B., & Smith, I. E. (2007). Transition from effusive to explosive phases in andesite eruptions - A case-study from the AD1655 eruption of Mt. Taranaki, New Zealand. *Journal of Volcanology and Geothermal Research*, *161*(1-2), 15–34. doi: 10.1016/j.jvolgeores.2006.11.005

Platz, T., Cronin, S. J., Procter, J., Neall, V. E., & Foley, S. F. (2012). Non-explosive, dome-forming eruptions at Mt. Taranaki, New Zealand. *Geomorphology*, *136*(1), 15–30. doi: 10.1016/j.geomorph.2011.06.016

Pola, A., Crosta, G., Fusi, N., Barberini, V., & Norini, G. (2012). Influence of alteration on physical properties of volcanic rocks. *Tectonophysics*, *566-567*, 67–86. doi: 10.1016/j.tecto.2012.07.017

Price, R., Stewart, R., Woodhead, J., & Smith, I. (1999). Petrogenesis of high-K arc magmas: evidence from Egmont volcano, North Island, New Zealand. *Journal of petrology*, *40*(1), 167–197. doi: 10.1093/petroj/40.1.167

Procter, J., Cronin, S., Zernack, A., Lube, G., Stewart, R., Nemeth, K., & Keys, H. (2014). Debris flow evolution and the activation of an explosive hydrothermal

system; Te Maari, Tongariro, New Zealand. *Journal of Volcanology and Geothermal Research*, *286*, 303–316. doi: 10.1016/j.jvolgeores.2014.07.006

Procter, J., Cronin, S. J., Platz, T., Patra, A., Dalbey, K., Sheridan, M., & Neall, V. (2010). Mapping block-and-ash flow hazards based on Titan 2D simulations: A case study from Mt. Taranaki, NZ. *Natural Hazards*, *53*(3), 483–501. doi: 10.1007/s11069-009-9440-x

Reid, M. E., Brien, D. L., & Waythomas, C. F. (2010b). *Preliminary slope-stability analysis of Augustine Volcano: Chapter 14 in The 2006 eruption of Augustine Volcano, Alaska* (Tech. Rep.). US Geological Survey. doi: 10.3133/pp176914

Reid, M. E., Keith, T. E., Kayen, R. E., Iverson, N. R., Iverson, R. M., & Brien, D. L. (2010a). Volcano collapse promoted by progressive strength reduction: New data from Mount St. Helens. *Bulletin of volcanology*, *72*(6), 761–766. doi: 10.1007/s00445-010-0377-4

Reid, M. E., Sisson, T. W., & Brien, D. L. (2001). Volcano collapse promoted by hydrothermal alteration and edifice shape, Mount Rainier, Washington. *Geology*, *29*(9), 779–782. doi: 10.1130/0091-7613(2001)029<0779:VCPBHA>2.0.CO;2

Revil, A., Coperey, A., Heap, M. J., & Carbillet, L. (2020). A geophysical index to map alteration, permeability, and mechanical properties within volcanoes. Application to the soft volcanic rocks from Whakaari/White Island (New Zealand). *Journal of Volcanology and Geothermal Research*, 106945. doi: 10.1016/j.jvolgeores.2020.106945

Revil, A., Le Breton, M., Niu, Q., Wallin, E., Haskins, E., & Thomas, D. (2017). Induced polarization of volcanic rocks–1. surface versus quadrature conductivity. *Geophysical Journal International*, *208*(2), 826–844. doi: 10.1093/gji/ggw444

Riveros, K., Veloso, E., Campos, E., Menzies, A., & Véliz, W. (2014). Magnetic properties related to hydrothermal alteration processes at the Escondida porphyry copper deposit, northern Chile. *Miner Deposita*, *49*(6), 693–707. doi: 10.1007/s00126-014-0514-7

Robb, L. (2013). Hydrothermal ore-forming processes. In *Introduction to ore-forming processes* (p. 129-216). John Wiley and Sons, Incorporated. Retrieved from `https://ebookcentral.proquest.com`

Rodríguez-Elizarrarás, S., Siebe, C., Komorowski, J.-C., Espíndola, J. M., & Saucedo, R. (1991). Field observations of pristine block-and ash-flow deposits emplaced April 16–17, 1991 at Volcan de Colima, Mexico. *Journal of volcanology and geothermal research*, *48*(3-4), 399–412. doi: 10.1016/0377-0273(91)90054-4

Roverato, M., Cronin, S., Procter, J., & Capra, L. (2015). Textural features as indicators

of debris avalanche transport and emplacement, Taranaki volcano. *Bulletin*, *127*(1-2), 3–18. doi: 10.1130/B30946.1

Rowe, G., & Brantley, S. L. (1993). Estimation of the dissolution rates of andesitic glass, plagioclase and pyroxene in a flank aquifer of Poás Volcano, Costa Rica. *Chemical Geology*, *105*(1-3), 71–87. doi: 10.1016/0009-2541(93)90119-4

Rowe, M., & Brewer, B. J. (2018). AMORPH: A statistical program for characterizing amorphous materials by X-ray diffraction. *Computers & Geosciences*, *120*, 21–31. doi: 10.1016/j.cageo.2018.07.004

Saxena, V., Krief, M., & Adam, L. (2018). *Handbook of Borehole Acoustics and Rock Physics for Reservoir Characterization*. Elsevier. doi: 10.1016/C2016-0-03411-3

Schindelin, J., Arganda-Carreras, I., Frise, E., Kaynig, V., Longair, M., Pietzsch, T., ... others (2012). Fiji: an open-source platform for biological-image analysis. *Nature methods*, *9*(7), 676–682. doi: 10.1038/nmeth.2019

Scolamacchia, T., & Cronin, S. J. (2016). Idiosyncrasies of volcanic sulfur viscosity and the triggering of unheralded volcanic eruptions. *Frontiers in Earth Science*, *4*, 24. doi: 10.3389/feart.2016.00024

Shanks, W. P. (2012). *Hydrothermal alteration in volcanogenic massive sulfide occurrence model* (Scientific Investigations Report No. 2010âĂŞ5070 âĂŞC). U.S. Geological Survey. Retrieved from `https://pubs.usgs.gov/sir/2010/5070/c/Chapter11SIR10-5070-C-3.pdf`

Shi, P. (1992, 10). Fluid fugacities and phase equilibria in the Fe-Si-O-H-S system. *American Mineralogist*, *77*(9-10), 1050-1066.

Spieler, O., Kennedy, B., Kueppers, U., Dingwell, D. B., Scheu, B., & Taddeucci, J. (2004). The fragmentation threshold of pyroclastic rocks. *Earth and Planetary Science Letters*, *226*(1-2), 139–148.

Sruoga, P., Rubinstein, N., & Hinterwimmer, G. (2004). Porosity and permeability in volcanic rocks: a case study on the Serie Tobífera, South Patagonia, Argentina. *Journal of Volcanology and Geothermal Research*, *132*(1), 31 - 43. doi: 10.1016/S0377-0273(03)00419-0

Stern, T., & Benson, A. (2011). Wide-angle seismic imaging beneath an andesitic arc: Central North Island, New Zealand. *Journal of Geophysical Research: Solid Earth*, *116*(B9). doi: 10.1029/2011JB008337

Stern, T., Stratford, W., & Salmon, M. (2006). Subduction evolution and mantle dynamics at a continental margin: Central North Island, New Zealand. *Reviews of Geophysics*, *44*(4). doi: 10.1029/2005RG000171

Stewart, R., Price, R., & Smith, I. (1996). Evolution of high-K arc magma, Egmont

volcano, Taranaki, New Zealand: evidence from mineral chemistry. *Journal of Volcanology and Geothermal Research*, *74*(3-4), 275–295. doi: 10.1016/S0377-0273(96)00049-2

Stix, J., & de Moor, J. M. (2018). Understanding and forecasting phreatic eruptions driven by magmatic degassing. *Earth, Planets and Space*, *70*(1), 83. doi: 10.1186/s40623-018-0855-z

Stoffregen, R. E. (1987). Genesis of acid-sulfate alteration and Au-Cu-Ag mineralization at Summitville, Colorado. *Economic Geology*, *82*(6), 1575–1591. doi: 10.2113/gsecongeo.82.6.1575

Szitkar, F., Dyment, J., Choi, Y., & Fouquet, Y. (2014). What causes low magnetization at basalt-hosted hydrothermal sites? Insights from inactive site Krasnov (MAR 16^{O}38'N). *Geochemistry, Geophysics, Geosystems*, *15*(4), 1441–1451. doi: 10.1002/2014GC005284

Tapia, J., Townley, B., Córdova, L., Poblete, F., & Arriagada, C. (2016). Hydrothermal alteration and its effects on the magnetic properties of Los Pelambres, a large multistage porphyry copper deposit. *Journal of Applied Geophysics*, *132*, 125–136. doi: 10.1016/j.jappgeo.2016.07.005

Tauxe, L. (2010). *Essentials of paleomagnetism*. University of California Press.

Technologies, V. (2022). *Steady state gas permeameter and porosimeter (Poroperm).* `https://www.vinci-technologies.com/rocks-and-fluids/routine-core-analysis/gas-permeability/poroperm-steady-state-gas-permeameter-and-porosimeter/113423/`. (Accessed: 2022-02-06)

Torrent, J., Liu, Q., & Barrón, V. (2010). Magnetic susceptibility changes in relation to pedogenesis in a Xeralf chronosequence in northwestern Spain. *European Journal of Soil Science*, *61*(2), 161–173. doi: 10.1111/j.1365-2389.2009.01216.x

Torres-Orozco, R., Cronin, S. J., Pardo, N., & Palmer, A. S. (2017). New insights into Holocene eruption episodes from proximal deposit sequences at Mt. Taranaki (Egmont), New Zealand. *Bulletin of Volcanology*, *79*(1), 1–25. doi: 10.1007/s00445-016-1085-5

Turner, G., Alloway, B. V., Dixon, B. J., & Atkins, C. B. (2018). Thermal history of volcanic debris flow deposits on the eastern flanks of Mt. Taranaki, New Zealand: Implications for future hazards. *Journal of Volcanology and Geothermal Research*, *353*, 55–67. doi: 10.1016/j.jvolgeores.2018.01.017

Turner, M., Cronin, S. J., Bebbington, M. S., Smith, I. E., & Stewart, R. B. (2011). Integrating records of explosive and effusive activity from proximal and distal sequences: Mt. Taranaki, New Zealand. *Quaternary International*, *246*(1-2), 364–

373. doi: 10.1016/j.quaint.2011.07.006

Valentine, G. A., & White, J. (2012). Revised conceptual model for maar-diatremes: Subsurface processes, energetics, and eruptive products. *Geology*, *40*(12), 1111–1114. doi: 10.1130/G33411.1

Varekamp, J. C., Ouimette, A. P., Herman, S. W., Bermúdez, A., & Delpino, D. (2001). Hydrothermal element fluxes from Copahue, Argentina: A "beehive" volcano in turmoil. *Geology*, *29*(11), 1059–1062. doi: 10.1130/0091-7613(2001)029<1059:HEFFCA>2.0.CO;2

Voight, B. (2000). Structural stability of andesite volcanoes and lava domes. *Philosophical Transactions of the Royal Society of London. Series A: Mathematical, Physical and Engineering Sciences*, *358*(1770), 1663–1703. doi: 10.1098/rsta.2000.0609

Voight, B., & Elsworth, D. (1997). Failure of volcano slopes. *Geotechnique*, *47*(1), 1–31. doi: 10.1680/geot.1997.47.1.1

Voight, B., Janda, R., Glicken, H., & Douglass, P. (1983). Nature and mechanics of the Mount St Helens rockslide-avalanche of 18 May 1980. *Geotechnique*, *33*(3), 243–273. doi: 10.1680/geot.1983.33.3.243

Wallace, L. M., Beavan, J., McCaffrey, R., & Darby, D. (2004). Subduction zone coupling and tectonic block rotations in the North Island, New Zealand. *Journal of Geophysical Research: Solid Earth*, *109*(B12). doi: 10.1029/2004JB003241

Walsh, J. (1965). The effect of cracks on the compressibility of rock. *Journal of Geophysical Research*, *70*(2), 381–389. doi: 10.1029/JZ070i002p00381

Wang, S., Chang, L., Wu, T., & Tao, C. (2020). Progressive dissolution of titanomagnetite in high-temperature hydrothermal vents dramatically reduces magnetization of Basaltic Ocean crust. *Geophysical Research Letters*, *47*(8), e2020GL087578. doi: 10.1029/2020GL087578

Werner, C., Hurst, T., Scott, B., Sherburn, S., Christenson, B., Britten, K., ... Mullan, B. (2008). Variability of passive gas emissions, seismicity, and deformation during crater lake growth at White Island Volcano, New Zealand, 2002–2006. *Journal of Geophysical Research: Solid Earth*, *113*(B1).

Werner, C., Schipper, I., Richardson, J., Barry, P. H., & Cronin, S. J. (2020). Detecting and quantifying magmatic tracers in cold springs on Mount Taranaki Volcano, New Zealand. In *AGU Fall Meeting Abstracts* (Vol. 2020, pp. V038–0004). Retrieved from `https://ui.adsabs.harvard.edu/abs/2020AGUFMV038.0004W/abstract`

White, D. (1974). Diverse origins of hydrothermal ore fluids. *Economic Geology*, *69*(6), 954–973. doi: 10.2113/gsecongeo.69.6.954

White, J., & McClintock, M. (2001). Immense vent complex marks flood-basalt eruption

in a wet, failed rift: Coombs Hills, Antarctica. *Geology*, *29*(10), 935–938. doi: 10.1130/0091-7613(2001)029<0935:IVCMFB>2.0.CO;2

White, J., & Ross, P. (2011). Maar-diatreme volcanoes: A review. *Journal of Volcanology and Geothermal Research*, *201*(1-4), 1–29. doi: 10.1016/j.jvolgeores.2011.01.010

Wilson, C., Houghton, B., McWilliams, M., Lanphere, M., Weaver, S., & Briggs, R. (1995). Volcanic and structural evolution of Taupo Volcanic Zone, New Zealand: a review. *Journal of volcanology and geothermal research*, *68*(1-3), 1–28. doi: 10.1016/0377-0273(95)00006-G

Winkler, K. W., & Murphy, W. F. (1995). Acoustic Velocity and Attenuation in Porous Rocks. In T. J. Ahrens (Ed.), *Rock physics & phase relations* (p. 20-34). American Geophysical Union. doi: 10.1029/RF003p0020

Wong, T.-f., & Baud, P. (2012). The brittle-ductile transition in porous rock: A review. *Journal of Structural Geology*, *44*, 25–53.

Woodward, D., & Caldwell, T. G. (1992). Apparent magnetisation from aeromagnetic data. *Exploration Geophysics*, *23*(1/2), 447–452. doi: 10.1071/EG992447

Woodward, D., & Mumme, T. (1993). Variation of magnetisation on White Island, New Zealand. *New Zealand Journal of Geology and Geophysics*, *36*(4), 447–451. doi: 10.1080/00288306.1993.9514590

Wyering, L., Villeneuve, M., Wallis, I., Siratovich, P., Kennedy, B., Gravley, D., & Cant, J. (2014). Mechanical and physical properties of hydrothermally altered rocks, Taupo Volcanic Zone, New Zealand. *Journal of Volcanology and Geothermal Research*, *288*, 76 - 93. doi: 10.1016/j.jvolgeores.2014.10.008

Xu, W., Van der Voo, R., Peacor, D. R., & Beaubouef, R. T. (1997). Alteration and dissolution of fine-grained magnetite and its effects on magnetization of the ocean floor. *Earth and Planetary Science Letters*, *151*(3-4), 279–288. doi: 10.1016/S0012-821X(97)81854-7

Yeganeh-Haeri, A., Weidner, D. J., & Parise, J. B. (1992). Elasticity of α-cristobalite: a silicon dioxide with a negative Poisson's ratio. *Science*, *257*(5070), 650–652. doi: 10.1126/science.257.5070.650

Zernack, A., Cronin, S., Neall, V., & Procter, J. (2011). A medial to distal volcaniclastic record of an andesite stratovolcano: detailed stratigraphy of the ring-plain succession of south-west Taranaki, New Zealand. *International Journal of Earth Sciences*, *100*(8), 1937–1966. doi: 10.1007/s00531-010-0610-6

Zernack, A., Cronin, S. J., Bebbington, M. S., Price, R. C., Smith, I. E., Stewart, R. B., & Procter, J. (2012). Forecasting catastrophic stratovolcano collapse: A model based on Mount Taranaki, New Zealand. *Geology*, *40*(11), 983–986. doi:

10.1130/G33277.1

Zernack, A., Procter, J., & Cronin, S. J. (2009). Sedimentary signatures of cyclic growth and destruction of stratovolcanoes: a case study from Mt. Taranaki, New Zealand. *Sedimentary Geology*, *220*(3-4), 288–305. doi: 10.1016/j.sedgeo.2009.04.024

Zhou, W., Van der Voo, R., Peacor, D. R., Wang, D., & Zhang, Y. (2001). Low-temperature oxidation in MORB of titanomagnetite to titanomaghemite: A gradual process with implications for marine magnetic anomaly amplitudes. *Journal of Geophysical Research: Solid Earth*, *106*(B4), 6409–6421. doi: 10.1029/2000JB900447

Zhu, W., Baud, P., Vinciguerra, S., & Wong, T.-f. (2011). Micromechanics of brittle faulting and cataclastic flow in Alban Hills tuff. *Journal of Geophysical Research: Solid Earth*, *116*(B6).

Zhu, W., & Wong, T.-f. (1997). The transition from brittle faulting to cataclastic flow: Permeability evolution. *Journal of Geophysical Research: Solid Earth*, *102*(B2), 3027–3041. doi: 10.1029/96JB03282

Zimbelman, D., Rye, R. O., & Breit, G. (2005). Origin of secondary sulfate minerals on active andesitic stratovolcanoes. *Chemical Geology*, *215*(1-4), 37–60. doi: 10.1016/j.chemgeo.2004.06.056

Zimbelman, D., Watters, R., Firth, I., Breit, G., & Carrasco-Nunez, G. (2004). Stratovolcano stability assessment methods and results from Citlaltépetl, Mexico. *Bulletin of Volcanology*, *66*(1), 66–79. doi: 10.1007/s00445-003-0296-8

Zorn, E. U., Rowe, M., Cronin, S. J., Ryan, A. G., Kennedy, L. A., & Russell, J. K. (2018). Influence of porosity and groundmass crystallinity on dome rock strength: A case study from Mt. Taranaki, New Zealand. *Bulletin of Volcanology*, *80*(4), 35. doi: 10.1007/s00445-018-1210-8

Zylberman, W., Quesnel, Y., Rochette, P., Osinski, G. R., Marion, C., & Gattacceca, J. (2017). Hydrothermally enhanced magnetization at the center of the Haughton impact structure? *Meteoritics & Planetary Science*, *52*(10), 2147–2165. doi: 10.1111/maps.12917